THE WHITE BOOK

JINR NEUTRINO PROGRAM

Editors: Vadim A.Bednyakov, Dmitry V.Naumov.
Dubna/JINR. May 13, 2014

In the end of 2013 the neutrino physics community of JINR has realised the need of a consolidated neutrino physics and astrophysics program to be formulated in our Institute. The relevant work has beed strated in the beginning of 2014 and this document summarizes our *first version* of the JINR neutrino program.

It is organized as follows. In Chapter 1 a short review of both modern challenges in the neutrino physics and the JINR neutrino program, aimed to address a considerable part of the open neutrino questions, is given. Basic concepts of neutrino physics in both theory and experiment are described in some more details in Chapter 2. Every experiment in which JINR participates in the framework of the neutrino program is described in a uniform format in the subsequent Chapters 3–14.

We would like to thank Igor Belolaptikov, Victor Brudanin, Vyacheslav Egorov, Maxim Gonchar, Konstantin Gusev, Yury Gornushkin, Sergey Dmitrievsky, Oleg Kochetov, Alexey Lubashevskiy, Dmitry Medvedev, Igor Nemchenok, Alexander Olshevsky, Oleg Samoylov, Oleg Smirnov, Anatoly Smolnikov, Mark Shirchenko, Evgeny Yakushev for their great efforts in drafting the corresponding experimental chapters. Our special thanks go to Maxim Gonchar, Christopher Kullenberg and Michail Potapov for their help in preparation of this Book.

Vadim A.Bednyakov, Dmitry V.Naumov

Contents

1 JINR Neutrino Program 5

2 Basic Concepts of Neutrino Physics 17

3 BAIKAL Experiment 45

4 BOREXINO Experiment 71

5 νGeN Project 101

6 DANSS Experiment 113

7 Daya Bay Experiment 127

8 GEMMA Experiment 163

9 GERDA Experiment 177

10 JUNO Project 195

11 NOVA Experiment 229

12 OPERA Experiment 239

13 SuperNEMO Experiment 251

14 EDELWEISS Experiment 269

Chapter 1

JINR Neutrino Program

1.1 World class level

If we ask ourselves "What scientific problem is most important and fundamental?", the obvious answer will be that it is the one which allows answering the maximum number of topical questions at the current stage of development of science.

In elementary particle physics this topical question is the nature of the neutrino, that is, the neutrino properties that govern their interactions with the outer world. By these properties it is meant their masses, the character of their transformations to one another (mixing), the total number of their types, whether they are Dirac or Majorana particles, whether they have electromagnetic properties, what their natural sources are, etc.

It is a key interdisciplinary problem indeed, which runs through entire elementary particle physics, cosmology, and astrophysics. Nonzero neutrino masses are of importance for devising modern theories of elementary particles and gaining better insight into the structure of the Universe and the origin of large-scale formations like clusters of galaxies. Here light massive neutrinos play the part of the so-called dark (or hidden) matter. Investigation of neutrino properties (including electromagnetic ones) is necessary for solving the solar neutrino problem, clarifying mechanisms for supernovae and energy production in stars (the Sun) and the Earth's interior, and understanding the whys and wherefores of ultrahigh-energy cosmic rays. Only the investigation of cosmic neutrino fluxes seems to provide information on the most remote corners of space. The problem of relic neutrinos, the existence of which follows from the modern concept of the early Universe, has not been solved so far. Neutrinos, along with photons, are believed to be the most abundant particles in the Universe. A possibility that neutrinos are a clue to the baryon asymmetry, i.e., that the excess of baryons (relative to antibaryons) could arise from violation of CP symmetry in the lepton sector with the participation of (heavy) neutrinos, is widely discussed now. It is thus impossible to even approach the answer to the question of why the surrounding world is as it is without understanding the neutrino properties.

On the other hand, the physics of neutrinos and weak interactions very closely borders with the so-called new physics beyond the Standard Model of elementary particles. It undoubtedly exists, and investigation into it will result in a new, more general theory of elementary particles (based on, for example, the idea of supersymmetry). Of major interest is the search for the processes, particles, and laws that contradict the theoretical concepts of the Standard Model.

Research in neutrino physics has gained particular importance after the mixing angle θ_{13} of the Pontecorvo–Maki–Nakagawa–Sakata matrix was measured in 2011–2012. The angle turned out to be quite large (about 0.15 rad), which allows a promising continuation of the reactor and accelerator experiments on the study of the neutrino mass hierarchy and CP violation effects in the lepton sector. Both issues are highly important for understanding the role of the neutrino in the evolution of the Universe and the origin of the baryon asymmetry.

Another topic of current interest is sterile neutrinos. This interest grew keenly after the deficit of the reactor antineutrino flux was discovered "with a tip of the pen" (by performing new calculations). The assumed effect can be interpreted as oscillations of reactor antineutrinos to sterile states at a small distance. There are already several groups that set the goal to observe this deficit and thus to find sterile neutrinos. JINR scientists appear to have the best prospects in this field with their DANSS experiment at the Kalinin Nuclear Power Plant using the reactor antineutrino flux of unique intensity.

In modern physics, there is nothing to compete with neutrino research with respect to fundamental and worldview-shaping importance and potential for new unexpected discoveries.

In addition, applied research in neutrino physics also holds unique promise. Quite recently, neutrinos from the Earth interior, so-called geoneutrinos, were detected with new, very sensitive equipment. With the fundamental nature of this phenomenon left aside, investigation of geoneutrino fluxes is of the utmost importance for understanding geophysical processes in the depth of our planet and thus the causes for various natural disasters and climate changes.

Applied neutrino investigations of processes in reactors performed with antineutrinos at industrial and research nuclear reactors for nuclear power production purposes come to a new level. They comprise continuous measurement of reactor power and a degree of fuel burnup, on-line fuel burnup tomography, development of compact antineutrino detectors for remotely monitoring (in real time) production and unauthorized extraction of plutonium during the operation of a reactor (to prevent proliferation of nuclear weapons), etc.

This is the most prominent example of benefits from fundamental science. To solve its specific problems, neutrino physics requires unique equipment never seen before. Its development gives rise to utterly new, equally unique technologies, materials, and instruments, which in turn are in demand in other fields of science and in everyday life.

Thus, the interdisciplinary character is inherent in neutrino physics. This general physical interdisciplinary property is behind the diverse manifestations of neutrinos and their significance in many areas of modern physics, astrophysics, and applied research.

The neutrino is a neutral fermion (spin 1/2) participating in weak and gravitational interactions. Today there are three known types of neutrino, each with its own mass. In the Standard Model, each of the massive neutrinos and the electron, muon, and tau lepton (charged leptons) are arranged in the corresponding lepton doublets. Interacting with the charged W boson, lepton doublets intermix, which is described by the lepton mixing matrix. The mixing lepton matrix, known as the Pontecorvo–Maki–Nakagawa–Sakata matrix, is parameterized by three mixing angles and a single phase related to charge-parity (CP) violation in weak interactions. If the neutrino is identical to the antineutrino (Majorana neutrino), two more phases related to CP violation are added to the mixing matrix. It is now known that neutrinos are massive and masses of two out of three types of neutrino are restricted to a rather narrow interval. All three neutrino mixing angles are also measured. Nevertheless, a lot of open fundamental questions remain in neutrino physics, for example,

- What is the mass of the lightest neutrino?
- Why is the neutrino mass extremely small and is it caused, on the contrary, by a very large mass parameter of any kind.
- What is mass hierarchy, i.e., the order of neutrino masses, $m_1 > m_3$ or vice versa?
- Why neutrino mixing angles are so large (in comparison with quark ones)?
- Do neutrinos have CP-odd phases and can they explain quantitative imbalance in matter and antimatter in the Universe?
- Are neutrinos Dirac particles or Majorana particles?
- How can relic neutrinos be found?
- Do neutrinos have non-standard properties, e.g., electromagnetic or others, the indication of which could be the large anomalous magnetic moment of the neutrino?
- Are there other types of neutrinos, namely, sterile, and what are their masses?

There are other fundamentally important questions regarding neutrinos, for example,

- How are neutrino properties manifested in extremely rare neutrinoless processes?
- How can coherent neutrino scattering from nuclei be detected?
- What is the origin of astrophysical neutrino fluxes?
- Is it possible to observe heavy neutrinos at accelerators, such as LHC etc.?

Physicists all over the world are making efforts to solve these immensely important questions. The number of experimental and theoretical groups engaged in the neutrino research increases every year, as does the number of the publications on this topic; more and more conferences are held. No doubt, this tendency will survive in the foreseeable future.

In the United States, it is neutrino physics that becomes a priority direction in high-energy physics in the post-Tevatron era. Apart from the already running experiments MINOS, MiniBooNe, Minerva, and SciBooNe, an accelerator experiment NOvA is being launched with the aim of determining the neutrino mass hierarchy and measuring the CP-violating phase. The next step under discussion in this direction is the LBNE project (Long-Baseline Neutrino Experiment), which is even more sensitive to these parameters.

In Japan, the traditionally strong neutrino program based on the world-known experiments SuperKamiokande, K2K, T2K, is reinforced with a new project HyperKamiokande.

China, after the nonzero value of the mixing angle θ_{13} was discovered in the Daya Bay reactor experiment, and Korea, after this result was confirmed in the RENO experiment, are also moving to the leading positions in neutrino physics.

In China (on the governmental level) another unique reactor experiment, JUNO (successor of Daya Bay), is planned for determining the mass hierarchy, performing precise measurements of mixing angles, and solving several other important questions of neutrino physics and astrophysics.

In Europe, important experiments on the search for the neutrinoless double decay of nuclei (SuperNEMO, GERDA, CUORICINO, etc.) are now under way in the Modane and Gran Sasso underground laboratories. Unique experiments with solar neutrinos (BOREXINO) and accelerator neutrinos (OPERA, ICARUS) are being conducted. The first data on cosmic neutrinos are arriving from the ANTARES neutrino telescope in the deep Mediterranean Sea. Despite current financial problems, the promising European neutrino project LBNO (for investigation of neutrino oscillations at a large distance from the accelerator) is still on the agenda. Such a unique detector as the Baikal Neutrino Telescope can be useful for the project.

As is known, after the discovery of the Higgs boson at the LHC and measurement of the mixing angle θ_{13} in the Daya Bay and RENO experiments (2012) the most impressive result was obtained in 2013 in the IceCube international Antarctic experiment, where the first ultrahigh-energy neutrinos of extraterrestrial—galactic or even extragalactic—origin were detected!

It is worth mentioning again that all these new steps were made using special large-scale physical facilities constructed by many countries that joined their efforts in developing fundamentally new physical and technological methods for research.

Neutrino physics and astrophysics, together with high-energy elementary particle physics, are the highways in the strategic development of modern fundamental elementary particle physics. They are expected to lead to the most fundamental and impressive discoveries that can change our vision of the world.

Today we have every reason to say that neutrino physics has entered into an era of precise measurements and systematic search for answers to the fundamental questions on the nature of the neutrino, and that is why it is “doomed to success”.

1.2 Neutrino physics and astrophysics in Russian Federation

At JINR, systematic experimental research in the fields of neutrino physics, weak interactions, rare processes, and astrophysics has been carried out by several divisions of the Dzhelepov Laboratory of Nuclear Problems (DLNP). This almost 55-year-old tradition is rooted in the works and ideas of B.M. Pontecorvo and his colleagues. DLNP physicists obtained quite a few fundamentally important results in this area. Now these investigations are carried on at the highest level both in Russia (Dubna) and abroad within prestigious and ambitious international collaborations.

1.2. NEUTRINO PHYSICS AND ASTROPHYSICS IN RUSSIAN FEDERATION

The endeavor of our institute to address the most fundamental and promising issues of modern nuclear physics, advancement of neutrino physics and astrophysics to the leading position due to the logic of world development, crucial results obtained in this field in 2011–2012 (with the participation of JINR), traditions preserved and successfully developing at JINR, experimental basis and appropriate experience, fruitful and mutually beneficial collaboration with (and not limited to) Russian institutes in this field, and talented and well-trained young scientists are the indications that neutrino physics and astrophysics research can, and should, be given top priority at JINR.

Equally, with the acknowledged “JINR leaders”, investigation of “superheavy elements and the island of stability” (FLNR), search for new physics at the LHC (DLNP, VBLHEP), condensed matter studies at the upgraded IBR–2M facility (FLNP), development of the NICA collider (VBLHEP), “Neutrino Physics and Astrophysics” must become a cornerstone of the updated long-term program of attractive research at our institute.

It is worth noting that the Seven-Year Plan for the Development of JINR adopted three years ago is being successfully fulfilled. Much has already been done (our superheavy elements were recognized, the IBR–2M was put into operation, the first results were obtained from LHC, etc.), and much has changed in the world as well (new important results were obtained, global plans and goals were revised).

Obviously, the Seven-Year Plan needs updating, especially with respect to enhancing the prestige of neutrino physics and astrophysics and their related rare process physics. Particularly noteworthy in this connection is the existing and continuously expanding cooperation in this field with Russian institutes, especially with the Institute for Nuclear Research, Russian Academy of Science (INR). It appears to be helpful to conclude an agreement on cooperation between JINR and INR which could formalize the already existing cooperation between JINR and INR in the field of neutrino physics and astrophysics.

In Russia all world-level research in neutrino physics and astrophysics are now carried out with the participation (sometimes decisive) of JINR and INR scientists. Apart from them, scientists from the Kurchatov Institute, Institute of Theoretical and Experimental Physics (ITEP), Petersburg Nuclear Physics Institute (PNPI), Lebedev Physical Institute (FIAN), Institute of High-Energy Physics (IHEP), etc. take part these researches.

The decision of the restored Neutrino Council at the Russian Academy of Sciences (summer 2012) clearly demonstrates this state of affairs. BAIKAL, BAKSAN, and Kalinin Nuclear Power Plant are three major “neutrino” infrastructure formations, and they are all closely connected with INR and JINR. Next follows participation in international neutrino experiments of the highest level like BOREXINO, T2K, OPERA, Daya Bay, NEMO, SuperNEMO, EDELWEISS, etc. Here again the participation and contribution of JINR and INR are decisive.

1.3 Neutrino Colloquium: review of the JINR Neutrino Program

At DLNP the neutrino physics research has been carried on since the time of Bruno Pontecorvo, who laid the foundation of the scientific school in this field. Now the JINR Neutrino Program includes a wide and diverse range of lines of research in neutrino physics, the flagship of the DLNP research program. To assess the state of affairs in the field, a special Neutrino Colloquium was held on 16–17 December 2013. Ten reports covering the entire DLNP neutrino program were presented within those two days. In his invited report, Academician V.A. Rubakov made a review of neutrino physics and cosmology.

JINR physicists are active in working with solar neutrinos (BOREXINO), accelerator neutrinos (OPERA, NOvA), reactor neutrinos (Daya Bay, DANSS, GEMMA–2, JUNO), and astrophysical and atmospheric neutrinos (BAIKAL) and also in searching for neutrinoless double beta decay (SuperNEMO, GERDA, Majorana). The program of the Colloquium also included a report on the EDELWEISS experiment aimed at searching for dark matter. The new experiments NOvA and JUNO are also expected to yield fundamentally important results. It is noted that high-level results have been obtained in the experiments

- The Daya Bay experiment, where the last unknown mixing angle θ_{13} was measured, which became one of the most significant results in physics in 2012. Later, in 2013, the effective difference of masses squared Δm^2_{ee} was precisely measured.

- The BOREXINO experiment, where the flux of beryllium, boron and pep solar neutrinos was measured. Limits were imposed on the effective magnetic moment of the neutrino, axion flux from the Sun, and Pauli principle violation. Day-night asymmetry was measured, and seasonal variations in the beryllium neutrino flux were investigated. The flux of geoneutrinos from decays of natural radioactive isotopes in the Earth was measured.

- The OPERA experiment, where three tau neutrino candidates from $\nu_\mu \to \nu_\tau$ oscillations were observed with a significance of 3.4 standard deviations.

- The GEMMA–2 experiment, where the world's best limit on the (anti)neutrino magnetic moment was obtained. The GERDA experiment, in its first phase obtained the new limit on the lifetime of ^{76}Ge nuclei against the two-neutrino double beta decay which overlaps with the known result of the Heidelnerg-Moscow Collaboration. The second phase of the GERDA experiment will further explore the degenerate Majorana neutrino mass scale aiming to increase its sensitivity by a factor of about 10.

- NEMO-3, where a new limit was obtained for the lifetime of the 100Mo nucleus (against the neutrinoless double beta decay). At the moment the collaboration is busy constructing the SuperNEMO Demonstrator module (one fourth is already constructed). It is expected to be commissioned in the low-background Modane Underground Laboratory, France, in 2015.

- BAIKAL, where atmospheric neutrino fluxes were measured and a deep-underwater neutrino detection technique was developed. In 2006–2010, all key elements and systems of the GVD (Gigaton Volume Detector) were developed, built, and tested. The prototyping phase of the GVD project was started in Lake Baikal and will conclude with deployment of a cluster comparable with ANTARES in 2015.
- DANSS, where the DANSSino prototype facility was created. Background conditions at the Kalinin Nuclear Power Plant were studied. The chosen general concept of the detector was shown to be correct. Improvements were made in its design. The reactor antineutrino spectrum was measured.
- EDELWEISS, dedicated to the search for dark matter in the Universe, where a wide range of dark-matter particle masses was excluded.

JINR also takes a noticeable part in implementation of new projects and upgrading of existing ones, which can provide the scientific community with new fundamental knowledge of the nature of the neutrino and physics beyond the Standard Model. These experiments are

- NOvA and JUNO, which will answer the question of the neutrino mass hierarchy. Note however that the potential of these experiments is not restricted to this fundamental problem; their research program is diverse and interesting.
- BAIKAL, a basic facility of DNLP. This experiment becomes immensely important in the light of observation of the first ultrahigh-energy astrophysical neutrinos in the IceCube experiment, which opens a new field in physics, namely, neutrino astronomy. The upgraded BAIKAL facility should play a major part in this field. BAIKAL will also allow the neutrino mass hierarchy to be studied using atmospheric neutrinos.
- DANSS and GEMMA–2, experiments conducted in the neutrino laboratory and on the basic facility of DNLP at the Kalinin Nuclear Power Plant. DANSS is intended for answering the question of whether there are sterile neutrinos with a mass in the range of 0.1 to 1 eV and for optimizing techniques for antineutrino diagnostics of intrareactor processes. Apart from increasing sensitivity to the neutrino magnetic moment, an important goal of the GEMMA–2 experiment will be searching for events of coherent neutrino scattering from germanium nuclei.
- GERDA and SuperNEMO, which can answer the question whether the neutrino is a Majorana particle and determine the absolute neutrino mass scale. Note that the potential of this possible discovery greatly depends on the answer to the question of the neutrino mass hierarchy sought for in other experiments, such as NOvA, JUNO, and BAIKAL, which again demonstrates interrelation of different approaches to the investigation of neutrinos.
- BOREXINO, with the precision considerably upgraded in its next phase. Its physics program has a noteworthy continuation, namely, the SOX project aimed at studying

sterile neutrinos using artificial neutrino sources. Sources placed outside (2014–2015) and inside (2016–2017) the BOREXINO detector, together with its remarkable energy and spatial resolution, will make it possible to obtain a tight limit on the region of allowable parameters. Another direction of research at BOREXINO will be dark matter searches using a new Dark Side facility.

- EDELWEISS, which will increase its sensitivity to dark matter particles.

The JINR Neutrino Program is aimed at searching for answers to all the aforementioned, so far unsolved fundamental questions of neutrino physics. It seems unlikely that there is any other research institution in the world with an equally wide neutrino research area. JINR scientists play a noticeable or leading part in all projects of the neutrino program due to their high skills and available modern experimental basis. Apart from experienced physicists, a large number of students, postgraduates, and young scientists are involved in the neutrino program, which allows for an optimistic view of the future of neutrino physics at JINR.

It should be stressed that the JINR Neutrino Program is based on a powerful infrastructure, at the heart of which there are three JINR basic facility complexes:

1. The unique neutrino telescope in Lake Baikal (BAIKAL–GVD).

2. The Kalinin Nuclear Power Plant (GEMMA, DANSS, DANSSino, low-threshold highly pure Ge detectors, etc.).

3. The unique (actually international) low-background underground laboratories in Gran Sasso (BOREXINO, Dark Side, OPERA, GERDA) and Modane (EDELWEISS, SuperNEMO, NEMO–3).

In addition, JINR, as a participant in international collaborations, conducts experiments with beams of reactor neutrinos (Daya Bay, JUNO) and accelerator neutrons (NOvA).

Note that further full-fledged participation in new breakthrough experiments in the scope of the JINR Neutrino Program requires a substantial increase in financing. For example, an additional amount of JINR investments in such experiments as JUNO and DANSS is estimated at about four million dollars for a period to the year 2020.

1.4 Baikal Neutrino Telescope: a new JINR basic facility

According to the report made by Academician V.A. Rubakov, now there are ideal conditions for building a first-rate world-competitive astrophysical neutrino observatory using the technologies developed in the BAIKAL experiment. Indeed, observation of astrophysical neutrinos in IceCube indicates a strong possibility of neutrino astronomy. It requires having a large, scanned sensitive volume, which can be achieved by installing more sections with PMTs. All R&D stages in the BAIKAL experiment have already been accomplished, and the increase in the volume of the detector therefore linearly depends on the invested amounts of money and time. In the years 2006–2010 prototypes of the main BAIKAL–GVD telescope elements and systems were developed, built, and tested using experimental strings in Lake Baikal. Since 2011, the elements and systems of the BAIKAL–GVD Cluster have been under comprehensive testing as stand-alone modules. The implementation of this program will result in the standard elements of the telescope systems being ready for mass production and the first Cluster (given the name Dubna) comparable in sensitivity with ANTARES (Mediterranean Sea) will be put into operation coming years (2015).

Investment of an additional five million dollars every year for three to four years will allow the scanned volume to be increased to a level comparable with IceCube. BAIKAL will enjoy the obvious northern hemisphere advantage of being able to detect particles from the center of our galaxy. In addition, of fundamental importance for emerging neutrino astronomy, is a good angular resolution of the detector, which is another advantage of BAIKAL over IceCube. Thus, in three to four years of dynamic and timely financing it will be possible to reach the world level in this field of science. The corresponding decision must be taken as soon as possible since ANTARES and IceCube are already giving the first results.

Now JINR has favorable conditions for taking this decision with its experienced team of scientists who play a major part in the BAIKAL experiment. There are a lot of young people in this team, which guarantees long and successful work. All the R&D stages are accomplished. Thus, the proposed upgrading of the detector is sure to be successful and yield scientific results at the world level.

In his talk at the Neutrino Colloquium Academician V.A. Rubakov summed up: *“A couple of years ago IceCube saw nothing, and BAIKAL was not so important. Today IceCube sees galactic neutrinos, but not very distinctly. The demand for the detector in Baikal has sharply increased. It is a long-term project with bright and considerable prospects, which is inevitable to produce unique results sooner or later!”*

- Reports from workshop on neutrino program:
  - http://indico.jinr.ru/conferenceDisplay.py?confId=756
- Report of V.A. Bednyakov on this topic at SC:
  - http://indico.jinr.ru/conferenceDisplay.py?confId=472
  - http://indico.jinr.ru/getFile.py/access?contribId=12&resId=0&materialId=1&confId=472
- Report of A.G. Olshevsky at SC:
  - http://indico.jinr.ru/conferenceDisplay.py?confId=644

Table 1.1: JINR Neutrino Program research financing profile till 2018
(boldly printed is necessary additional funding)

Project	2013 (actual)	2014	2015	2016	2017	2018	Total
BAIKAL	JINR: $180K Extra-budget: $300K JINR 470K rub grants = $500K	$500K +$600K	$500K +**$5M**	$500K +**$5M**	$500K +**$5M**	$500K +**$5M**	$26M +**$20M**
Daya Bay	JINR: 20K$ Extra-budget: $45K 500K rub RFBR 500K rub ГК = $95K	$100K +$300K	$100K				$0.5M
BOREXINO	JINR: $10K Extra-budget: 200K rub = $15K	$20K	$20K	$20K	$20K	$20K	$0.1M
OPERA	JINR: $60K Extra-budget: $50K = $110K	$110K	$70K				$0.18M
SuperNEMO	JINR 50K$ Extra-budget: 1500K rub = $95K	$95K	$105K	$100K	$100K	$100K	$0.5M
GEMMA-2/3	JINR: $57K Extra-budget: $40K = $100K	$100K	$100K	$100K	$100K	$100K	$0.5M
GERDA	JINR: $39K Extra-budget: 510K rub = $55K	$50K	$50K	$50K	$50K	$50K	$0.25M
DANSS	JINR: $203K Extra-budget: 1M rub RFBR = $235K	$235K	$200K +**$250K**	200K$ +**$250K**	200K$ +**$250K**	200K$ +**$250K**	$2.035M +**$1M**
EDELWEISS	JINR: $67K Extra-budget: 2900K rub RFBR = $155K	$155K	$150K	$100K	$100K	$100K	$0.605M
NOvA		$150K	$150K	$150K	($100K)	($100K)	$0.450M
JUNO			$100K +**$250K**	$100K +**$250K**	$100K +**$250K**	$100K +**$250K**	$1.400M +**$1M**
TOTAL	7-Year Plan ⟶	$2415K ($2300K)					

Thus, in order to

- keep and strengthen the leading positions of JINR in neutrino physics and astrophysics, the most fundamental and rapidly developing fields of modern physics,
- give top priority to JINR research in this area and attract young scientists from JINR member states,
- strengthen international cooperation between JINR and institutes all over the world, and especially with Russian research centers,
- make a decisive breakthrough in the development of the unique JINR basic facility BAIKAL-GVD and thus take the lead in the world neutrino astrophysics research,
- maintain long-term fundamental and applied (anti)neutrino-beam investigations at the Kalinin Nuclear Power Plant,

i.e., to fulfill successfully the JINR neutrino physics and astrophysics program described above, **the following should be approved by the order of the JINR Director:**

- Targeted yearly investment of additional $5 million from the JINR budget in the BAIKAL-GVD project for a period of four years, which will allow JINR and the Russian Federation to have a unique installation superior to IceCube by 2018.
- Additional funding in an amount of $1 million (until the year 2018) for construction of the necessary infrastructure for the experiments at the Kalinin Nuclear Power Plant (DANSS, GEMMA, etc.).
- Additional funding in the amount of $1 million (till the year 2018) for the JUNO experiment to be mainly spent for constructing the necessary infrastructure for the manufacture of the facility elements at DLNP.

The total addition to the DLNP budget from the JINR budget is $22M for a period of four years.

Chapter 2

Basic Concepts of Neutrino Physics

2.1 Short history of the neutrino

The neutrino is a light weakly interacting fermion. There are plenty of neutrinos around us with various energies and from various sources. Probably the oldest particles in our Universe are relic neutrinos whose flux on Earth is one of the most intensive at $\sim 10^{13} - 10^{14}(\nu+\bar{\nu})/\text{cm}^2\text{s}$, while their energies are tiny, around 10^{-4} eV. A nuclear power plant witch emits about 10^{20} antineutrinos per each GWt of thermal energy with energies ranging from hundreds of keV to about ten MeV. A typical flux of antineutrinos at 10 meters from the reactor core is about $10^{13}\bar{\nu}_e/\text{cm}^2\text{s}$. The sun, through chains of nuclear reactions, produces many neutrinos with energies ranging from keV to 15 MeV and the flux on Earth is about $10^{10}\nu/\text{cm}^2\text{s}$. The Earth's interior emits antineutrinos with energies from keV to MeV and the flux on the Earth surface is about $10^6\bar{\nu}/\text{см}^2\text{c}$. Cosmic rays (mostly protons and light nuclei) bombard the Earth's atmosphere producing neutrinos and antineutrinos with energies ranging from some 100 MeV to hundreds of GeV with the flux about $10^6\nu/\text{cm}^2\text{s}$. Active galactic nuclei (AGN) are expected to produce nearly the same amount of (anti)neutrinos but with energies at the TeV scale. Scatterings of ultra high energy cosmic rays on relic microwave background in a sequence of weak decays produce diffusive cosmic neutrinos with energies above 10^3 TeV and vanishing fluxes about $10^{-12}\nu/\text{cm}^2\text{s}$. Characteristic fluxes of neutrinos and antineutrinos are displayed in Fig. 2.1.

How was the neutrino discovered? Everything began, as often happens, from an experimental puzzle. Early in the 20th century, after the discovery of the atomic structure of matter, active experimental studies of different atoms and nuclei started, and it was soon revealed that certain nuclei are unstable: they emit α, β, γ rays. These rays, having received their names from the first three letters of the Greek alphabet, differed from each other in electric charge (the positively and negatively charged α and β rays, respectively, and the neutral γ rays) and in their penetrability. The α and γ rays had one common feature: they had monochromatic lines in the energy spectra. The lines in the spectra are determined by the difference in the energy of initial and final nuclei, which is undoubtedly in agreement with the law of energy conservation. Against this background, the observable continuous spectrum of electrons in β decays of nuclei appeared to violate the laws of conservation of energy, momentum and angular momentum.

W. Pauli was the first to give the correct explanation of the observable facts by writing in his famous letter "To radioactive ladies and gentlemen" of December 4, 1930, among

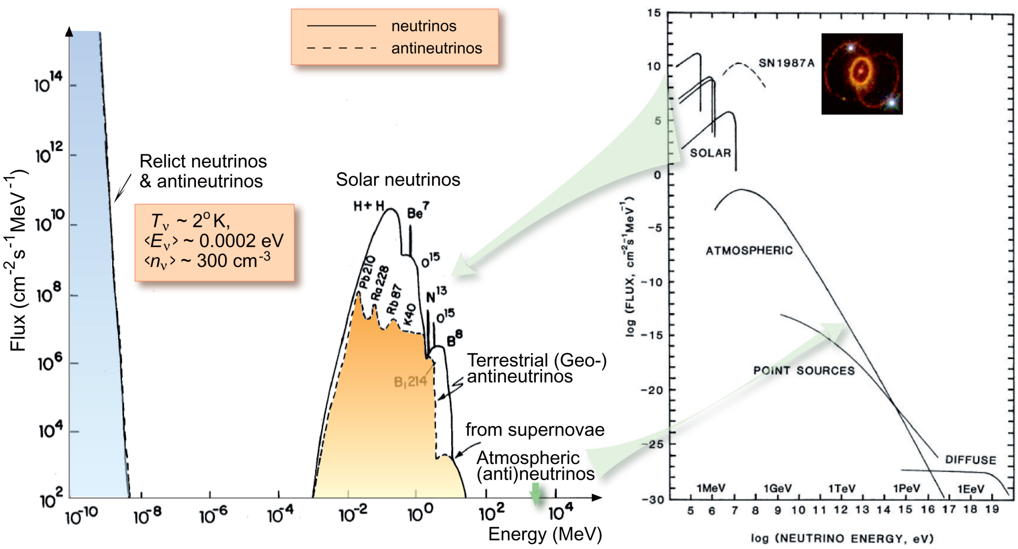

Figure 2.1: Characteristic fluxes of neutrinos and antineutrinos from natural sources.

other things, the following: "The continuity of beta spectrum will become understandable if we suppose that a neutron is emitted together with each electron during beta decay, with the sum of the energies of neutron and electron being constant ...." The "neutron" suggested by Pauli had to possess a very small mass and to interact weakly with matter in order to leave the experimental facility unnoticeable. Therefore, when a short time later Chadwick detected a neutron (a neutral but strongly interacting and, above all, heavy particle), E. Fermi proposed to call the hypothetical Pauli's "neutron" a "small neutron" or, in Italian, *neutrino*. Only 26 years after Pauli's hypothesis was proposed Reines and Cowan experimentally detected the electron antineutrino in the series of reactions:

$$
\begin{aligned}
\bar{\nu}_e + p \to & e^+ + n \\
& \hookrightarrow e^+ e^- \to \gamma\gamma \\
& \qquad \hookrightarrow n + \mathrm{Cd} \to \gamma + \ldots ,
\end{aligned}
$$

for which, in 1995, Reines received a Nobel Prize. In 1962, Lederman, Schwartz, and Steinberger detected a muonic neutrino, being born as a pair with a muon in the pion decays $\pi^+ \to \mu^+\nu$. The neutrino detector was separated from the region of production of muons and neutrinos by a shield of steel 13.5 m thick, through which muons could not penetrate in contrast to neutrinos. The interactions of the penetrating neutrinos in the detector were accompanied in the majority of cases by the production of muons rather than electrons, which is evidence that ν_e and ν_μ are two different particles. In 1988, Lederman, Schwartz, and Steinberger received a Nobel Prize for their discovery of muonic neutrinos. Finally, only in 2000 was the existence of a third neutrino type ν_τ proved in the experiment of the

DONUT collaboration in the series of reactions:

$$\begin{aligned}p + \text{Target} \to & D_s X \\ & \hookrightarrow D_s \to \tau\bar{\nu}_\tau \\ & \qquad \hookrightarrow \tau \to \nu_\tau X \\ & \qquad\qquad \hookrightarrow \nu_\tau + \text{photoemulsion} \to \tau X.\end{aligned}$$

Thus, it took a full 44 years before three generations of neutrinos were discovered, and 70 years passed from the date of Pauli's famous letter to the discovery of the third neutrino type.

2.2 The neutrino and the Standard Model (and beyond)

The neutrino participates in weak interactions and violates P-parity[1] in a maximal way. This suggested an important idea that the Standard Model (SM) gauge symmetry group should be built upon the fermions with left handed *chirality*. A left handed field is defined as $\psi_\mathrm{L}(x) \equiv P_\mathrm{L}\psi(x)$, where $P_\mathrm{L} = (1-\gamma_5)$ is the matrix projecting Dirac spinors onto states with left chirality. The SM combines all fermions and quarks into left handed chiral doublets in the form

$$L = \begin{pmatrix} \nu_L^f \\ \ell_L^f \end{pmatrix} \tag{2.1}$$

for leptons, where $f = e, \mu, \tau$ and analogously for quarks

$$Q = \begin{pmatrix} U_L \\ D_L \end{pmatrix}, \tag{2.2}$$

where $U = (u, c, t), D = (d, s, b)$. One may single out the three most important points of the SM: the invariance under group transformation of gauge fields, spontaneous breaking of gauge invariance and mass generation mechanisms for fermions.

2.2.1 Gauge invariance

The SM is a gauge invariant theory in which it is required that the Lagrangian of the model does not change in the transformation $\psi(x) \to e^{-i\alpha(x)}\psi(x)$, where $\alpha(x)$ is an arbitrary parameter depending on the space time point x. In order to satisfy this requirement, it is necessary to introduce into the Lagrangian the gauge bosons ($\gamma, W^\pm, Z, g$) compensating the additional terms in the kinetic term of the Lagrangian which arise due to differentiation $\partial_\mu e^{-i\alpha(x)}\psi(x)$.

The masslessness of fields in the SM Lagrangian follows from the invariance under the gauge group transformations[2]

[1] P-parity is a symmetry of the physical system under the coordinate transformation $\mathrm{x} \to -\mathrm{x}$

[2] It is easy to see that mass term $m_e\bar{\psi}_L\psi_R$ is not invariant under the gauge transformation because ψ_R transforms by $U(1)$ group, while ψ_L transforms by $SU(2)$ group.

SM is a renormalizable theory. A group of gauge transformations in the SM is the group $\mathrm{SU_C}(3) \times \mathrm{SU_L}(2) \times \mathrm{U_Y}(1)$, where C - color, L stays for left handed chiral fields, and Y — hypercharge of ψ field. Additional gauge fields are placed in kinetic term of the Lagrangian $\mathcal{L}_{\text{kinetic}}$:

$$\begin{aligned}\mathcal{L}_{\text{kinetic}} &= \sum_{\psi} \overline{\psi} i\gamma^{\mu} D_{\mu}\psi - \sum_{A=B,W,g} \frac{1}{4} F^{a}_{\mu\nu}(A) F^{a\mu\nu}(A),\\ D_{\mu} &= \partial_{\mu} + i g_s g^{A}_{\mu} T_A + i g W^{a}_{\mu} T_a + i g' B_{\mu} Y,\\ F^{a}_{\mu\nu}(A) &= \partial_{\mu} A^{a}_{\nu} - \partial_{\nu} A^{a}_{\mu} - g f_{abc} A^{b}_{\mu} A^{c}_{\nu},\end{aligned} \tag{2.3}$$

where g_s, g, g' are constants coupling fermions with gauge fields of gluons ($g^A_\mu, A \in (1,8)$), W_a bosons ($W^a_\mu, a \in (1,3)$) and B_μ field. f_{abc} are the structure constants of the appropriate group with commutator of group generators $[T_a, T_b] = i f_{abc} T_c$. The summation $\sum_\psi$ is performed over fields of leptons and quarks. In this case, each field may carry on itself up to three indices by the group $SU_\mathrm{C}(3) \times SU_\mathrm{L}(2) \times U_\mathrm{Y}(1)$. For example, all left handed components of fields are arranged in doublets in the form (2.1),(2.2) and the right handed ones are singlets. Additionally, quarks are located in colored triplets and leptons are singlets in this group. Finally, each field is a singlet in the "hypercharge" group. In (2.3) T_A, T_a, Y are the generators of gauge transformations: $T_A = \lambda_A/2$, where λ_A are 3×3 are 3×3 Gell–Mann matrices; $T_a = \tau_a/2$, where τ_a are the 2×2 Pauli matrices; and Y are the numbers (or 1×1 matrices). The arrangement by the SM multiplets in the $SU_\mathrm{L}(2)$ group is related to an experimental fact of maximal breaking of P-parity in weak interactions. Thus, only the left handed chiral doublets of fields L and Q (see Eqs. (2.1) and (2.2)) interact with the W boson. It is easy to see, as well, that direct transitions from one doublet to another are impossible, i.e., there are no vertices of interaction of the ν_f, $\ell_{f'}$ and W boson where $f \neq f'$.

2.2.2 Spontaneous breaking of gauge invariance

The SM Lagrangian is supplemented by the Lagrangian $\mathcal{L}_{\text{Higgs}}$ with a scalar (Higgs) field of $H = \begin{pmatrix}\phi^+\\ \phi^0\end{pmatrix}$:

$$\mathcal{L}_{\text{Higgs}} = |D_\mu H|^2 - \frac{\lambda^2}{4}(|H|^2 - v^2)^2.$$

The added Lagrangian possesses a minimum of the self action potential with nonzero vacuum expectation of the field of $v = \langle 0|\phi^0|0\rangle$, which results in an interesting effect: the Lagrangian itself and the equations of motion have gauge symmetry, while the solutions to these equations in the general case may not possess such a symmetry. The reason for this is that a system "spontaneously" falls in one of local minima. With the spontaneous breaking of gauge symmetry, $\mathcal{L}_{\text{Higgs}}$ gives nonzero masses to three of the four gauge bosons W^1, W^2, W^3, B:

$$W^{\pm}_{\mu} = \frac{1}{\sqrt{2}}(W^1_\mu \pm i W^2_\mu),\; Z_\mu = \cos\theta_W W^3_\mu - \sin\theta_W B_\mu,\; \cos\theta_W = \frac{g}{\sqrt{g^2 + g'^2}},$$

which are interpreted as fields of the $W^{\pm}$ and Z bosons, respectively, with the masses $m_{W^{\pm}} = gv/2$, $m_Z = gv/2\cos\theta_W$. Since the gauge symmetry $SU(2)_{\mathrm{L}} \times U(1)_{\mathrm{Y}}$ is violated not completely but to $U(1)$ (thus conserving the electric charge), one of the gauge fields remains massless and is interpreted as the field of photon:

$$A_\mu = \cos\theta_W B_\mu + \sin\theta_W W^3_\mu, \quad m_\gamma = 0.$$

2.2.3 Masses of fermions and their mixing

Although the vector bosons acquire mass owing to the Higgs mechanism, briefly stated above, fermions, in the meantime, remain, in theory, massless. In order that they might acquire mass, it must be postulated that fermions can interact with a scalar Higgs field. This interaction is called a Yukawa interaction and is defined by the Lagrangian $\mathcal{L}_{\text{Yukawa}}$:

$$\mathcal{L}_{\text{Yukawa}} = \lambda_{ij}\psi_i\psi_j H + \text{ h.c.}, \tag{2.4}$$

where λ_{ij} are dimensionless constants. It is assumed in (2.4) that all possible combinations of the ψ_i, ψ_j and H fields are taken so that the thus obtained scalar $\psi_i\psi_j H$ remains singlet for SM group transformations. For example, the term $\lambda_e \overline{L^e} H e_R$ transforms to $\lambda_e \bar{\psi}_e \psi_e v$ after spontaneous symmetry breaking, which is interpreted as the mass term $m\bar{\psi}_e\psi_e$ of the field of the electron with $m = \lambda_e v$. Since fields from different doublets can interact generally with a Higgs field, then, in order for the terms in (2.4) to be interpreted as “mass terms” after the spontaneous symmetry breaking, it is necessary at first to diagonalize them in terms of new fields which are linear combinations of massless interaction fields. The unitary matrix V, connecting the states with a certain mass to massless interaction fields, is known under the name of the Cabibbo–Kobayashi–Maskawa (CKM) mixing matrix for quarks and as the Pontecorvo–Maki–Nakagawa–Salata (PMNS) mixing matrix for leptons (also often called neutrino mixing matrix).

As a result, the transitions from one doublet to another that are impossible for massless fields now become possible for massive fields with the transition amplitude proportional to the appropriate mixing matrix element $V_{ff'}$. For example, the amplitude of transition between the u and d quarks is proportional to the matrix element V_{ud} , and between the u and s quarks it is V_{us}, and so on. Similarly, for neutrinos and leptons, the amplitude of transition between the lepton of α flavor and the neutrino with mass m_i is proportional to $V_{\alpha i}$.

Let us make a brief summary of the SM. Interactions of fermions and bosons are introduced by demand of gauge invariance of the theory. It also forbids fermions and bosons from having a mass. A field of the scalar Higgs boson with the self action potential with nonzero vacuum expectation value is introduced in the theory. The Higgs field interacts both with all gauge bosons of the theory and with fermions. The nonzero vacuum expectation spontaneously breaks the gauge symmetry, which gives masses to the $W^{\pm}$ and Z bosons and to fermions. The minimum possible group of gauge symmetry $SU_{\mathrm{C}}(3) \times SU_{\mathrm{L}}(2) \times U_{\mathrm{Y}}(1)$ is postulated as motivated by experiment.

As a result, we obtain a fine and simple theory agreeing perfectly with experiment. The SM Lagrangian consists of just three terms:

$$\mathcal{L}_{\text{SM}} = \mathcal{L}_{\text{kinetic}} + \mathcal{L}_{\text{Higgs}} + \mathcal{L}_{\text{Yukawa}} \tag{2.5}$$

It is impossible to calculate within the SM some parameters that have to be assumed as free. These are the interaction constants ($g_i = g_s, g, g'$), masses of leptons (m_l, m_ν) and quarks (m_q), neutrino mixing angles ($\theta^\nu_{12}, \theta^\nu_{23}, \theta^\nu_{13}$ and CP-vilating phase δ^ν_{CP}), quark mixing angles ($\theta^q_{12}, \theta^q_{23}, \theta^q_{13}$ and CP-violating phase δ^q_{CP}), QCD vacuum parameter[3] (θ_{qcd}), and parameters of the self action potential of the Higgs field (λ and v). The number of these parameters in the SM is 19 if neutrinos are massless (3 m_l + 6 m_q + 3 θ^q_i + 1 δ_{CP} + 3 g_i + θ_{qcd} + v + λ), or 26 if a neutrino has a mass (19 + 3 m_ν + 3 θ^ν_i + 1 δ_{CP}).

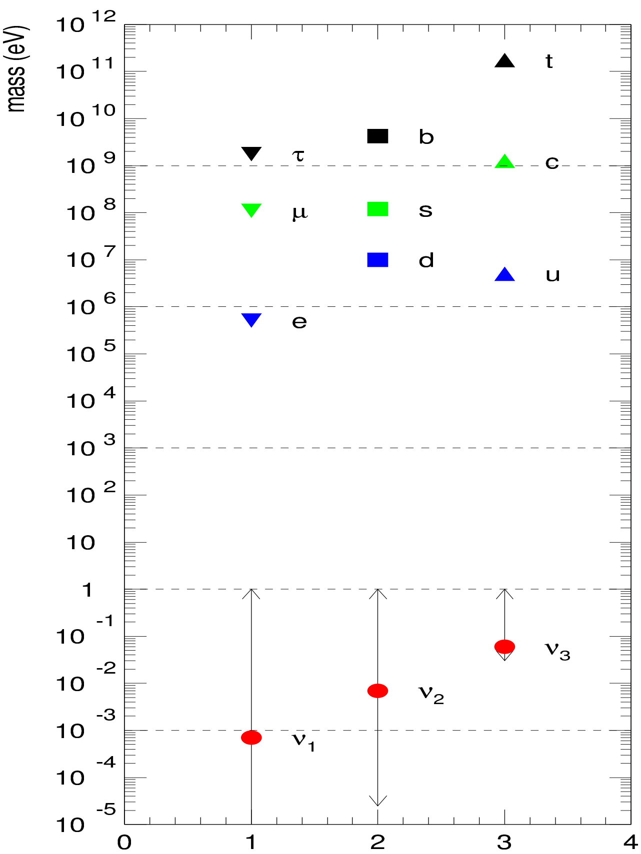

Figure 2.2: Masses of quarks and leptons for each of the three generations.

The discovery of the Higgs boson at LHC in 2012 can be considered as a great triumph of the Standard Model.

[3] One of the unsolved enigmas of QCD is the problem of CP breaking in strong interactions, namely, the question of "why strong interactions do not break CP parity" (called also as "strong CP problem"), whereas weak interactions do not possess CP invariance. A nonzero value of the θ_{qcd} angle in the kinetic term of the QCD of the Lagrangian might lead to the CP breaking strong interactions. The choice of $\theta_{\text{qcd}} \approx 0$ is one of the examples of fine tuning of the SM.

Despite the great successes of the SM, there are some indications that the SM is not a final theory. For example, how are the measured values of the coupling constants could be explained? Why is there a strong hierarchy of masses in the SM as can be seen from Fig. 2.2 where the masses of quarks and leptons for each of the three generations are shown. The mass of the Higgs boson requires the fine tuning of the parameters of the theory to protect it against becoming infinitely large. Additionally, the SM cannot explain dark matter and the baryon asymmetry of the Universe, or inflation and the nature of cosmological perturbations of density. Finally, the SM has to be extended to include a neutrino mass.

2.2.4 Neutrino mass generation mechanisms. Physics beyond the SM

How can the neutrino mass be generated with SM or beoynd? If the neutrino is a Dirac fermion, as are all other leptons, then it is quite easy to generate its mass by adding $\mathcal{L}_{\text{Yukawa}}$ to the SM Langangian (2.5):

$$\lambda_\nu \left(\bar{\nu}_L, \bar{l}_L\right) \begin{pmatrix} v \\ 0 \end{pmatrix} \nu_R = m_\nu \bar{\nu}_L \nu_R,$$

where $m_\nu \equiv \lambda_\nu v$. The smallness of λ_ν, as well as values for other fermions, cannot be explained in the context of the SM. However, the fact that a neutrino carries no electric charge opens another possibility: a neutrino may be a Majorana particle; i.e., the particle and antiparticle can be identical to each other. Nowdays we do not know whether neutrino is a Dirac particle or a Majorana particle. The suggestion that the neutrino is a Majorana particle extends our possibilities on construction of $\mathcal{L}_{\text{Yukawa}}$ for neutrinos. Generally, the "mass" term consists of the Dirac and Majorana terms:

$$\mathcal{L}_{\text{mass}} = -\frac{1}{2}\left(\overline{\nu_L}, \overline{(\nu_R)^c}\right) \begin{pmatrix} m_L & m_D^T \\ m_D & m_R \end{pmatrix} \begin{pmatrix} (\nu_L)^c \\ \nu_R \end{pmatrix} + \text{ h.c.} \tag{2.6}$$

Here m_L, m_R, m_D are the mass matrices. The vector of left handed neutrinos, which take part in interaction with the W and Z bosons, $\nu_L = (\nu_{eL}, \nu_{\mu L}, \nu_{\tau L}, \dots)^T$ is combined with the vector of left handed neutrinos, which are charge conjugates to the right handed chiral noninteracting field, $(\nu_R)^c = ((\nu_{eR})^c, (\nu_{\mu R})^c, (\nu_{\tau R})^c, \dots)^T$.

The Lagrangian (2.6) possesses a broad spectrum of predictions for neutrino masses. Let us first consider the case of a single generation of neutrinos; then m_L, m_R, m_D are simply numbers, or 1×1 matrices. In this case, diagonalization of (2.6) yields the following eigenvalues of neutrino masses $|m_1|, |m_2|$ and the angle of mixing θ:

$$m_{1,2} = \frac{m_L + m_R}{2} \pm \sqrt{\frac{(m_L - m_R)^2}{4} + m_D^2}, \quad \tan 2\theta = \frac{2m_D}{m_R - m_L} \tag{2.7}$$

Phenomenologically some special cases of formula (2.7) are:

(A) $m_L = m_R = 0$. In this case, $m_{1,2} = m_D$, $\theta = \frac{\pi}{4}$ and the maximum mixing takes place. Here, two Majorana fields of neutrinos are equivalent to one Dirac field.

(B) $m_L = m_R \ll m_D$. In this case, there are two nearly degenerate Majorana states with the masses $m_{1,2} = m_L \pm m_D$ and almost maximal angle of mixing $\tan 2\theta \gg 1$. These neutrinos are called "pseudo Dirac" and in this case oscillations are possible between ν_L ("active") and $(\nu_R)^c$ ("sterile") neutrinos.

(C) $m_L = 0, m_R \gg m_D$. This case is interesting because a strong hierarchy of neutrino masses arises in a natural manner: one is very heavy with a mass of $m_1 = m_R(1 + m_D^2/m_R^2) \approx m_R$, another is very light with $m_2 = m_D^2/m_R \ll m_D$. For example, if we assume that the mass m_D is close in order of magnitude to masses of leptons or quarks, i.e., within the limits of 0.5 MeV to 200 GeB, and mass $m_R \sim 10^{15-16}$ GeV, then the mass m_2 can be within the limits of 10^{-14} eV to 0.04 eV. In this case, the angle of mixing of a light neutrino with a heavier one is very small: $\theta \approx m_D/m_R \sim 10^{-20} - 10^{-13} \ll 1$. This mechanism is called a "seesaw mechanism". A heavy neutrino is almost unobservable in modern experiments.

The appearance of large masses $m_R \simeq 10^{15-16}$ GeV is characteristic of Grand Unified Theories such as the left–right symmetric $SO(10)$ model. The seesaw mechanism provides the possibility of obtaining naturally the small neutrino mass when rather heavy masses of leptons and quarks m_D and a very heavy Majorana neutrinos are available. If neutrinos are Majorana particles in the SM, then this may have far reaching implications. For example, it is possible to know something about physics beyond the SM on the energy scale of $m_R \sim 10^{15}$ GeV, much exceeding the possibilities of accelerator technology (at least modern ones). In addition to that, the existence of a Majorana neutrino with mass m_R allows one to explain the baryon asymmetry of the Universe by means of leptogenesis at the early stage of its evolution.

2.2.5 Sterile neutrinos

An interesting concept of *sterile* neutrinos is exploited as a natural explanation of various anomalies in neutrino physics and is used in cosmology as an additional relativistic degree of freedom in plasma of the early Universe. One can often find in the literature the following statement about sterile neutrinos: that these are states which do not interact with matter, i.e. is not mixed with $W^\pm, Z$ but "active" neutrinos can "oscillate" into these "sterile" states. This picture, being quantitatively acceptable, is, however, not quite correct at given the following. Neutrino oscillations are not mutual transformations of one neutrino type into another one. Instead neutrino oscillations are effects of interference of amplitudes with massive neutrinos as intermediate states when we can not tell for sure which mass eigenstate is exactly involved in the lepton number violating process. How can the idea of sterile neutrino can be implemented in theory?

Let us consider $\mathcal{L}_{\text{mass}}$from (2.6) with the number of right-handed fields exceeding three. Let, for definiteness, n be the length of N_L. The length of ν_L^m is apparently equal to three. We should diagonalize $\mathcal{L}_{\text{mass}}$ in terms of new fields (ν_L^m, N_L):

$$\begin{pmatrix} \nu_{f,L} \\ (\nu_R)^c \end{pmatrix} = \begin{pmatrix} V_{3\times3} & M_{3\times n} \\ K_{n\times3} & U_{n\times n} \end{pmatrix} \begin{pmatrix} \nu_L^m \\ N_L \end{pmatrix} \tag{2.8}$$

The matrix

$$\begin{pmatrix} V & M \\ K & U \end{pmatrix} \tag{2.9}$$

is unitary from which the following relationships take place:

$$\begin{gathered}(VV^\dagger)_{3\times 3} + (MM^\dagger)_{3\times 3} = 1_{3\times 3}, \quad (KK^\dagger)_{n\times n} + (UU^\dagger)_{n\times n} = 1_{n\times n}, \\ (VK^\dagger)_{3\times n} + (MU^\dagger)_{3\times n} = 0,\end{gathered} \tag{2.10}$$

and in general:

$$VV^\dagger \neq 1, \quad UU^\dagger \neq 1. \tag{2.11}$$

Let us see now how this mathematical construction deals with Z^0 and $W^\pm$ widths.

(ν_L^m, N_L) are all active fields. N_L are not sterile fields anymore. They all interact with $W^\pm$

$$\begin{aligned}\mathcal{L}_{\text{cc}} &= -\frac{g}{\sqrt{2}}\sum_\alpha \bar{\ell}_{\alpha,L}\gamma_\mu\nu_{\alpha,L}W^\mu + \text{h.c.} \\ &= -\frac{g}{\sqrt{2}}\sum_\alpha V_{\alpha i}\bar{\ell}_{\alpha,L}\gamma_\mu\nu_{i,L}^m W^\mu - \frac{g}{\sqrt{2}}\sum_\alpha M_{\alpha i}\bar{\ell}_{\alpha,L}\gamma_\mu N_{i,L}W^\mu + \text{h.c.}\end{aligned} \tag{2.12}$$

and with Z^0

$$\begin{aligned}\mathcal{L}_{\text{nc}} &= -\frac{g}{\cos\theta_W}\sum_\alpha \bar{\nu}_{\alpha,L}\gamma_\mu\nu_{\alpha,L}Z^\mu + \text{h.c.} \\ &= -\frac{g}{\cos\theta_W}V^\dagger V\bar{\nu}_{i,L}^m\gamma_\mu\nu_{i,L}^m Z^\mu - \frac{g}{\cos\theta_W}M^\dagger M\bar{N}_{i,L}^m\gamma_\mu N_{i,L}Z^\mu \\ &\quad -\frac{g}{\cos\theta_W}V^\dagger M\bar{\nu}_{i,L}^m\gamma_\mu N_{i,L}Z^\mu - \frac{g}{\cos\theta_W}M^\dagger V\bar{N}_{i,L}\gamma_\mu\nu_{i,L}^m Z^\mu + \text{h.c.}\end{aligned} \tag{2.13}$$

Now Z boson decays into all possible channels (not diagonal anymore!):

$$\begin{aligned}Z &\to \sum_{i,j}\bar{\nu}_i^m\nu_j^m && \propto \sum_{i,j,\alpha,\beta} V_{j\alpha}^\dagger V_{\alpha i}V_{i\beta}^\dagger V_{\beta j} \\ &\to \sum_{m,n}\bar{N}_m N_n && \propto \sum_{m,n,\alpha,\beta} M_{n\alpha}^\dagger M_{\alpha m}M_{n\beta}^\dagger M_{\beta m} \\ &\to \sum_{i,n}\bar{N}_n\nu_i && \propto \sum_{i,n,\alpha,\beta} M_{n\alpha}^\dagger V_{\alpha i}V_{i\beta}^\dagger M_{\beta n} \\ &\to \sum_{i,n}\bar{\nu}_i N_n && \propto \sum_{i,n,\alpha,\beta} V_{n\alpha}^\dagger M_{\alpha i}M_{i\beta}^\dagger V_{\beta n}\end{aligned} \tag{2.14}$$

Taking into account the identities (2.11) the total decay width of Z^0 boson is proportional to (in the limit of small masses relative to m_Z):

$$\begin{aligned}
\Gamma(Z \to \text{all}) \propto & \\
& \text{Tr}\left(V^\dagger V V^\dagger V\right) + \text{Tr}\left(M^\dagger M M^\dagger M\right) + \text{Tr}\left(M^\dagger V V^\dagger M\right) + \text{Tr}\left(V^\dagger M M^\dagger V\right) \\
& = \text{Tr}\left(V^\dagger V V^\dagger V + M^\dagger M M^\dagger M + M^\dagger V V^\dagger M + V^\dagger M M^\dagger V\right) \\
& = \text{Tr}\left(V^\dagger V V^\dagger V + M^\dagger M M^\dagger M + M M^\dagger V V^\dagger + V V^\dagger M M^\dagger\right) \\
& = \text{Tr}\left(\left(V^\dagger V + M^\dagger M\right)\left(V^\dagger V + M^\dagger M\right)\right) \\
& = \text{Tr} 1^2_{3\times 3} = \text{Tr} 1_{3\times 3} = 3
\end{aligned} \tag{2.15}$$

And this is the main trick about sterile neutrinos: all fields are actually active (thus all contributing to the sum of amplitudes), but their contribution to the Z boson is determined by the number of charged leptons being equal to three.

How new degrees of freedom could be visible? Let us mention briefly how new degrees of freedom could be visible, keeping in mind that (ν_L^m, N_L) are all active fields.

- In the cosmology of the early Universe. In thermodynamic equilibrium they all give the same contribution to the number of degrees of freedom despite their coupling constants
- In measurements of effective neutrino masses from decays sterile neutrinos can be visible.
  - In tritium decays the effective mass reads:

$$m_{\text{ee}} = \sqrt{\sum_{i=1,3} |V_{\text{ei}}|^2 m_i^2 + \sum_n |M_{\text{en}}|^2 m_n^2} \tag{2.16}$$

  - In $0\nu 2\beta$ decays the effective mass reads:

$$m_{\beta\beta} = \left| \sum_{i=1,3} V_{\text{ei}}^2 m_i + \sum_n M_{\text{en}}^2 m_n \right| \tag{2.17}$$

As we discuss below in Sec. 2.4 a correct treatment of neutrino oscillations deals with coherence of massive neutrino states and loss of their coherence with space and time. This effect is also important in discussions of sterile neutrinos. Te truly sterile state $(\nu_R)^c = K\nu_L^m + UN_L$ does not interact with $W^\pm, Z^0$. However, it can appear in a coherent mixture $\nu_{f,L} = V\nu_L^m + MN_L$ when this state evolves in time and space.

- The coherence of $\nu_{f,L} = V\nu_L^m + MN_L$ is controlled by energy-momentum uncertainty in the production and detection regions.
- If the uncertainty is small relative to $\Delta m^2/E_\nu$ one can observe an oscillation-like pattern with sterile Δm^2 driving frequency.

- If the uncertainty is too small compared to $\Delta m^2/E_\nu$ the coherence is lost. In this case no oscillation with "sterile" degrees of freedom will be visible. However, the sterile state will be visible as non-unitarity of V matrix.
- The coherence will be lost anyway at distances exceeding the coherence length. Again, the sterile state will be visible as non-unitarity of V matrix.
- Considering the coherence and decoherence effects one can see that oscillation pictures in flavor states and mass eigenstates differ. Within the coherence length both descriptions lead to the same results.

2.3 Current status of neutrino mixing

Leptons and quarks do mix in their interactions with $W^\pm$ bosons in the Standard Model (SM). The mixing of leptons is governed by the Pontecorvo-Maki-Nakagawa-Sakata (**PMNS**) mixing matrix:

$$V = \begin{pmatrix} 1 & 0 & 0 \\ 0 & \cos\theta_{23} & \sin\theta_{23} \\ 0 & -\sin\theta_{23} & \cos\theta_{23} \end{pmatrix} \begin{pmatrix} \cos\theta_{13} & 0 & \sin\theta_{13}e^{-i\delta} \\ 0 & 1 & 0 \\ -\sin\theta_{13}e^{i\delta} & 0 & \cos\theta_{13} \end{pmatrix} \begin{pmatrix} \cos\theta_{12} & \sin\theta_{12} & 0 \\ -\sin\theta_{12} & \cos\theta_{12} & 0 \\ 0 & 0 & 1 \end{pmatrix},$$

where θ_{ij} are mixing angles, and $e^{-i\delta}$ is the CP-violating phase. The mixing angles θ_{12}, θ_{23} are measured in a number of experiments with solar, atmospheric, reactor and accelerator neutrinos. θ_{13} was the only unknown angle until 2012, when a non-zero value of this angle was discovered by Daya Bay Collaboration [1]. This discovery was later on confirmed by the RENO Collaboration [2]. The first indication for a non-zero value of θ_{13} was reported by Double Chooz [3], MINOS [4], and T2K [5] one year earlier in 2011.

The main source of information about lepton mixing angles comes to us from *neutrino oscillations*, a macroscopic display of quantum interference which we will briefly discuss in the next section. The neutrino oscillations are determined via squared mass differences Δm^2 and mixing angles θ_{ij} which are measured today as summarized in Eq. 2.18.

This summary contains also limits from cosmology ($\sum_i m_i$), from direct mass measurements of particle decays $m_\alpha = \sqrt{\sum_i |V_{\alpha i}|^2 m_i^2}$ and from neutrinoless double beta decays ($m_{\beta\beta} = |\sum_i V_{ei}^2 m_i|$).

$$\begin{aligned} & & \Delta m_{21}^2 &= 7.54^{+0.26}_{-0.22} \times 10^{-5}\text{eV}^2, \\ \sin^2\theta_{12} &= 0.307^{+0.018}_{-0.016} & |\Delta m_{31}^2| &= 2.43^{+0.06}_{-0.10} \times 10^{-3}\text{eV}^2, \\ \sin^2\theta_{23} &= 0.386^{+0.024}_{-0.021} & m_e &< 2.05\text{eV}, \\ \sin^2\theta_{13} &= 0.024^{+0.0025}_{-0.0025} & \textstyle\sum_i m_i &< 0.66\text{eV} \\ & & m_{\beta\beta} &< (0.2-0.4)\text{eV} \end{aligned} \tag{2.18}$$

2.4 Neutrino oscillations

2.4.1 Neutrino oscillations in vacuum

The neutrino, accompanied by lepton ℓ_α, is presumably[4] produced as a *coherent mixture* of massive states. Due to their different masses the relative phase between these states varies with distance and time. The probability to detect this mixture is a periodic function of distance and travel time. This phenomenon is known as *neutrino oscillations*. The corresponding survival probability in vacuum reads:

$$P_{\alpha\alpha} = \sum_{i,j} |V_{\alpha i}|^2 |V_{\alpha j}|^2 \mathrm{e}^{-i\frac{\Delta m^2_{ij} L}{2E_\nu}}, \tag{2.19}$$

while the flavor-changing probability $P_{\beta\alpha}$ reads as follows:

$$P_{\beta\alpha} = \sum_{i,j} V^*_{\alpha i} V_{\beta i} V_{\alpha j} V^*_{\beta j} \mathrm{e}^{-i\frac{\Delta m^2_{ij} L}{2E_\nu}}. \tag{2.20}$$

Neutrino oscillations have been discovered experimentally within the past two decades. Figs. 2.3, 2.4 display the survival probabilities vs L/E_ν as measured by KamLAND [6], SuperKamiokande [7] and Daya Bay [8]. All of them show a spectacular oscillating pattern as expected from the oscillation probability formula. Let us note that so far no experiment has detected more than one "oscillation wave". This remark is important in view of the fact that the oscillation formulas (2.19) and (2.20) are known to be approximate as the theory behind their derivation has a limited range of applicability. A more rigorous approach involving wave packets in either relativistic quantum mechanics [9] or quantum field theory [10–20] suggests that the formula (2.20) should be modified at least as follows:

$$P_{\beta\alpha} = \sum_{i,j} V^*_{\alpha i} V_{\beta i} V_{\alpha j} V^*_{\beta j} \mathrm{e}^{-i\frac{2\pi L}{L^{\text{int}}_{ij}} - \left(\frac{L}{L^{\text{coh}}_{ij}}\right)^2 - \left(\frac{\delta x_\nu}{L^{\text{int}}_{ij}}\right)^2}, \tag{2.21}$$

where

$$\begin{aligned} L^{\text{int}}_{ij} &= \frac{4\pi E_\nu}{|\Delta m^2_{ij}|}, \\ L^{\text{coh}}_{ij} &= L^{\text{int}}_{ij} \frac{E_\nu}{2\pi\delta E_\nu}, \\ \delta x_\nu &= \frac{\pi\xi}{2\delta E_\nu}, \end{aligned} \tag{2.22}$$

where ξ is a dimensionless function of kinematic variables of all particles involved in neutrino production and detection. Two new terms in the exponent in (2.21) both suppress the

[4]The coherence of mass eigenstates strongly depends on the characteristic time-space "size" of the interaction region of all particles in the production and detection processes as well as on the event kinematics

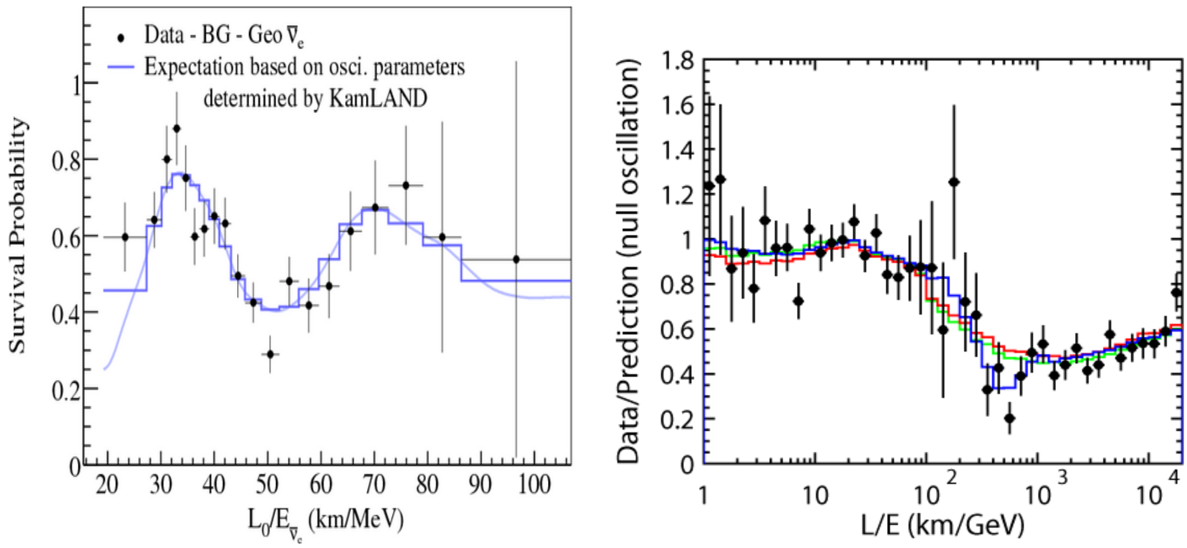

Figure 2.3: Survival probability $\bar{\nu}_e$ as a function of $L/E_{\bar{\nu}}$, as measured by KamLAND (left). Ratio of observed to expected number of events in no oscillation hypothesis as a function of L/E, as measured by SuperKamiokande (right).

interference terms and thus oscillations. $L_{ij}^{\rm coh}$ is the coherence length for the pair i, j of massive neutrinos. Neutrinos loose their coherence at distances exceeding the coherence length due to spatial separation of their corresponding wave packets. $L_{ij}^{\rm coh}$, which gives the width of the neutrino wave packet in momentum space, is inversely proportional to δE_ν. δE_ν is a function of kinematic variables involved in the neutrino production and detection processes. δE_ν is proportional to the mean energy of neutrino wave packet E_ν, thus $\delta E_\nu / E_\nu$ is a Lorentz invariant. The second suppressing term does not depend on the distance. Instead this term suppresses the *coherence production (or detection)* if the neutrino wave packet size δx_ν exceeds the interference length $L_{ij}^{\rm int}$. δx_ν is inversely proportional to δE_ν. This suppression term is responsible for coherence of the neutrino mixture at production (or detection). Let us note that this term completely removes any interference of charged leptons because their interference length $L_{ij}^{\rm int}$ is much shorter than typical values for the charged lepton wave packet size $\delta x_\ell \simeq \delta x_\nu$.

It is very important to have both theoretical and an experimental estimates or limits on δE_ν in order to have an estimate for the importance of decoherence effects for future experiments in which many oscillation waves are expected, such as NOVA, LBNE, LBNO, JUNO, RENO-50.

2.4.2 Neutrino oscillations in matter

In a similar manner by which fermions acquire their masses due to interactions with Higgs field with non-zero vacuum expectation value, neutrinos propagating through matter and scattering at zero angle acquire effective mass which depends on matter number

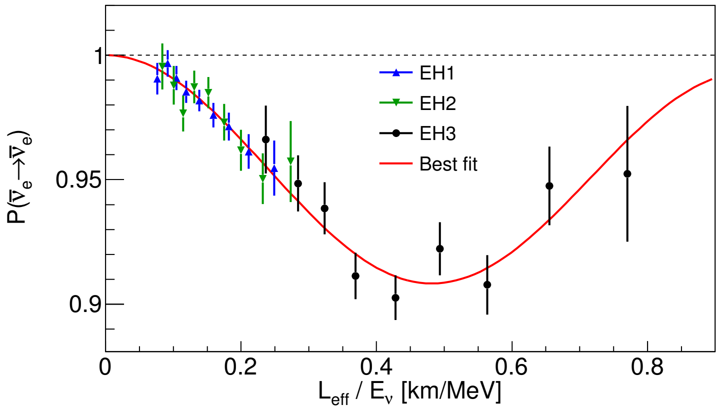

Figure 2.4: Prompt positron energy spectra in the three experimental halls, re-expressed as the electron antineutrino survival probability versus propagation distance L over antineutrino energy E_ν. An effective detector-reactor distance L_{eff} is determined for each experimental hall equating the multi-core oscillated flux to an effective oscillated flux from a single baseline. The best estimate of the detector response is used to convert the background-subtracted positron energy spectrum into the antineutrino energy spectrum E_ν. The horizontal location of each data point is given by the average of the counts in each bin ($\langle L_{\text{eff}}/E_\nu \rangle$). The vertical position is determined by the ratio of the counts in each bin relative to the counts expected assuming no oscillation, corrected for the reduction of analyzing power (energy dependent) due to multiple baselines and the binning in L/E. Error bars represent the statistical uncertainty only. The oscillation survival probability using the best estimates of $\sin^2 2\theta_{13}$ and $|\Delta m^2_{ee}|$ is displayed for reference.

density. The neutrino mixing matrix in matter differs from the vacuum one as well. As a result neutrino oscillations in matter occur with new effective masses and mixing angles. Neutrino scattering with Z boson exchange is equal for every ν_i and gives the same phase shift in the oscillation amplitude. Therefore, these scatterings do not modify the oscillation picture with respect to the vacuum. However, the presence of electrons in matter (and lack of muons and tau leptons) opens another scattering channel via W^+ boson exchange. The amplitude of this process $\nu_i e \to \nu_j e$ is proportional to $V^*_{ei}V_{ej}$, thus the contribution of this process is different for different massive neutrinos. Additionally the neutrino scattering off electrons "mixes" ν_i, ν_j.

Therefore, energy eigenstates of neutrinos in matter $\nu^M = (\nu_1^M, \nu_2^M, \nu_3^M)^T$ and vacuum $\nu = (\nu_1, \nu_2, \nu_3)^T$ are different states: $\nu^M = U_M \nu$. The matrix U_M diagonalizes the energy operator $\hat{H} = \hat{H}_0 + \hat{W}$ by means of $\hat{H}_{diag} = U_M \hat{H} U_M^\dagger$. The matrix elements of the hamiltonian are the sum of the neutrino free energy and the energy of interaction of neutrinos with electrons:

$$H_{ij} = \left(E_\nu + \frac{m_i^2}{2E_\nu}\right)\delta_{ij} + V^*_{ei}V_{ej}\sqrt{2}G_F n_e. \tag{2.23}$$

The energy of neutrino-electron elastic scattering is small, of the order of $10^{-10} - 10^{-11}$ eV in the Sun's center. However, it plays an important role in neutrino oscillations in matter because it is comparable by order of magnitude with the vacuum energy difference $\Delta E_{ij} = \Delta m_{ij}^2/2E_\nu$ for Δm^2 about $(10^{-4} - 10^{-5})$ eV^2 and E_ν on the order of several MeV.

A general $3-\nu$ oscillation scheme within matter is given in [21]. Here we consider these oscillations in a simple way assuming the matter with constant density and two generations of neutrinos with mixing angle θ. The hamiltonian $\hat{H}$ is 2×2 matrix:

$$\hat{H} = \begin{pmatrix} E_\nu + \frac{m_1^2}{2E_\nu} + \cos^2\theta\sqrt{2}G_F n_e & \cos\theta\sin\theta\sqrt{2}G_F n_e \\ -\cos\theta\sin\theta\sqrt{2}G_F n_e & E_\nu + \frac{m_2^2}{2E_\nu} + \sin^2\theta\sqrt{2}G_F n_e \end{pmatrix}. \tag{2.24}$$

In order to diagonalize (2.24) one should "rotate" the basis $\nu = (\nu_1, \nu_2)^T$ to the states $\nu^M = (\nu_1^M, \nu_2^M)^T$ related to each other via "rotation" matrix U_M also by 2×2 dimension. New mixing angle and mass squared differences read:

$$\sin^2 2\theta_M = \frac{\sin^2 2\theta}{\cos^2 2\theta(1-\lambda)^2 + \sin^2 2\theta}, \; \Delta m_M^2 = \Delta m^2 \frac{\sin 2\theta}{\sin 2\theta_M}, \; \lambda = \frac{2\sqrt{2}G_F E_\nu n_e}{\Delta m^2 \cos 2\theta}.$$

The dimensionless number λ can be written as a ratio:

$$\lambda = \frac{L_{\text{vac}}}{L_e \cos 2\theta},$$

where L_{vac} is the vacuum oscillation length and $L_e = 2\pi/\sqrt{2}G_F n_e$. $L_e \approx 110$ km at matter density about 150 g/cm^3. The energy eigenstates in matter read:

$$|\nu_1^M\rangle = |\nu_e\rangle\cos\theta_M - |\nu_\mu\rangle\sin\theta_M = |\nu_1\rangle\cos(\theta_M - \theta) - |\nu_2\rangle\sin(\theta_M - \theta)$$
$$|\nu_2^M\rangle = |\nu_e\rangle\sin\theta_M + |\nu_\mu\rangle\cos\theta_M = |\nu_1\rangle\sin(\theta_M - \theta) + |\nu_2\rangle\cos(\theta_M - \theta).$$

The neutrino oscillation length in matter reads

$$L_M = L_{\text{vac}}\frac{\sin 2\theta_M}{\sin 2\theta} = L_{\text{vac}}\left[1 + \left(\frac{L_{\text{vac}}}{L_e}\right)^2 - \frac{2L_{\text{vac}}}{L_e}\cos 2\theta\right]^{-1/2}.$$

The oscillation probability in matter is written in analogy to the vacuum case, but with a modification $\theta \to \theta_M, L_{\text{vac}} \to L_M$:

$$P_{ee} = \sin^2 2\theta_M \sin^2 \pi L/L_M, \quad P_{e\mu} = 1 - \sin^2 2\theta_M \sin^2 \pi L/L_M,$$

Considering, for definiteness, that $|\theta| < \pi/4$, then $|\nu_1\rangle$ dominates in $|\nu_e\rangle$. Matter can both amplify and weaken the oscillations depending on the sign of Δm^2.

In the case of $\Delta m^2 < 0$ one obtains $\theta_M < \theta$, i.e. in this case matter suppresses the neutrino mixing and oscillations. The mass squared difference Δm_M^2 increases by its absolute value with respect to the vacuum value.

In the case of $\Delta m^2 > 0$, θ_M can reach the maximal value $\pi/2$ even at a small mixing angle in vacuum. In such a case the neutrino oscillations are enhanced and the mass squared difference Δm_M^2 decreases relative to Δm^2 in vacuum.

Let us discuss in more details three important cases.

- $\lambda \to 0$ corresponds to vanishing number density of electrons $n_e \to 0$. In this case the oscillations in matter coincide with vacuum oscillations:

$$\theta_M \to \theta, |\nu_1^M\rangle = |\nu_1\rangle \text{ and } |\nu_2^M\rangle = |\nu_2\rangle,$$

- $\lambda \to \infty$ corresponds to infinitely large electron number density. Then $\theta_M \to \pi/2$, $|\nu_1^M\rangle = -|\nu_\mu\rangle$ and $|\nu_2^M\rangle = |\nu_e\rangle$. Neutrino oscillations in this limit are strongly suppressed:

$$P_{e\mu} = \left(\frac{L_e}{L_{\text{vac}}}\right)^2 \sin^2 2\theta \sin^2 \pi L/L_e \ll 1,$$

- $\lambda \to 1$. In this case there is a resonance effect: $\theta_M \to \pi/4$. The oscillation length becomes $L_M = L_{\text{vac}}/\sin 2\theta$ and the probability $P_{e\mu} = \sin^2 \pi\left(\sin 2\theta L/L_{\text{vac}}\right)$. The resonance density

$$n_e^{\text{res}} = \frac{\Delta m^2 \cos 2\theta}{2\sqrt{2}G_{\text{F}}E_\nu}$$

  depends on the neutrino energy. Therefore, in matter with constant density one might see $\nu_e \to \nu_\mu$ conversion for a neutrino energy "window" satisfying the relationship $n_e E_\nu = \Delta m^2 \cos 2\theta/2\sqrt{2}G_F$. Let us note that the presence of this resonance is not enough for the conversion $\nu_e \to \nu_\mu$, because the opposite process $\nu_\mu \to \nu_e$ takes place as efficiently as the direct conversion.

In the case of matter with variable density a combination of all three limiting cases just discussed leads to a nice physical effect: ν_e conversion to ν_2 mass state. It can happen in the following way. If the electron number density in the production region is infinitely large then ν_e coincides with second mass eigenstate $|\nu_e\rangle = |\nu_2^M\rangle$. If the density changes rather weakly in respect to L_e then the neutrino leaves the matter adiabatically. In this case the neutrino, which has emerged from the matter, remains in the second mass eigenstate $|\nu_2^M\rangle$, which, upon exiting the matter, coincides with ν_2 in vacuum. At later times such a neutrino will not oscillate because it is in a pure quantum mass eigenstate. Interaction of ν_e in a detector by means of W boson exchange is by a factor $\sin^2\theta$ less intense with respect to ν_e. In summary, it leads to a stronger suppression of electron-like events for smaller values of mixing angle in vacuum. This is known as the MSW effect [22, 23]. Matter effects are expected to play an important role in long baseline experiments like accelerator experiments NOVA, LBNE, LBNO and, at the percent level, even for reactor experiment at baselines of about 50 km like JUNO, RENO-50.

2.5 Open questions and experimental searches

2.5.1 Mass hierarchy

As shown in Eq. 2.18 currently we know both the value and sign of Δm^2_{21} and only the absolute value, and not the sign, of Δm^2_{31}. Thus, we do not know if $m_3 > m_1$ or

$m_3 < m_1$. To be more precise, let us label by superscripts (N,I) the neutrino masses in normal $m_1^{\rm N} < m_2^{\rm N} < m_3^{\rm N}$ and inverted $m_3^{\rm I} < m_1^{\rm I} < m_2^{\rm I}$ hierarchies. Therefore, one has two sets of Δm_{ij}^2: $\Delta m_{21}^{2,\rm N}, \Delta m_{31}^{2,\rm N}, \Delta m_{32}^{2,\rm N}$ and $\Delta m_{21}^{2,\rm I}, \Delta m_{31}^{2,\rm I}, \Delta m_{32}^{2,\rm I}$. Only two Δm_{ij}^2 are linearly independent because obviously:

$$\Delta m_{31}^2 = \Delta m_{32}^2 + \Delta m_{21}^2. \tag{2.25}$$

The mass hierarchy is defined as follows:

$$\begin{aligned} \text{NH:} \quad & \Delta m_{31}^2 \geq 0, \Delta m_{32}^2 \geq 0, \quad |\Delta m_{31}^2| = |\Delta m_{31}^2| + \Delta m_{21}^2 \\ \text{IH:} \quad & \Delta m_{31}^2 \leq 0, \Delta m_{32}^2 \leq 0, \quad |\Delta m_{31}^2| = |\Delta m_{31}^2| - \Delta m_{21}^2 \end{aligned} \tag{2.26}$$

As one can see from this definition, the mass hierarchy is defined by **both the sign and absolute value** of $\Delta m_{31}^2, \Delta m_{32}^2$, in contrast to a simplified definition which is modified by the sign only, and can occasionally be encountered in literature.

Currently we do not know if this mass ordering is a fundamental property of the correct theory beyond the Standard Model. However it *might be* important, and therefore must be accurately measured. Another reason for our interest in the mass ordering is that the sensitivity to the nature of the neutrino (Dirac or Majorana) drastically depends on the mass hierarchy as discussed in Sec. 2.5.4.

How can the mass hierarchy of neutrinos be probed? It can be done with neutrino oscillations in both vacuum and matter.

Mass hierarchy with neutrino oscillations in vacuum

The key point is that the oscillation probability does depend on the mass hierarchy. Let us consider the survival probability $P_{\rm ee}$:

$$1 - P_{\rm ee} = \cos^4\theta_{13}\sin^2 2\theta_{12}\sin^2\Delta_{21} + \sin^2 2\theta_{13}(\cos^2\theta_{12}\sin^2\Delta_{31} + \sin^2\theta_{12}\sin^2\Delta_{32}), \tag{2.27}$$

where $\Delta_{ij} \equiv \Delta m_{ij}^2 L/4E_\nu$.

Changing the mass hierarchy leads to a difference in the survival probability:

$$P_{\rm ee}^{\rm N} - P_{\rm ee}^{\rm I} = -\sin^2 2\theta_{13}\left(\cos^2\theta_{12}\left[\sin^2\Delta_{31}^{\rm N} - \sin^2\Delta_{31}^{\rm I}\right] + \sin^2\theta_{12}\left[\sin^2\Delta_{32}^{\rm N} - \sin^2\Delta_{32}^{\rm I}\right]\right) \tag{2.28}$$

From (2.28) it follows immediately that if the mass hierarchy would be determined simply by the sign of $\Delta m_{31}^2, \Delta m_{32}^2$ then $P_{\rm ee}^{\rm N} - P_{\rm ee}^{\rm I}$ would be identically zero. However, since both the sign and value of $\Delta m_{31}^2, \Delta m_{32}^2$ are changed then $P_{\rm ee}^{\rm N} - P_{\rm ee}^{\rm I} \neq 0$ in general.

It is not trivial, however, to know *what the value of* $P_{\rm ee}^{\rm N} - P_{\rm ee}^{\rm I}$ *is*. Indeed,

- if we *assume* that what we have measured as atmospheric $\Delta m_{\rm A}^2$ is Δm_{32}^2, then

$$P_{\rm ee}^{\rm N} - P_{\rm ee}^{\rm I} = -\sin^2 2\theta_{13}\cos^2\theta_{12}\sin 2\Delta_{32}\sin 2\Delta_{21} \tag{2.29}$$

- if we *assume* that what we have measured as atmospheric $\Delta m_{\rm A}^2$ is Δm_{31}^2, then

$$P_{\rm ee}^{\rm N} - P_{\rm ee}^{\rm I} = +\sin^2 2\theta_{13}\sin^2\theta_{12}\sin 2\Delta_{31}\sin 2\Delta_{21} \tag{2.30}$$

According to these formulas the maximum of $P^{\rm N}_{\rm ee}-P^{\rm I}_{\rm ee}$ occurs at $L/E\simeq 7.5$ km/MeV. What is disturbing, however, is that for seemingly similar assumptions we get different signs and magnitude for the "effect". This raises at least two questions:

- What we actually measure as the atmospheric $\Delta m^2_{\rm A}$?
- How to make an appropriate, unbiased predictions and detector optimization in a search for mass hierarchy?

An attempt to address the first question has been given in [24]. Since $|\Delta m^2_{31,32}|/\Delta m^2_{21}\simeq 30$ all current neutrino oscillation experiments are degenerate in $\Delta m^2_{31,32}$ and they can not measure Δm^2_{31} and Δm^2_{32} simultaneously. What do they measure? They measure flavor-averaged quantities like:

$$\begin{aligned}\Delta m^2_{\alpha\alpha} &\equiv \eta_\alpha \Delta m^2_{31} + (1-\eta_\alpha)\Delta m^2_{32} \\ &= \Delta m^2_{32} + \eta_\alpha \Delta m^2_{21} = \Delta m^2_{31} - (1-\eta_\alpha)\Delta m^2_{21},\end{aligned} \tag{2.31}$$

where

$$\eta_\alpha \simeq \frac{|V_{\alpha 1}|^2}{|V_{\alpha 1}|^2+|V_{\alpha 2}|^2} \tag{2.32}$$

and thus

$$\Delta m^2_{\rm ee} \simeq c^2_{12}\Delta m^2_{31} + s^2_{12}\Delta m^2_{32} \tag{2.33}$$

$$\Delta m^2_{\mu\mu} \simeq s^2_{12}\Delta m^2_{31} + c^2_{12}\Delta m^2_{32} + 2\Delta m^2_{21} s_{12}c_{12}s_{13}\tan\theta_{23}\cos\delta \tag{2.34}$$

$$\Delta m^2_{\tau\tau} \simeq s^2_{12}\Delta m^2_{31} + c^2_{12}\Delta m^2_{32} - 2\Delta m^2_{21} s_{12}c_{12}s_{13}\cot\theta_{23}\cos\delta \tag{2.35}$$

If we assume now that what is measured as atmospheric $\Delta m^2_{\rm A}$ is $\Delta m^2_{\mu\mu}$ then

$$P^{\rm N}_{\rm ee}-P^{\rm I}_{\rm ee} = -\sin^2 2\theta_{13}\sin^2 2\Delta_{ee}\left(c^2_{12}\sin(2s^2_{12}\Delta_{21}) - s^2_{12}\sin(2c^2_{12}\Delta_{21})\right) \tag{2.36}$$

From (2.36) one can see that there is no way to measure the mass hierarchy with vacuum neutrino oscillations if $s^2_{12}=c^2_{12}$. For $\Delta m^2_{ee}=2.44\cdot 10^{-3}$ eV^2 the maximum of $P^{\rm N}_{\rm ee}-P^{\rm I}_{\rm ee}$ can be reached at $L/E\simeq 10\pi$km/MeV. The amplitude of this effect is $\sin^2 2\theta_{13}=9\%$. A relatively large value of $\sin^2 2\theta_{13}$ measured by Daya Bay, RENO opens the possibility for measurement of the mass hierarchy with vacuum oscillations.

As one can see, while the potential to measure the mass hierarchy with vacuum oscillations is there, the actual determination of the detector location and optimization requires careful study. The design study suggests that the mass hierarchy could be observed by a 20 kton liquid scintillator detector placed about 50 km away from a power nuclear reactor. Therefore, the reactor antineutrinos could be used to address the mass hierarchy problem.

Mass hierarchy with neutrino oscillations in matter

Accelerator neutrinos cannot be used to probe the mass hierarchy with vacuum oscillations because the baseline needed for this kind of experiment would significantly exceed the Earth's diameter. This is because neutrinos produced by accelerators typically have energies 1000 times larger. However, Nature is kind enough to provide us with the matter effect, which has unavoidable consequences for long baselines experiments on the Earth.

We have discussed briefly how matter modifies neutrino mixing angles and masses in Sec. 2.4.2. Considering the Earth's mean mass density $\rho \simeq 5.5\text{g/cm}^3$ one gets that $L_e = 2\pi/\sqrt{2}G_F n_e \simeq 3300$ km, which is a characteristic length for the matter effect in the Earth. Effectively, electron neutrinos becomes heavier in matter and thus couple more strongly to ν_τ for the normal mass hierarchy and to ν_μ for the inverted mass hierarchy. Qualitatively, this effect can be explained by the following chains:

Normal Hierarchy	Inverted Hierarchy
$\nu_e \to \nu_3^m \to \nu_\tau$	$\nu_e \to \nu_2^m \to \nu_\mu$
$\nu_\tau \to \nu_2^m \to \nu_\mu$	$\nu_\mu \to \nu_1^m \to \nu_\tau$
$\nu_\mu \to \nu_1^m \to \nu_e$	$\nu_\tau \to \nu_3^m \to \nu_e$

Due to the matter effect $P_{\mu e}$ is enhanced for the normal hierarchy and suppressed for the inverted hierarchy. The effect can be as large as 30% for $E_\nu = 6$ GeV and $L = 6000$ km.

Currently, T2K (295 km) and NOVA (810 km), each with their own sensitivity, are exploiting this effect to address the mass hierarchy problem. Future experiments include LBNE (US) and LBNO (Europe) projects which should typically have more powerful beams, more massive detectors and larger baselines (about 1300/2200 km) and thus better sensitivities to the mass hierarchy.

Matter effects can also be used with atmospheric neutrinos (PINGU/ORCA and INO projects) to address the mass hierarchy problem. Let us also mention an idea to direct the CERN neutrino flux towards Baikal Lake, where the BAIKAL-GVD detector is being installed.

Cosmology can also assess the neutrino mass hierarchy problem because of the following. For the case of normal mass hierarchy one meets a situation when two neutrino masses are light (m_1, m_2) and third mass is heavier m_3 and their sum $\sim_i m_i$, as measured from cosmological data, is dominated mainly by m_3. For the case of inverted mass hierarchy now two masses (m_1, m_2) are both heavier than m_3 and the sum $\sum_i m_i$ is dominated by both m_1 and m_2 making the sum heavier in respect to the normal mass hierarchy case. Therefore, a precise measurement of $\sum_i m_i$ by Planck may exclude the inverted hierarchy scenario or get a 2-3 sigma evidence for it. The next generation of galaxy and galaxy clusters catalogs promises to achieve 10 percent sensitivity to the neutrino mass scale even for the normal hierarchy.

Summary of various proposals to address the mass hierarchy

A summary of various proposals addressing the mass hierarchy problem is given in Tab. 2.1. Not every project among those mentioned in this table are in equally good shape. Some of these have problems in realization, but are kept in the table for the purpose or providing perspective. As can be seen, none of these projects **alone** can promise a mass hierarchy discovery at 5σ confidence level before 2025. The mass hierarchy will most probably be discovered by a global analysis of all available and forthcoming neutrino data. In JINR we are developing the corresponding tools.

Project	ν source	Detector	Goal	Problems
NOVA	LBL (810 km)	14 kt tracking calorimeter	2σ (2020)	parameter degeneracy
JUNO	Reactor (52 km)	20 kt LS	3σ (2025)	energy resolution
PINGU/ORCA	Atmosphere	1-10 Mt ice	3–5σ (unknown)	energy resolution, systematics
INO	Atmosphere	50 kt magnetized calorimeter	3σ (2030)	low statistics (10 years)
T2HK	LBL (295 km)	1 Mt water	3σ (2030)	parameter degeneracy
LBNE	LBL (1300 km)	10 kt liquid argon	2–5σ (2030)	parameter degeneracy
LAGUNA/Glacier	LBL (2300 km)	20 kt liquid argon	5σ (2030)	beam line from CERN
LAGUNA/LENA	LBL (2300 km)	50 kt LS	5σ (2030)	beam line from CERN
Planck/Cosmology	VERY LONG		2–3σ (<2020?)	cosmology model dependent

Table 2.1: Summary of various proposals addressing the mass hierarchy problem.

2.5.2 CP violation

CP violation was discovered in the quark sector. The corresponding phase $\delta_{\text{quark}} = (68.76 \pm 4.58)^o$. The corresponding phase in the lepton sector has not been measured yet. The global analysis currently indicates a preference for $\delta_{\text{lepton}} = (194 \pm 67)^o$ [25]. The statistical significance is about 2.9σ. This is not, however, a direct measurement.

A direct measurement of δ in the lepton sector is possible by studying neutrino oscillations. The CP violation displays itself as $P_{\alpha\beta} \neq P_{\bar{\alpha}\bar{\beta}}$ if $\delta \neq 0, \pi$. The asymmetry

$$\frac{P_{\alpha\beta} - P_{\bar{\alpha}\bar{\beta}}}{P_{\alpha\beta} + P_{\bar{\alpha}\bar{\beta}}} \propto \frac{1}{\sin 2\theta_{13}} \tag{2.37}$$

Large values of θ_{13} makes the asymmetry (2.37) smaller and the CP-violation phase measurement harder. Experimentally it is most practical to study $\nu_\mu \leftrightarrow \nu_e$ transitions. Matter effects mimic the CP-violation as $P_{\alpha\beta} \neq P_{\bar{\alpha}\bar{\beta}}$ even if $\delta \neq 0, \pi$. Therefore, an understanding and careful control of matter effects in a study of CP-violation in the lepton sector is needed. In Fig. 2.5 we display the potential to measure δ_{CP} CP-violating phase at 1 σ confidence level by various experimental facilities [26]. T2HK, NOVA and LBNE do not cover

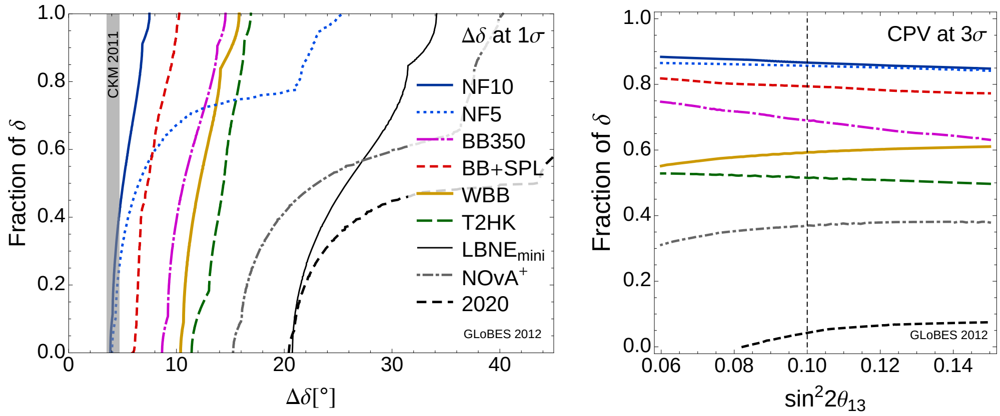

Figure 2.5: Fraction of δ_{CP} which can be measured at 1 σ confidence level by various experimental facilities. The figure is from [26].

all possible values of δ. LBNO, neutrino factories and beta beams might have much wider coverage if these projects are realized. It appears that the CP-violating phase is a high bar in neutrino physics.

2.5.3 Tests of mixing matrix unitarity

The lepton mixing matrix should be unitary if there are no degrees of freedom unaccounted for, like yet unknown neutrinos. However, currently we are not yet able to test the unitarity of the mixing matrix because of lack of precision. Instead, oscillation analyses *assume* that the matrix is unitary. Unitarity implies certain relationship between the matrix elements:

$$\sum_k V_{ik} V^*_{kj} = \delta_{ij}. \tag{2.38}$$

Since the matrix elements of V are, in general, complex numbers the relationship (2.38) can be visualized on the complex plane as a unitarity triangle. A spectacular demonstration of the unitarity of the quark mixing matrix is shown in Fig. 2.6.

A test of the unitarity of neutrino mixing matrix is a high bar to be reached by the next generation of experiments. However, we already have some doubts about its unitarity due to still hypothetical sterile neutrinos. There are several hints which favor the sterile neutrino's existence.

- Reactor anomaly: new calculations [28, 29] of reactor $\bar{\nu}_e$ flux predict about 3% higher flux mainly due to:
  - decrease in neutron lifetime
  - inclusion of long-lived isotopes (non-equilibrium correction)
- Gallium anomaly

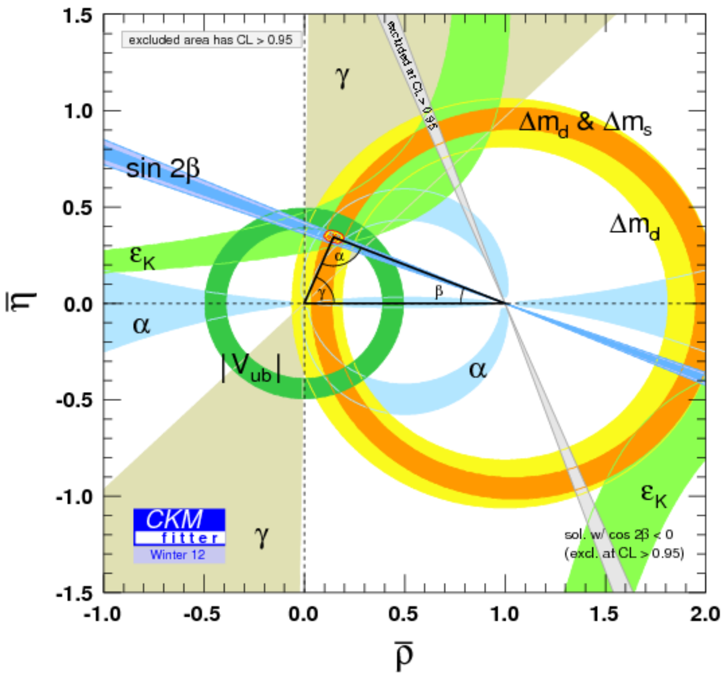

Figure 2.6: Unitarity triangle for the quark mixing matrix. The figure is taken from CKM fitter group [27]

  - SAGE detector exploits the reaction $\nu_e + {}^{71}\text{Ga} \to {}^{71}\text{Ge} + e^-$
  - During the calibration campaign they have used two calibration sources ^{51}Cr and ^{37}Ar which emit ν_e with 6 fixed energies in total.
  - The ratio measured/predicted was found to be 0.86 ± 0.05, which deviates from unity at 2.8σ

- LSND and MiniBooNE $\nu_\mu \to \nu_e$ data show an excess over the expectations.

- WMAP measurements of CMB anisotropy favors four neutrinos as relativistic degrees of freedom.

- However, there are some limits on the existence of sterile neutrinos:

  - LSND and KARMEN measured the cross-section of the $\nu_e + {}^{12}\text{C} \to {}^{12}\text{N} + e^-$ reaction and found it to be consistent with expectations thus limiting ν_e disappearance
  - Planck CMB data combined with other CMB and astrophysical data yields $N_\nu = 3.73^{+0.54}_{-0.51}$. While the central value also differs from the expected 3.046 available for three degrees of freedom, it certainly agrees within the uncertainties.

Various approaches for sterile neutrino search and a number of proposals are summarized in [30].

2.5.4 Dirac or Majorana?

If a fermion is different from its charge conjugated state (anti-particle) then this fermion is classified as a Dirac particle. If a fermion coincides with the charge conjugated state then this is known as a Majorana fermion. Quarks and charged leptons are Dirac fermions as their antiparticles are apparently different states because of opposite electric charge. The neutrino, a truly neutral fermion, could be either a Dirac or Majorana particle. So far there is no solid experimental evidence favoring either of these possibilities. Some cosmology models prefer to assume neutrinos are Majorana particles. Experimental search exploits the following diagram in Fig. 2.7 possible only for massive Majorana neutrinos. Let us discuss

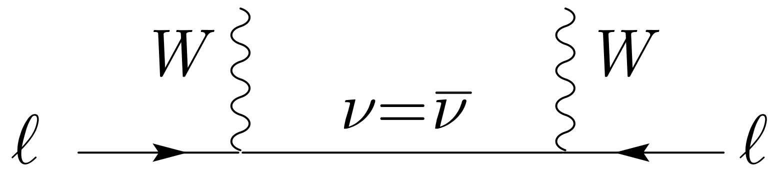

Figure 2.7: $\Delta L = 2$ violating process possible only for massive Majorana neutrinos.

the diagram in more detail. This diagram corresponds to an exchange of a virtual neutrino (antineutrino) between two pairs of particles (ℓ, W). It is easy to see that this diagram does not exist in the SM if the neutrino is a Dirac fermion. This diagram is possible only if neutrino is a Majorana particle. Therefore, an observation of the processes described by this diagram will unambiguously tell us that neutrino is a Majorana fermion. The amplitude for such a process is, however, small because of smallness of neutrino mass:

$$A \propto m_{\text{eff}} = \sum_i V_{ei}^2 m_i .$$

The proportionality of the amplitude to neutrino mass is explained as being due to mixing of left and right helicity states of neutrino field. At zero neutrino mass the helicity and chirality states coincide making the overall amplitude equal to zero. The diagram in Fig. 2.7 can describe the following processes.

- Considering the W bosons in this diagram as virtual particles which interact with a d-quark in the neutron transforming it to u-quark, and ℓ as final state electrons then this diagram will correspond to a transformation of two neutrinos into two protons and two electrons without a final state neutrino or antineutrino:

  $$2n \to 2p\, 2e^- .$$

  This reaction is known as neutrinoless double beta decay $0\nu\beta\beta$. This reaction is most sensitive to the nature of the neutrino if the neutrino mass is in sub-eV–eV region.

Searches for these decays have been carried out for several decades and no decay of this kind has been observed, aside from a claim by the Heidelberg-Moscow experiment [31–34], made by Prof. H.V.Klapdor-Kleingrothaus — the leader of the collaboration. He has estimated the observed effective Majorana neutrino mass to be in a window 0.2–0.6 eV. This result has been criticized [35, 36] and recently has been questioned by GERDA Collaboration [37, 38]. The authors of the Heidelberg-Moscow claim have, however, disagreed with the interpretation of the GERDA limit [39].

- Heavy Majorana neutrinos (with a mass of hundreds GeV, TeV) could be searched for in accelerators by looking for collisions of charged leptons of equal sign producing two W bosons:

$$l^- l^- \to W^- W^- .$$

The cross-section of this process strongly depends on the neutrino mass. It vanishes at $m_\nu \to 0$ and $m_\nu \to \infty$ and is potentially measurable at colliders if $m_\nu \sim$ TeV [40–42].

A summary of neutrino experiments setting upper limits on neutrino effective masses in neutrinoless double beta decay, as well as planned sensitivities of future experiments, are collected in Tab. 2.2. Effective $|m_{\beta\beta}|$ as a function of the lightest mass in the normal NS and

Experiment	Nucleus	$m_{\beta\beta}$, eV
Heidelberg-Moscow	^{76}Ge	$< 0.22 - 0.64$
Cuoricino	^{130}Te	$< 0.30 - 0.71$
NEMO-3	^{100}Mo	$< 0.44 - 1.00$
KamLAND-Zen	^{136}Xe	$< 0.26 - 0.64$
EXO	^{136}Xe	$< 0.14 - 0.38$
GERDA	^{76}Ge	$< 0.073 - 0.2$
CURE	^{130}Te	$< 0.04 - 0.094$
KamLAND-Zen	^{136}Xe	< 0.025
EXO	^{136}Xe	$< 0.026 - 0.040$

Table 2.2: Summary of neutrino experiments setting upper limits on neutrino effective masses in neutrinoless double beta decay, as well as planned sensitivities of future experiments (after double line).

inverted IS neutrino mass spectra after Daya Bay measurement are shown in Fig. 2.8 (figure from Ref. [43]). Next-generation experiments will be sensitive to the Majorana nature of neutrinos for the inverted mass hierarchy scenario. A factor of ten increase to the sensitivity is needed to probe the Majorana nature of neutrinos in the case of normal mass hierarchy. If these events are not observed in future experiments it will unambiguously indicate that neutrino is a Dirac fermion. The experiments exploring if neutrino is Majorana or Dirac particle also probe the absolute scale of neutrino mass — an important quantity which could not probed by neutrino oscillation experiments.

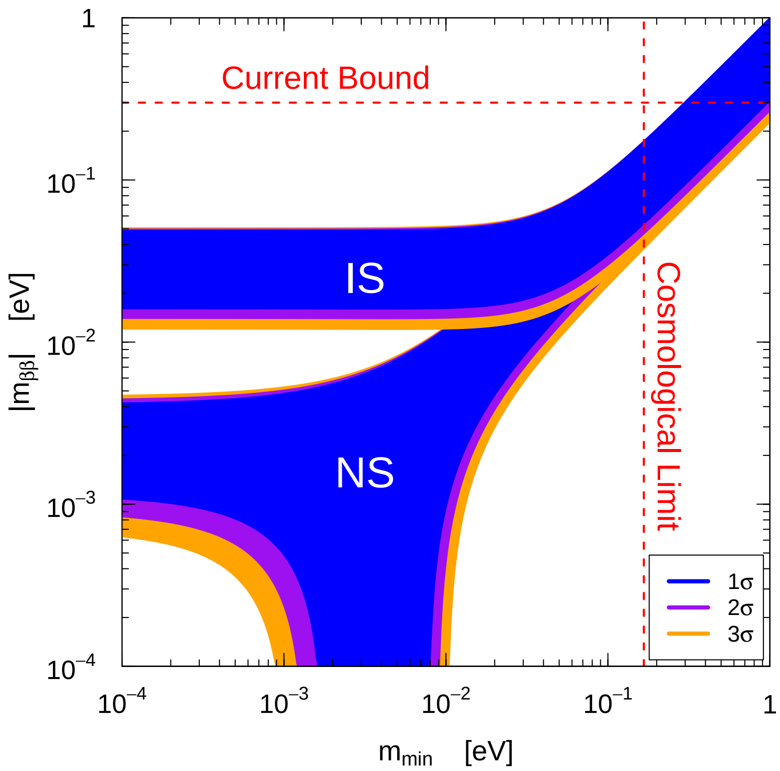

Figure 2.8: Effective $|m_{\beta\beta}|$ as a function of the lightest mass in the normal (NS, $m_{\text{min}} = m_1$) and inverted (IS, $m_{\text{min}} = m_3$) neutrino mass spectra after Daya Bay measurement [43].

References

[1] F.P. An et al. “Observation of electron-antineutrino disappearance at Daya Bay”. In: *Phys.Rev.Lett.* 108 (2012), p. 171803. arXiv: 1203.1669 [hep-ex].

[2] J.K. Ahn et al. “Observation of Reactor Electron Antineutrino Disappearance in the RENO Experiment”. In: *Phys.Rev.Lett.* 108 (2012), p. 191802. arXiv: 1204.0626 [hep-ex].

[3] Y. Abe et al. “Indication for the disappearance of reactor electron antineutrinos in the Double Chooz experiment”. In: *Phys.Rev.Lett.* 108 (2012), p. 131801. arXiv: 1112.6353 [hep-ex].

[4] P. Adamson et al. “Electron neutrino and antineutrino appearance in the full MINOS data sample”. In: *Phys.Rev.Lett.* 110.17 (2013), p. 171801. arXiv: 1301.4581 [hep-ex].

[5] K. Abe et al. “Evidence of Electron Neutrino Appearance in a Muon Neutrino Beam”. In: *Phys.Rev.* D88 (2013), p. 032002. arXiv: 1304.0841 [hep-ex].

[6] S. Abe et al. “Precision Measurement of Neutrino Oscillation Parameters with KamLAND”. In: *Phys.Rev.Lett.* 100 (2008), p. 221803. arXiv: 0801.4589 [hep-ex].

[7] Y. Ashie et al. "Evidence for an oscillatory signature in atmospheric neutrino oscillation". In: *Phys.Rev.Lett.* 93 (2004), p. 101801. arXiv: hep-ex/0404034 [hep-ex].

[8] F.P. An et al. "Spectral measurement of electron antineutrino oscillation amplitude and frequency at Daya Bay". In: *Phys.Rev.Lett.* 112 (2014), p. 061801. arXiv: 1310.6732 [hep-ex].

[9] M. Beuthe. "Towards a unique formula for neutrino oscillations in vacuum". In: *Phys.Rev.* D66 (2002), p. 013003. arXiv: hep-ph/0202068 [hep-ph].

[10] Christian Y. Cardall. "Coherence of neutrino flavor mixing in quantum field theory". In: *Phys.Rev.* D61 (2000), p. 073006. arXiv: hep-ph/9909332 [hep-ph].

[11] P. Stockinger. "Introduction to a field-theoretical treatment of neutrino oscillations". In: *Pramana* 54 (2000), pp. 203–214.

[12] W. Grimus, S. Mohanty, and P. Stockinger. "Neutrino oscillations and the effect of the finite lifetime of the neutrino source". In: *Phys.Rev.* D61 (2000), p. 033001. arXiv: hep-ph/9904285 [hep-ph].

[13] W. Grimus, S. Mohanty, and P. Stockinger. "Field theoretical treatment of neutrino oscillations: The Strength of the canonical oscillation formula". In: (1999), pp. 123–137. arXiv: hep-ph/9909341 [hep-ph].

[14] W. Grimus, S. Mohanty, and P. Stockinger. "Field theoretical treatment of neutrino oscillations". In: (1999). arXiv: hep-ph/9904340 [hep-ph].

[15] Evgeny Kh. Akhmedov. "Do charged leptons oscillate?" In: *JHEP* 0709 (2007), p. 116. arXiv: 0706.1216 [hep-ph].

[16] Evgeny Kh. Akhmedov and Alina Wilhelm. "Quantum field theoretic approach to neutrino oscillations in matter". In: *JHEP* 1301 (2013), p. 165. arXiv: 1205.6231 [hep-ph].

[17] Evgeny Kh. Akhmedov and Joachim Kopp. "Neutrino oscillations: Quantum mechanics vs. quantum field theory". In: *JHEP* 1004 (2010), p. 008. arXiv: 1001.4815 [hep-ph].

[18] D.V. Naumov and V.A. Naumov. "A Diagrammatic treatment of neutrino oscillations". In: *J.Phys.* G37 (2010), p. 105014. arXiv: 1008.0306 [hep-ph].

[19] Dmitry V. Naumov and Vadim A. Naumov. "Relativistic wave packets in a field theoretical approach to neutrino oscillations". In: *Russ.Phys.J.* 53 (2010), pp. 549–574.

[20] Vadim A. Naumov and Dmitry S. Shkirmanov. "Extended Grimus-Stockinger theorem and inverse square law violation in quantum field theory". In: *Eur.Phys.J.* C73 (2013), p. 2627. arXiv: 1309.1011 [hep-ph].

[21] Mattias Blennow and Alexei Yu. Smirnov. "Neutrino propagation in matter". In: *Adv.High Energy Phys.* 2013 (2013), p. 972485. arXiv: 1306.2903 [hep-ph].

[22] S.P. Mikheev and A. Yu. Smirnov. "Resonance Amplification of Oscillations in Matter and Spectroscopy of Solar Neutrinos". In: *Sov.J.Nucl.Phys.* 42 (1985), pp. 913–917.

[23] L. Wolfenstein. “Neutrino Oscillations in Matter”. In: *Phys.Rev.* D17 (1978), pp. 2369–2374.

[24] Hiroshi Nunokawa, Stephen J. Parke, and Renata Zukanovich Funchal. “Another possible way to determine the neutrino mass hierarchy”. In: *Phys.Rev.* D72 (2005), p. 013009. arXiv: hep-ph/0503283 [hep-ph].

[25] G.L. Fogli et al. “Global analysis of neutrino masses, mixings and phases: entering the era of leptonic CP violation searches”. In: *Phys.Rev.* D86 (2012), p. 013012. arXiv: 1205.5254 [hep-ph].

[26] Pilar Coloma et al. “Systematic uncertainties in long-baseline neutrino oscillations for large θ_{13}”. In: *Phys.Rev.* D87.3 (2013), p. 033004. arXiv: 1209.5973 [hep-ph].

[27] J. Charles et al. “CP violation and the CKM matrix: Assessing the impact of the asymmetric B factories”. In: *Eur.Phys.J.* C41 (2005), pp. 1–131. arXiv: hep-ph/0406184 [hep-ph].

[28] Th.A. Mueller et al. “Improved Predictions of Reactor Antineutrino Spectra”. In: *Phys.Rev.* C83 (2011), p. 054615. arXiv: 1101.2663 [hep-ex].

[29] Patrick Huber. “On the determination of anti-neutrino spectra from nuclear reactors”. In: *Phys.Rev.* C84 (2011), p. 024617. arXiv: 1106.0687 [hep-ph].

[30] K.N. Abazajian et al. “Light Sterile Neutrinos: A White Paper”. In: (2012). arXiv: 1204.5379 [hep-ph].

[31] H.V. Klapdor-Kleingrothaus et al. “Evidence for neutrinoless double beta decay”. In: *Mod.Phys.Lett.* A16 (2001), pp. 2409–2420. arXiv: hep-ph/0201231 [hep-ph].

[32] Hans Volker Klapdor-Kleingrothaus. “First evidence for neutrinoless doubly beta decay: And world status of double beta experiments”. In: (2005), pp. 215–237. arXiv: hep-ph/0512263 [hep-ph].

[33] H.V. Klapdor-Kleingrothaus and I.V. Krivosheina. “The evidence for the observation of 0nu beta beta decay: The identification of 0nu beta beta events from the full spectra”. In: *Mod.Phys.Lett.* A21 (2006), pp. 1547–1566.

[34] H.V. Klapdor-Kleingrothaus. “Lessons after the evidence for neutrinoless double beta decay: The next step”. In: *Int.J.Mod.Phys.* E17 (2008), pp. 505–517.

[35] Ferruccio Feruglio, Alessandro Strumia, and Francesco Vissani. “Neutrino oscillations and signals in beta and 0nu2beta experiments”. In: *Nucl.Phys.* B637 (2002), pp. 345–377. arXiv: hep-ph/0201291 [hep-ph].

[36] C.E. Aalseth et al. “Comment on ‘Evidence for neutrinoless double beta decay’”. In: *Mod.Phys.Lett.* A17 (2002), pp. 1475–1478. arXiv: hep-ex/0202018 [hep-ex].

[37] Carla Macolino. “Results on neutrinoless double beta decay from GERDA Phase I”. In: *Mod.Phys.Lett.* A29.1 (2014), p. 1430001. arXiv: 1312.0562 [hep-ex].

[38] M. Agostini et al. “Results on neutrinoless double beta decay of 76Ge from GERDA Phase I”. In: *Phys.Rev.Lett.* 111 (2013), p. 122503. arXiv: 1307.4720 [nucl-ex].

[39] Hans Volker Klapdor-Kleingrothaus and Irina V. Krivosheina. “Why is the conclusion of the Gerda experiment not justified”. In: *Phys.Part.Nucl.Lett.* 10 (2013), pp. 704–709. arXiv: 1308.2524 [hep-ex].

[40] C.A. Heusch. “Can heavy Majorana neutrinos be found in TeV electron electron scattering? The nuclear connection”. In: *Nucl.Phys.* A629 (1998), pp. 545C–551C.

[41] C.A. Heusch and P. Minkowski. “Heavy Majorana neutrinos in high-energy e- e- collisions compared with their effects inducing neutrinoless double beta decay”. In: *Int.J.Mod.Phys.* A15 (2000), pp. 2429–2446.

[42] J. K. Singhal et al. “Heavy neutrino mixing effects in helicity amplitudes for the process $\mu^+\mu^- \to W^+W^-$”. In: *Phys.Rev.* D63 (2001), p. 017302.

[43] S.M. Bilenky and Carlo Giunti. “Neutrinoless double-beta decay: A brief review”. In: *Mod.Phys.Lett.* A27 (2012), p. 1230015. arXiv: 1203.5250 [hep-ph].

Chapter 3

BAIKAL Experiment

Editors: I.A.Belolaptikov, V.B.Brudanin

Project Title

BAIKAL Experiment. Deep underwater muon and neutrino detector in the Baikal Lake.

Project Leaders

- I.A.Belolaptikov

Abstract

The BAIKAL-GVD Project in the Lake Baikal [1] is an extension of the research and development work performed over the past several years by the BAIKAL Collaboration on the first phase. The optical properties of the deep water lake have been established, and the detection of high-energy neutrinos has been demonstrated with the existing detector NT200/NT200+. This achievement represents a proof of concept for commissioning a new instrument, the Gigaton Volume Detector (**BAIKAL-GVD**), with superior detector performance and an effective telescope size at or above the kilometer-scale.

The second-stage neutrino telescope BAIKAL-GVD will be a new research infrastructure aimed primarily at studying astrophysical neutrino fluxes. The detector will utilize Lake Baikal water instrumented at depth with optical sensors that detect the Cherenkov radiation from secondary particles produced in interactions of high-energy neutrinos inside or near the instrumented volume. The concept of BAIKAL-GVD is based on a number of evident requirements to the design and architecture of the recording system of the new array: the utmost use of the advantages of array deployment from the ice cover of Lake Baikal, the extendability of the facility and provision of its effective operation even in the first stage of deployment, and the possibility of implementing different versions of arrangement and spatial distribution of light sensors within the same measuring system.

keywords: neutrino oscillations, neutrino mass hierarchy, astrophysical neutrinos

Project Members From JINR

I. Belolaptikov, V. Brudanin, Y. Honz, Z. Honz, A. Klimenko, K. Konischev, A. Kuznetsov, L. Perevozschikov, E. Pliskovskiy, A. Smagina, B. Shaibonov

Project Duration. Approval Date(s)

Start of R&D	2008
Trial section	2010
Project PAC approval (within JINR Theme #1100)	2012
Tests with Prototypes	2010-2012
Mounting of demonstration cluster **Dubna** at	2013-2015
Full detector	2020

List of Participating Countries and Institutions

Joint Institute for Nuclear Research, Dubna, Russia; Institute for Nuclear Research, Moscow, Russia; Irkutsk State University, Irkutsk, Russia; Skobeltsyn Institute of Nuclear Physics MSU, Moscow, Russia; Nizhny Novgorod State Technical University, Russia; St.Petersburg State Marine University, Russia; EvoLogics Gmb., Berlin, Germany

3.1 Project Description

3.1.1 Fundamental Scientific Problem Addressed by the Project

The next generation neutrino telescope, BAIKAL-GVD (Figs. 3.1a and 3.1b), will be aimed primarily at studying astrophysical neutrino fluxes and, in particular, mapping the high-energy neutrino sky in the Southern Hemisphere including the region of the galactic center. Other topics include indirect search for dark matter by detecting neutrinos produced in WIMP annihilation in the Sun or in the center of the Earth. BAIKAL-GVD will also search for exotic particles like magnetic monopoles, super-symmetric Q-balls or nuclearites.

3.1.2 Specific Project Objectives and Expected Results

Neutrinos from local astrophysical objects

The natural high-energy neutrino fluxes are produced by physical processes in astrophysical objects characterized by enormous energy release at a rates from 10^{39} to 10^{52} erg/s or higher. The nearest (with respect to a terrestrial observer) astrophysical objects that are currently assumed to be capable of emitting high-intensity neutrino fluxes are located mainly in the vicinity of the Galactic center and in the Galactic plane. Supernova remnants, pulsars, the neighborhood of the black hole Sgr A* at the Galactic center, binary systems containing a black hole or a neutron star, and clusters of molecular clouds that are targets for cosmic-ray protons and nuclei are the most promising Galactic sources with respect to

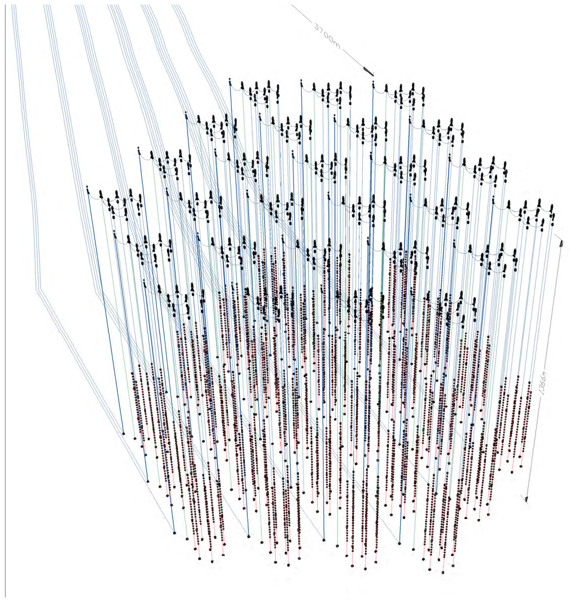

(a) BAIKAL-GVD design: top view (27 clusters)

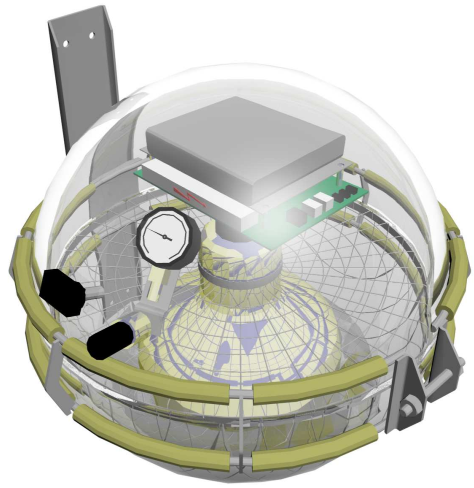

(b) Optical module is a basic element of the detector.

the detection of their neutrino emission. The energy spectrum of neutrinos from Galactic sources fills the energy range $10^3 \div 10^6$ GeV.

Extragalactic objects — active galactic nuclei (**AGN**), gamma-ray bursts (**GRB**), starburst galaxies and galaxy clusters — belong to another class of neutrino sources whose emission can be recorded by ground-based facilities. This class of sources is characterized by much greater energy release and generates neutrinos in the energy range $10^4 \div 10^8$ GeV or higher. Searching for a neutrino signal from identified sources imposes stringent requirements on the resolution of neutrino telescopes from the viewpoint of measuring both neutrino energy and direction.

Diffuse neutrino flux

The other direction of research on the astrophysical neutrinos is to investigate the energy spectrum, global anisotropy, and neutrino flavor composition of the diffuse neutrino flux from unidentified sources at energies above 10^4 GeV, at which the background from atmospheric neutrinos is comparable to or lower than the expected flux. The diffuse high-energy neutrino flux near the Earth is produced by neutrino emission from the entire set of sources during the period from remote cosmological epochs to the present day. Extragalactic sources make a major contribution to this flux. The neutrinos produced by the interaction of cosmic rays with interstellar matter and, in the case of ultra-high-energy cosmic rays, with electromagnetic radiation from a wide energy range, including the cosmic microwave background, also contribute to the diffuse flux. It should be noted that the neutrinos from the decay of supermassive particles associated, in particular, with Grand Unified Theories (GUT) (top-down scenario) could account for a certain fraction of the diffuse flux.

The standard approach used by a wide range of theoretical models describing the formation of neutrino fluxes in cosmic-ray sources suggests the production of neutrinos mainly during the decay of π-mesons produced in pp and $p\gamma$ interactions. In this case, the flavor ratio of emitted neutrino flux is approximately $\nu_e : \nu_\mu : \nu_\tau \approx 1 : 2 : 0$. This ratio changes with distance to the source due to the neutrino oscillations. According to Super-Kamiokande experimental data [2], the ν_μ–ν_τ oscillation length when choosing the oscillation parameters $\delta m^2 = 2.5 \times 10^{-3}$ eV^2 and $\sin 2\theta = 1$ is about of $L_{osc} \sim 1.3 \times 10^{-4}(E_\nu/1$ PeV) parsecs. Thus, the oscillation length turns out to be much smaller than the characteristic distances to the presumed astrophysical sources of high-energy neutrinos and the flavor ration is transformed in $\nu_e : \nu_\mu : \nu_\tau \approx 1 : 1 : 1$.

Dark matter

One of the challenges of modern natural science is to find dark matter particles. Observational data in the field of astronomy and cosmology irrefutably suggest that, apart from ordinary matter, there is matter of a new type - dark matter - in galaxies, galaxy clusters, and the Universe as a whole. Moreover, on the whole, the mass of dark matter in the Universe exceeds that of ordinary matter by a factor of 5–6.

To all appearances, dark matter is composed of as yet unknown particles with the masses which exceed appreciably that of the heaviest known stable elementary particle - the proton. These new particles must have a lifetime comparable to or exceeding the age of the Universe. Undoubtedly, such a long lifetime is related to new conservation laws in fundamental physics. It can be said with great confidence that a whole stratum of new phenomena in particle physics occurring at ultra-high energies and inaccessible to investigation on existing accelerators stands behind the dark matter particles.

Dark matter particles would interact very weakly with ordinary matter. Therefore, their direct detection, if at all possible, is an extremely complicated problem of experimental physics. An indirect approach to detect dark matter particles associated with the search for the products of their annihilation at the center of the Earth, the Sun, or the Galaxy is also very promising. There must be neutrinos of fairly high energies among these products, which, in turn, interact very weakly with matter and pass through the Earth or the Sun virtually without absorption. Neutrinos of such energies are successfully recorded on large underground facilities and neutrino telescopes placed in natural media.

The methods of searching for dark matter particles with underground detectors and neutrino telescopes in natural media consist in recording an excess of the muon flux in a direction away from the center of the Earth or the Sun or from the Galactic center above the background from atmospheric neutrinos. The constraints on the additional muon flux in a direction away from the Earth's center and the Sun have been obtained on the Baksan, Super-Kamiokande, and MACRO underground facilities as well as on the underwater and under-ice neutrino telescopes NT200 (Lake Baikal), ANTARES (Mediterranean Sea), AMANDA and IceCube (South Pole). Underground neutrino detectors have a lower muon detection energy threshold ($\simeq 1 \div 3$ GeV) than deep underwater (under-ice) facilities. Therefore, these two classes of detectors complement each other. The former are efficient at searching for particles with a mass below 80 GeV (the threshold W-boson production energy), while the latter are efficient at investigating particles with a mass of about 100 GeV or higher.

A further substantial increase in the sensitivity of an experiment to the muon flux from the annihilation of dark matter particles can be achieved only by increasing their effective area. In the case of neutrino telescopes, the problem is reduced to creating cubic-kilometer facilities. In the case of underground facilities, such an increase in the effective area implies an increase in the characteristic detector sizes to a hundred meters or more. Creating such a huge underground facility seems extremely unrealistic at present.

Atmospheric neutrinos

Cosmic rays generate the most intense neutrino flux observed in ground-based experiments in the energy range from hundreds of MeV to hundreds of TeV. A large number of pions and kaons are produced when cosmic rays interact with atmospheric matter. The pion, kaon, and muon decay reactions

$$\pi^{\pm} \to \mu + \nu_\mu; \;\; K^{\pm} \to \mu + \nu_\mu; \;\; \mu \to e + \nu_\mu + \bar{\nu}_e$$

produce the neutrinos which are referred to as *conventional* atmospheric neutrinos. In the energy range 100 GeV – 100 TeV, the spectrum of *conventional* atmospheric neutrinos is described by the expression:

$$\frac{d^2N}{dE_\nu d\Omega}(E_\nu, \theta) = A_\nu (E_\nu/\text{ГэВ})^{-\gamma} \left[\frac{1}{1 + 6E_\nu/E_\pi(\theta)} + \frac{0.213}{1 + 1.44E_\nu/E_K(\theta)} \right],$$

where $A_\nu = 0.0285$ GeV^{-1} cm^{-2} s^{-1} ster^{-1}, $\gamma = 2.69$, E_π and E_K are the critical energies of the pions and kaons (the energies at which the decay probability is equal to the interaction probability) dependent on the zenith angle θ.

The primary cosmic rays are distributed isotropically near the Earth, but the development of cascades initiated by primary radiation in the atmosphere breaks the isotropy of the fluxes of secondary particles. The pions and kaons produced by a primary particle at large zenith angles spend much of their time in a rarefied atmosphere, where the decay probability is higher than the interaction probability. Therefore, the horizontal neutrino flux exceeds the vertical one. As the energy grows, the lifetime of pions and kaons increases and, accordingly, the decay probability decreases compared to the interaction probability. Therefore, the energy spectrum of the neutrinos produced by pions and kaons becomes steeper with growing energy (the exponent γ increases by one) than the primary cosmic-ray spectrum. The uncertainty in the predictions of the neutrino fluxes from pions and kaons is related to the uncertainty in the cosmic-ray flux and energy spectrum as well as to the uncertainty in the fraction of the kaons and pions produced in a nuclear interaction at high energies. The difference in the spectra of atmospheric neutrinos from pions and kaons calculated by different authors is about 25%.

A different neutrino production mechanism is possible at energies above 100 TeV. The *prompt* neutrinos can be produced in the decays of charmed mesons and baryons with a lifetime of the order of or less than 10^{-12} s. The spectrum of prompt neutrinos essentially follows the cosmic-ray spectrum and is flatter than that of conventional neutrinos. No prompt neutrinos have been experimentally detected so far. According to calculations, the energy at which the fluxes of prompt neutrinos become equal to and then exceed the conventional neutrino fluxes depends on the model for the interaction of primary cosmic rays with the air nuclei and on the zenith angle. For the vertical neutrino flux, this energy lies within the range 100–1000 TeV and increases with zenith angle.

From the viewpoint of experiments on neutrino telescopes, atmospheric neutrinos are the source of the natural irreducible background that complicates significantly the detection of astrophysical neutrinos. On the other hand, since the theoretical prediction level of the intensity and characteristics of the atmospheric neutrino flux is fairly high, this flux can be effectively used as a calibration neutrino flux. In addition, searching for prompt neutrinos is an important scientific task.

Magnetic monopoles

The concept of a magnetic monopole was introduced into the modern physical theory in 1931 by Dirac [3]. He showed that any magnetic charge should be a multiple of the minimum possible charge g uniquely related to the minimum electric charge:

$$g = (\hbar c/2e) \approx (137/2e).$$

Thus, the minimum magnetic charge is approximately a factor of 68.5 larger than the minimum electric charge. In particular, this implies that the ionization energy losses for relativistic monopoles in a medium are much larger than those for relativistic muons. This opens good possibilities for the detection of fast monopoles in experiments with neutrino telescopes. The theory of Cherenkov radiation from magnetic monopoles was first examined by I.M. Frank [4]. The linear density of Cherenkov radiation with a wavelength λ (under the assumption that the permeability of the medium is $\mu \sim 1$) is described by the expression

$$\frac{d^2 n_c}{dx d\lambda} = \frac{2\pi\alpha}{\lambda^2}\left(\frac{ng}{e}\right)^2\left(1 - \frac{1}{n^2\beta^2}\right),$$

where g is the magnetic charge of the monopole, e is the charge of electron, n is the refractive index of the medium (for water, $n = 1.33$), $\beta = v/c$ is a monopole velocity expressed in units of the speed of light in vacuum and α is the fine-structure constant.

The Cherenkov radiation from a relativistic monopole in water is a factor of $(ng/e)^2 \approx 8300$ more intense than that from a relativistic muon. Thus, a magnetic monopole with a speed $\beta \sim 1$ is a bright light source corresponding in intensity to a muon with an energy of $\sim 1.4 \times 10^4$ TeV. Intense searches for magnetic monopoles stimulated by the works [5, 6] have been performed since the mid-1970s. In these works, it was shown for the first time that the possibility of the existence of topological defects in the form of magnetic monopoles in the Universe is a corollary of Grand Unified Theories (GUT). The masses of these particles lie in a wide range from $\sim 10^8$ GeV to $\sim 10^{21}$ GeV, depending on the GUT versions. The most reliable astrophysical constraints on the natural flux of monopoles are:

the Chudakov-Parker limit [7–9] derived from the condition for the conservation of the observed Galactic magnetic field strength

$$F_{\text{mon}} < 10^{-15}\text{cm}^{-2}\text{s}^{-1}\text{ster}^{-1},$$

and the *cosmological* constraint following from the obvious condition

$$4\pi F_{\text{mon}} m_{\text{mon}} (c\beta)^{-1} < \rho_{cr} = 10^{-29}\text{g} \cdot \text{cm}^{-3},$$

which yields

$$F_{\text{mon}} < 1.4 \cdot 10^{-12} \beta [(10^{16}\text{GeV}/c^2)/m_{\text{mon}}]\text{cm}^{-2} \cdot \text{sec}^{-1} \cdot \text{ster}^{-1} \;.$$

Both these constraints do not rule out the possibility of a local excess above these limiting fluxes of monopoles, for example, in the Solar system. As a result of its acceleration in Galactic magnetic fields, the kinetic energy of a heavy monopole can reach $\sim 10^{11}$ GeV. On the other hand, when passing through the Earth, the energy losses of quasi-relativistic monopoles with $\beta \geq \beta_c$ ($\beta_c = 0.75$ is the threshold speed of the monopole with respect to the generation of Cherenkov radiation) are $\sim 10^{11}$ GeV. It thus follows that monopoles with a mass of less than 10^{11} GeV passing through the Earth remain quasi-relativistic and can be detected by their Cherenkov radiation with neutrino telescopes.

In 1981, V. Rubakov [10] published a paper where he concluded that the processes with baryon number nonconservation are not suppressed in the presence of a monopole predicted by Grand Unified Theories. A similar conclusion was reached in 1982 by Callan [11]. The cross section for the reaction of monopole catalysis of baryon decay was estimated as

$$\sigma_{\text{cat}} = \sigma_0 \beta_{\text{mon}}^{-1},$$

where σ_0 was taken to be equal in order of magnitude to the characteristic values of strong interactions: $\sigma_0 \sim 10^{-28}$ cm^2. When the electromagnetic interaction between a monopole and a nucleus incorporating a nucleon is taken into account, the factors $F(\beta_{\text{mon}}) = 2.4 \cdot 10^7 \beta_{\text{mon}}^{3.1}$ for the nucleons constituting the ^{16}O nucleus and $F(\beta_{\text{mon}}) = 0.17 \cdot \beta_{\text{mon}}^{-1}$ for free protons appear in the expression for the catalysis cross section. A monopole moving in water with a speed less than or of the order of 10^{-3} of speed of light must initiate mainly the decay of hydrogen nuclei with the cross section

$$\sigma_{\text{cat}}^{p} = 0.17 \sigma_0 \beta_{\text{mon}}^{-2}.$$

The energy being released in a single catalysis event ($m_p c^2 = 938$ MeV) is distributed between the proton decay products. While propagating in water, the latter become the sources of Cherenkov radiation, which is also generated by their daughter particles, δ-electrons, e^+e^- pairs, etc. As a result of each proton decay, up to $N_\gamma = 1.1 \cdot 10^5$ Cherenkov photons are emitted in the wavelength range $300 < \lambda < 600$ nm. Thus, the trajectory of the muon inducing proton decays when crossing a water volume must appear as a chain of flashes with a Cherenkov spectrum. If the decays occur frequently, for example, $10-10^3$ per 1 cm of the monopole path, then the detection rate of Cherenkov photons emitted by decay products can noticeably exceed the pulse count rate attributable to the photomultiplier dark current and water luminescence. The method of searching for slow monopoles in experiments on neutrino telescopes is based on the selection of such events [12].

Neutrino Interactions

Natural high-energy neutrinos interact with the target material of neutrino telescopes mainly through the reactions on nucleons via the channels of charged (**CC**) and neutral (**NC**) currents:

$$\nu_l(\bar{\nu}_l) + N \overset{\text{CC}}{\rightarrow} l^-(l^+) + \text{hadrons}, \tag{3.1}$$

$$\nu_l(\bar{\nu}_l) + N \overset{\text{NC}}{\rightarrow} \nu_l(\bar{\nu}_l) + \text{hadrons}, \tag{3.2}$$

where $l = e$, μ or τ. The interaction of neutrinos with target electrons makes virtually no contribution to the total number of recorded events, except for the resonant scattering of electron antineutrinos in the W-resonance region:

$$\bar{\nu}_e + e^- \rightarrow W^- \rightarrow \text{anything}, \tag{3.3}$$

with the energy at resonance $E_0 = M_W^2/2m_e = 6.3 \times 10^6$ GeV and a cross section of 5.02×10^{-31} cm^2. The final products of reactions (3.1)–(3.3) — leptons and high-energy cascades — carry information about the energy, direction, and, in principle, flavor of neutrinos.

In experiments on deep underwater and under-ice Cherenkov detectors, the effective target size depends on the neutrino energy and flavor. In the case of muon neutrinos, both the transparent medium around the telescope and the bedrock are the neutrino target, because the secondary muons have a high penetrating power. In the former case, the muon neutrino energy can be determined by reconstructing the energies of the muon and the shower generated at the neutrino interaction vertex. During a muon neutrino interaction in rock, the neutrino energy in each individual event cannot be reconstructed exactly due to the energy losses of the muon as it propagates from the interaction vertex to the facility. However, when the statistics of recorded events is large enough, the energy spectrum of the muon neutrino flux can be derived by the reconstruction of the muon energy. The astrophysical fluxes of ν_e and ν_τ, which account for two thirds of the total flux, can be investigated in experiments on neutrino telescopes only by recording the secondary showers generated in a water target. Hadronic showers are produced in the interactions of neutrinos of all flavors with nuclei via the channels of charged and neutral currents. In addition, in the case of the CC interaction of electron and τ-neutrinos, the electron energy is converted into the energy of an electromagnetic shower, while a significant fraction of the τ-lepton energy is transferred to the hadronic or electromagnetic shower as a result of its decay. Thus, achieving a high accuracy of reconstructing the energy and direction of showers is an indispensable requirement for efficient detection of neutrinos of all flavors.

3.1.3 Basic Methods and Approaches Used in the Project

The astrophysical neutrino fluxes are investigated with neutrino telescopes in two main directions of research [13–15]. The first direction of research is concerned with the search for a neutrino signal from known astrophysical objects or the detection of unidentified local sources from observations of the signal excess above the background level over the entire celestial sphere. Figure 3.2 sketches the two basic detection modes of underwater

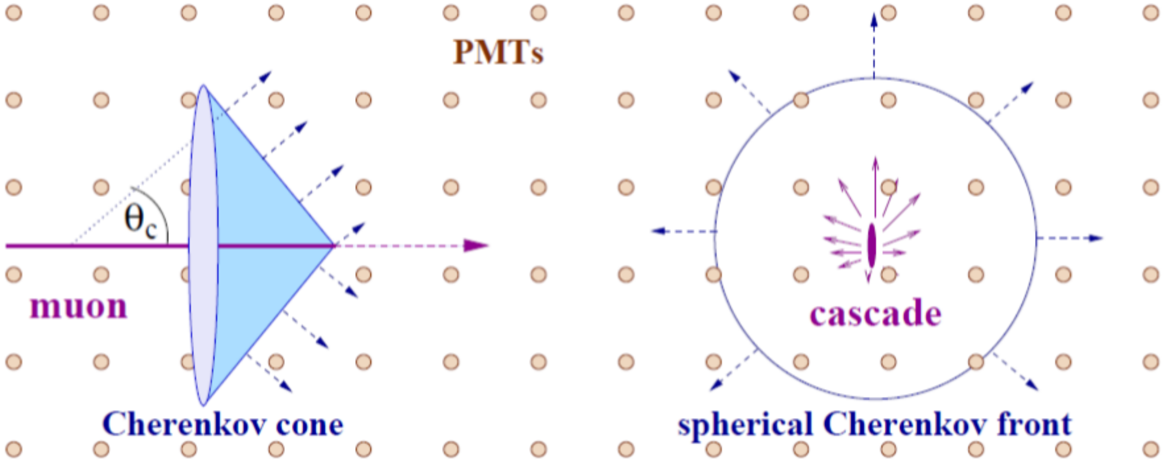

Figure 3.2: Detection principles for muon tracks (left) and cascades (right) in underwater detectors. Note that the Cherenkov light emission by cascades is peaked at the Cherenkov angle θ_c with respect to the cascade axis but has a wide distribution covering the full solid angle.

neutrino telescopes. CC muon neutrino interactions produce a muon track (left), whereas other neutrino reaction types cause hadronic and/or electromagnetic cascades (right). This is, in particular, true for NC reactions (hadronic cascade) or CC reactions of electron neutrinos (overlapping hadronic and electromagnetic cascades). CC tau neutrino interactions can have either signature, depending on the τ decay mode.

The objective of the optimization of the BAIKAL-GVD design was to provide a large cascade detection volume with the requirement of effectively recording high energy muons. Muon effective areas for two optimized BAIKAL-GVD configurations are shown in Fig. 3.3a. The curves labeled by GVD*4 and BAIKAL-GVD relate to configurations with 10368 OMs and 2304 OMs, respectively. Muon effective area (6/3 condition — at least 6 hit channels on at least 3 strings) rises from 0.3 km^2 at 1 TeV to 1.8 km^2 asymptotically. The fraction of events with mismatch angle between generated and reconstructed muon directions less than a given value ψ is shown in Fig. 3.3b. Muon arrival direction resolution (median mismatch angle) is about of 0.25 degree.

Shower effective volumes for two BAIKAL-GVD configurations are shown in Fig. 3.4a. Shower effective volumes (11/3 condition — at least 11 hit channels on at least 3 strings) for basic configuration are about of 0.4–2.4 km^3 above 10 TeV. The accuracy of shower energy reconstruction is about of 20-35% depending on shower energy. The accuracy of a shower direction reconstruction is about 3.5-06.5 degrees (median value). Distribution of the mismatch angle between generated and reconstructed 1 PeV shower directions is shown in Fig. 3.4b.

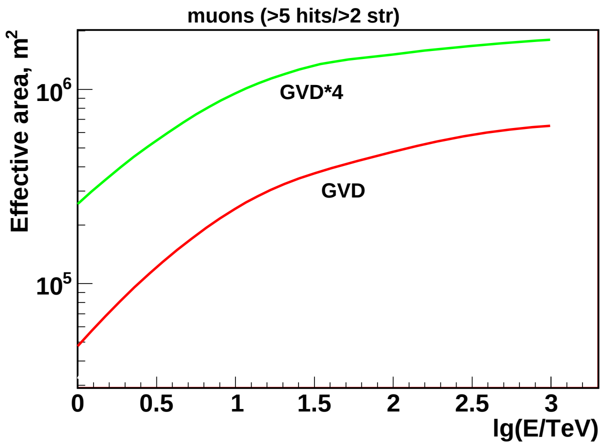

(a) Muon effective area. The curves labeled by GVD*4 and GVD relate to configurations with 10368 OMs and 2304 OMs, respectively.

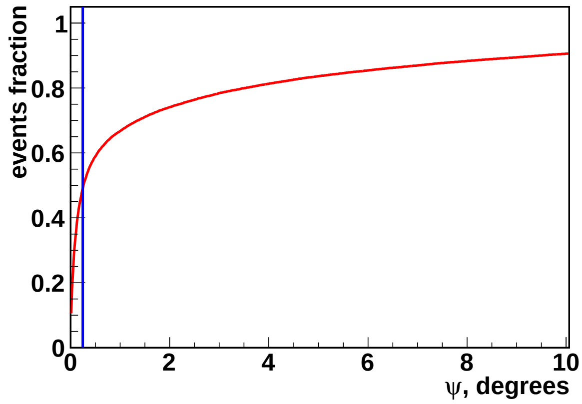

(b) The fraction of muon events with mismatch angle between generated and reconstructed muon flight direction less than a given value ψ.

Reconstruction

The reconstruction procedure for a muon track consists of several consecutive steps which are typically:

- Rejection of noise hits;
- Simple pre-fit procedures providing a first-guess estimate for the following iterative maximum-likelihood reconstruction;
- Maximum-likelihood reconstruction;
- Quality cuts in order to reduce background contaminations and to enrich the sample with signal events. This step is strongly dependent on details of the actual analysis diffuse fluxes at high energies, searches for steady point sources, searches for transient sources etc.

An infinitely long muon track can be described by an arbitrary point $\mathbf{r_0}$ on the track which is passed by the muon at time t_0, with a direction $\mathbf{p}$ and energy E_0. Photons emitted under the Cherenkov angle θ_c and propagating on a straight path are expected to arrive at PMT i located at $\mathbf{r_i}$ at a time

$$t_{\text{geo}} = t_0 + \frac{\mathbf{p} \cdot (\mathbf{r_i} - \mathbf{r_0}) + d \cdot \tan\theta_c}{c},$$

where d is the closest distance between PMT i and the track, and c the vacuum speed of light. The time residual t_{res} is given by the difference between the measured hit time t_{hit} and the hit time expected for a direct photon, t_{geo}:

$$t_{\text{res}} = t_{\text{hit}} - t_{\text{geo}}.$$

An unavoidable symmetric contribution around $\Delta_t = 0$ in the range of a nanosecond comes from the PMT/electronics time jitter, σ_t. Electromagnetic and hadronic cascades along the

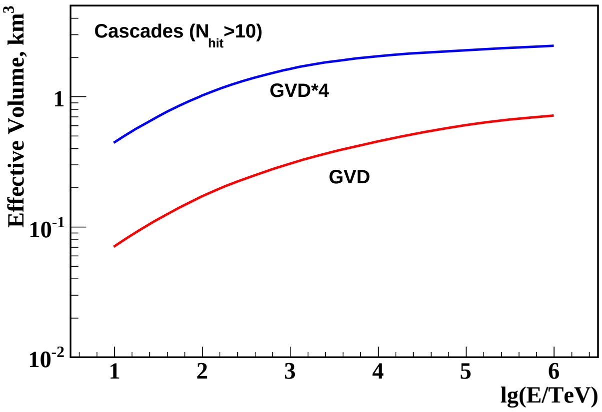

(a) Effective volume of cascades detection. The curves labeled by GVD*4 and GVD relate to configurations with 10368 OMs and 2304 OMs, respectively

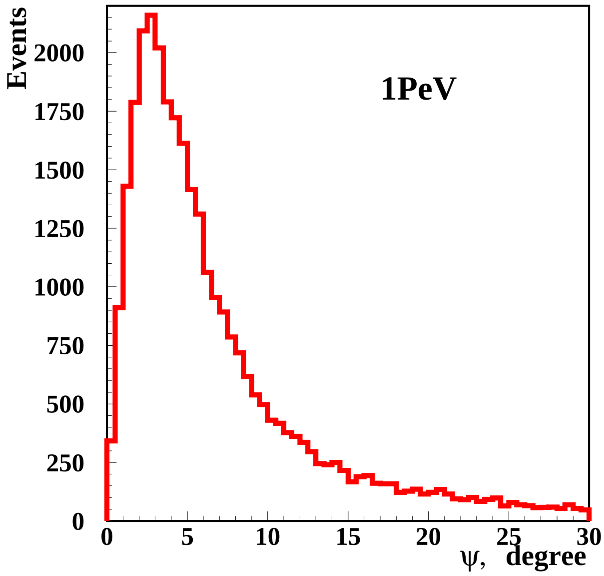

(b) Distribution of the mismatch angle between generated and reconstructed 1 PeV shower directions.

track lead to a tail towards larger (and only larger) time residuals. Scattering of photons can lead to an even stronger delay of the arrival time. These residuals must be properly implemented in the probability density function for the arrival times used in the maximum-likelihood procedure.

The simplest likelihood function is based exclusively on the measured arrival times. It is the product of all N_{hit} probability density functions p_i to observe, for a given value of track parameters $\{a\}$, photons at times t_i at the location of the PMTs hit:

$$L_{\text{time}} = \prod_{i=1}^{N_{\text{hit}}} p(t_{\text{res},i} \mid \{a\}).$$

More complicated likelihood functions include the probability of PMTs hit to be hit and of non-hit PMTs not to be hit, or of the respective amplitudes. Instead of referring only to the arrival time of the first photon for a given track hypothesis and the amplitude for a given energy hypothesis, one may also refer to the full waveform from multiple photons hitting the PMT. For efficient background suppression, the likelihood may also incorporate information about the zenith angular dependence of background and signal (Bayesian probability). The reconstruction procedure finds the best track hypothesis by maximizing the likelihood.

3.1.4 Detector Description

The detector will utilize Lake Baikal water instrumented at depth with light sensors that detect the Cherenkov radiation from secondary particles produced in interactions of high-energy neutrinos inside or near the instrumented water volume. Signal events consist of up-going muons produced in neutrino interactions in the bedrock or the water, as well as of electromagnetic and hadronic showers (cascades) from CC-interactions of ν_e and ν_τ or NC-interactions of all flavors inside the array detection volume. Background events are mainly downward-going muons from cosmic ray interactions in the atmosphere above the detector.

The concept of BAIKAL-GVD is based on a number of evident requirements to the design and architecture of the recording system of the new array: the utmost use of the advantages of array deployment from the ice cover of Lake Baikal as can be seen from Fig. 3.5, the extendability of the facility and provision of its effective operation even in the first stage of deployment, and the possibility of implementing different versions of arrangement and spatial distribution of light detectors within the same measuring system.

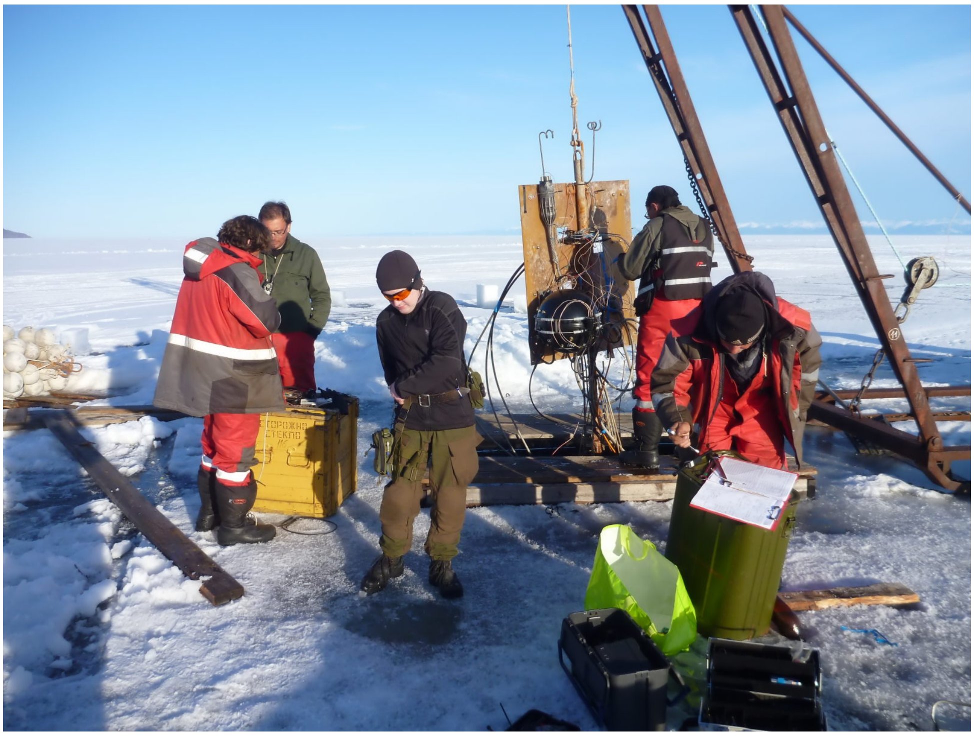

Figure 3.5: Installation of the demonstration cluster "Dubna".

With all above requirements taken into account, the following conceptual design of BAIKAL-GVD has been developed. The Data Acquisition System of BAIKAL-GVD is formed from three basic building blocks: optical modules, sections of OMs and clusters of strings. The OM consists of a photomultiplier tube (**PMT**) with large hemispherical photocathode and attendant electronics, which are placed in pressure-resistant glass sphere. The OMs are arranged on vertical load-carrying cables to form strings. Optical modules of each string are grouped into two, three or four sections. A section is a basic detection unit (**DU**) of array. Each section consists of 12–16 OMs and the central module (**CM**). PMT signals from all OMs of a section are transmitted to the CM, where they are digitized by ADC boards. The CM consists of ADC boards, an OM slow-control unit, and a Master board. The digitized signals from each ADC are transferred to a FPGA which handles the data. A memory buffer allows for accumulating the waveform data from the ADC. An ADC trigger request channel includes a request builder, which forms the request signals to the trigger logic, which are transferred to the Master board. The Master board provides trigger logic, data readout from ADC boards, connection via local Ethernet to the cluster DAQ center, and control of the section operation. The request analyzer forms the section trigger request (local trigger) on the basis of requests from ADC channels. The section trigger request is transferred to the cluster DAQ center.

The cluster DAQ center is placed near the water surface. It provides the string triggering, power supply control, and communication to shore. The organizations of central and section trigger systems are the same. The section local triggers come to inputs of the central ADC board. The central Master board works out the global trigger for all sections. The global trigger produces the stop signal for all ADC channels and initiates waveform information readout. Waveform information is accumulated in the event buffer and then transmitted via an Ethernet connection to the cluster DAQ center. The cluster DAQ center is connected to shore station by an about 6 km long electro-optical cable.

Each BAIKAL-GVD cluster is a functionally complete and independent sub-array, which can operate both as a part of unified configuration and autonomously. This allows for easy upgrade of the array configuration, as well as putting into operation its individual parts within the telescope deployment phase.

Optical Module

The basic measuring units of the BAIKAL-GVD are optical modules (**OM**s), which are

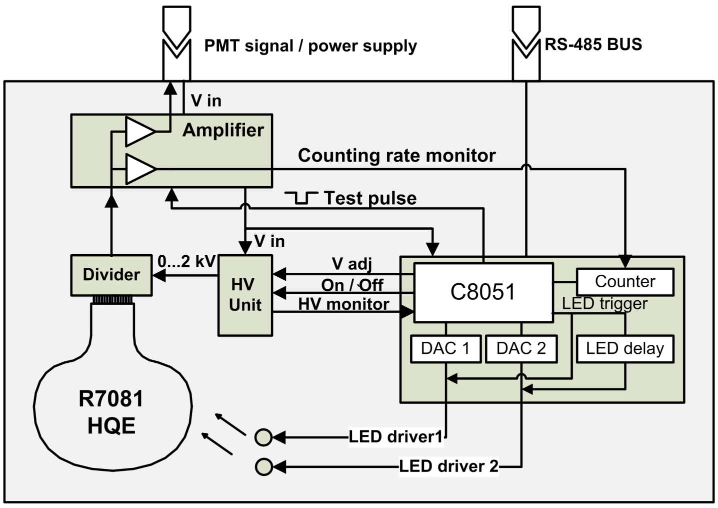

(a) Block diagram of optical module.

design to convert the Cherenkov radiation of muons and showers into electric signals. An OM consists of the following elements: a photo-multiplier tube (Hamamatsu-R7081HQE), a controller, an amplifier, LED calibration unit, and a high-voltage converter. The OM block scheme is shown in Fig. 3.6a.

Section — Detection Unit of the BAIKAL-GVD

Optical modules are mounted on vertical load-carrying cables to form strings. A low-level data collecting unit of a string is a section of optical modules. Each section contains 12 OMs, a central module (**CEM**), and a service module (**SM**). The section functional scheme is shown in Fig. 3.7. The central module collects and transfers data and controls the section electronics operation. Analog signals from optical modules arrive at CEM through coaxial cables 90 m long. Digitization of the PMT signal is performed in a 15-μs window by three boards of four-channel 12-bit ADC (FADC) with a discretization frequency of 200 MHz. Waveform stamps of events are formed in the channels, the analysis of which makes it possible to determine the amplitude and detection time of OM signals. Two ring buffers are

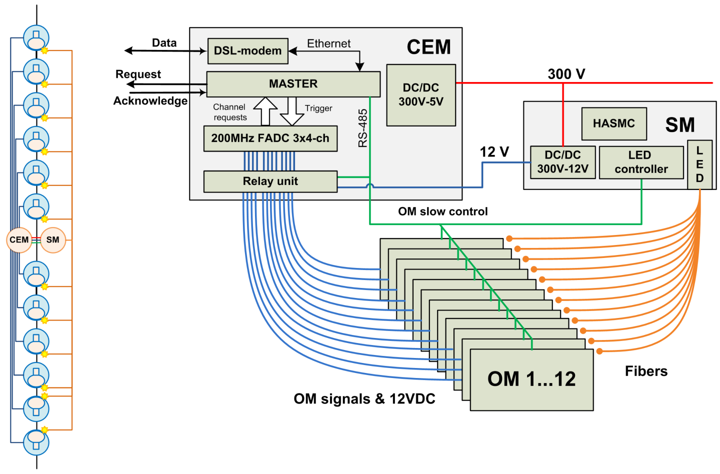

Figure 3.7: Functional scheme of BAIKAL-GVD section.

provided in each channel to record signal waveform with dead-time minimized. Along with the conversion of analog signals and intermediate data storage, the ADC boards form the so-called channel *request* signals. A *request* signal is formed when the input signal amplitude exceeds the specified threshold. The threshold function is implemented on digital comparators (two comparators per channel). The comparator thresholds are controlled with a step of 1.4 mV. *Request* signals from all ADC channels arrive at the *Master board*, which forms a section *request*. This signal is formed when the *request* signals from the section channels fulfill specified conditions. The information about the allowed combinations of the signals is loaded dynamically into the *Master* board memory (the so-called coincidence matrix is formed). The *request* signals of sections are transferred to the cluster center through coaxial cables 1200 m long. A *acknowledge* signal is formed in the cluster center; it serves as a global trigger for all sections and provides their synchronous operation. This signal initiates readout of the data of all ADC channels and their transfer to the data acquisition center of the cluster (DAQ-center), which is in turn connected with the shore station through an electro-optical cable.

Data from OMs of the section are read through the Ethernet channel of the *Master* board, which is elongated to 1200 m via DSL modems (transfer rate up to 8 Mbit/s). A local underwater RS-485 data bus, based on the ASCII protocol, is used for slow control (setting the modes of OM operation, calibration, and monitoring the equipment). The Ethernet to RS485 converter for slow control channel is implemented on the *Master* board. The power supply voltage is fed to optical modules from 300 V – 12 V DC/DC converters, which are mounted in the section SM. A relay control of OM switching makes it possible to switch off optical modules from the power supply unit in the case of short circuit. Along with DC/DC converters, the SM includes elements of the calibration system and the acoustic positioning system.

A section is calibrated by two pulsed LED light sources, the signals of which are branched through optical cables to all optical modules of the section. The monitoring system of the section provides information on the power supply voltage across the section and each optical module, on the temperature inside OM, on the high voltage across the photomultipliers, and on the count rate of PMT noise pulses.

String

A string is the basic structural unit of the BAIKAL-GVD detector. It is an assembly composed of several sections, positioned on the same backbone cable. The string includes two or four sections and communication module (**COM**). The functional scheme of a string is shown in Fig. 3.8.

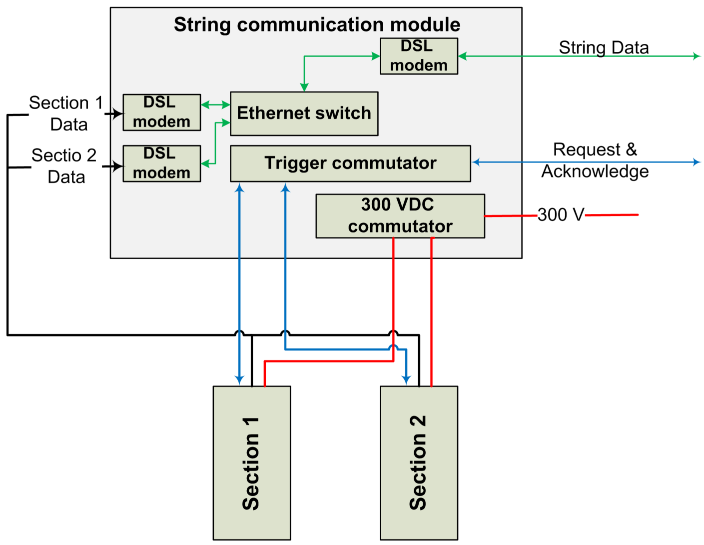

Figure 3.8: Functional scheme of the string communication module of BAIKAL-GVD.

The string communication module provides connection of data transfer, synchronization, and power supply systems of individual sections to the load-carrying cable, which connects the string to the cluster DAQ-center. The cable consists of two coaxial RK50 cables to translate *request* and *acknowledge* signals, three power supply wires with a cross section of 0.5 mm2 and a screened twisted pair for data transfer. The data from sections are transferred through DSL modem lines to the COM and translated (through the Ethernet switch and additional DSL modem) to the cluster DAQ-center. The *request* signals from sections are combined by a logical *OR* element in the trigger commutator unit to form the string *request* signal. The *acknowledge* signal from COM is branched to arrive at string sections. The string configuration, composed of two sections, does not need additional switching of power supply lines: each section is connected to its own power supply wire in the load-carrying cable. The power supply voltage 300 VDC is controlled in the cluster DAQ-center through a relay commutator. The relay commutator is also planned to be used for a larger number of sections in the string communication module.

Cluster

The basic configuration of BAIKAL-GVD cluster comprises eight strings, a data acquisition center (DAQ-center), and electro-optical cable, which connects the cluster to the shore station (see Fig. 3.9). The DAQ-center of a cluster consists of 3 underwater modules, located at a shallow depth of about 30 m: a cluster communication center, a PC sphere, and an optical cable clutch.

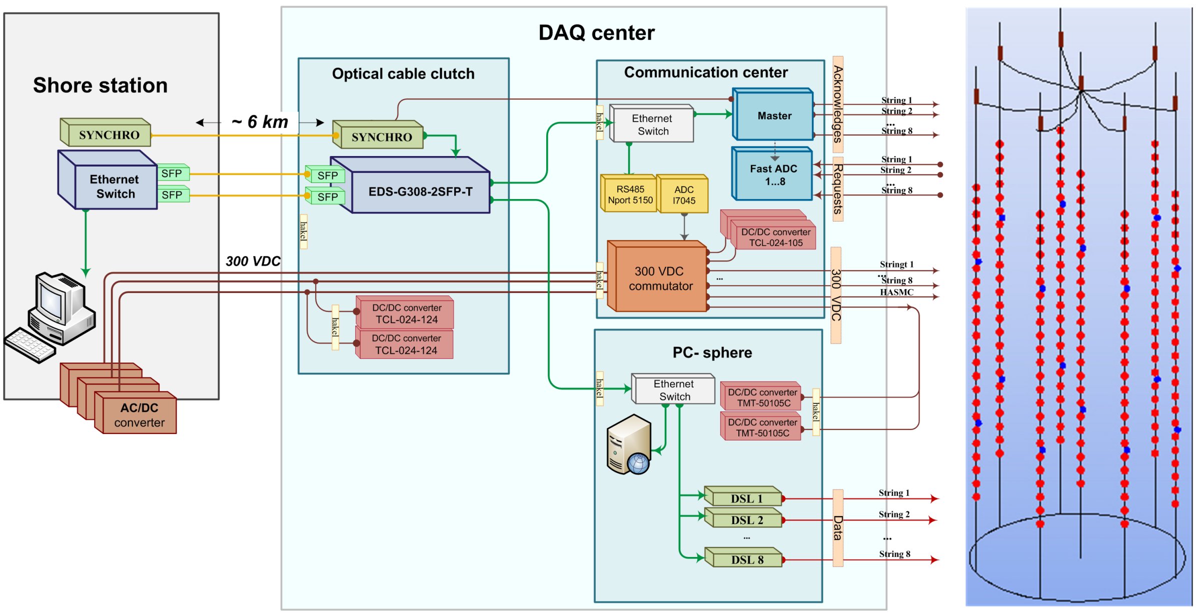

Figure 3.9: Functional scheme of the data acquisition center of a cluster (on the left) and a cluster composed of eight strings (on the right).

Strings are connected to the DAQ-center of cluster through 1.2 km long cables, which serve to transfer data, supply power, and synchronize the operation of sections. Data from

8 strings are transferred through two-wire communication lines based on DSL modems, located in the PC-sphere (data transfer rate up to 15 Mbit/s). This module also contains an underwater microcomputer to perform on-line analysis of the information received. The string's data are transferred from the PC-sphere to the optical cable clutch through an underwater 100-Mbit Ethernet line for their subsequent translation to the shore through the Gigabit Ethernet switch EDS-G308-2SFP-T.

The cluster DAQ-center is connected to the shore by an electro-optical cable about 6 km long. This cable serves to feed the cluster and transfer digital data through a gigabit optical fiber communication line (**OFCL**). An OFCL consists of 3 pairs of single-mode fibers (AHWave FLEX ZWP). Two pairs are used to transfer data (main and reserve lines), and one pair is aimed at synchronizing the operation of BAIKAL-GVD clusters. Shore power supply units (AC/DC converters) with an output voltage up to 450 VDC and power up to 1 kW are used to feed a cluster. The output power supply voltage is controlled so as to provide a voltage of 300 V at the end of the 6-km underwater feed line. The underwater part of the equipment, which is designed to control the cluster power supply and to synchronize the operation of the sections, is located in the cluster communication center. Independent switching on and off the 300V power supply of each section is performed by a relay commutator, which is controlled via a 16-channel digital output module (I-7045) and RS485 serial device server (NPort 5150A-T). The relay commutator and its control devices are fed by TCL-024-124 sources, which are located in the optical cable clutch.

The operation of the measuring systems of cluster sections is synchronized by the DAQ-center *Master* and 8-channel FADC units, which are identical to the units of the section CEMs. *Request* signals from all strings arrive at the cluster DAQ-center, where their arrival times are measured. The *Master* unit analyzes the string requests and generates a *acknowledge* signal, which is branched to all sections of all strings as a global trigger. The arrival times of photons detected by section channels are measured with respect to this signal. The differences in the transit times of the *request* and *acknowledge* signals of different sections are measured with FADC units of the CEMs with an error of < 5 ns.

Trigger Formation and Data Transfer Systems

The BAIKAL-GVD data transfer and trigger systems are closely interrelated. The neutrino telescope records fairly rare events. However, to detect signal events from muons or showers by the selected trigger system at the instrumental level with a high detection efficiency, one has to reduce maximally the channel detection thresholds. As a result, background (noise) events make the main contribution to the total data flux. The background is filtered in the stage of on-line analysis of the data in the shore station. The data transfer system is aimed at transmitting the total data flow (which can be as high as several tens of Mbit/s) from the underwater part of the system to the shore station without loss.

Shore Data Acquisition and Control Center

The shore DAQ-system for collecting and processing events should be organized as follows. Electro-optical bottom cable lines (one line per cluster) are used for power supply and data exchange of clusters. Data channels are connected to the Host PC Station through a 16-port Ethernet switch to the input of the Host Station, where the data flow is processed. The Host Station (enterprise-level server, designed, in particular, for scientific computations) is a multiprocessor platform (processors based on four or more cores) with 128-Gb RAM, in the address space of which a unified dataset is formed from the input data flow. The Host Station must have a sufficiently high reliability (up to hot replacement of components), be easy in maintenance, and flexible in distributing resources. Preliminary estimates show that this system is minimally sufficient for stable processing of the total data flow, concerning all main purposes of the system. However, in the case of unforeseen increase in the necessary computational resources of the server, the solution chosen has an advantage: its resources can easily be increased by scaling. The dataset formed is filtered, and the events that did not pass through the trigger chosen for a specific physical problem are rejected, while the events passed through the trigger are directed to the output data flow. The output data are saved either on the RAID-5 array or on external carriers. The predicted data flow from the system suggests the annual amount of the output data to be no larger than few terabytes. Thus, this configuration not only makes it possible to store data but also allows one to use, process, and transfer them on-line through the Internet. The accuracy in timing the experimental data to the world time should be better than 100 μs. Such accuracy has been achieved by installing and tuning local GPS receivers and tuning the *ntp (network time protocol)* service.

The functions of the basic service program of the software system (Basic Program, BP), which is run at the Host PC, are as follows:

- Choice of the static configuration of the telescope (number of clusters, strings, addresses of data transfer controllers, etc.). Change in the dynamic parameters of the state of strings and optical modules of the telescope (setting PMT high voltages, channel thresholds, modes of the LED-flasher operation, and setting parameters in the data transfer controllers of the strings).
- Time and amplitude calibration of the detector.
- Saving the data obtained in the real-time format using a large set of information messages. The obtained data of different types are saved (after preprocessing) in data files and are indicated by corresponding marks.
- Automatic logging sessions performed and tests of measurement systems.
- Provision of an integrated set of low-level utilities that are necessary for handling separate OMs and data transfer controllers.
- Generation of monitor data (amplitude and time distributions, statistical distributions, spectra of the shape of measurement channel pulses), which is necessary for on-line monitoring the information received.

The Host PC software is developed under the Linux OS on the C and C++ languages, using Qt and ROOT graphical libraries (and the tools existing in the ROOT for developing and designing applied user interfaces). One of the key features of the shore software developed is the possibility of full remote control of the detector through specialized network protocols SSH and VNC, which are provided at the OS level. This possibility is necessary for solving current problems, maintaining the standard mode of detector operation during data collection sessions, and on-line monitoring the quality of the information received.

The use of the system for remote monitoring and controlling the detector increases significantly the efficiency of the system; however, a threat of unauthorized access to the local computational network of the telescope arises in this case. To protect the computational network from unauthorized access, it is divided into two zones: a users' zone, which contains user computers with access to the Internet, and a safety zone, with the equipment that is necessary for the telescope operation. The safety zone contains the computers of the data collection system of the telescope (Host PC); the systems for monitoring the telescope operation; and the underwater local computer network, which is connected to the shore part of the control system through a fiber cable. The local network is connected to the Internet through a router for controlling access. The router is also equipped with a firewall to exclude all unauthorized entry connections. When entering the local network, one can get access to the shore-center computers only after the corresponding authentication procedures.

Positioning System of the BAIKAL-GVD

To obtain coordinates of each OM during data taken period a custom Long-Base-Line (**LBL**) Underwater Acoustic Positioning System (**L-UAPS**) [16], developed by EvoLogics GmbH (Germany), was deployed at the detector. The system consists of a bottom LBL-antenna, comprised of nodes moored at the bottom of the telescope strings, and acoustic beacons, attached to the strings (three per string).

The measurement cycles are launched by an operator at the shore center (the minimum duration of a measurement cycle is limited to 30 s). The L-UAPS's positioning accuracy of 5 mm was experimentally proven for beacons 160 m away from the bottom antenna, thus allowing to track even the smallest movements of the drifting beacons. Measurements performed since the Cluster-2012 starts to operate. Figure 3.10 shows a distance monitoring between the bottom and top beacons of the string in April 2012.

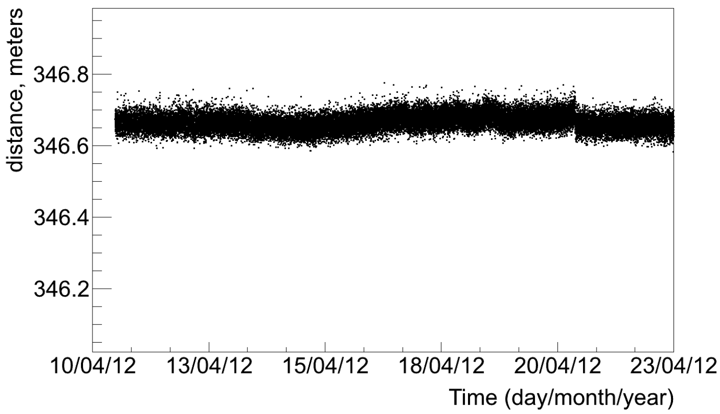

Figure 3.10: Measured distance between top and bottom beacons of string vs time.

Prototype Arrays

The first prototype of BAIKAL-GVD electronics was deployed in Lake Baikal in April 2008. It was a reduced-size section with six OMs. The prototype string 2009 consisted of 12 optical modules with six photomultipliers R8055 and six XP1807, which were combined in two sections. In April 2010, a prototype of the BAIKAL-GVD string with eight PMTs R7081HQE and four PMTs R8055 was deployed and had been tested until August 2010 in Lake Baikal.

The tests of the experimental string were aimed at a complex check of the operation of all electronic units, underwater cable communications, and load-carrying structures under long-term exposure of the equipment. On the whole, during the period from 2008 to 2010, the experimental string in different configurations worked for about 12 months. During this time we did not observe any significant errors in the operation or seal failure for the basic string units: optical modules, ADC and control units, and deep underwater cables. The breaks in the string operation were caused by failures of DC/DC converters of the service module. Based on the results of this experiment, systems of lightning protection and string power supply redundancy were developed and implemented.

An analysis of the background detection conditions for the experimental string in Lake Baikal did not reveal any new effects in comparison with those observed previously in the experiments with the NT200 detector. Fig. 3.11 shows the time dependence of the noise pulse count rate (threshold 0.5 p.e.) for OMs at the different depth. The pronounced correlation in the channel count rates indicates that the luminescence of Baikal water contributes significantly to the PMT noise. Independent investigations showed that this water emission has a chemiluminescence nature. Along with relatively stable luminescence periods, there are intensity bursts, which increase the noise pulse rate by more than twice. These bursts

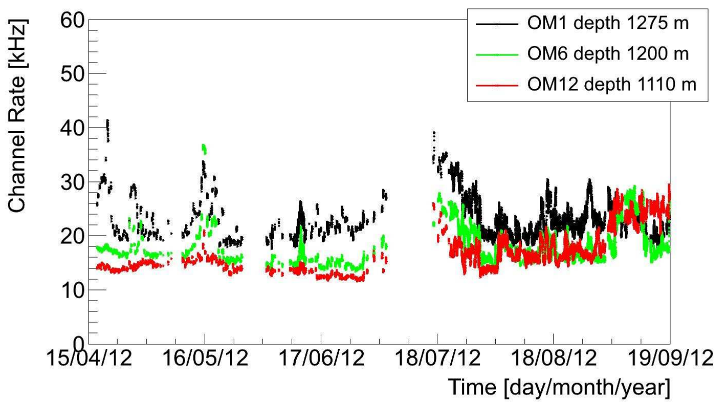

Figure 3.11: Counting rates of the optical modules in 2012. Empty gaps mean that monitoring was stopped.

are due to the transport of luminous masses by deep-water flows in Lake Baikal.

The key parameter of the BAIKAL-GVD telescope is its angular resolution, which should be much better than 1^o. The angular resolution depends primarily on the accuracy in measuring the Cherenkov radiation arrival time for each measuring channel. This error is determined by two parameters of the recording system: the time resolution of the channels and error of their time calibration. In situ tests of the prototype strings allow to estimate the accuracy of photon arrival time measurements. The measurements were performed with the LED-flasher, laser calibration source and cosmic ray muons.

The time resolution of the channels was measured using a LED-flasher. A LED-flasher was located in the central part of the string (in the service module). It generated a series of double pulses with a strictly fixed time delay between them. The delay about 0.5 μs was chosen so as to make both pulses fall in the same event time window (5 μs). The light pulses were transferred to all OMs of the string through optical fibers. The positions of pulses on the time tracks of channels were determined by excess over a fixed threshold, which was chosen at a level of 0.5 p.e. The value of the time delay averaged over all channels (498.3 ns) differs from the expected value (497.5 ns) by less than 1 ns. The delay rms deviation, averaged over all channels, is 1.6 ns. This value characterizes a time resolution of the string channel. Note that the time resolution can be somewhat improved by fitting the shapes of pulses on a track to determine their position. The significant spread in rms deviations is explained by the difference in the light pulse amplitudes (from 1 to 100 p.e.), which is due to the different focusing conditions for the light from LED-flasher at the inputs of optical fibers.

The accuracy of time calibration is the second factor that affects the detector time characteristics. This calibration implies determination of relative time shifts in channels, t_{shift}, which are due to the difference in the lengths of communication cables and PMT transit times. The values of the calibration parameters t_{shift}, obtained by two methods (measurement of the detection times of LED-flasher signal, common for all channels, and measurement of the PMT intrinsic delays), are consistent within 3 ns, which exceeds somewhat the expected value of 2 ns. The analysis probing the source of the discrepancy between the calibration results will be continued.

More detailed studies of the time accuracy were performed with a laser based calibration source. It is an isotropic light source with intensity up to 5×10^{13} photons per pulse at a wavelength of 475 nm and light pulse width less than 1 ns. The laser source was located at a distance of about 100 m from the experimental string, at a depth of about 1.2 km. The acoustic positioning system provides an error in determining the mutual position of the laser source and the optical modules of the string at a level of 0.5 m. Hence, one can compare the expected radiation arrival time at the string channels with the experimental values. The measured parameter was a difference in the response times of string channels, ΔT. The results suggest that the error in measuring the detection times of string channels does not exceed 2 ns, which provides the necessary angular resolution of the BAIKAL-GVD detector.

The atmospheric muon flux makes it possible to investigate the performance of the time measuring channels of the experimental string under the conditions that are very close to the real experiment. The muon events were analyzed for a pair of OMs with up-ward faced PMTs, which imitate most adequately the detection conditions for the neutrino events from the lower hemisphere. The experimental distribution of time difference ΔT was compared with the results of simulation (Fig. 3.12a). The experimental distribution is in good agreement with the expected one. The relative displacement of the distributions on the time scale is 2–3 ns. This value characterizes the time error of the experimental string as a whole, including all sources of time measurement errors. The atmospheric muon flux is a natural

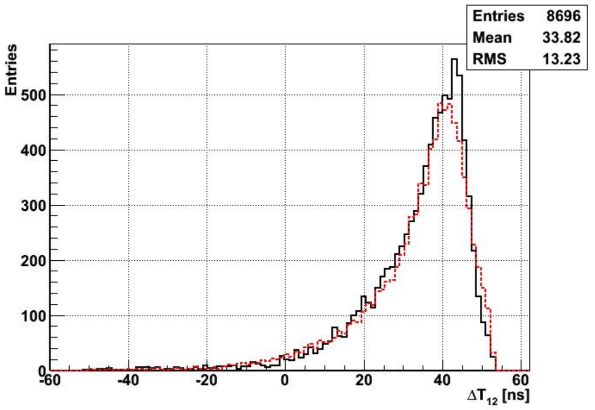

(a) Distribution of time difference ΔT between muon pulses for two up-ward faced PMTs: experiment (solid histogram) and calculation (dotted histogram).

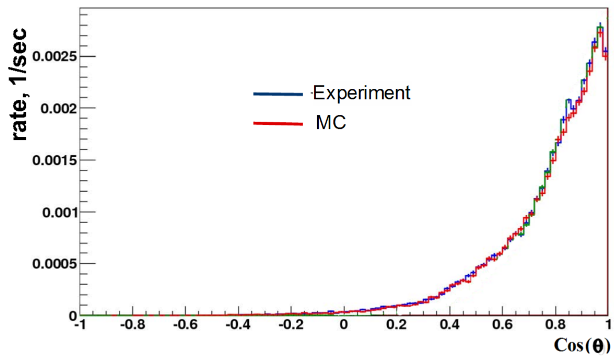

(b) Experimental and theoretically expected event rates vs zenith angle after final cuts.

calibration source which allows one to test the performance of the array measuring systems, as well as to estimate the efficiency of background suppression and event reconstruction procedures. Prototype string data allow to reconstruct the zenith angle distribution of downward going atmospheric muons. A selected sample of 2010 prototype string data was used for the atmospheric muons analysis. A sample of MC-events from atmospheric muons has been generated, taking into account the features of prototype string measuring system and actual counting rates of optical modules. At the first step of analysis a causality criterion, as well as a special muon selection conditions were applied to events for elimination of background signals caused by PMTs noise and water luminescence background, muon bundles and electro-magnetic showers induced by muons. At the next step the cleaned time information of OMs was used for track reconstruction with a trigger condition 3 hit OMs. Finally, soft cuts on χ^2 value and on the error of reconstructed zenith angle were applied for muon event selection. Zenith angular distributions of experimental and MC-simulated event rates are shown in Fig. 3.12b. The good consistency between the data and theoretical expectation confirms the expected performance of the time measuring systems and the efficiency of used calibration methods, as well as the efficiency of event selection and noise suppression procedures.

Progress of the demonstration cluster **DUBNA**

An important step towards realization of the BAIKAL-GVD project was made in 2013 by the deployment of the first stage of demonstration cluster "DUBNA" which contains 72 OMs arranged on three 345 m long full-scale strings, as well as equipment of an acoustic positioning system and instrumentation string with an array calibration and environment monitoring equipment. This configuration has been upgraded to 5 string array in 2014. Deployment of the demonstration cluster will be completed in 2015.

3.1.5 Contribution of JINR Members

JINR Members are playing significant roles in all key parts of the BAIKAL experiment:

- Assembly and test of deep water components.
- Continuous monitoring of the detector operation and remote control.
- Development of on-line and off-line software for the experiment.
- Development of databases, data acquisition software.
- Detector calibration and mass processing of data.
- Monte Carlo simulation and creation of the data bank.
- Development of new methods of event selection and reconstruction.
- Data analysis with respect to extraterrestrial high energy neutrinos and neutrinos from dark matter annihilation.

3.1.6 Publications, Theses and Conferences

As a result of the project the following:

- papers has been published [16–27].
- Master theses defended: A.L.Pakhorukov (ISU, 2011).
- PhD theses defended: B.A. Shaibonov. “Events separation from cascades, initiated by muons and neutrino, in the Baikal underwater neutrino experiment.” (2011).
- talks [28–35] given at conferences.

3.1.7 Finances

Major sources and amount of finances and major equipment acquired during the project runtime are listed in Tab. 3.1.

Source	Obtained (k$)	Major Equipment acquired
JINR	122	Construction elements
1100	414	Elements of optical modules
+	108	Underwater connectors
extra-	17	Elements of DAQ system
-budget	8	Elements of underwater cable communications
	22	Computers and components
	20/year	Travel and living expenses at BNO (Baikal lake)

Table 3.1: Major sources and amount of finances and major equipment acquired.

References

[1] BAIKAL Collaboration. *BAIKAL - GVD*. Tech. rep. Gigaton Volume Detector in Lake Baikal(Scientific-Technical Report). 2011. URL: http://baikalweb.jinr.ru/gvd/BAIKAL-GVD_En.pdf.

[2] Y. Fukuda et al. "Evidence for oscillation of atmospheric neutrinos". In: *Phys. Rev. Lett.* 81 (1998), p. 1562.

[3] P.-A. M. Dirac. In: *Proc. Roy. Soc.* A133 (1931), p. 60.

[4] Frank I.M. *Vavilov-Cherenkov radiation*. Russian. Moscow: Nauka, 1988, p. 192.

[5] G. t'Hooft. In: *Nucl. Phys.:Proc. Suppl.* 79 (1974), p. 276.

[6] A. Polyakov. In: *JETP Lett.* 20 (1974), p. 194.

[7] Domogatskii G.V. and Zheleznykh I.M. In: *Sov. J. Nucl. Phys.* 10 (1969), p. 702.

[8] Parker E.N. In: *Astrophys. J.* 160 (1970), p. 383.

[9] Turner M.S. et al. In: *Phys. Rev.* D26 (1982), p. 1296.

[10] Rubakov V. A. In: *JETP Lett.* 33 (1981), p. 644.

[11] C. G. Callan. In: *Phys. Rev. D* 26 (1982), p. 2058.

[12] Bezrukov L. B. et al. In: *Sov. J. Nucl. Phys.* 52 (1990), p. 86.

[13] Berezinsky V. S. and Zatsepin G. T. Russian. In: *Sov. Phys.- Uspekhi* 122.1(500) (1977), pp. 1–36.

[14] J. Learned and K. Mannheim. "High-energy neutrino astrophysics". In: *Annu. Rev. Nucl. Part. Sci* 50 (2000), pp. 679–749.

[15] Katz U. and Spiering Ch. In: *Prog. Part. Nucl. Phys.* 67 (2012), p. 651.

[16] A. Avrorin et al. "A Hydroacoustic Positioning System for the Experimental Cluster of the Cubic-Kilometer-Scale Neutrino Telescope at Lake Baikal". In: *Instruments and Experimental Techniques* 56.4 (2013), p. 449.

[17] A. Avrorin et al. "The Baikal neutrino experiment". In: *Nucl. Instr. and Meth., A* 626 (2011), p. 13.

[18] A. Avrorin et al. "The Baikal neutrino project: Present and Perspectives". In: *Nucl. Instr. and Meth., A* 628 (2011), p. 115.

[19] A. Avrorin et al. "The Baikal neutrino telescope – Results and plans". In: *Nucl. Instr. and Meth., A* 630 (2011), p. 115.

[20] A. Avrorin et al. "The Gigaton Volume Detector in Lake Baikal". In: *Nucl. Instr. and Meth., A* 639 (2011), p. 30.

[21] A. Avrorin et al. "Status of the BAIKAL neutrino experiment". In: *Bulletin of the Russian Academy of Sciences. Physics* 75.3 (2011), p. 414.

[22] A. Avrorin et al. "Search for neutrino events from Gamma Ray Bursts in NT200". In: *Lett. To Astron. J.* 37.10 (2011), p. 1.

[23] A. Avrorin et al. “Acoustic search for high-energy neutrinos in the Lake Baikal: Results and plans.” In: *Nucl. Instr. and Meth., A* 662 (2012), p. 210.

[24] A. Avrorin et al. “Status of the BAIKAL-GVD project”. In: *Nucl. Instr. and Meth., A* 692 (2012), p. 46.

[25] A. Avrorin et al. “ASP-15 – A stationary device for the measurement of the optical water properties at the NT200 neutrino telescope site”. In: *Nucl. Instr. and Meth., A* 693 (2012), p. 186.

[26] A. Avrorin et al. “Current status of the BAIKAL-GVD project”. In: *Nucl. Instr. and Meth., A* 725 (2013), p. 23.

[27] A. Avrorin et al. “Present status of the BAIKAL-GVD project development”. In: *Journal of Physics:Conference Series* 409 (2013), p. 012141.

[28] Zh.-M.Dzhilkibaev. In: 3rd Roma International Conference on Astro-particle Physics (RICAP 2011), Rome. 2011.

[29] V.Aynutdinov. In: 2nd International Cosmic Ray Conference (ICRC-2011), Beijing, China. 2011.

[30] Zh.-M.Dzhilkibaev. In: Mediterranean and Antarctic Neutrino Telescope Symposium (MANTS), Bologna, Italy. 2011.

[31] I.Belolaptikov. In: 23rd European Cosmic Ray Symposium, Moscow, Russia. 2012.

[32] B. Shoybonov. In: The XXV International Conference on Neutrino Physics and Astrophysics, Kyoto, Japan. 2012.

[33] N.Budnev. “Status of the BAIKAL-GVD neutrino project”. In: International Cosmic Ray Conference (ICRC-2013), Rio de Janeiro, Brazil. 2013.

[34] Zh.Dzhilkibaev. “The prototyping/early construction phase of the BAIKAL-GVD project”. In: Roma International Conference on AstroParticle Physics (RICAP-13), Rome, Italy. 2013.

[35] O. Suvorova. “Search for Neutrinos from Dark Matter Annihilation in the Sun with the Baikal Neutrino Experiment”. In: Workshop EPNT13: ”Exotic Physics with Neutrino Telescopes 2013”, Marseille, France. 2013.

Chapter 4

BOREXINO Experiment

Editors: O.Yu.Smirnov

Project Title

Borexino experiment

Project Leaders

- O.Yu.Smirnov for JINR group

Abstract

Borexino is a unique detector able to perform measurements of solar neutrino fluxes in the energy region below 1 MeV due to its low level of radioactive background. It was constructed at the LNGS underground laboratory with the primary goal of solar ^{7}Be neutrino flux measurement with 5% precision. The goal has been successfully achieved in 2011 marking the end of the first stage of the experiment. The collaboration then conducted a successful liquid scintillator repurification campaign aiming at reducing main contaminants in the sub-MeV energy range. With the new levels of radiopurity Borexino can improve existing, and challenge a number of, new measurements including: improvement of the results on the Solar and terrestrial neutrino flux measurements; measurement of pp and CNO solar neutrino fluxes; search for non-standard interactions of neutrino; study of short baseline neutrino oscillations with an artificial neutrino source (search for sterile neutrino); search for dark matter with the modified prototype of the Borexino detector (project DarkSide-50).

keywords: Solar neutrino; neutrino oscillations; geoneutrino; sterile neutrino

Project Members From JINR

K.A.Fomenko, D.E.Korablev, O.Yu.Smirnov, A.P.Sotnikov, O.A.Zaimidoroga

Project Duration. Approval Date(s)

- 1992–1995 Work on Borexino prototype — Counting Test Facility (CTF) — ultrasensitive detector able to trace U/Th down to 10^{-16} g/g;
- 1995–1998 The project was approved by funding agencies, start of works on detector construction;
- 2002–2004 The project was suspended because of the known problems;
- 2005 Recommissioning of all setups;
- May 2006 Restart of operations;
- May 2007 Start of the regular data taking;
- 2007–2011 Phase I program completed;
- 2012–2015 Phase II (including SOX Phase A);
- after 2015 SOX Phases B and C.

List of Participating Countries and Institutions

Laboratoire AstroParticule et Cosmologie, France; Joint Institute for Nuclear Research, Dubna, Russia; NRC Kurchatov Institute, Moscow, Russia; St. Petersburg Nuclear Physics Institute, Gatchina, Russia; Institute of Nuclear Physics, Lomonosov Moscow State University, Moscow, Russia; Dipartimento di Fisica, Università e INFN, Genova, Italy; INFN Laboratori Nazionali del Gran Sasso, Assergi, Italy; Dipartimento di Fisica, Università degli Studi e INFN, Milano, Italy; Dipartimento di Chimica, Università e INFN, Perugia, Italy; M. Smoluchowski Institute of Physics, Jagellonian University, Krakow, Poland; Max-Plank-Institut für Kernphysik, Heidelberg, Germany; Physik Department, Technische Universität München, Garching, Germany; Institut für Experimentalphysik, Universität Hamburg, Germany, USA; Chemical Engineering Department, Princeton University, Princeton, USA; Physics Department, Princeton University, Princeton, USA; Physics Department, University of Massachusetts, Amherst, USA; Physics Department, Virginia Polytechnic Institute and State University, Blacksburg, USA

4.1 Project Description

4.1.1 Fundamental Scientific Problem Addressed by the Project

The study of Solar neutrino fluxes provides information on the nuclear processes in the core of the Sun that can be used in particular by astrophysicists in their modeling of stars. On the other hand valuable information on the neutrino physics can be obtained studying the flavor composition of the Solar neutrino flux at the Earth's surface. At the time of the formation of the Borexino collaboration in 1990, the discrepancy between the measured Solar neutrino fluxes and signal observed by three different solar neutrino experiments led to the understanding that new neutrino physics is involved. The most popular solution to the "Solar neutrino problem", being neutrino oscillation, was at the time highly uncertain, as the joint fit of the data has had 3 different solutions. The measurement of the neutrino flux from monoenergetic ^{7}Be reaction would gave an answer on the oscillation scenario. But when the Borexino experiment started to take data in 2007, another experiment (namely the reactor experiment KamLAND) already constrained the oscillation parameter space. Thus the focus of the Borexino experiment has shifted to the precise measurement of the Solar neutrino fluxes.

The study of the solar neutrino fluxes with energy below $\sim$2 MeV provides key information for accurate solar (or star) modeling. The spectrum of electron neutrinos (ν_e) generated in the core of the Sun is shown in Fig. 4.1 [1]. One of the goals of the Borexino experiment is the measurement of all the solar neutrino fluxes, with the exception of the hep flux, too faint for detection in Borexino. The ^{7}Be, pep and ^{8}B (this last with the lowest threshold to date) neutrino fluxes have been already measured, but their experimental uncertainties can still be reduced with more data. In addition Borexino will try to measure the pp and CNO neutrino fluxes.

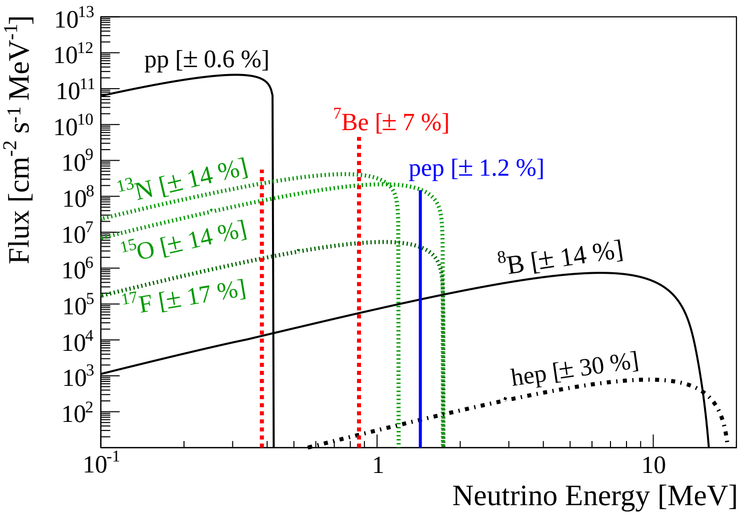

Figure 4.1: Energy spectrum of solar (ν_e) neutrinos from [1]. The numbers in parenthesis represent the theoretical uncertainties.

The future contribution of Borexino to studying the workings of stars is directly connected to the possibility of measuring the CNO flux. The detection of Solar neutrinos has not only confirmed the basic theory of how the Sun shines, via the proton-proton nuclear reaction chain in the solar interior, but has revolutionized particle physics by the discovery that neutrino oscillates and has a non-zero mass. But the complete theory of how stars shine and what generates the enormous amount of energy emitted by billions of stars throughout the Universe has yet to be fully tested. The theory of energy generation in stars posits that two processes power stars during their main sequence lifetime: the proton-proton (p-p) chain which builds helium from hydrogen and is the dominant energy source in stars like the Sun and lower mass stars, and the CNO cycle, which is theorized to be the primary channel for hydrogen burning in stars more massive than the Sun, and is in fact the primary channel for hydrogen burning in the Universe.

The CNO cycle is considered to produce a small but detectable fraction of the Sun's energy. Larger stars, however, with central temperatures higher than the Sun's, should generate their energy mostly via the CNO cycle. The model of energy generation in more massive stars has never been tested and demands observational confirmation. While neutrinos from the center of distant massive stars cannot easily be detected, we can detect CNO neutrinos from the center of our Sun. This, by appropriate scaling, would experimentally test the theory of energy generation in other stars. Similar to the pioneering work of John Bahcall and Ray Davis the observation of CNO neutrinos will test how massive stars shine by providing the experimental evidence of the existence of these neutrinos from the Sun, confirming our current understanding of energy generation in the core of stars. Such an investigation might also reveal the unexpected, as was the case with Solar neutrinos.

4.1.2 Specific Project Objectives and Expected Results

Solar neutrino program

One of the goals of the Borexino experiment is the measurement of all solar neutrino fluxes, with the exception of the hep flux, too faint for detection in Borexino. The ^{7}Be, pep and ^{8}B have already been measured, but the experimental uncertainties can be reduced. In addition Borexino will try to measure the pp and CNO fluxes.

ν flux	GS98	AGSS09	cm^{-2}s^{-1}	Experimental result
pep	1.44 ± 0.012	1.47 ± 0.012	$\times 10^{8}$	1.6$\pm$0.3 Borexino
^{7}Be	5.00 ± 0.07	4.56 ± 0.07	$\times 10^{9}$	4.87 ± 0.24 Borexino
^{8}B	5.58 ± 0.14	4.59 ± 0.14	$\times 10^{6}$	5.2$\pm$0.3 SNO + SK + Borexino + KamLAND $5.25 \pm 0.16^{+0.011}_{-0.013}$ SNO-LETA
^{13}N	2.96 ± 0.14	2.17 ± 0.14	$\times 10^{8}$	
^{15}O	2.23 ± 0.15	1.56 ± 0.15	$\times 10^{8}$	$<$7.4 Borexino (total CNO)
^{17}F	5.52 ± 0.17	3.40 ± 0.16	$\times 10^{8}$	

Table 4.1: Standard Solar Model (**SSM**) predictions for low (GS98) and high (AGSS09) metallicity and current experimental results

In Tab. 4.1 the solar fluxes measured by Borexino so far are compared with the SSM prediction, for low and high metallicity. The experimental results agree, within the errors, with the SSM predictions, but cannot distinguish between the two metallicities, due to the uncertainties of the model and the experimental errors. It would be useful, at this moment, to recall what the metallicity puzzle is.

The solar surface heavy element abundance was calculated about ten years ago with a 1D model, which uses data from spectroscopic observations of the elements present in the photosphere (GS98 [2]). This model agrees with the helioseismology observations, namely the measurement of the speed of the acoustic waves in the Sun. More recently a 3D hydrodynamical model (AGSS09 [3]) of the near-surface solar convection, with improved energy transfer, has changed the Z/X ratio with respect to the previous 1D treatment: 0.0178 (low metallicity) to be compared with the previous 0.0229 (high metallicity). The 3D model results perfectly reproduce the observed solar atmospheric line (atomic and molecular) profiles and asymmetries, but are in clear disagreement with the helioseismology data. At present there is no satisfactory solution to this controversy [1]. The 1D and the 3D models predict different neutrino fluxes from the various nuclear reactions, as shown in Tab. 4.1, where they are compared with the experimental results obtained until now.

As stated above, it is not possible, at present, to decide which of the two solutions is best due to model uncertainties and experimental errors. A measurement of the CNO flux, with reasonable errors, could distinguish between the two models, which predict substantially different fluxes. The pp solar neutrino flux has never been measured directly. GALLEX and SAGE experiments have measured the integrated solar flux from 233 keV, which, together with the Borexino ^{7}Be neutrino flux measurement and the experimental data on the ^{8}B neutrino flux, can be used to infer the pp neutrino flux with a relatively small uncertainty, once the luminosity constraint is applied as can be seen from Fig. 4.2. Nevertheless, a direct

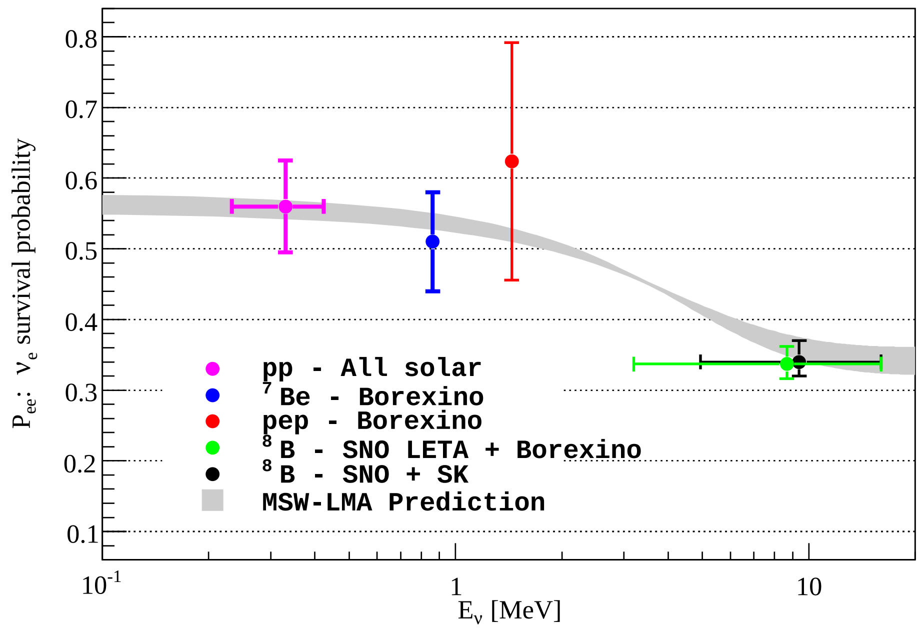

Figure 4.2: Electron neutrino survival probability as a function of energy. The gray band shows theoretical prediction with $\pm 1\sigma$ uncertainty.

experimental observation, which can be compared with the solar luminosity and the SSM prediction, would be an important achievement. The pp neutrino flux measurement is part of the Borexino phase II program.

Improvement of the ^{7}Be solar neutrino flux measurement

Improving the ^{7}Be flux measurement is one of the goals for Borexino phase II. The physical reasons of this study can be summarized in the three main points:

1. Reduction of the total error (statistical + systematic) below 3% is needed. Even with the 3%-precision this measurement cannot solve the metallicity puzzle, because of the uncertainties of the SSM. The ^{7}Be flux measured in phase I falls in between the two flux values, for high and low metallicities, and a smaller uncertainty would not help if this will be the case also for phase II. A very precise experimental determination of the ^{7}Be flux remains nonetheless an important tool for testing the Solar Model as well as a remarkable technical achievement.

2. In the context of neutrino physics, the Non Standard neutrino Interactions (**NSI**) are currently hotly debated. One way to study them is to analyze the shape of the oscillation vacuum-matter transition region. While ^{7}Be cannot have a conclusive role in this matter, it can nevertheless help in restricting the range of the NSI flavor diagonal terms.

3. It is possible to constrain the NSI parameters by studying ν-e elastic scattering, as discussed below. Bounds are imposed by various other experiments on solar, atmospheric and reactor (anti)neutrinos. But ^{7}Be neutrinos have the strong advantage of being monoenergetic (^{8}B neutrino detected by the other solar experiments in real time have a continuous energy spectrum). In Borexino, the limitation to this analysis comes from the residual background, especially ^{85}Kr, and, to lesser extent, ^{210}Bi, which can mimic non-zero values of the NSI parameters. An increase of statistics does not help much if not accompanied by a reduction of such background. The successful repurification campaign was performed after the closing of Phase I of the experiment. The results of the repurification are shown below in Table 4.3.

Measurement of neutrino flux from “pp” reaction in the Sun

This is the most important target of opportunity for Phase II. The very low ^{85}Kr and reasonably low ^{210}Bi achieved, make a direct pp measurement to be a reality. A careful understanding of the spectrum response in the ^{14}C end-point region is crucial, its study is possible through a dedicated effort. The main problem in the pp-neutrino study is the disentanglement of the tail of the ^{14}C spectrum (with possible pile-up) from the pp-neutrino spectrum. A series of calibrations with a specially designed ^{14}C source are envisaged in order to calibrate the detector performance at the very low energies (down from 200 keV). The feasibility of the measurement is still under study. A direct detection of pp neutrinos would be a spectacular result and would alone justify phase II.

The analysis group performed a study of sensitivity to pp solar neutrinos with the current background levels achieved. The expected precision of the pp-neutrino flux measurement is 10%.

pep Solar neutrino measurement

The first indication for pep solar neutrinos has been reported by BOREXINO Collaboration [4]. The value for the pep interaction rate obtained in Phase I (590 live-days) was

3.1 ± 0.6(stat) $\pm$ 0.3(syst) counts/day/100 tons, the absence of a pep signal was rejected at 98% C.L. The current measurement, in conjunction with the SSM (the uncertainty in the pep flux is as low as 1.2%), yields a survival probability of $P_{ee} = 0.62 \pm 0.17$ though the uncertainties are far from Gaussian. The precision is dominated by the statistical uncertainty (about 20%), though with more (background-free) data, systematic uncertainties (10%) will start to become important.

This is an extremely important result, but not yet the first measurement of pep solar neutrinos. The addition of a modest batch of data with ^{210}Bi reduced at or below 30 counts/(100 ton $\times$ day) will result in the first measurement (3σ) of pep solar neutrinos. A much prolonged data taking could also result in a 5σ precision measurement. The measurement will allow to gauge the survival probability in the immediate proximity of the transition between two different oscillation regimes.

Solar ^{8}B neutrino flux measurements

The Borexino detector is the first large volume liquid scintillator detector sensitive to the low-energy solar neutrinos. It possesses a very good energy resolution in comparison to the water Cherenkov detectors, which allows the search for the solar ^{8}B neutrinos starting practically from the energies of the so called Thallium limit (maximum energy of γ rays from the chains of radioactive decay of ^{232}Th and ^{238}U; gamma-quantum with maximum energy E = 2.6 MeV is emitted in the decay of ^{208}Tl). The measurements of ^{8}B above 2.8 MeV has been performed using one year of statistics (246 days of live time) of the Borexino data [5]. The threshold of 2.8 MeV is the lowest achieved so far in the ^{8}B neutrino real-time measurements. The interest in the neutrino flux measurement with low threshold comes from the peculiar properties of the survival probability in this energy region. The electron neutrino oscillations at E < 2 MeV are expected to be driven by the so called vacuum oscillation, and at energies E > 5 MeV by resonant matter-enhanced mechanism. The energy region in-between has never been investigated in spectrometric regime, and is of particular interest because of the expected smooth transition between the two types of oscillations.

The rate of ^{8}B solar neutrino interactions as measured through their scattering on the target electrons is 0.22±0.04(stat)±0.01(sys) counts/day/100 tons. This corresponds to an equivalent electron neutrino flux of $\Phi^{ES}_{^8B} = (2.4 \pm 0.4 \pm 0.1) \times 10^6$ cm^{-2}s^{-1}, as derived from the elastic scattering only, in good agreement with existing measurements and predictions. The corresponding mean electron neutrino survival probability, assuming the BS07(GS98) Standard Solar Model (High Z model), is 0.29±0.10 at the effective energy of 8.6 MeV. The ratio between the measured survival probabilities for ^{7}Be and ^{8}B is 1.9σ apart from unity (see Fig.4.2). For the first time the presence of a transition between the low energy vacuum-driven and the high-energy matter-enhanced solar neutrino oscillations is confirmed using the data from a single detector, the result is in agreement with the prediction of the MSW-LMA solution for solar neutrinos.

Acquiring more statistics (of up to 5 years of the calendar time) the Borexino will provide the competitive measurement of the ^{8}B neutrino flux.

Supernova neutrino detection

Calculations suggest that in the case of a “typical” galactic supernova (at 10 kpc away and 3×10^{53} ergs of binding energy release) about 150 events with energy above 200 keV will occur in the inner vessel of the Borexino detector within tens of seconds. The reaction rates and the energy of the signal are summarized in Tab. 4.2.

Interaction	Prompt energy release, MeV	Delayed energy release, MeV	Delay, ms	Events $E > 200$ keV
$\nu_e + e \rightarrow \nu_e + e$	0–30	—	—	5
$\overline{\nu}_e + p \rightarrow n + e^+$	0.9–50	1.9	0.26	78
$^{12}\mathrm{C}(\nu_e, e^-)^{12}\mathrm{N}$	0–40	0.9–17	11	9
$^{12}\mathrm{C}(\overline{\nu}_e, e^+)^{12}\mathrm{B}$	0.9–50	0–13	20	3
$^{12}\mathrm{C}(\nu, \nu')^{12}\mathrm{C}^*$	—	13	—	15
$\nu + p \rightarrow \nu + p$	0–2	—	—	52

Table 4.2: The supernova induced neutrino interactions that are observable in Borexino. The energy of the prompt signal from the primary interaction products is presented in the second column, while the the delayed signal from secondary decays and de-excitations (not shown in the table) are presented in the third column. The average time difference between prompt and delayed signal is shown in the fourth column. The expected number of interactions from a “typical” supernova for each interaction is shown in the last column.

The event rates for supernova neutrino interactions are expected to be 1 to 3 orders of magnitude larger than the uniform background and, therefore, the Borexino detector is well suited for the early detection of a galactic supernova.

The Borexino collaboration is working in order to met the requirements of the Super Nova Early Warning System (**SNEWS**) and to join it in the near future. The SNEWS is a collaboration between multiple neutrino detectors (LVD, Super Kamiokande, SNO(+) and AMANDA/Ice Cube) that takes advantage of time correlation between possible supernova neutrino signals among the different detectors to offer the astronomical community with a reliable alert in the case that a galactic supernova is imminent.

The physics of geo-neutrinos

Geo-neutrinos — electron anti-neutrinos ($\bar{\nu}_e$) — are produced in the β-decays of ^{40}K and of several nuclides in the chains of the long-lived radioactive isotopes ^{238}U and ^{232}Th, which are naturally present in the Earth. The Earth emits geo-neutrinos with a flux of about 10^6 cm^{-2}s^{-1}. It is important to note that the released radiogenic heat and the geo-neutrino flux is in a well fixed and known ratio. Therefore, it is possible, in principle, to determine the amount of radiogenic heat contributing to the total terrestrial surface heat flux (Urey ratio) by measuring the geo-neutrino flux. The knowledge of the geo-neutrino flux at different locations through the Globe, in different geological settings and/or by identifying the incoming direction of detected geo-neutrinos, may make it possible to:

- study the distribution of radioactive elements within the Earth, to determine their abundances in the crust and in the mantle;
- determine if there are radioactive elements in the Earth's core;
- understand if the mantle composition is homogeneous or not;
- test, validate, and discriminate among different geological models;
- exclude or confirm the presence of a geo-reactor in the core;
- determine the so called Urey ratio by measuring the radiogenic heat flux, an important parameter for both geochemistry and geophysics;
- study the bulk U and Th ratio in the silicate Earth, an important parameter for geochemistry, which could shed light on the process of the Earth's formation.

We can see that geo-neutrinos can be used as a unique direct probe of the Earth interior, not accessible by any other means. All of this information could provide important data used as inputs for geological, geophysical, and geochemical models describing such complex processes as the mantle convection, movement of tectonic plates, geo-dynamo (the process of the generation of the Earth's magnetic field), Earth formation etc.

Until now Borexino and KamLAND demonstrated the existence of geo-neutrino [6]. But the data are not yet enough to discriminate among the various Earth models and to fix some of the open problems mentioned before. Borexino, with its unprecedented radio-purity and the advantage of a low reactor ν rate at the Gran Sasso site, is able to produce further important insights in this physics.

With Borexino phases I + II the geo-neutrino rate with a relative precision of about 13% will be measured. Borexino's anti-neutrino measurement was already nearly background free in phase 1, so the error reduction is mostly statistical. The potential of geological predictions of a rate measurement with 13% relative error will depend, of course, on its central value with respect to the predictions of different geological models. It is not expected that such a measurement would discriminate with high significance among these models, but it can give hints of discrimination for some models and for the evidence of the presence of radioactive elements in the Earth mantle.

Even the existing data from KamLAND and Borexino, in a combined analysis, give hints of the exclusion of a fully radiogenic model and of the detection of mantle geoneutrinos. Such analyses indicate also that it is of a great importance to gather geo-neutrino measurements at different locations around the Globe. In the near future it is possible that also KamLAND will release a new geo-neutrino measurement, probably with increased precision, since many Japanese reactors were switched off. In that case a common Borexino + KamLAND data analysis could produce a further tool able to discriminate among different geological approaches.

Neutrino physics

Three topics, which have important impacts on neutrino physics, can be studied in phase II of Borexino experiment: the neutrino oscillation model, the Non Standard neutrino Interactions (**NSI**) and the possible existence of a sterile neutrino. The conventional MSW-LMA oscillation model has already been experimentally validated in vacuum and in matter regimes by Borexino and the Cherenkov experiments. On the other hand, the Borexino data, already obtained, on pep and CNO, are not precise enough to provide a stringent check of the so called transition region between the vacuum and matter plateaus (see Fig. 4.2). Therefore one of the phase II goals is the determination of its shape. This analysis involves directly the NSI study, because the intermediate region would be strongly influenced by the existence of the Non Standard Interactions and by the value of related parameters.

The Non Standard neutrino Interactions

The possibility of Non Standard neutrino interactions with other fermions can presently be considered a hot topic in the neutrino physics. The NSI has been predicted by many models beyond the Standard Model, for instance, the left-right symmetric models and supersymmetric models with R-parity violation. The NSI can be described at low energy by effective four fermion interactions:

$$\mathcal{L}_{\text{NSI}} = -2\sqrt{2}\, G_{\text{F}}\, \epsilon^{e,u,d}_{\alpha,\beta}\, (\overline{\nu}_\alpha \gamma^\mu P_L \nu_\beta)(\overline{f}\gamma^\mu P_C f')$$

where G_{F} is the Fermi constant, α and β are the neutrino flavors, f and f' are the electron or the light quarks, C can be L or R, i.e. the chirality of the operator P, and finally $\epsilon^{e,u,d}_{\alpha,\beta}$ is a dimensionless number which, coupled with the weak coupling constant, parameterizes the strength of the interaction.

Borexino can contribute to the search of NSI study by further studying neutrino oscillations, and in particular the transition region between vacuum and matter oscillations, and by a careful study of ν–e elastic scattering.

In the neutrino oscillation framework the NSI mixing matter matrix will be diagonal in flavor, if we assume the lepton flavor conservation:

$$\begin{pmatrix} \sqrt{2}G_{\text{F}}N_e(1+\epsilon_{ee}) & 0 & 0 \\ 0 & \sqrt{2}G_{\text{F}}N_e\epsilon_{\mu\mu} & 0 \\ 0 & 0 & \sqrt{2}G_{\text{F}}N_e\epsilon_{\tau\tau} \end{pmatrix}$$

where N_e is the electron density and $\epsilon_{\alpha\alpha}$ are the effective NSI seen by ν_α crossing the medium. This matrix replaces the standard MSW matter contribution to the evolution. The effect of the NSI influences the shape of the survival probability in the vacuum-to-matter oscillation transition region [7]. This effect can either enhance or weaken the oscillation matter effect, following the term with matter that modifies the vacuum oscillation. If the term

$$\sqrt{2}\, G_{\text{F}}N_e(1+\epsilon_{ee} - \cos^2\theta_{23}\epsilon_{\mu\mu} - \sin^2\theta_{23}\epsilon_{\tau\tau}) > \sqrt{2}G_{\text{F}}N_e,$$

the matter effect is enhanced. If, on the other hand, this term is below $\sqrt{2}G_{\text{F}}N_e$ then the matter effect is weakened. In Fig. 4.3 two examples of transition region shapes are shown. They are calculated for $\epsilon_{ee}, \epsilon_{\mu\mu}, \epsilon_{\tau\tau} = 0.25, 0.0, -0.5$, respectively (punctuated line), and $-0.25, 0., 0.5$ (dashed line). It is clear that refined experimental measurements of the ^{7}Be, pep, CNO neutrino fluxes can restrict the possible ranges of the NSI parameters.

Another way to investigate the NSI hypothesis with the solar neutrino data is to study the energy spectrum of the recoiled electron from the ν–e scattering [8]. The ν–e scattering

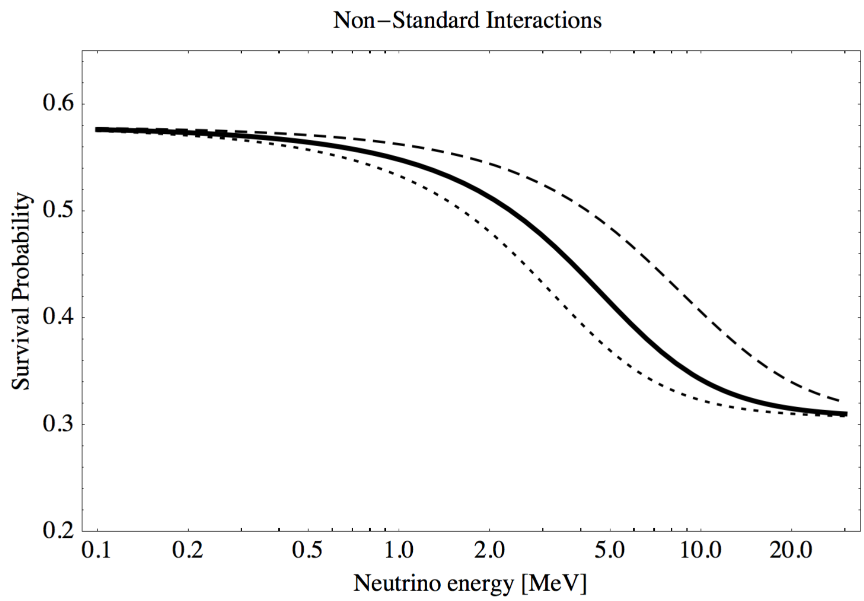

Figure 4.3: Survival probability in transition region with presence of NSI. Details in text.

can be written, in the NSI frame, as:

$$\mathcal{L}_{\text{NSI}} = -2\sqrt{2}G_{\text{F}}(\overline{\nu}_\alpha \gamma^\mu P_L \nu_\alpha)[\overline{g}_{\alpha L}(\overline{e}\gamma^\mu P_L e) + \overline{g}_{\alpha R}(\overline{e}\gamma^\mu P_R e)],$$

$$\overline{g}_{\alpha L} = g_{\alpha L} + \epsilon_{\alpha L}, \qquad \overline{g}_{\alpha R} = g_{\alpha R} + \epsilon_{\alpha R},$$

where α labels the neutrino flavor, $P_{L,R} = (1 \mp \gamma_5)/2$ are chiral projector operators, $g_{\alpha R} = \sin^2\theta_W$ and $g_{\alpha L} = \sin^2\theta_W \pm \frac{1}{2}$ ("+" stands for $\alpha = e$ and "−" stands for $\alpha = \mu$ or τ). The differential cross section for monoenergetic ^{7}Be flux does not need any convolution with the incident neutrino spectrum, as in the case of ^{8}B. Therefore, the cross section (as function of electron energy T) has the form :

$$\frac{d\overline{\sigma}(T)}{dT} = \frac{2G_{\text{F}}^2 m_e}{\pi}\left[\overline{g}_{eL}^2 + \overline{g}_{eR}^2(1 - \frac{T}{E_{\nu_e}}) - \overline{g}_{eL}\overline{g}_{eR}\frac{m_e T}{E_{\nu_e}}\right].$$

For the ^{7}Be flux measurement, $T_{\text{max}} = 0.665$ MeV. Also, in this case we report two examples of the shape of the recoiled electron energy spectrum for two reasonable values of ϵ parameters: ϵ_{eL},$\epsilon_{eR} = 0.01, 0.2$ respectively (dashed line), and $-0.01, -0.05$ (punctuated line). The result is shown in Fig. 4.4, where the cross section for the weak interaction alone is shown by the black continuous line in bold. The possible contribution of the electromagnetic interaction, calculated for a neutrino magnetic moment $\mu_\nu = 3 \times 10^{-11}\mu_B$ (close to the present world best limit) is also drawn just for comparison (black continuous thin line).

Borexino intends to study the NSI both with the ^{7}Be solar neutrino data and with the data collected from the ^{51}Cr external source.

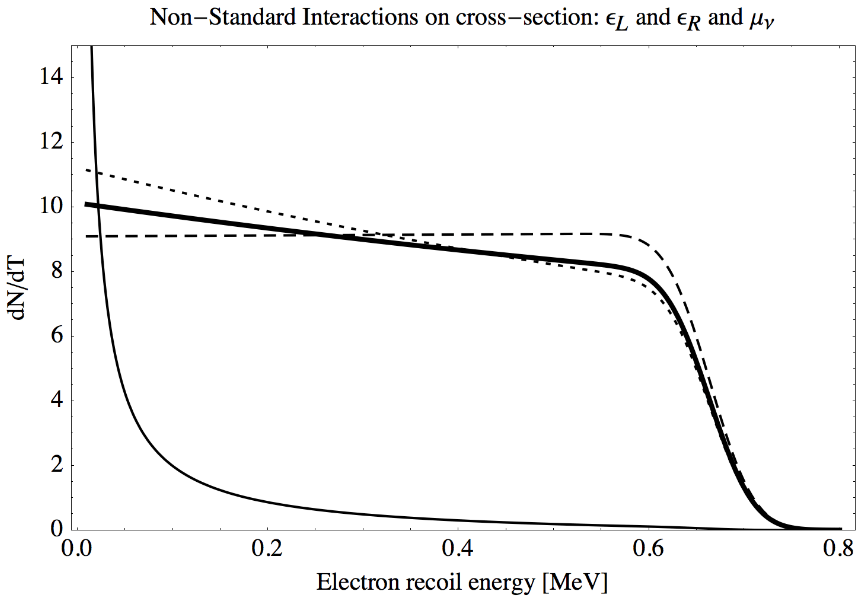

Figure 4.4: The shape of the recoiled electron energy spectrum for two values of ϵ parameter. The possible contribution of the electromagnetic interaction, calculated for a neutrino magnetic moment $\mu_\nu = 3 \times 10^{-11}\mu_B$ is shown for comparison (black continuous thin line).

Neutrino Magnetic Moment

A minimal extension of the Standard Model with a massive neutrino allows a non-zero value of the neutrino magnetic moment (proportional to the neutrino mass). The experimental observation of neutrino oscillations has already demonstrated that neutrinos are massive, and may thus possess a magnetic moment. In case of a non-zero neutrino magnetic moment, the electroweak cross section is modified by the addition of an electromagnetic term proportional to $1/T$, where T is electron recoil kinetic energy. The best limit on the effective neutrino magnetic moment obtained so far using solar neutrino data comes from the SuperKamiokande detector above a 5-MeV threshold. It is $\mu_\nu < 1.1 \cdot 10^{-10}$ Bohr magnetons (μ_B). The best limit on magnetic moment from the study of reactor anti-neutrinos (GEMMA experiment) is $\mu_\nu < 3.2 \cdot 10^{-11}\mu_B$ (90% CL).

The study of the maximum allowed deviations from the pure electroweak electron recoils shape for ^{7}Be neutrinos performed with Borexino 192 days live-time data lead to the new limit on the effective neutrino magnetic moment of $\mu_\nu < 5.4 \cdot 10^{-11}\mu_B$ at 90% CL [9]. The measurement is unique in neutrino physics due to the large statistics involved, which allows the self-calibration of the neutrino flux. The result doesn't contain any errors on the fiducial volume, parameters of oscillations and solar neutrino flux. It is worth mentioning that the best limits from the reactor experiments are based on the absence of any signal.

The limit on the magnetic moment is correlated with the (unknown) ^{85}Kr content, the shape distortions due to the additional electromagnetic contribution could be partially compensated by decreasing the ^{85}Kr contribution. By increasing the statistics the backgrounds will be restricted, in particular the ^{85}Kr content will be defined by the number of the events in the low probability (0.4% branching ratio) branch providing the delayed coincidences tag. Thus, the limit on the effective neutrino moment can be improved with the more statistics, down to $\sim 10^{-11}\mu_B$.

The Borexino program for the next years includes measurements with an artificial neutrino source, which would also allow the precise definition of the electron's recoil profile and the neutrino magnetic moment measurements. The option of the existing ^{51}Cr source irradiation on one of the Russian nuclear plants is under study. The source has been used for GALLEX setup calibration, the electron capture with strongest monoenergetic neutrino line of 756 keV is very close to those of the solar ^{7}Be. The estimated sensitivity to the neutrino magnetic moment is of the order of 3×10^{-11} μ_B.

Short Baseline Neutrino Oscillation Experiment with Borexino

The collected experimental data on neutrinos generally fits into the three-flavor oscillation model. Nevertheless, there is a number of experimental indications that oscillations of neutrinos with Δm^2 ~1 eV^2 are possible. The existence of oscillations at a scale of 1 eV naturally entails the existence of an extra type of neutrino. Indeed, $\Delta m^2_{12} \sim 10^{-5}$ eV^2 and $\Delta m^2_{23} \sim 10^{-3}$ eV^2 have been established by now. If there are three types of neutrinos then Δm^2_{13} is not an independent parameter, and it is inevitably of the same order of magnitude as the greatest of Δm^2. The number of types of neutrino $n \simeq 3 \pm 0.01$ was determined from the experimental Z^0 boson decay width. Therefore, if there is a fourth type of neutrino, it must be sterile in terms of the weak interactions (see more details in Section 2.2.5). Thus the search for neutrino oscillations at the Δm^2 ~1 eV^2 scale turns out to be a search for a sterile neutrino. Regardless of the theoretical interpretations, the existence of experimental anomalies is a problem to be solved. If interpretation of the anomalies as neutrino short-base oscillations is the case, the corresponding oscillations pattern with characteristic dimension of the order of 1 meter can be searched for with a large position-sensitive detector irradiated with a compact neutrino source.

Borexino detector and SOX experiment

Borexino's large size (the spherical sensitive volume has 8.5 m in diameter) and possibility to reconstruct an interaction point (with a precision of 14 cm at 1 MeV energy deposit) makes it an appropriate tool in the search for sterile neutrinos. If the oscillation baseline is about 1 m (which corresponds to Δm^2 ~1 eV^2), exposure of the detector to a compact powerful neutrino source should give rise to a typical oscillation picture with dips and rises in the spatial distribution of events density with respect to the source. Right beneath the Borexino detector, there is a cubical pit (side 105 cm) accessible through a small squared tunnel (side 95 cm) that was built at the time of construction with the purpose of housing neutrino sources for calibration. Using this tunnel, an experiment with the neutrino source can be done with no changes to the Borexino layout. The center of the pit is at 8.25 m from the detector center, requiring a relatively high activity of the neutrino source in order to provide detectable effect.

The experiment SOX (for Short distance neutrino Oscillations with BoreXino) [10] will be carried in three stages with gradually increasing sensitivity:

Phase A a ^{51}Cr neutrino source of 200-400 PBq activity deployed at 8.25 m from the detector center (external with respect to the detector);

Phase B deploying a ^{144}Ce-^{144}Pr antineutrino source with 2-4 PBq activity at 7.15 m from the detector center (placed in the detector's water buffer);

Phase C a similar ^{144}Ce-^{144}Pr source placed right in the center of the detector.

Figure 4.5 shows a schematic layout of the Borexino detector and the approximate location of the neutrino and anti-neutrino sources in the three phases.

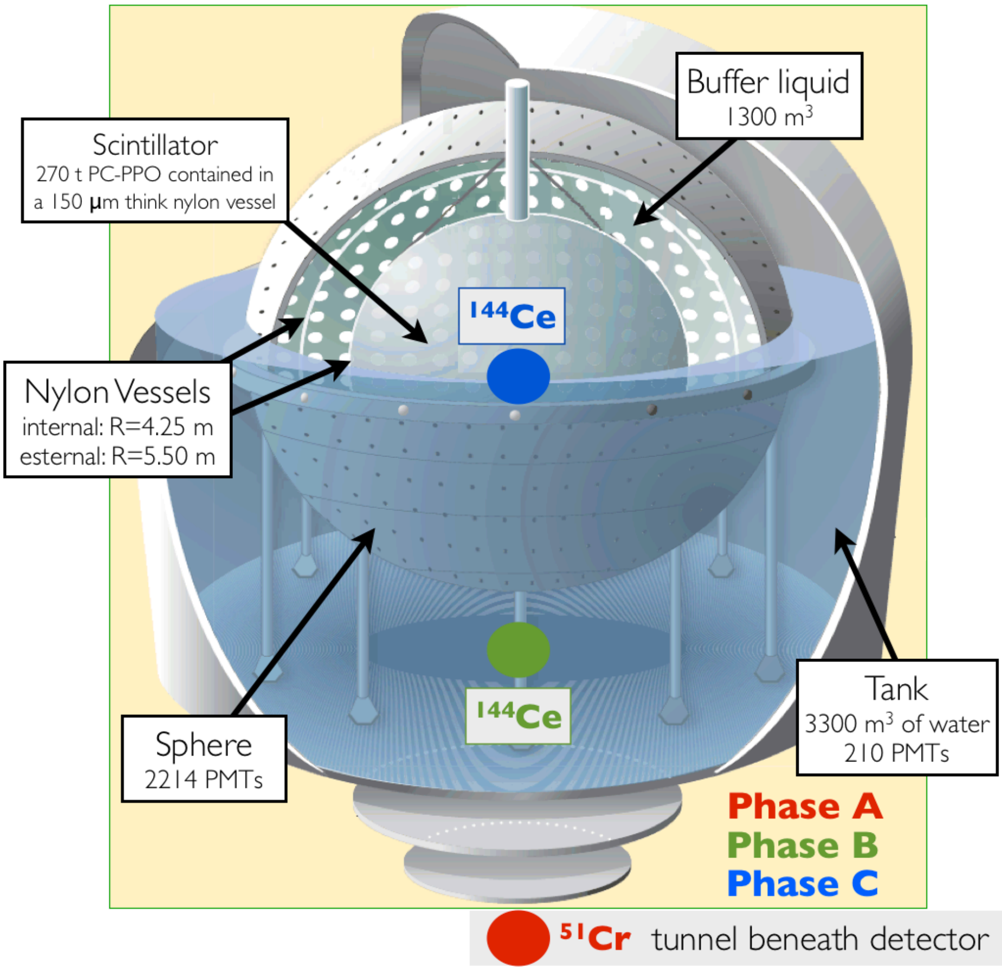

Figure 4.5: Layout of the Borexino detector and the approximate location of the neutrino and anti-neutrino sources in the three phases.

Two types of neutrino sources are considered. The ^{51}Cr source will be produced by irradiating a large sample of highly enriched ^{50}Cr in a nuclear reactor providing a high thermal neutron flux ($\approx 10^{15}$ cm^{-2} s^{-1}). The ^{144}Pr based source could be produced by chemical extraction of Ce from exhausted nuclear fuel [11]. ^{51}Cr decays via electron capture into ^{51}V, emitting two neutrino lines of 750 keV (90%) and 430 keV (10%), while ^{144}Pr β-decays into ^{144}Nd with an end-point of 3 MeV (parent ^{144}Ce decays too, but the end-point of its β-decay is below the inverse β decay registration threshold).

Figure 4.6 shows the decay levels of ^{144}Ce and ^{144}Pr (Fig. 4.6 left) and the energy spectrum of the emitted $\bar{\nu}_e$ (Fig. 4.6 right). As it is clear from the figure, the ^{144}Pr life-time is too short to allow the fabrication of a pure ^{144}Pr source, but the parent ^{144}Ce nucleus has acceptable life-time of the order of one year. The portion of the spectrum above the 1.8 MeV detection threshold is the only one of importance for the experiment. Elastic scattering of $\bar{\nu}_e$ on electrons induces negligible background.

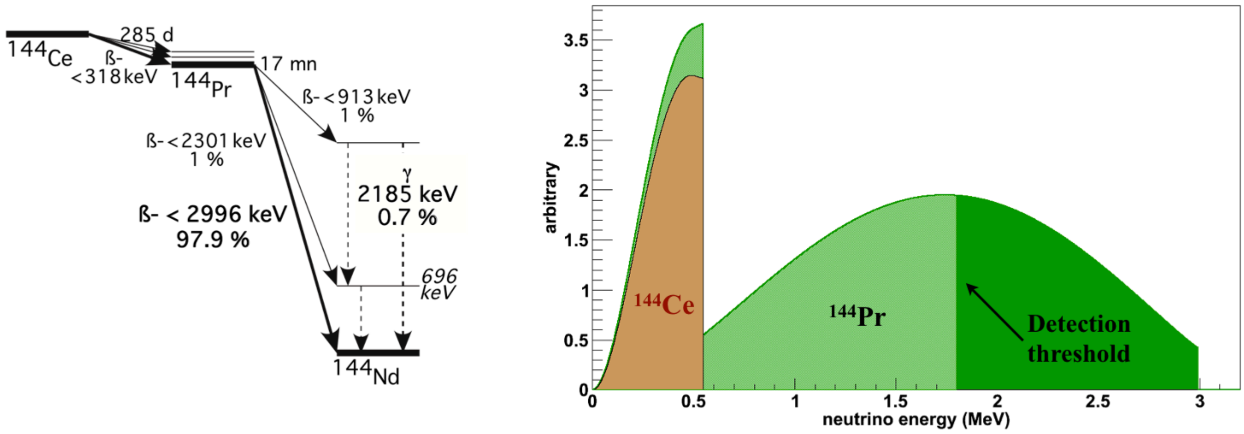

Figure 4.6: Left: decay scheme of ^{144}Ce and ^{144}Pr source; Right: energy spectrum of the emitted $\bar{\nu}_e$. Only the portion of the spectrum above 1.8 MeV can be detected via inverse β decay on protons.

Backgrounds for neutrino source measurements consist of the spectrum of electron recoil from solar neutrinos, and of spectra from residual radioactive contaminations. The experimental spectrum for Phase I of the Borexino experiment, with all identified spectral contributions, is shown in left side of Fig. 4.7. After the purification performed before passing to the Phase II the contamination in ^{210}Bi decreased from 40 do 20 cpd/100 tons, ^{85}Kr is now compatible with zero, monoenergetic ^{210}Po has decayed and its count is $\sim$1 cpd/t. Thus, in general, the sensitivity of the Phase II has improved compared to the first Phase.

Backgrounds for antineutrino source measurements contain mainly geoneutrino and reactor antineutrino components as shown in right side of Fig. 4.7. The spectrum shown corresponds to 1353 days of data taking and contains 46 events thus the background for an antineutrino source is negligible. We expect an increase of the random coincidences count in the Phase C, but it can be suppressed by excluding region close to the source ($\sim$1.5 m).

The ^{51}Cr experiment, in Phase A, will benefit from the experience of GALLEX and SAGE that used similar sources in the past [13, 14]. The source activity of 200-400 PBq is challenging, but only a factor 2–4 higher than what was already done by Gallex and SAGE in

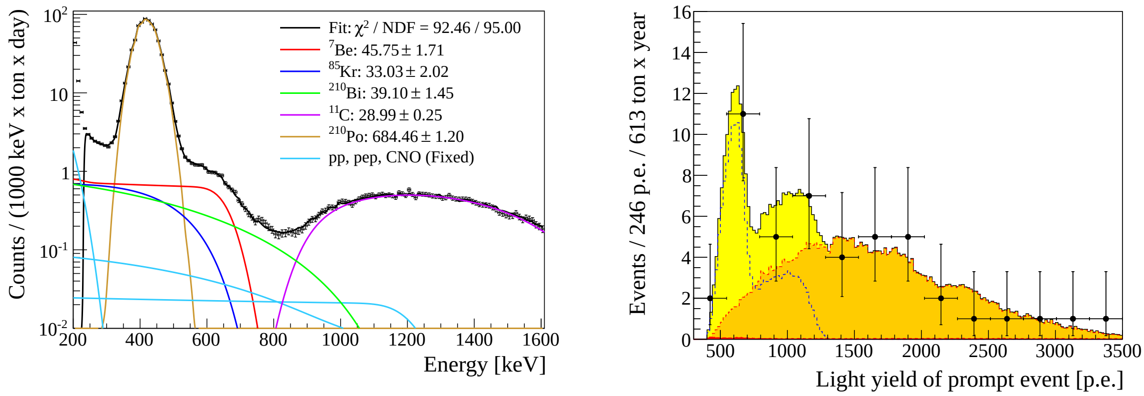

Figure 4.7: Left: experimental Borexino neutrino spectrum from the Phase I [12] fitted with spectral components including spectra of recoil electrons for solar neutrino and spectra of identified radioactive backgrounds (count is presented in counts/day/100 tons of LS); Right: experimental Borexino antineutrino spectrum obtained with 1353 days of data [6].

the 90's. The ^{144}Ce–^{144}Pr experiment in Phases B and C do not require high source activity. The activity of the source in these cases should be 2.3 PBq for the external source and about 1.5 PBq for the internal one. In both cases, the sensitivity can be enhanced by inserting PPO in the buffer liquid, in order to increase the scintillator volume.

Phase C is the most sensitive but it can be done only after the shutdown of the solar neutrino program, because it needs modification of the detector. Phases A and B will not disturb the solar neutrino program of the experiment, which is supposed to continue until the end of 2015, and do not require any change to Borexino hardware. They will not only probe a large fraction of the parameter space governing the oscillation into the sterile state, but also provide a unique opportunity to test low energy ν_e and $\bar{\nu}_e$ interactions at sub-MeV energy.

The challenge for Phase C is constituted by the large background induced by the source in direct contact with the scintillator, that can be tackled, in principle, thanks to the correlated nature of the $\bar{\nu}_e$ signal detection. In Phase B this background, though still present, is mitigated by the shielding of the buffer liquid.

Borexino can study short distance neutrino oscillations in two ways: by comparing the detected number of events with expected value (disappearance technique, or total counts method), or by observing the oscillation pattern in the event density over the detector volume (waves method). In the latter case the typical oscillations length is of the order of 1 meter, taking into account the values of Δm^2_{41} inferred from the neutrino anomalies and considering the typical energy of radioactive decay of 1 MeV. The two-flavor oscillations are described by:

$$P_{\mathrm{ee}} = 1 - \sin^2 2\theta_{14} \sin^2 \frac{1.27 \Delta m^2_{41} (\mathrm{eV}^2) L(\mathrm{m})}{E(\mathrm{MeV})}$$

where θ_{14} is the mixing angle of the ν_e (or $\bar{\nu}_e$) and fourth massive neutrino, Δm^2_{41} is the corresponding squared mass difference, L is the distance of the source to the detection point, and E is the neutrino energy. The variations in the survival probability P_{ee} could be seen on the spatial distribution of the detected events as the waves superimposed on the spatial distribution of events. Oscillation parameters can be directly extracted from the analysis of the waves. The result may be obtained only if the size of the source is small compared to the oscillation length. The ^{51}Cr source will be made by about 10-35 kg of highly enriched Cr metal chips which have a total volume of about 4-10 l. The linear size of the source will be about 15-23 cm, comparable to the spatial resolution of the detector. The ^{144}Ce–^{144}Pr source is even more compact. All simulations shown below take into account the source size.

In Phase A the sensitivity of the total counts method is enhanced by exploiting the fact that the life-time of the ^{51}Cr is relatively short. The known time-dependence of the signal, and the concurrent assumption of the stable background, significantly improves the sensitivity. In Phases B and C this time-dependent method is not effective because the source life-time is longer (411 days), but this is compensated by the very low background and by the larger cross-section. The total counts and waves methods combined together yield a very good sensitivity for both experiments. Besides, the wave method is independent of the intensity of the source, of detector efficiency, and is potentially a nice probe for un-expected new physics in the short distance behavior of neutrinos or anti-neutrinos.

Sensitivity of SOX

The sensitivity of SOX with respect to oscillation into sterile neutrino was evaluated with a toy Monte Carlo. Expected statistical samples (2000 events) were generated for each pair of oscillation parameters. We assume a period of 15 weeks of stable data taking before the source insertion in order to accurately constrain the background. The background model includes all known components, identified and accurately measured during the first phase of Borexino. We built the confidence intervals from the mean χ^2 for each couple of parameters with respect to the non-oscillation scenario. The result is shown in Fig. 4.8, as one can see from the figure the reactor anomaly region of interest is mostly covered.

The simulations for Phase A are shown for a single irradiation of the ^{51}Cr source up to the initial intensity of 370 PBq (10 MCi) at the site. A similar result can be obtained with two irradiations of about 200 PBq if higher intensity turns out to be beyond the technical possibilities. The single irradiation option is preferable and yields a slightly better signal to noise ratio.

The physics reach for the ^{144}Ce–^{144}Pr external (Phase B) and internal (Phase C) experiments, assuming 2.3 PBq (75 kCi) source strength and one and a half year of data taking) is shown in the same figure (Fig. 4.8). The χ^2 based sensitivity plots are computed assuming significantly bigger volume of liquid scintillator (spherical vessel of 5.5 m radius), compared to the actual volume of liquid scintillator (limited by a sphere with 4.25 m radius) used for the solar phase. Such an increase will be made possible by the addition of the scintillating fluor (PPO) in the inner buffer region (presently inert) of the detector.

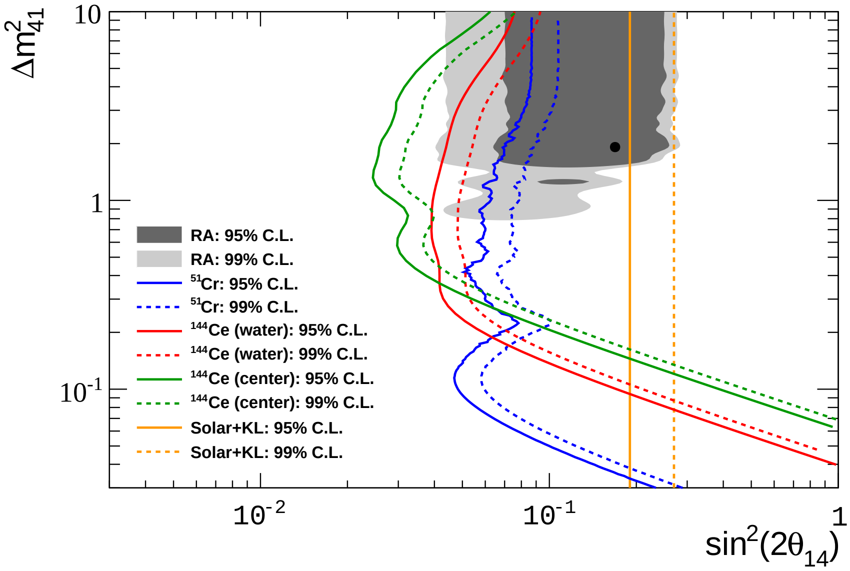

Figure 4.8: Sensitivity of Phase A (^{51}Cr external, blue), of Phase B (^{144}Ce–^{144}Pr external, red) and Phase C (^{144}Ce–^{144}Pr center, green). The gray area is indicated by the reactor anomaly, if interpreted as oscillations to sterile neutrinos. Both 95% and 99% C.L. are shown for all cases. The yellow line indicates the region already excluded in [15].

We have also conservatively considered exclusion of the innermost sphere of 1.5 m radius from the analysis in order to reject the gamma and bremsstrahlung backgrounds from the source assembly. Under all these realistic assumptions, it can be noted from Fig. 4.8 that the intrinsic ^{144}Ce–^{144}Pr sensitivity is very good. For example, the 95% C.L. exclusion plot predicted for the external test covers adequately the corresponding reactor anomaly zone, thus ensuring a very conclusive experimental result even without deploying the source in the central core of the detector. The background included in the calculation is negligible, being represented by about 5 $\bar{\nu}_e$ events per year from the Earth (geo-neutrinos) and from distant reactors, with negligible contribution from the accidentals (see Fig. 4.7). It is worth stressing that the three ingredients at the origin of this good performance are the very low background due to the $\bar{\nu}_e$ coincidence tag, the larger cross-section due to the higher source energy, and the deployment of the source closer or directly within the active volume detector, yielding a larger geometrical acceptance.

4.1.3 Basic Methods and Approaches Used in the Project

Solar neutrinos have been detected in the last 40 years by two methods, the earliest one is based on radiochemical nuclear isotope separation after neutrino nuclear absorption which yields only the integrated ν_e flux above an energy threshold. Individual components of the neutrino spectrum cannot be determined by such measurements. The low energy solar neutrinos have been observed so far only by this method. The second method —

direct spectroscopy using kiloton scale water Cherenkov detectors has been limited to the high energy solar neutrino flux above 5 MeV, owing to the low signal light yield of the Cherenkov process and to the natural radioactivity background.

Borexino employs a liquid scintillator that produces sufficient light to observe low energy neutrino events via elastic scattering by electrons. The reaction is sensitive to all neutrino flavors by the neutral current interaction, but the cross section for ν_e is larger due to the combination of charged and neutral currents. The recoil electron profile for a mono-energetic neutrino is similar to that of Compton scattering of a single γ-ray. Thus, the recoil electron profile is basically a rectangular shape with a sharp cut-off edge at 665 keV in the case of ^{7}Be neutrinos.

The PC/PPO solution adopted as liquid scintillator satisfies specific requirements: high scintillation yield ($\sim 10^4$ photons/MeV), high light transparency (the mean free path is typically 8 m) and fast decay time ($\sim$3 ns), all essential for good energy resolution, precise spatial reconstruction, and good discrimination between β-like events and events due α particles. Furthermore, several conventional petrochemical techniques are feasible to purify the hundred of tons of fluids needed by Borexino.

Analysis of the first Borexino data showed that the main goals concerning the natural radioactivity have been achieved. The contamination of the liquid scintillator with respect to the U/Th is at the level of 10^{-17} g/g; the contamination with ^{40}K is at the level of 10^{-14} g/g; the ^{14}C content is $(2.7 \pm 0.7) \times 10^{-18}$ g/g with respect to the ^{12}C.

Among the other contamination sources only ^{85}Kr and ^{210}Po have been identified. The ^{85}Kr counts $\sim$0.3 events/day/ton, it is β-emitter with 687 keV end-point. The ^{210}Po is the most intense contamination (60 counts/day/ton), it decays emitting monoenergetic α with 5.41 MeV energy, the half-life time of the isotope is 134 days. The residual contaminations do not obscure the expected neutrino signal, the presence of the 862 keV monoenergetic ^{7}Be solar neutrinos is clearly seen in the experimental spectrum. The radiopurity levels achieved in Counting Test Facility (**CTF**) and Borexino are summarized in Table 4.3.

Note that the reported levels are the highest ever measured. The details of the radiopurity tests with CTF have been reported in [16–18].

The achieved general level of radiopurity allowed to fulfill successfully the physics program of the first stage of Borexino project.

Background	Typical abundance (source)	CTF	Borexino goals	Phase I	Phase II
^{14}C in g/g of ^{14}C	$\sim 10^{-12}$ (cosmogenic)	$1.8 \cdot 10^{-18}$	$\sim 10^{-18}$	$2.7 \cdot 10^{-18}$	$2.7 \cdot 10^{-18}$
^{232}Th in g/g of LS by ^{212}Bi-Po	10^{-6} – 10^{-5} (dust)	$< 8.4 \cdot 10^{-16}$	$\sim 10^{-16}$	$(6.8 \pm 1.5) \cdot 10^{-18}$	$< 9.2 \cdot 10^{-19}$ (95% C.L.)
^{238}U in g/g of LS by ^{214}Bi-Po	10^{-6} – 10^{-5} (dust)	$< 4.8 \cdot 10^{-16}$	$\sim 10^{-16}$	$(1.6 \pm 0.1) \cdot 10^{-17}$	$< 1.2 \cdot 10^{-19}$ (95% C.L.)

Table 4.3: Radiopurity levels achieved in CTF and Borexino (continued).

Background	Typical abundance (source)	CTF	Borexino goals	Phase I	Phase II
^{222}Rn by ^{214}Bi-Po cpd/100 t	100 atoms/cm^3 (air) (emanation from materials)	∼100	∼10	∼1	∼0.1
^{40}K g[K$_{nat}$]/g[LS]	$2 \cdot 10^{-6}$ (dust)	$< 10^{-11}$ sensitivity limit	$\sim 10^{-15}$	$< 1.7 \cdot 10^{-15}$ (95% C.L.)	no data
^{210}Bi cpd/100 t	high	no data	not specified	20-70	∼20
^{210}Po cpd/t	high (surface contamination)	500 (min observed)	not specified	80 (initial) $T_{1/2} = 134$ d	2
^{85}Kr in μBq/t	1 Bq/m^3 (technogenic in air)	< 600	$\sim 10^{-1}$ cpd/100t	30.4 ± 5.5	compatible with 0
^{39}Ar in μBq/t	17 mBq/m^3 in air (cosmogenic in air)	< 800	$\sim 10^{-1}$	$\ll$ ^{85}Kr activity	

Table 4.3: Radiopurity levels achieved in CTF and Borexino.

4.1.4 Detector Description

Borexino is a unique detector able to perform measurements of solar neutrinos fluxes in the energy region around 1 MeV or below because of its low level of radioactive background. After several years of efforts and tests with the prototype CTF detector the design goals have been reached and for some of the radioactive isotopes (internal ^{238}U and ^{232}Th) largely exceeded. The low background is an essential condition to perform the measurement: in fact solar neutrinos induced scintillations cannot be distinguished on an event-by-event analysis from those due to background. The energy shape of the solar neutrino is the main signature that has to be recognized in the experimental energy spectrum by a suitable fit procedure that includes the expected signal and the background. The basic signature for the mono-energetic 0.862 MeV ^{7}Be neutrinos is the Compton-like edge of the recoil electrons at 665 keV.

The detector is located deep underground (approximately 3800 m of water equivalent, mwe) in the Hall C of the Laboratori Nazionali del Gran Sasso (Italy), where the muon flux is suppressed by a factor of 10^6. The main goal of the experiment was the detection of the monochromatic neutrinos that are emitted in the electron capture of ^{7}Be in the Sun with 5% precision.

The complete up-to-date technical description of the Borexino detector has been reported in [19] and [20]. The detector is schematically depicted in Fig.4.9.

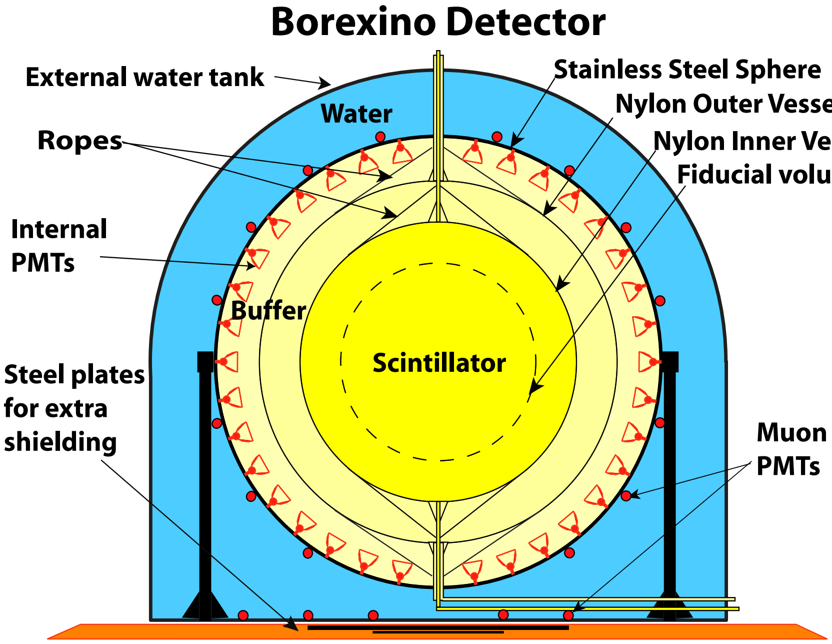

Figure 4.9: Sketch of the Borexino detector. The base of the dome-like structure is 18 m in diameter.

The inner part is an unsegmented stainless steel sphere (**SSS**) that is both the container of the scintillator and the mechanical support of the photomultipliers. Within this sphere, two nylon vessels separate the scintillator volume in three shells of radii 4.25 m, 5.50 m and 6.85 m, the latter being the radius of the SSS itself. The inner nylon vessel (**IV**) contains the liquid scintillator solution, namely PC (pseudocumene, 1,2,4-trimethylbenzene $C_6H_3(CH_3)_3$) as a solvent and the fluor PPO (2,5-diphenyloxazole, $C_{15}H_{11}NO$) as a solute at a concentration of 1.5 g/l (0.17% by weight). The second and the third shell contain PC with a small amount (5 g/l) of DMP (dimethylphthalate) that is added as a light quencher in order to further reduce the scintillation yield of pure PC.

The scintillation light is collected by 2212 photomultiplier (PMTs) that are uniformly attached to the inner surface of the SSS. All but 384 photomultipliers are equipped with light concentrators that are designed to reject photons not coming from the active scintillator volume, thus reducing the background due to radioactive decays originating in the buffer liquid or γ's from the PMTs. The tank has a cylindrical base with a diameter of 18 m and a hemispherical top with a maximum height of 16.9 m. The Water Tank (**WT**) is a powerful shield against external background (γ-rays and neutrons from the rock) and is also used as a Cherenkov muon counter and muon tracker. The muon flux, although reduced by a factor of 10^6 by the 3800 m.w.e. depth of the Gran Sasso Laboratory, is of the order of 1 m^{-2} h^{-1}, corresponding to about 4000 muons per day crossing the detector. This flux is well above Borexino requirements and a strong additional reduction factor (about 10^4) is necessary. Therefore the WT is equipped with 208 photomultipliers that collect the Cherenkov light emitted by muons in water. In order to maximize the light collection efficiency the SSS and the interior of the WT surface are covered with a layer of Tyvek, a white paper-like material made of polyethylene fibers.

The Borexino has an excellent energy resolution for its size (Tab. 4.4), this is the result of the high light yield of ~ 500 p.e./MeV/2000 PMTs. The energy resolution (1σ) at the ^{7}Be Compton edge energy (662 keV) is as low as 44 keV (or 6.6%).

Borexino technical data	
Light yield	$>$500 p.e./MeV/2000 PMTs (31% of 4π)
Energy resolution (1σ)	~5% @ 1 MeV
Mass	full 278 t; FV mass 78.5 t (used in ^{7}Be analysis)
Practical threshold on the electrons recoil	180 keV (corresponds to $E_\nu = 320$ keV)
Muons registering efficiency	close to 100% (10^{-4} inefficiency)
Triggers rate	11 cps (mainly ^{14}C, 2.70·10^{18} g/g ^{14}C/^{12}C)
Spatial resolution	14 cm @ 1 MeV

Table 4.4: Main technical characteristics of the Borexino detector.

4.1.5 Contribution of JINR Members

Dubna scientists have been working in the Borexino collaboration starting from the initial stage of the project. The group participated in the construction of a prototype of the Borexino detector, the Counting Test Facility (CTF), and its further exploitation (including regular shifts during data taking). The specific responsibilities of the group were mainly the on-line software and the data analysis.

Another significant contribution provided by the Dubna group consisted in building and operating the so called *PMT test facility* used for testing all PMTs for both CTF campaigns (200 PMTs in total) and Borexino (2400 PMTs in total). The very first version of the test facility has been used for the PMT selection for Borexino, on the base of the test the ETL 9351 8" PMTs have been selected [21]. Later the test facility has been upgraded to operate with a maximum of 128 electronic channels providing the possibility of fast PMTs testing [22]. The PMT test facility has been used for the PMTs characterization, the amplitude [23] and time response of ETL9351 [24] has been studied in detail. On the basis of these tests a fast HV tuning algorithm has been developed [25] and applied for the automated PMT gain control system for the Borexino PMTs test facility and for the CTF.

The test facility has been used for tests of the PMT sealing. This was a long term test in the conditions very close to those of Borexino. The PMTs were completely immersed in the pseudocumene with the base left in the ultrapure water. A specially designed stainless steal tank containing water and PC was installed at the laboratory (the two liquids test tank, **TLTT**). The test lasted for 3 years and proved the reliability of the chosen design for the sealing. Later, on a multiplexed optical-fiber system, the PMT calibration of the Borexino experiment was tested using TLTT and the PMT test facility [26]. Using the test facility 2000 PMTs with the best performance were selected for installation in the Borexino detector. The high efficiency of the equipment permitted completion of PMT testing within 4 months. The analysis software was developed on the basis of the CERN ROOT libraries under a Linux system. The program automatically analyzes the charge spectrum, the transit time spectrum, and the spectrum of the ionic afterpulses, and then plots all of the data in the test sheet. All numerical data were inserted in a database immediately. The results of the acceptance test were reported in [27].

In March 2012 we performed a bulk testing of 100 PMTs dismounted from the CTF with the aim of installing them into the DarkSide muon veto system. We also completed the tests of 120 new Hamamatsu PMTs for the DarkSide neutron veto.

The PMT test facility is still in operation and will be used in a number of important tests for future developments. One of the important tasks will be the testing of new PMTs for the DarkSide-G2 detector.

Data Taking

Borexino will continue to collect data for the next 3 years. Next year data collection will begin in the DarkSide-50 facility.

In accordance with the rules accepted by the collaboration, each participating group covers the number of the data taking shifts proportional to the authors in the collaboration papers.

Physics analysis of the CTF data

The Dubna group gained unique experience operating the CTF. The complete MC model for the CTF detector has been developed on the basis of EGS4 code. A number of important results for the physics beyond the Standard Model were obtained with CTF data [28–35], with a review of the results published in [36].

An accurate analysis of the CTF data with dissolved radon has been performed in order to investigate the precise shape of the ^{214}Bi beta decay, a process that accounts for about one-half of the total geo-neutrino signal. This study is of primary importance in view of the geoneutrinos studied with Borexino. The intensities of two most energetic beta transitions have been measured directly for the first time [37]. As a by-product of theses studies we extracted the precise life-time of two isotopes of Po [38].

In 2010–2011 a set of measurements with a specially designed radon sources were performed. We acquired the data for ^{212}Bi decay from the ^{232}Th chain and for ^{214}Bi decay from the ^{238}U chain. The data are being analyzed, and the measured shapes of the beta-spectra will lead to a better prediction of geoneutrino signal.

Borexino software development

The Dubna group participated in the development of the off-line code for the Borexino experiment. In particular, the position reconstruction code, module for the CNGS muons identification, and module for noise events analysis have been developed. The group provided monitoring of the natural radioactive backgrounds and developed software for the detector stability monitoring. Much effort have been spent on the calibration of the Borexino energy scale and understanding of the detector's performance. The sophisticated physical models developed for the description of scintillation detector energy resolution [39] and the scintillator response function shape [40] have been successfully applied to the Borexino data and are now being included in the official Borexino data analysis code as standard functions.

Data analysis

The Dubna group is taking an active part in the data analysis. The experience gained with the CTF was a very good starting point for the Borexino data analysis. The group played a leading role in the ^{7}Be neutrino flux analysis (including analysis of limits on the neutrino effective magnetic moment), analysis of the antineutrino data, and analysis of rare processes.

At present the responsibility of the group includes the ^{7}Be, pp and CNO solar neutrino fluxes analysis and the analysis of the rare processes. The group is also involved in the antineutrino analysis (geoneutrino). The group plays a leading role in pp-neutrino analysis. It is worth noting that the possibility to search for the pp-neutrino with liquid scintillator was first discussed by Dubna group [41, 42].

4.1.6 Publications, Theses and Conferences

- The following papers has been published since the start of the data taking in 2007: [4–6, 9, 10, 12, 20, 35, 37, 38, 40, 43–63].

- 1 PhD defended by O.Smirnov "Study of ultralow-background of natural radioactivity with a prototype of liquid scintillator Solar neutrino detector" [64] and one is ready to be defended in 2014 by K. Fomenko "Search for Solar Axions emitted in p(d,^{3}He)A reaction and Pauli-forbidden transitions in ^{12}C nuclei with Borexino detector";

- 15 talks have been presented by JINR group in last 5 years at following conferences: 18th International Conference on Particles And Nuclei (PANIC08), Eilat, Israel, 2008 [65]; XXXI International workshop "Neutrino physics at accelerators", DLNP, JINR, Dubna, 2009; BUE-CTP Conference on Neutrino Physics in the LHC Era, Egypt, 2009; XXIèmes Rencontres de Blois Windows on the Universe, Blois, France, 2009; XXXIX International Symposium on Multiparticle Dynamics "Gold Sands", Gomel Region, Belarus, 2009 [66]; 5-th International Workshop on Low energy neutrino physics, Reims, France, 2009; session of Nuclear Physics of RAS, ”Physics of fundamental interactions”, Moscow, 2009 and 2011; the Xth International Conference on Heavy Quarks and Leptons, CNR and Sapienza, Università di Roma, Frascati, Italy, 2010 [67]; XV Lomonosov Conference on Elementary Particle Physics, Moscow, 2011; CTP: Speakable in quantum mechanics: atomic, nuclear and subnuclear physics tests, Italy, 2011; 12th and 13th International Conference on Topics in Astroparticle and Underground Physics, 2011, Munich, Germany and 2013, USA [68, 69]; Nonaccelerating New Physics workshop, 2013, Valdai, Russia; International Workshop on Prospects in Particle Physics, 2014, Valdai, Russia.

4.1.7 Finances

Major sources and amount of finances requested and obtained in 2013 for travel expenses are summarized in Tab. 4.5

Source	Amount requested (k$)	Amount obtained (k$)
1099	10	10
grant of Ministry of Education	6	6

Table 4.5: Major sources and amount of finances requested and obtained for travel expenses

References

[1] A. M. Serenelli, W. C. Haxton, and C. Peña-Garay. “Solar Models with Accretion. I. Application to the Solar Abundance Problem”. In: *Astrohpys.Journal.* 743, 24 (Dec. 2011), p. 24. arXiv: 1104.1639 [astro-ph.SR].

[2] N. Grevesse and A. J. Sauval. “Standard Solar Composition”. In: *Space Sci.Rev.* 85 (May 1998), pp. 161–174.

[3] Martin Asplund et al. “The Chemical Composition of the Sun”. In: Annual Review of Astronomy and Astrophysics 47 (2009). Ed. by Blandford, R and Kormendy, J and VanDishoeck, E, 481–522. ISSN: 0066-4146.

[4] G. Bellini et al. “First evidence of pep solar neutrinos by direct detection in Borexino”. In: *Phys.Rev.Lett.* 108 (2012), p. 051302. arXiv: 1110.3230 [hep-ex].

[5] G. Bellini et al. “Measurement of the solar 8B neutrino rate with a liquid scintillator target and 3 MeV energy threshold in the Borexino detector”. In: *Phys.Rev.* D82 (2010), p. 033006. arXiv: 0808.2868 [astro-ph].

[6] G. Bellini et al. “Measurement of geo-neutrinos from 1353 days of Borexino”. In: *Phys.Lett.* B722 (2013), pp. 295–300. arXiv: 1303.2571 [hep-ex].

[7] Hisakazu Minakata and Carlos Pena-Garay. "Solar Neutrino Observables Sensitive to Matter Effects". In: *Adv.High Energy Phys.* 2012 (2012), p. 349686. arXiv: 1009.4869 [hep-ph].

[8] SanjibKumar Agarwalla, Francesco Lombardi, and Tatsu Takeuchi. "Constraining non-standard interactions of the neutrino with Borexino". English. In: *Journal of High Energy Physics* 2012.12 (2012), pp. 1–21. URL: http://dx.doi.org/10.1007/JHEP12(2012)079.

[9] C. Arpesella et al. "Direct Measurement of the Be-7 Solar Neutrino Flux with 192 Days of Borexino Data". In: *Phys.Rev.Lett.* 101 (2008), p. 091302. arXiv: 0805.3843 [astro-ph].

[10] G. Bellini et al. "SOX: Short distance neutrino Oscillations with BoreXino". In: *JHEP* 1308 (2013), p. 038. arXiv: 1304.7721 [physics.ins-det].

[11] Michel Cribier et al. "Proposed Search for a Fourth Neutrino with a PBq Antineutrino Source". In: *Phys. Rev. Lett.* 107 (20 Nov. 2011), p. 201801. URL: http://link.aps.org/doi/10.1103/PhysRevLett.107.201801.

[12] G. Bellini et al. "Precision measurement of the 7Be solar neutrino interaction rate in Borexino". In: *Phys.Rev.Lett.* 107 (2011), p. 141302. arXiv: 1104.1816 [hep-ex].

[13] W Hampel et al. "Final results of the 51Cr neutrino source experiments in {GALLEX}". In: *Physics Letters B* 420.1–2 (1998), pp. 114–126. ISSN: 0370-2693. URL: http://www.sciencedirect.com/science/article/pii/S0370269397015621.

[14] J.N. Abdurashitov et al. "Measurement of the response of the Russian-American gallium experiment to neutrinos from a Cr-51 source". In: *Phys.Rev.* C59 (1999), pp. 2246–2263. arXiv: hep-ph/9803418 [hep-ph].

[15] ANTONIO PALAZZO. "PHENOMENOLOGY OF LIGHT STERILE NEUTRINOS: A BRIEF REVIEW". In: *Modern Physics Letters A* 28.07 (2013), p. 1330004. eprint: http://www.worldscientific.com/doi/pdf/10.1142/S0217732313300048. URL: http://www.worldscientific.com/doi/abs/10.1142/S0217732313300048.

[16] G. Alimonti et al. "Ultra-low background measurements in a large volume underground detector". In: *Astropart.Phys.* 8 (1998), pp. 141–157.

[17] G. Alimonti et al. "Measurement of the C-14 abundance in a low-background liquid scintillator". In: *Phys.Lett.* B422 (1998), pp. 349–358.

[18] C. Arpesella et al. "Measurements of extremely low radioactivity levels in BOREXINO". In: *Astropart.Phys.* 18 (2002), pp. 1–25. arXiv: hep-ex/0109031 [hep-ex].

[19] G. Alimonti et al. "Science and technology of BOREXINO: A Real time detector for low-energy solar neutrinos". In: *Astropart.Phys.* 16 (2002), pp. 205–234. arXiv: hep-ex/0012030 [hep-ex].

[20] G. Alimonti et al. "The Borexino detector at the Laboratori Nazionali del Gran Sasso". In: *Nucl.Instrum.Meth.* A600 (2009), pp. 568–593. arXiv: 0806.2400 [physics.ins-det].

[21] G. Ranucci et al. “Characterization and magnetic shielding of the large cathode area PMTs used for the light detection system of the prototype of the solar neutrino experiment Borexino”. In: *Nucl.Instrum.Meth.* A337 (1993), pp. 211–220.

[22] A. Brigatti et al. “The Photomultiplier tube testing facility for the Borexino experiment at LNGS”. In: *Nucl.Instrum.Meth.* A537 (2005), pp. 521–536. arXiv: physics/0406106 [physics].

[23] R. Dossi et al. “Methods for precise photoelectron counting with photomultipliers”. In: *Nucl.Instrum.Meth.* A451 (2000), pp. 623–637.

[24] O. Yu. Smirnov, P. Lombardi, and G. Ranucci. “Precision measurements of timing characteristics of the 8’ ETL9351 series photomultiplier”. In: *Instrum.Exp.Tech.* 47 (2004), pp. 69–79. arXiv: physics/0403029 [physics].

[25] O. Yu. Smirnov. “Setting of the predefined multiplier gain of a photomultiplier”. In: *Instrum.Exp.Tech.* 45 (2002), pp. 363–370.

[26] B. Caccianiga et al. “A multiplexed optical-fiber system for the PMT calibration of the Borexino experiment”. In: *Nucl.Instrum.Meth.* A496 (2003), pp. 353–361.

[27] A. Ianni et al. “The Measurements of 2200 ETL9351 type photomultipliers for the Borexino experiment with the photomultiplier testing facility at LNGS”. In: *Nucl. Instrum. Meth.* A537 (2005), pp. 683–697. arXiv: physics/0406138 [physics].

[28] H.O. Back et al. “Search for electron decay mode e –> gamma + nu with prototype of Borexino detector”. In: *Phys.Lett.* B525 (2002), pp. 29–40.

[29] H.O. Back et al. “Study of the neutrino electromagnetic properties with prototype of Borexino detector”. In: *Phys.Lett.* B563 (2003), pp. 35–47.

[30] A.V. Derbin and O. Yu. Smirnov. “Search for neutrino radiative decay with a prototype Borexino detector”. In: *JETP Lett.* 76 (2002), pp. 409–413.

[31] H.O. Back et al. “New limits on nucleon decays into invisible channels with the BOREXINO counting test facility”. In: *Phys.Lett.* B563 (2003), pp. 23–34. arXiv: hep-ex/0302002 [hep-ex].

[32] H.O. Back et al. “New experimental limits on heavy neutrino mixing in B-8 decay obtained with the Borexino Counting Test Facility”. In: *JETP Lett.* 78 (2003), pp. 261–266.

[33] H.O. Back et al. “New experimental limits on violations of the Pauli exclusion principle obtained with the Borexino counting test facility”. In: *Eur.Phys.J.* C37 (2004), pp. 421–431. arXiv: hep-ph/0406252 [hep-ph].

[34] M. Balata et al. “Search for electron antineutrino interactions with the Borexino counting test facility at Gran Sasso”. In: *Eur.Phys.J.* C47 (2006), pp. 21–30. arXiv: hep-ex/0602027 [hep-ex].

[35] G. Bellini et al. “Search for solar axions emitted in the M1-transition of Li-7* with Borexino CTF”. In: *Eur.Phys.J.* C54 (2008), pp. 61–72.

[36] A.V. Derbin, O. Yu. Smirnov, and O.A. Zaimidoroga. "Nonaccelerator experiments on the search for rare processes with low-background detectors". In: *Phys.Part.Nucl.* 36 (2005), pp. 314–339.

[37] Gianni Fiorentini et al. "Nuclear physics for geo-neutrino studies". In: *Phys.Rev.* C81 (2010), p. 034602. arXiv: 0908.3433 [nucl-ex].

[38] G. Bellini et al. "Lifetime measurements of 214Po and 212Po with the CTF liquid scintillator detector at LNGS". In: *Eur.Phys.J.* A49 (2013), p. 92. arXiv: 1212.1332 [nucl-ex].

[39] O. Yu. Smirnov. "Energy and spatial resolution of a large-volume liquid-scintillator detector". In: *Instrum.Exp.Tech.* 46 (2003), pp. 327–344.

[40] O. Ju. Smirnov. "An Approximation of the ideal scintillation detector line shape with generalized gamma distribution". In: *Nucl.Instrum.Meth.* A595 (2008), pp. 410–418. arXiv: 0705.3225 [physics.ins-det].

[41] O. Yu. Smirnov, O.A. Zaimidoroga, and A.V. Derbin. "Search for solar pp neutrinos with an upgrade of CTF detector". In: *Phys.Atom.Nucl.* 66 (2003), pp. 712–723.

[42] A.V. Derbin, O. Yu. Smirnov, and O.A. Zaimidoroga. "On the possiblity of detecting solar pp neutrino with a large volume liquid organic scintillator detector". In: *Phys.Atom.Nucl.* 67 (2004), pp. 2066–2072. arXiv: physics/0403030 [physics].

[43] H.O. Back et al. "Pulse-shape discrimination with the counting test facility". In: *Nucl.Instrum.Meth.* A584 (2008), pp. 98–113. arXiv: 0705.0239 [physics.ins-det].

[44] C. Arpesella et al. "First real time detection of Be-7 solar neutrinos by Borexino". In: *Phys.Lett.* B658 (2008), pp. 101–108. arXiv: 0708.2251 [astro-ph].

[45] H.O. Back et al. "Study of phenylxylylethane (PXE) as scintillator for low energy neutrino experiments". In: *Nucl.Instrum.Meth.* A585 (2008), pp. 48–60.

[46] G. Bellini et al. "New experimental limits on the Pauli forbidden transitions in C-12 nuclei obtained with 485 days Borexino data". In: *Phys.Rev.* C81 (2010), p. 034317. arXiv: 0911.0548 [hep-ex].

[47] G. Alimonti et al. "The liquid handling systems for the Borexino solar neutrino detector". In: *Nucl.Instrum.Meth.* A609 (2009), pp. 58–78.

[48] G. Bellini et al. "Observation of Geo-Neutrinos". In: *Phys.Lett.* B687 (2010), pp. 299–304. arXiv: 1003.0284 [hep-ex].

[49] G. Bellini et al. "Study of solar and other unknown anti-neutrino fluxes with Borexino at LNGS". In: *Phys.Lett.* B696 (2011), pp. 191–196. arXiv: 1010.0029 [hep-ex].

[50] G. Bellini et al. "Muon and Cosmogenic Neutron Detection in Borexino". In: *JINST* 6 (2011), P05005. arXiv: 1101.3101 [physics.ins-det].

[51] G. Bellini et al. "Absence of day–night asymmetry of 862 keV ^{7}Be solar neutrino rate in Borexino and MSW oscillation parameters". In: *Phys.Lett.* B707 (2012), pp. 22–26. arXiv: 1104.2150 [hep-ex].

[52] G. Bellini et al. "Cosmic-muon flux and annual modulation in Borexino at 3800 m water-equivalent depth". In: *JCAP* 1205 (2012), p. 015. arXiv: 1202.6403 [hep-ex].

[53] G. Bellini et al. "Search for Solar Axions Produced in $p(d, {}^3\mathrm{He})\mathrm{A}$ Reaction with Borexino Detector". In: *Phys.Rev.* D85 (2012), p. 092003. arXiv: 1203.6258 [hep-ex].

[54] T. Alexander et al. "Light yield in DarkSide-10: A prototype two-phase argon TPC for dark matter searches". In: *Astropart.Phys.* 49 (2013), pp. 44–51. arXiv: 1204.6218 [astro-ph.IM].

[55] H. Back et al. "Borexino calibrations: Hardware, Methods, and Results". In: *JINST* 7 (2012), P10018. arXiv: 1207.4816 [physics.ins-det].

[56] P. Alvarez Sanchez et al. "Measurement of CNGS muon neutrino speed with Borexino". In: *Phys.Lett.* B716 (2012), pp. 401–405. arXiv: 1207.6860 [hep-ex].

[57] I.R. Barabanov et al. "A Nd-loaded liquid organic scintillator for the experiment aimed at measuring double beta decay". In: *Instrum.Exp.Tech.* 55 (2012), pp. 545–550.

[58] O. Yu. Smirnov. "Nonaccelerator neutrino physics". In: *Phys. Part. Nucl. Lett.* 9 (2012), pp. 696–732.

[59] G. Bellini et al. "Cosmogenic Backgrounds in Borexino at 3800 m water-equivalent depth". In: *JCAP* 1308 (2013), p. 049. arXiv: 1304.7381 [physics.ins-det].

[60] G. Bellini et al. "Final results of Borexino Phase-I on low energy solar neutrino spectroscopy". In: (2013). arXiv: 1308.0443 [hep-ex].

[61] G. Bellini et al. "New limits on heavy sterile neutrino mixing in ${}^8\mathrm{B}$-decay obtained with the Borexino detector". In: *Phys.Rev.* D88 (2013), p. 072010. arXiv: 1311.5347 [hep-ex].

[62] T. Alexander et al. "DarkSide search for dark matter". In: *JINST* 8 (2013), p. C11021.

[63] O. Yu. Smirnov. "Topical problems in low-energy neutrino physics". In: *Phys. Part. Nucl. Lett.* 10 (2013), pp. 751–756.

[64] O. Smirnov. *Study of ultralow-background of natural radioactivity with a prototype of liquid scintillator Solar neutrino detector*. Ed. by JINR. Dubna. 2001, p. 180.

[65] O. Smirnov et al. "The first year of Borexino". In: *Eilat 2008. Particles and nuclei (PANIC08), pp.788-790*. 2008.

[66] O. Smirnov. "Borexino: Real-time sub-MeV solar neutrino detection and beyond". In: *Nonlin.Phenom.Complex Syst.* 12 (2009), pp. 448–452.

[67] Oleg Smirnov. "Geoneutrino: Models and data". In: *PoS* HQL2010 (2011), p. 061.

[68] G. Bellini et al. "Nuclear physics inputs needed for geo-neutrino studies". In: *J. Phys. Conf. Ser.* 120 (2008), p. 052007. arXiv: 0712.0298 [hep-ph].

[69] Oleg Smirnov. "Antineutrino studies with Borexino detector". In: *J. Phys. Conf. Ser.* 375 (2012), p. 042033.

Chapter 5

νGeN Project

Editors: V.B.Brudanin, E.A.Yakushev

Project Title

νGeN: Experiment at the Kalininskaya Nuclear Power Plant for Detection Coherent **N**eutrino – **Ge N**ucleus Elastic Scattering.

Project Leaders

- V.B.Brudanin

Abstract

Recent Neutrino and Dark Matter search experiments revolutionized detection of rear events, and rear events with low energies, in particular. Experiments achieved sensitivities on the level of several events per hundreds kg of detector material per day with energy thresholds below of 1 keV. This opens a new unique possibility for experimental detection of neutrino-nucleus coherent scattering that was considered to be impossible thus far.

The present project uses low threshold high-puruty Ge-detectors (**HPGe**) developed by JINR (Dubna) for creation of a setup designated for first observation of neutrino coherent scattering on Ge. As a powerful neutrino source the experiment will use antineutrinos from one of the power-generating units of the Kalininskaya nuclear power plant (**KNPP**).

The coherent neutrino scattering will be observed using a differential method that compares the spectra measured at the reactor operation and shut-down periods. For a setup placed at a 10 m distance from the center of reactor core and with an energy threshold of 300 eV up to tens of events of the neutrino coherent scattering on Ge are expected to be detected per day in the constructed setup with 4 HPGe low-energy-threshold detectors (450 grams each). The setup sensitivity will be further increased by using new detectors with total mass up to 5 kg.

Due to unique prospects of the HPGe detectors together with unique antineutrino fluxes available at the KNPP the νGeN Project has a very high probability to observe for the first time the coherent neutrino-nucleus scattering.

keywords: Reactor antineutrinos, Coherent neutrino-nucleus scattering, Neutrino detector, HPGe, Low-background measurements

Project Members From JINR

V. Belov, V. Brudanin, V. Egorov, D. Filosofov, M. Fomina, Yu. Gurov, A. Lubashevskiy, D. Medvedev, I. Rozova, S. Rozov, V. Timkin, , E. Yakushev, I. Zhitnikov

List of Participating Countries and Institutions

Laboratory of Nuclear Problems, JINR, Dubna, Russia; National Research Nuclear University "MEPhI", Moscow, Russia

5.1 Project Description

5.1.1 Fundamental Scientific Problem Addressed by the Project

Detection of low energy neutrinos (with energy below 50 MeV) via coherent scattering off a nuclear target $\nu + A \to \nu + A$ (Fig. 5.1) remains a sought-after goal in modern neutrino physics. This mode of neutrino interaction with matter is well allowed in the Standard

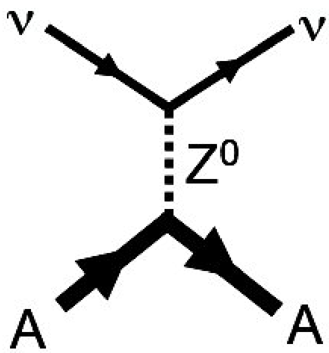

Figure 5.1: The coherent neutral current neutrino-nucleus elastic scattering.

Model and its cross section is enhanced by several orders of magnitude being proportional to the number of nuclear target neutrons squared, N^2: [1, 2]:

$$\frac{d\sigma}{d\Omega} \simeq \frac{G_{\rm F}^2}{16\pi^2} E_\nu^2 (1 + \cos\theta) N^2 F^2(Q^2).$$

Here, E_ν is the neutrino energy, θ is the scattering angle, Q is the momentum transfer ($Q^2 = 2E_\nu^2(1-\cos\theta)$), $G_{\rm F}$ is Fermi constant and $F(Q^2)$ is the elastic nuclear form-factor, which strongly vanishes the coherent effect with Q increase ($F(Q^2) \propto \mathrm{e}^{-R^2Q^2/6}$, R is the nucleus radius).

In the coherent process, due to the small momentum transfer Q the neutrino interacts in the same phase (similtaneously) with all nuclear nucleons. Coherent scattering occurs by exchange of Z^0-boson between neutrino and all nucleons of a nucleus and does not depend on the neutrino flavor as shown in Fig. 5.1.

The coherent effect is especially important from practical point of view as usually massive detectors are required for neutrino detection in this energy region due to small probability of interaction via all other channels. The large coherent scattering enhancement of the cross-section results in expected nuclear recoil rates at a level of 10 events per kilogram of matter per day for antineutrinos produced by a typical industrial reactor and a detector displaced by ~10 m from the reactor core. As a result one can significantly reduce the size and mass of the relevant neutrino detector. Therefore, developing a technology for detection of neutrinos through the coherent scattering is one of the priorities for neutrino physics and would help to develop neutrino based applied research in future (for example, non-intrusive monitoring of nuclear reactors). In particular, any detection of neutrinos with energy in the MeV region from supernovae explosion (**SN**) will be very important for our understanding of the SN evolution.

The aim of this project is the first observation of the coherent scattering of reactor (anti)neutrinos off Ge nuclei.

As noted above the coherent scattering cross-section is proportional to the square of the number of neutrons in the nucleus. This process was first described about 40 years ago by D.Z. Freedman [1]. Later it was regularly discussed, but it has yet remained undetected. This is because the only signature of the process is a nuclear recoil. Any detection of recoiled nuclei due to the coherent neutrino scattering is an extremely challenging task, mainly due to the tiny energy transfer from neutrino to the nucleus (E_A in Fig. 5.2).

The recoil energy for Ge nuclei from reactor antineutrinos, for instance, is $\lesssim 3$ keV. Moreover, only a small fraction (about ~20%) of this kinetic energy of the recoiled nucleus is converted into energy of ionizing radiation, i.e. detected ionization will be $\lesssim$600 eV. Reactor neutrinos are referred because among all artificial neutrino sources nuclear power reactors offer the largest (anti)neutrino flux. Energies of neutrinos produced in reactors can be below of 50 MeV, thus reactor neutrinos are able to interact coherently with atomic nuclei.

The interest in the observation of coherent scattering has many motivations. The process of coherent neutrino scattering on nuclei was very important in the early Universe and is crucial for star evolution. It is expected that the neutrino coherent scattering is a quite sensitive test for non-standard neutrino interactions, and could be a probe of new physics. In view of recent developments in neutrino physics, the building of a detector for search for coherent neutrino scattering becomes even more important. This is because the neutral-current interaction is independent from known neutrino types. Therefore, observation of neutrino oscillations with a neutrino coherent scattering detector would be evidence for the

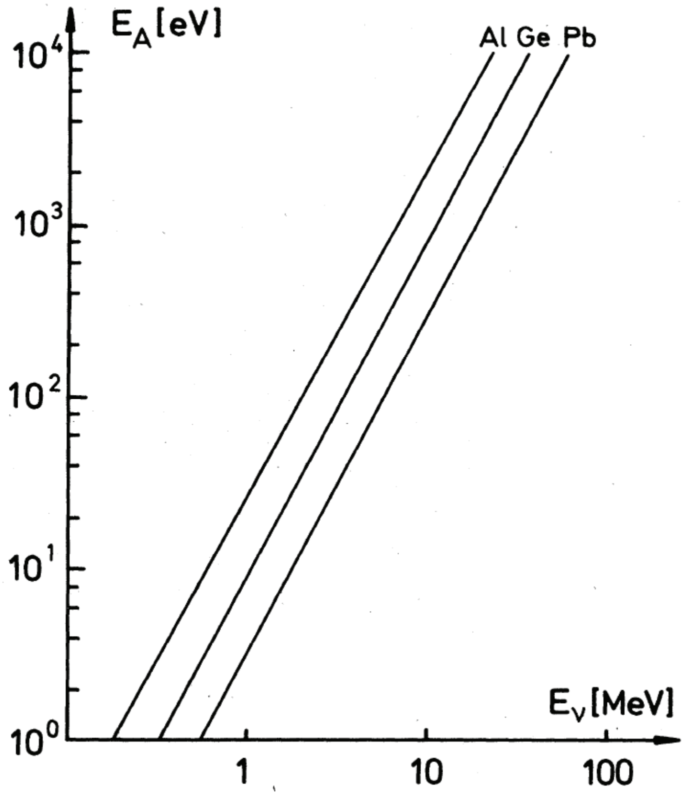

Figure 5.2: Average recoil energy, E_A, for various nuclei as a function of neutrino energy, from [2].

existence of sterile neutrino(s). Additionally, precise knowledge of the cross-section for this process is critically important for the next generation of dark matter search experiments where the interaction of solar neutrinos through this channel can become a background for direct WIMP observation.

Therefore, the detection of the coherent neutrino scattering process is a very important problem for modern particle physics. Thus, creation of an experimental setup that will be able to detect low-energy events of neutrino-nucleus coherent scattering will be a breakthrough in neutrino physics.

5.1.2 Specific Project Objectives and Expected Results

About 10 years ago CANBERRA (USA) was able to produce point contact germanium detectors with a mass above 100 g working with energy threshold below of 1 keV. The detectors were immediately considered as a possible instrument for detection of coherent neutrino scattering. These detectors were used by CoGeNT [3, 4] and C4 [5] experiments and are mainly known for the intriguing results (considered as 7 GeV/c^2 WIMP signals) obtained with them during the background study in the underground laboratory. The position available for measurements in the above-mentioned experiments is at a distance of 25 m from a commercial reactor with shielding from cosmic rays below 30 m.w.e. (the set-up is located on the side from the reactor) are not allowed undoubted detection of neutrino coherent scattering.

In this project the neutrino coherent scattering off germanium nuclei will be searched for with unique low-threshold germanium detectors developed by JINR (Dubna). The P-type point contact detectors with masses of 240 and 450 grams were produced by JINR group. The detector's design has several improvements with respect to the CANBERRA detectors. The JINR detectors have guard rings for noise suppression and a rounded shape of the Ge crystals, which reduces the number of surface events. These detectors will be placed into a low-background, low-noise setup giving an energy threshold at $\sim$300 eV. The existing possibility to perform the experiment at the **Kalininskaya nuclear power plant** provides us with an antineutrino flux greater than $5.4{\cdot}10^{13}$ per cm^2 each sec. This is our significant advantage to any other experiment and opens a new unique possibility to perform, during next 3-5 years, the first experimental search of neutrino-nucleus coherent scattering with a sensitivity level sufficient for it observation.

In addition, we will work on the creation and investigation of new low-threshold semiconductor detectors made from cadmium-zinc-tellurium (**CZT**), that exhibit high stopping power, low thermal noise, usability at room temperature; and detectors made from such a promising semiconductor as silicon carbide (**SiC**). The aim of this work is in the developing and building of new detectors with energy threshold 200 eV and below. After first detecting coherent scattering such detectors will be used for further studying of the process in detail.

The νGeN project basis is: low-threshold germanium detectors (with total mass of Ge up to $\sim$5 kg); the low-background setup placed in the proximity of # 3 power generated unit of the KNPP, with highest available neutrino flux greater than $5.4{\cdot}10^{13}$ cm^{-2} sec^{-1}; the background on the level of 0.5 events/kg/keV/day; accumulated experience in low-background neutrinoless double beta decay search experiments as well as in low-threshold experiments at the KNPP designated to search for neutrino magnetic moment.

Expected results for this project are the detection of neutrino-nucleus coherent scattering and measurement of the cross-section for the coherent scattering of Ge nuclei. It is expected to achieve these results during the next 3–5 years with the experiment at the KNPP. Undoubtedly these results will be of world-class level.

It must be pointed out that in case of successful accomplishment of the coherent detection experiment, the setup created will be extremely useful for investigation of a number of interesting applications. For example: sensitive search for neutrino magnetic moment or direct search for light WIMPs. In addition, the detector for the neutrino coherent scattering may have the direct practical application: technical difficulties with low threshold and backgrounds will be resolved, neutrino study with detectors of moderate sizes will be possible thanks to the high probability of the coherent scattering.

Usually the mass of neutrino detectors range from tons to thousands of tons. An increase in the probability of the process by thousand times enables the use of detectors with masses staring from a few kilograms. Thus, one of the possible applications of detectors sensitive to coherent scattering will be the task of monitoring of nuclear reactors with low-mass neutrino detectors. In the project semiconductor SiC (silicon carbide) and

CZT (cadmium-zinc-tellurium) detectors will be investigated with the aim of further energy threshold reduction, down to 200 eV and below. This opens up the prospect of not only detecting coherent neutrino scattering on nuclei, but also studying the process in detail.

5.1.3 Basic Methods and Approaches Used in the Project

To achieve the desired aim of coherent neutrino detection we are going to use large HPGe detectors with modified p-electrodes. Thanks to the small size ($\sim$5 mm) of the p-contact the total capacitance of such detectors is below of 1 pF. Because of this, energy thresholds lower than 500 eV can be reached. For confirmation of coherent scattering signal the experiment will use different methods of measurements. Energy spectra received with working ("on") and stopped ("off") reactor will be compared. Apart from this, in long periods of working reactor the measurements will be conducted at several points located at different distances (from 10 to 12 m) from the reactor. This will provide substantial data about coherent neutrino signal and the background. The device allowing 2.5 m vertical lifting of the total setup, including cryostat with detectors and shielding, is already available at the experimental site at the Kalininskaya nuclear power plant (KNPP).

A low background environment for the set-up will be created with the knowledge of building complex shieldings (active and passive) accumulated during neutrino-related and dark matter search experiments with our participation. Members of our group have many years experience in the building of low background multi-detector setups with the aim of direct WIMP detection, search for neutrinoless double beta decay, etc.

Considering the experimental task two main questions must be answered: 1) expected number of events in energy region of interest (**ROI**); 2) the background level in the ROI.

Let us first estimate the number of expected events. This number will be result of: cross-section of coherent neutrino scattering, which depends on the neutrino energy; neutrino energy spectrum and flux; detector mass and duration of measurements.

Macroscopic cross-section of neutrino coherent scattering for 1 kg of a material can be expressed as: $2.5{\cdot}10^{-18}\,N^2/A{\cdot}(E/1\,\mathrm{MeV})^2$ cm^2/kg [2], where N is the number of neutrons in material's nuclei, A is the atomic number, E is the neutrino energy in MeV. For germanium the factor $N^2/A = 22.7$, thus the cross section will be $5.7 \cdot 10^{-17} \cdot (E/1$ MeV) cm^2/kg.

In the beginning stage of the experiment for the detection of coherent scattering 4 detectors with mass of 450 grams each will be used, i.e. total mass of detectors will be 1.8 kg. The energy spectrum of the reactor neutrinos and their flux is known with relatively high (several percent) accuracy. Taking into account that detectors could be placed on a minimal distance from the reactor core equal to about 10 meters, up to 10 events of coherent neutrino scattering can be detected above an energy threshold 350 eV [3]. The exact number depends on the energy resolution at threshold. Our aim is to run detectors with stable energy threshold no less than 300 eV. The estimation of event numbers for a threshold 350 eV is conservative, and takes into account uncertainties with detector response at threshold.

For estimation of expected background, we can use data received in the GEMMA experiment [6]. The modified shield of this experiment will be used for coherent neutrino detection. In the GEMMA experiment the background level for energies at several keV was found to be 2.5 cpd (counts per day) per 1 keV. Point contact detectors have an advantage in comparison with traditional HPGe detectors due to thick ($\sim$ 1 mm) external lithium layer (the only exception where such layer is not present is the point contact). This layer provides additional suppression for external low energy background. Our estimation for possible backgrounds in 1 kg of point contact detectors is 0.5 cpd per 1 keV. The main source of background is cosmogenic activation. The most intensive one is decay of ^{71}Ge, which could be up to 100 decays per 1 kgd. The decay will mainly manifest as a 10.4 keV line (in case of K EC) or with 10 times lower probability as $\sim$1.3 keV lines (in case of EC from L-subshells). Both these lines will not cause a problem for the much lower energy region around 0.5 keV. Some other radioactive isotopes of cosmogenic origin in Ge are: ^{49}V, ^{51}Cr, ^{54}Mn, ^{55}Fe, ^{56,57,58}Co, ^{56}Ni. Their EC activities (energy lines 4.97–7.71 keV) are < 5 events per 1 kgd [7]. For L EC, with energies 0.45–0.93 keV, total activity is expected to be < 1 events per kgd. Further reduction of this background is possible with detectors placed in a deep underground environment. Such a possibility is available for our experiment.

Thereby, taking into account estimated levels of expected background given above and the coherent scattering signals, the ratio of signal/background should be above 1 (for energy threshold 300 eV). This means that observation of coherent neutrino scattering of germanium nuclei in our experiment will be possible.

5.1.4 Detector and Experiment Description

The technology and methods developed at JINR for construction of low energy threshold detectors described in Ref. [8]. The proposed experiment for coherent neutrino detection will be based on:

1. Our expertise in the production of low-threshold HPGe detectors.

2. Four point contact detectors already built at JINR (Dubna) (Fig. 5.3) with total mass 1.8 kg.

3. Experimentally achieved energy threshold of 350 eV (Fig. 5.4) for the above detectors.

4. The cryostat built by Baltic Scientific Instruments (**BSI**) in which 4 above detectors were implemented. The setup has also integrated low noise FET and preamplifiers. Low radioactive materials were selected for the cryostat. Additionally, presently complex work has been made to study different parameters of the constructed setup, including the methods of calibration of the energy scale and the fiducial volume for the low energy region. Parameters of the setup were studied in the deep underground laboratory LSM (the depth is 4800 m.w.e.) using extremely low background shield (Fig. 5.5) made from layers of low radioactive copper (located during last 10 years underground); the roman lead; and selected low radioactive lead. Internal part of the shield was continuously purified with radon-free air (radon level < 10 mBq/m^3).

5. In 2013 BSI made (by our order and with our participation) one more additional germanium detector with point contact (Fig. 5.6). The detector has been made from

Figure 5.3: Photo of 4 HPGe point contact detectors built at JINR (Dubna). Each detector is 450 g.

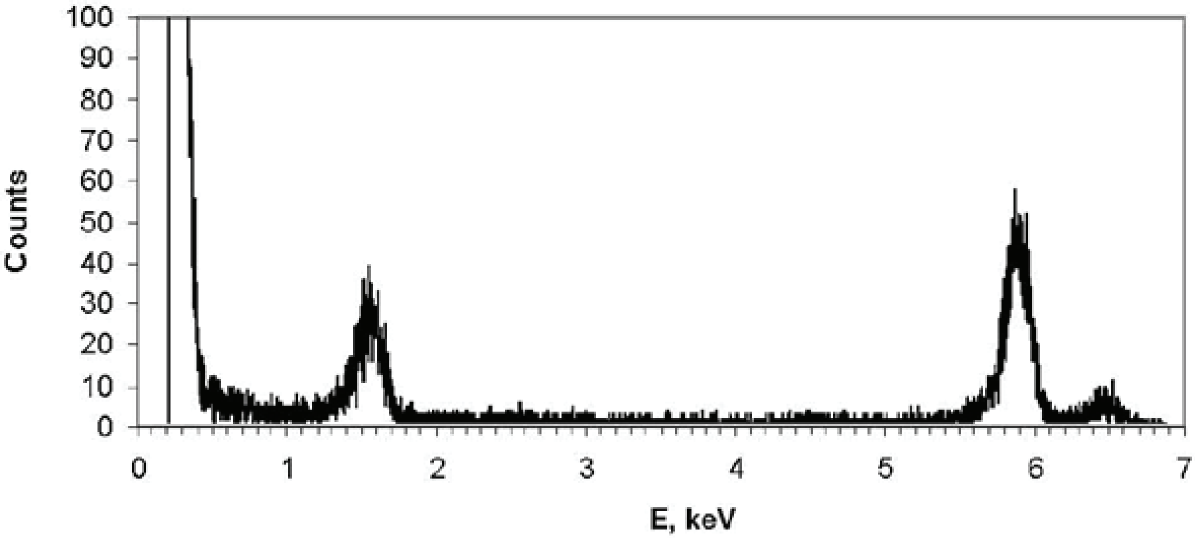

Figure 5.4: Calibration energy spectrum (^{55}Fe, Al), received at Dubna with HPGe point contact detector. Energy threshold achieved during the measurements is 350 eV. Energy resolution (FWHM) at 5.9 keV is 177 eV.

Figure 5.5: The low background cryostat built by BSI. Left: internal part; center: assembled; right: test of low radioactive shield at LSM underground site.

cleanest available germanium. In the present time tests with the detector are ongoing, after which the detector will be implemented in the coherent neutrino detection setup. The main reason to make additional detector(s) at BSI is connected with the further increase of the sensitivity of the setup (the plan is to have up to 10 detectors with total mass up to 5 kg). Additionally the detector produced by slightly different technology could reveal an unexpected effects due to different parities of germanium crystals.

6. The main reason why our experiment will be capable of detecting coherent neutrino scattering is the possibility to perform measurements on the KNPP in the region where neutrino flux is greater of $5.4{\cdot}10^{13}$ per cm^2 per sec. This neutrino intensity is about 10 times higher with respect to that available for other groups worldwide. Furthermore the available region for measurement is located just under the reactor, which provides about 70 m.w.e. shielding from cosmic rays. The shield of our setup from γ- and neutrons will be based on the shield of the GEMMA experiment. The shield will be improved with active muon veto system made from plastic scintillator panels and with active anti-compton shield made from 12 NaI(Tl) detectors.

7. We have more than 15 years experience in development and building of low threshold and low background germanium detectors.

8. Our group has extensive experience in precise spectroscopy using all types of detectors, in particular with semiconductors and with scintillators; We have a plastic scinitillator production line.

9. Members of our team participate in a number of low background experiments in several underground laboratories (Baksan, LSM, LNGS, Kamioka). We have notable yield in world leading experiments searching for neutrinoless double beta decay (NEMO-2, NEMO-3, GERDA). For instance, we designed and built active μ-veto systems for all

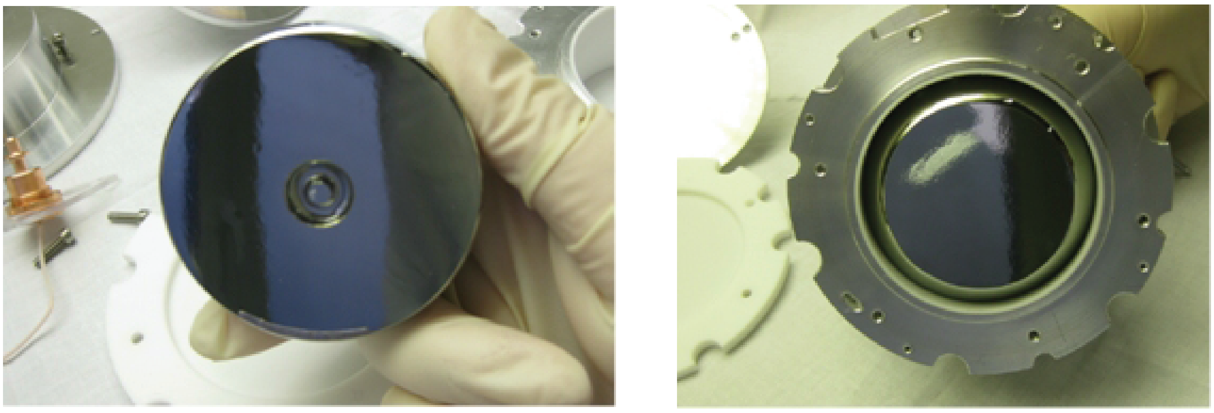

Figure 5.6: The detector with point contact created with JINR participation and using of JINR technology by Baltic Scientific Instruments. Left — without holder, right — the detector in the low radioactivity holder.

these 3 experiments. We participate in building, commissioning and running of the EDELWEISS direct dark matter search experiment. We built unique multi-detector low-background HPGe assembly for search of new type of radioactivity, double electron capture (TGV-1 and TGV-2 experiments).

10. The group has experience in building of complex models and MC simulations for low background experiments, as well in the data analysis for such experiments;

11. The radiochemistry group of DLNP provides the possibility to use radioactive calibration sources with almost any desired type of radioactivity, energy spectrum, and intensity.

12. The most important point is that we already have unique experience in conducting neutrino measurements on the Kalininskaya nuclear power plant.

In conclusion, all items listed above — the low-threshold germanium detectors (with total mass of Ge up to 5 kg); the tested low-background setup placed in the proximity to #3 power generated unit of the Kalininskaya nuclear power plant, with highest available neutrino flux greater than $5.4 \cdot 10^{13}$ cm^{-2} sec^{-1}; the background on the level of 0.5 events/kg/keV/day; the accumulated experience in low-background neutrinoless double beta decay search experiments, as well as in low-threshold experiments at the KNPP designated to search for neutrino magnetic moment; available man power — all these achievements **contribute coherently** into this unique scientific project, and give us a confidence in the achievement of its goals.

References

[1] Daniel Z. Freedman. “Coherent neutrino nucleus scattering as a probe of the weak neutral current”. In: *Phys.Rev.* D9 (1974), pp. 1389–1392.

[2] A. Drukier and Leo Stodolsky. “Principles and Applications of a Neutral Current Detector for Neutrino Physics and Astronomy”. In: *Phys.Rev.* D30 (1984), p. 2295.

[3] P.S. Barbeau, J.I. Collar, and O. Tench. “Large-Mass Ultra-Low Noise Germanium Detectors: Performance and Applications in Neutrino and Astroparticle Physics”. In: *JCAP* 0709 (2007), p. 009. arXiv: nucl-ex/0701012 [nucl-ex].

[4] C.E. Aalseth et al. “CoGeNT: A Search for Low-Mass Dark Matter using p-type Point Contact Germanium Detectors”. In: *Phys.Rev.* D88.1 (2013), p. 012002. arXiv: 1208.5737 [astro-ph.CO].

[5] R.M. Bonicalzi et al. “The C-4 Dark Matter Experiment”. In: *Nucl.Instrum.Meth.* A712 (2013), pp. 27–33. arXiv: 1210.6282 [astro-ph.CO].

[6] A.G. Beda et al. “Gemma experiment: The results of neutrino magnetic moment search”. In: *Phys.Part.Nucl.Lett.* 10 (2013), pp. 139–143.

[7] C.E. Aalseth et al. “Search for an Annual Modulation in a P-type Point Contact Germanium Dark Matter Detector”. In: *Phys.Rev.Lett.* 107 (2011), p. 141301. arXiv: 1106.0650 [astro-ph.CO].

[8] V.B. Brudanin et al. “Large Volume HPGe Detectors for Rare Events with a Low Deposited Energy”. In: *Instruments and Experimental Techniques* 54 (2011), pp. 470–472.

Chapter 6

DANSS Experiment

Editors: V.B.Brudanin, V.G.Egorov

Project Title

Detector of the Reactor **AntiN**eutrino based on **S**olid **S**cintillator

Project Leaders

- JINR: V.B. Brudanin, V.G. Egorov
- ITEP: M.V. Danilov, A.S. Starostin

Abstract

The DANSS project is aimed at creating a relatively compact neutrino spectrometer which does not contain any flammable or other dangerous liquids and may therefore be located very close to the core of an industrial power reactor. As a result, it is expected that a high neutrino flux will provide about 15,000 inverse beta decay (**IBD**) interactions per day in the detector with a sensitive volume of 1 m^3. High segmentation of the plastic scintillator will allow to suppress a background down to a $\sim$1% level. Numerous tests performed with a simplified pilot prototype DANSSino under a 3 GW$_{\mathrm{th}}$ reactor of the Kalinin nuclear power plant (**KNPP**) have demonstrated operability of the chosen design.

The DANSS detector surrounded with a composite shield will be movable by means of a special lifting gear, varying the distance to the reactor core in a range from 9.7 m to 12.2 m. Due to this feature, it could be used not only for the reactor monitoring, but also for fundamental research including neutrino oscillations to the sterile state.

keywords: Reactor antineutrino, Neutrino detector, Sterile neutrino

Project Members From JINR

V. Belov, V. Brudanin, V. Egorov, M. Fomina, Z. Hons, A. Kuznetsov, D. Medvedev, A. Olshevsky, N. Rumyantseva, Ye. Shevchik, M. Shirchenko, Yu. Shitov, I. Zhitnikov, D. Zinatulina

Project Duration. Approval Date(s)

Start of R&D	2006
Trial section #0	2010
Project PAC approval (within JINR Theme #1100)	2010
Producing of Detector elements in JINR	2011 – 2013
Tests with Prototype	2012 – 2013
Mounting at KNPP	2013 – 2014
Start of data taking (planned)	2014

List of Participating Countries and Institutions

JINR — Joint Institute for Nuclear Research, Dubna, Russia; ITEP — Institute of Experimental and Theoretical Physics, Moscow, Russia

6.1 Project Description

6.1.1 Fundamental Scientific Problem Addressed by the Project

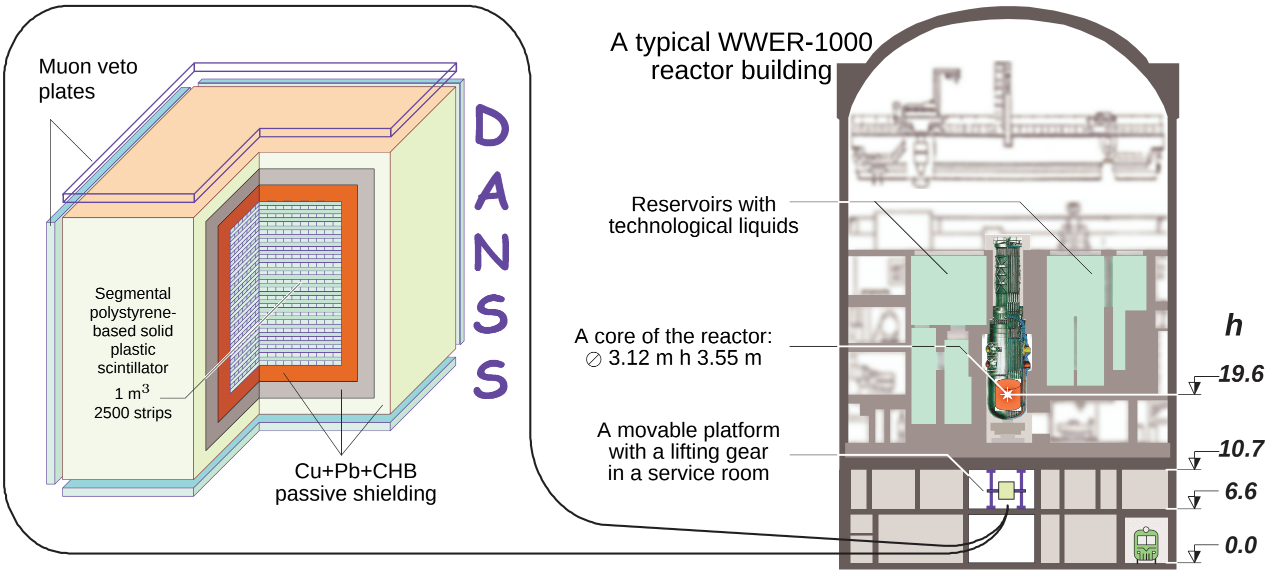

Figure 6.1: Design of the DANSS neutrino detector (left) and its position under the industrial reactor WWER-1000 (right).

The neutrino is probably one of the most enigmatic, and at the same time the most wide-spread particles in the Universe. Due to its very weak interaction with matter, a target would have to be light-years thick before efficiently stopping a neutrino. Therefore, direct investigation of neutrino properties requires an intensive neutrino source and a low background detector with a sensitive volume of at least a cubic meter scale.

The most intensive laboratory neutrino source is provided by nuclear fission. A typical 3 GW_{th} industrial reactor produces about 10^{21} antineutrinos per second. As the particle flux falls down very quickly with distance, it is desirable to install the detector as close to the reactor core as possible. On the other hand, security rules do not allow the use of large amounts of flammable, caustic, toxic, or other dangerous liquids in a reactor building. That is why conventional liquid scintillator (**LS**) becomes "persona non grata" at the nuclear power plant (**NPP**), and detectors of other types are needed.

If such a detector exists it could be efficiently used for many applied and fundamental goals based on the precise measurement of the neutrino energy spectrum: on-line monitoring of the reactor power, fuel composition, burning space pattern (up to tomography), etc. If made movable, the detector would probably be best suited for testing the hypothesis of short-range neutrino oscillation to a sterile state [1].

6.1.2 Specific Project Objectives and Expected Results

The aim of the project is to develop and create a relatively compact ($\sim 1\ m^3$) detector of reactor antineutrinos which does not contain LS, has appropriate Signal-to-Background (S/B) ratio and can be moved within few meters from the reactor core. Being installed under the WWER-1000 industrial reactor, the detector will register about 10,000 neutrinos per day and measure their energy spectrum. Varying the core-detector distance in a range 9.8 – 12.2 m, the detector will allow us to confirm or disprove the "reactor neutrino anomaly" hypothesis [2, 3] within few weeks of data taking. Supposing a one-year measurement, the sensitivity to the oscillation parameters will reach a level of $\sin^2(2\theta) \sim 5 \times 10^{-3}$ with $\Delta m^2 \in (0.02 - 5.0)$ eV^2.

6.1.3 Detector Description

The DANSS detector [4–7] consists of highly segmented plastic scintillator with a total volume of 1 m^3, surrounded with a composite shield of copper (Cu), lead (Pb) and borated polyethylene (CHB), and vetoed against cosmic muons with a number of external scintillator plates. It does not contain any flammable or other dangerous liquids and may therefore be located very close to the core of an industrial power reactor (Fig.6.1). In addition to extremely high neutrino flux ($\sim 5 \times 10^{13}\ \bar{\nu}_e/\mathrm{cm}^2/\mathrm{s}$ at a distance of 11 m) such location provides very good shielding against cosmic rays. Indeed, huge reservoirs with technological liquids, thick walls of heavy concrete, the reactor body and equipment placed above the room provide excellent shielding ($\simeq$50 m w. e.) which completely removes fast cosmic neutrons. The muon component is suppressed by a factor of $\simeq$6 also.

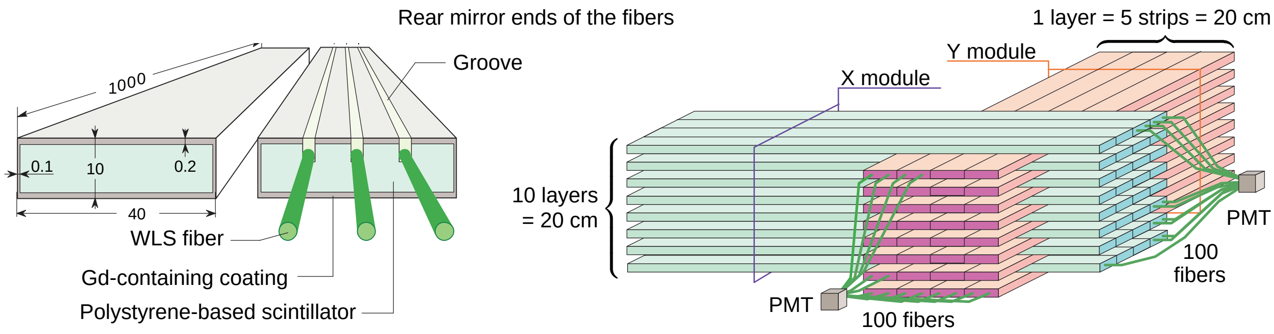

Figure 6.2: The basic element (left) and two of fifty intersecting modules (right) of the DANSS detector.

The basic element of DANSS is a polystyrene-based extruded scintillator strip ($1 \times 4 \times 100$ cm^3) with a thin Gd-containing surface coating, which is a light reflector and an (n, γ)-converter simultaneously (Fig. 6.2). The coating (about $0.1 - 0.2$ mm) is produced by co-extrusion and consists of polystyrene with 18% admixture of rutile and 6% of gadolinium oxide, so that the final Gd density is about 1.6 mg/cm^2, which corresponds to $\sim$0.35%$_{\mathrm{wt}}$. Light collection from the strip is done via three wavelength-shifting Kuraray fibers Y-11, ⌀ 1.2 mm, glued into grooves along the entire strip. An opposite (blind) end of each fiber is polished and covered with a mirror paint, which decreases the total lengthwise attenuation of a light signal down to $\sim$5 %/m.

Each set of 50 parallel strips are combined into a module, so that the whole detector (2500 strips) is a structure of 50 intercrossing modules (Fig. 6.2). Each module is viewed by a compact photomultiplier tube (Hamamatsu R7600U) coupled to all 50 strips of the module via 100 WLS fibers, two per strip. In addition, to get more precise energy and space pattern of an event, each strip is equipped with an individual multipixel photosensor (SiPM) operating in the Geiger mode and coupled to the strip via the third WLS fiber.

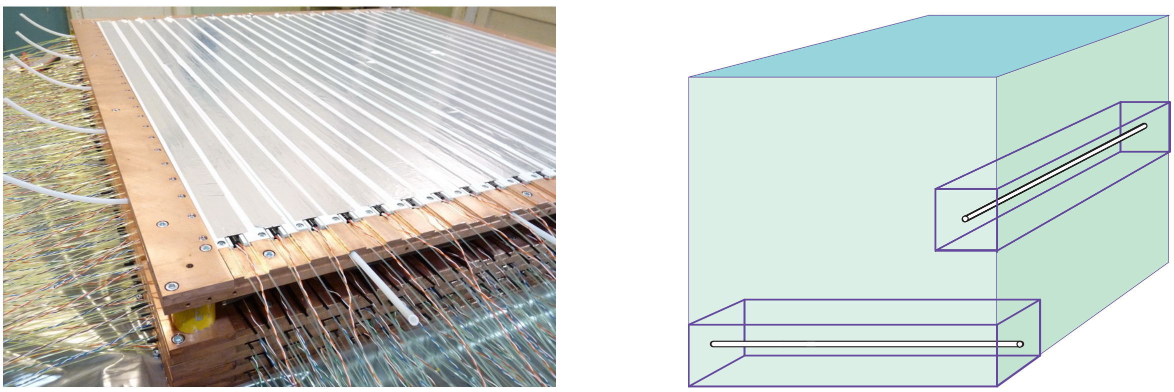

Figure 6.3: Teflon calibration tubes installed into one of the DANSS XY-plates (left). 25 X- and 25 Y-tubes at the modules axes will permeate the whole detector body (right).

To perform energy calibration, a teflon tube is placed inside the center of each DANSS module (Fig. 6.3), so that a tiny radioactive source can be inserted in the detector with a thin flexible string. For this purpose several gamma and neutron sources (^{137}Cs, ^{60}Co, ^{22}Na, ^{248}Cm) with activity of few Bq were produced and soldered hermetically in ampoules (Fig. 6.4).

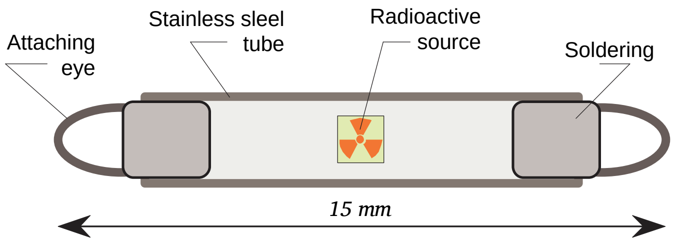

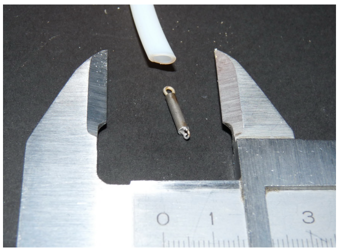

Figure 6.4: Construction of a compact radioactive source for DANSS energy calibration.

All scintillator strips and calibration tubes are carried by copper frames, which at the same time act as an internal part of gamma-shielding (Fig. 6.5). An outer surface of framing is used as a matching site and heatsink for the PMT and SiPM front-end electronics.

The detector is surrounded with a combined CHB-Pb-CHB passive shield. A set of large scintillator plates ($200 \times 50 \times 3$ cm^3) form an active veto system which is used to tag the events associated with cosmic muons.

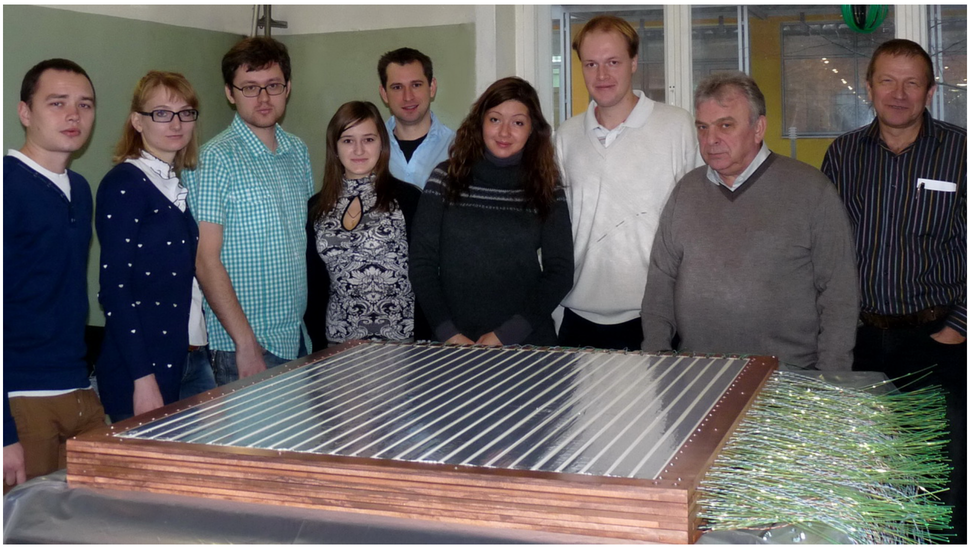

Figure 6.5: The JINR DANSS team with the trial “Zero” section. Copper carrying frames act as an internal part of the gamma-shield.

To make the detector movable, a special lifting system was designed on the basis of commercial hoisting gear PS16 which is commonly used in auto-repair centers to lift heavy tracks (Fig. 6.6). After modification, it is able to move the DANSS detector with shielding ($m \simeq 15$ ton) to varying heights from 0 to 2.4 m, so that the distance between the centers of the detector and the reactor core varies from 9.8 to 12.2 m.

Figure 6.6: Commercial hoisting gear PS16 used in auto-repair centers to lift heavy tracks (left) and the DANSS lifting system based on updated PS16 (right).

The Inverse Beta-Decay (**IBD**) of hydrogen atoms in the detector body is used to detect the reactor antineutrino

$$\overline{\nu}_e + p \to e^+ + n \ . \tag{6.1}$$

The detection proceeds in two steps: the first one applies to the positron and the second to the neutron. The energy threshold of the IBD reaction is 1.8 MeV, while most of the remaining neutrino energy is transferred to the positron. The positron deposits its energy within a short range of few cm and then annihilates emitting two 511 keV photons at 180°. As a result, the first (Prompt) energy deposit is distributed in space in a very specific way. The second (Delayed) step is the detection of the neutron. Initial energy of the neutron is only few keV. After moderation in the plastic scintillator it is captured by ^{157}Gd or ^{155}Gd with a very high cross-section. In both cases a cascade of γ-rays is emitted with a total energy of about 8 MeV. Because of high multiplicity and deep penetration in plastic these γ-rays produce a flash which is spread widely within a sphere with a diameter of about 30-40 cm, so that a number of strips in several X and Y modules are usually fired. Distribution of time between the Prompt and Delayed signals is described by a combination of two exponents

$$f_1(t) = \left(e^{-t/\tau_c} - e^{-t/\tau_m}\right) / \left(\tau_c - \tau_m\right) \ , \tag{6.2}$$

where the characteristic times τ_m and τ_c correspond to the neutron moderation and capture respectively and depend on the detector structure.

Though the IBD event has a very specific signature, it occurs under intense external and internal γ, n and μ background. Therefore, an adequate *hardware trigger* should be worked out in advance.

There are two obvious types of this kind of hardware trigger. The most reliable of them is detection of the Delayed neutron capture, as the amplitude and multiplicity of the neutron signal are much higher than those of the natural γ-background. This method (Fig. 6.7a) requires digitization of the total data stream with flash ADCs and subsequent on-line analysis of the preceding signals (in this way one can spot the Prompt signal, which could happen a few tens of a microsecond before the hardware trigger HT and have relatively low energy).

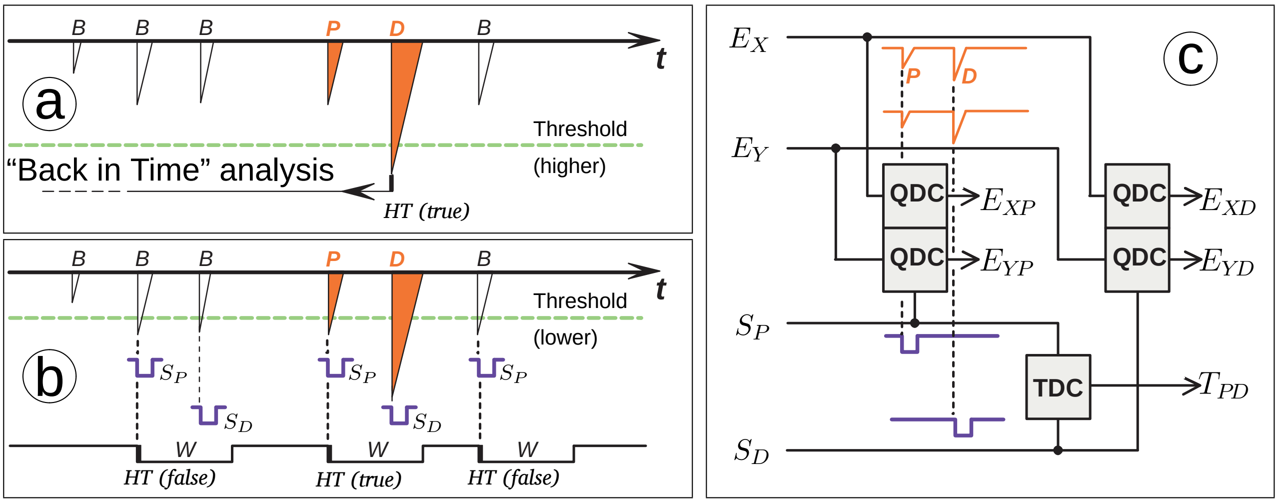

Figure 6.7: Left – two alternative types of the hardware trigger (HT) for the true IBD event consisting of the Prompt (P) and Delayed (D) signals in presence of background pulses (B). Right – a simplified diagram of the QDC-based acquisition system.

This trigger is planned to be used in the final DANSS spectrometer, but at the initial stage it seems to be untimely and impractical.

The other trigger is simpler but less reliable because it can successfully function only under a lower background count rate. Within this method (Fig. 6.7b), the hardware trigger HT is produced by any Prompt signal, and then the system waits for the Delayed signal during some fixed time W. The energy of both Prompt and Delayed signals (E_P and E_D) detected by all X and Y fired modules are measured with a number of Charge-to-Digital Converters (QDC_P and QDC_D), which are gated separately by the S_P and S_D strobes (Fig. 6.7c). Finally, each collected event contains two energies (E_P and E_D) with their specific space patterns, time between the P and D pulses (T_{PD}), and information about the muon veto (which of the plates were fired and when).

6.1.4 Test Measurements with the DANSSino Pilot Detector

In order to check the operability of the DANSS design, compare different acquisition schemes and measure the real background conditions, a pilot version of the detector was created. Figure 6.8 shows this small simplified prototype, DANSSino, which is 1/25th part of the whole DANSS detector (2 modules of 50). It consists of exactly the same basic elements as the main DANSS detector. One hundred strips of DANSSino form a bar $20 \times 20 \times 100$ cm^3 divided into two modules: the odd strip layers are coupled to the X-PMT and the even ones to the Y-PMT. Together with an additional neutron counter both modules are equipped with preamplifiers and placed into a light-tight box. Individual photodiodes of each strip are not used in this prototype.

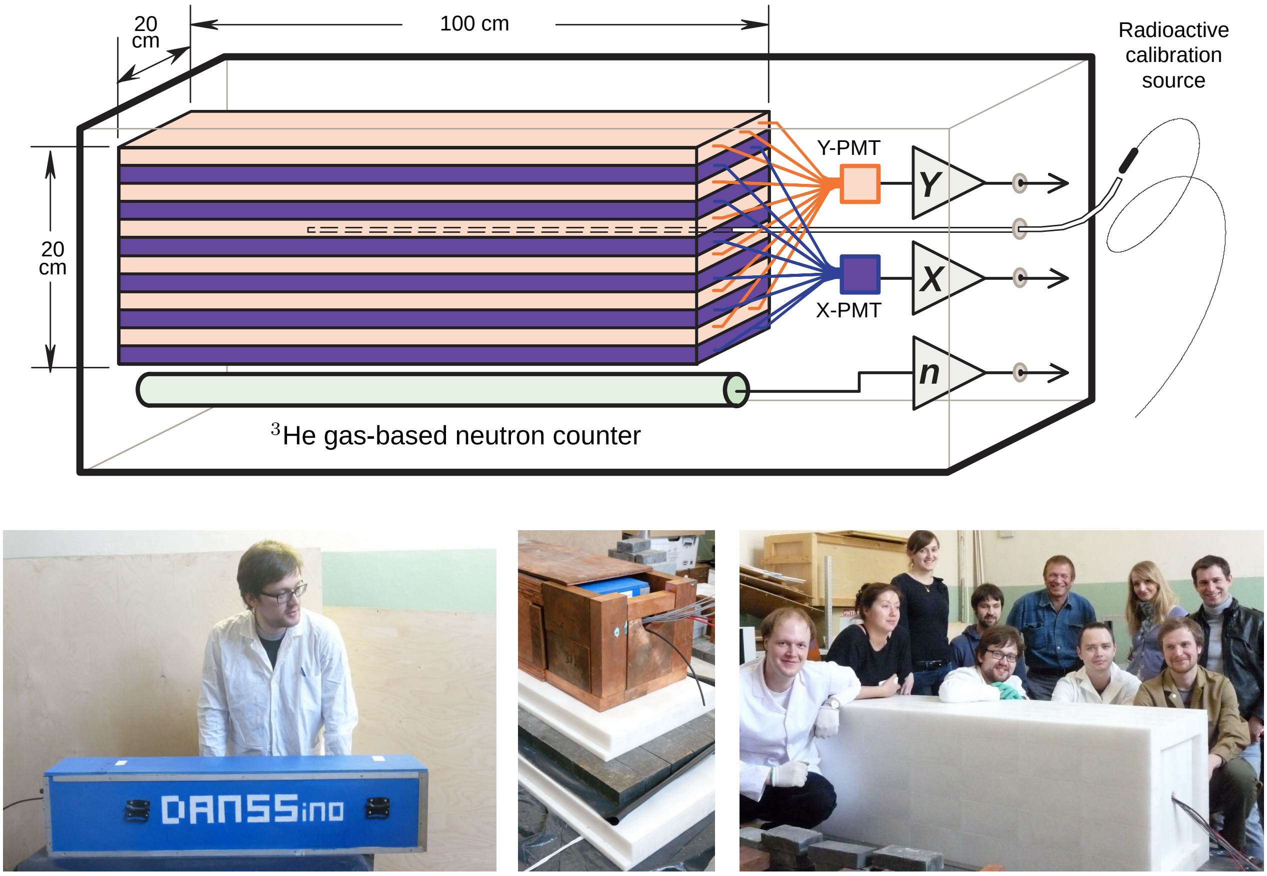

Figure 6.8: The DANSSino detector (unshielded and shielded with CHB against neutrons).

Numerous tests done with DANSSino in the JINR laboratory, and under the industrial 3 GW$_{\mathrm{th}}$ reactor of the Kalinin Nuclear Power Plant at a distance of 11 m from the reactor core have demonstrated [8, 9] operability of the chosen design and revealed the main sources of background. Despite of its small size ($20 \times 20 \times 100$ cm^3), the pilot detector turned out to be quite sensitive to reactor antineutrinos, detecting about 70 IBD events per day (Fig. 6.9) with the signal-to-background ratio about unity. Energy and time distribution of the neutrino-like events (Fig. 6.10) are in a good agreement with our MC simulations, thus confirming that the events observed are really the IBD events.

As a result of tests performed with DANSSino, the following conclusions are made:

— The most important background under the WWER-1000 reactor originates from fast neutrons produced by cosmic muons in high-Z surroundings. Therefore, one should not place heavy materials inside the neutron moderator.

— Efficiency of the muon-veto system should be increased up to 95-97%. To reach this level, a double layer of scintillator plates in coincidence mode with lower thresholds and will be used.

— In spite of the small size, big edge effects, incomplete passive and active shielding and extremely simplified acquisition system, DANSSino is able to detect reactor antineutrinos with the signal-to-background ratio around unity and efficiency at a level of

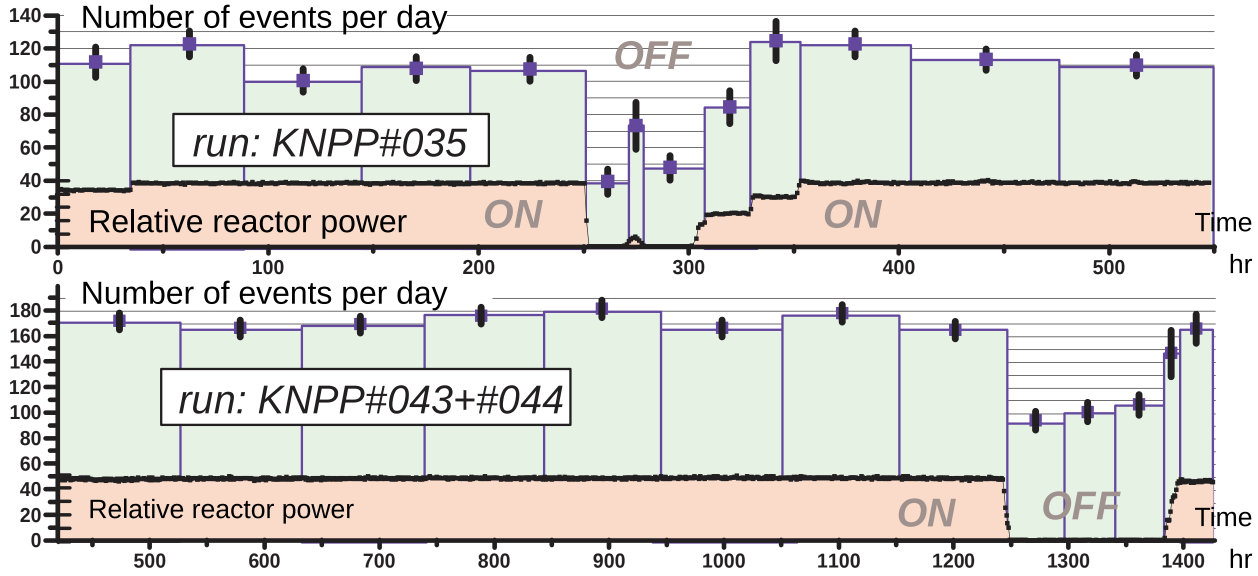

Figure 6.9: Time plot of the reactor power (bottom of each diagram) and the number of the neutrino-like events detected by DANSSino (top of each diagram) for two measurement periods.

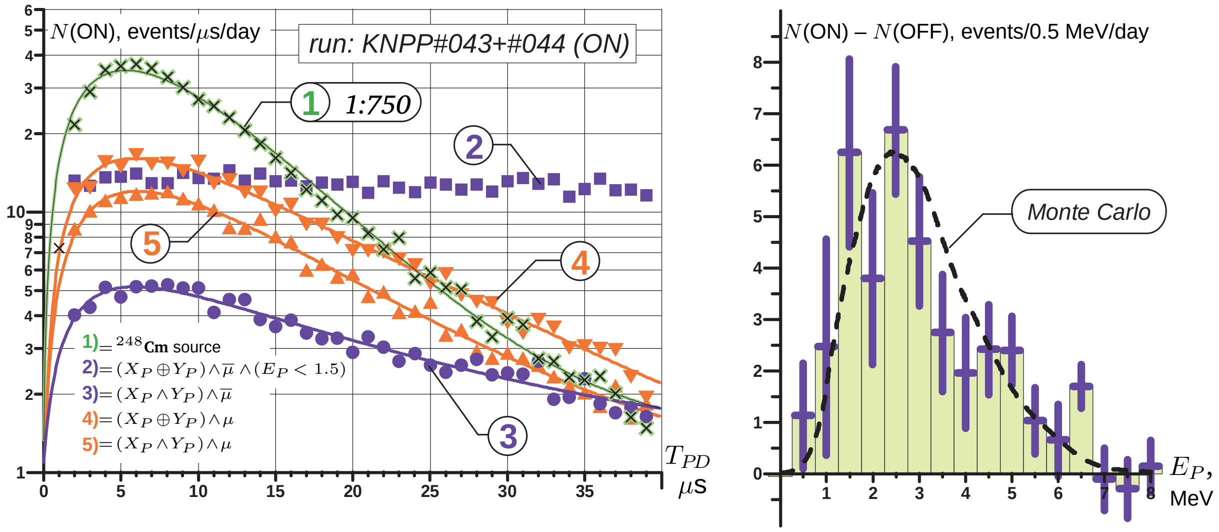

Figure 6.10: The T_{PD} time distribution (left) and differential E_P energy spectrum (right) of the neutrino-like events measured with DANSSino under the operating reactor.

10%, which is in good agreement with the MC simulations. As the full-scale DANSS detector is of much larger volume, its response function is expected to be considerably better and efficiency significantly higher ($\simeq$70%) because of a lower relative contribution from the edge detector parts (fewer neutrons and γ-rays after n-capture in Gd would leave the sensitive volume without detection). Together with the additional information from the individual photo sensors providing the space pattern of each event, it will suppress the background down to a negligible value.

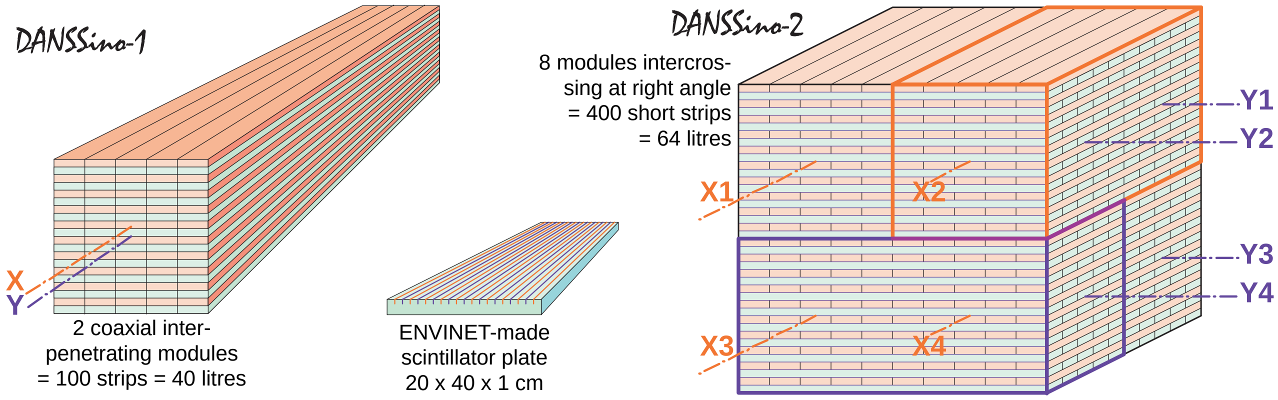

Figure 6.11: Composition of the trial DANSSino-1 and more efficient DANSSino-2 detectors.

— Operation of such detectors at a shallow depth with overburden ≤10-20 m w.e. seems to be questionable, as the neutron component of cosmic rays is not tagged by any veto system and produces a signature similar to the IBD but outnumbers it by orders of magnitude.

Parallel to the main DANSS detector creation, the next trial version DANSSino-2 (see Fig. 6.11) is under mounting now in order to test other signal extraction and another basic element, the scintillator plate made by ENVINET firm (Czech Republic). This work is done together with the Institute of Experimental and Applied Physics, CTU in Prague.

6.1.5 Estimated "Sterile" Sensitivity of DANSS

As it was shown more than once[1], the neutrino energy spectrum $S_Z(E_\nu)$ depends on the fuel composition (which changes during the reactor campaign) and therefore could be used for on-line reactor monitoring (Fig. 6.12a).

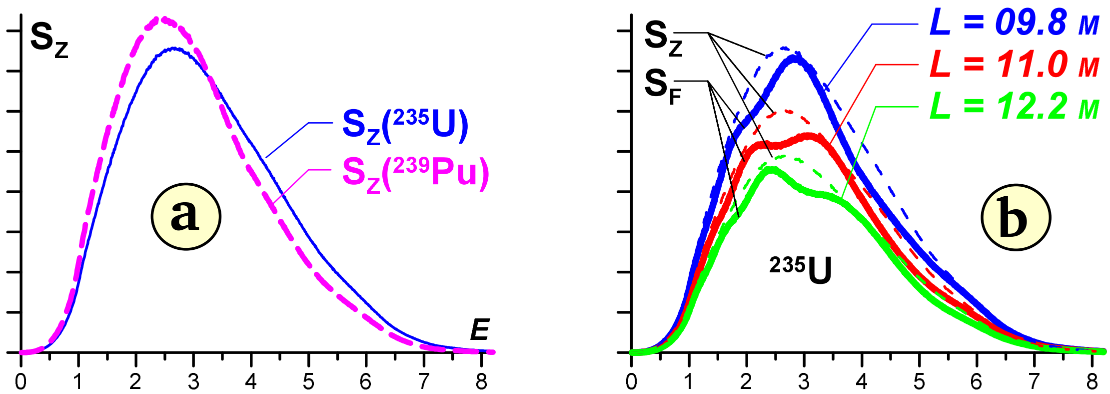

Figure 6.12: Energy Prompt spectra simulated for different conditions. a) Fission of ^{235}U and ^{239}Pu without oscillation effect. b) Fission of ^{235}U without (dashed curves) and with (solid curves) oscillation under assumption (6.3) at different distances.

[1]See, e.g., proceedings of AAP Int. Workshops – AAP2013, AAP2011, AAP2009, etc.

DANSS sensitivity to the amount of bomb-grade ^{239}Pu produced in the reactor core is estimated as 1 SQ (Significant Quantity[2]) per 2 weeks of measurement. It should be mentioned that this value is rather rough and depends very much on the real conditions, which are not yet known at this stage of the project.

In addition to the above **applied goal**, the main **fundamental goal** of the project is searching for short-range oscillation of reactor neutrinos to a sterile state. As it was recently claimed by our French colleagues [2], neutrinos oscillate to a new 4th type with the following oscillation parameters:

$$\left.\begin{array}{lcl}\sin^2(2\theta) & = & 0.17\,, \\ \Delta m^2 & = & 2.0\mathrm{eV}^2\end{array}\right\}\ (F) \tag{6.3}$$

Neutrino survival probability is expressed as

$$P_{\mathrm{osc}}(\nu_e \to \nu_e) \;=\; 1-\sin^2(2\theta)\cdot\sin^2\left(1.267\,\frac{\Delta m^2\, L}{E_\nu}\right)\,, \tag{6.4}$$

where the source-detector distance L is given in meters and the neutrino energy E_ν in units of MeV. For the typical E_ν range of 2–8 MeV these oscillations manifest themselves mainly at a 10–20 m distance, transforming both the spectrum shape and integral count rate (Fig. 6.12b).

Taking into account the size of the reactor core, the spatial distribution of the fission probability, realistic energy resolution, and other detector parameters we have estimated the neutrino spectral density $S(E)$ which could be measured by DANSS in two cases: when the above oscillation with “French” parameters really exists (S_F) and when the phenomenon probability is zero (S_Z).

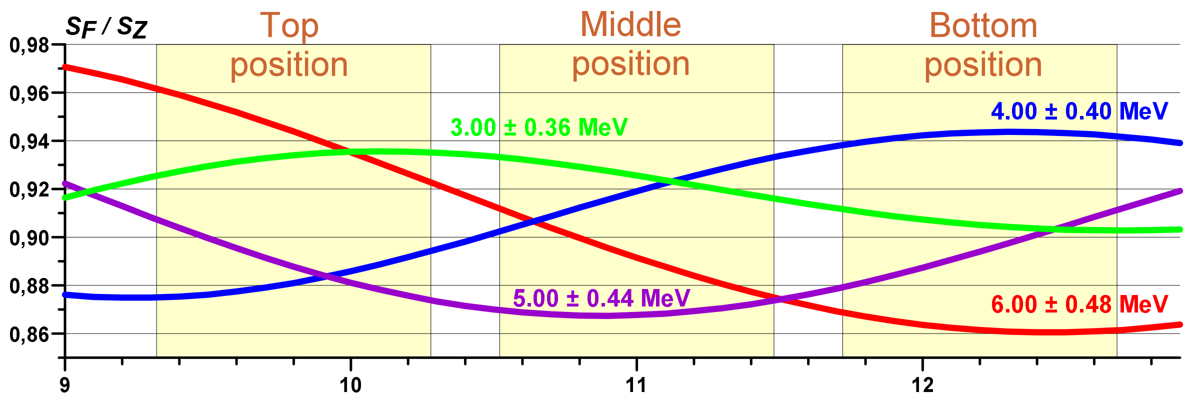

Figure 6.13: Oscillation curves simulated for DANSS conditions under assumption (6.3).

Figure 6.13 shows the S_F/S_Z ratio for different energy spectrum fragments as a function of the distance L. In fact, each curve corresponds to the oscillation of neutrinos with given energy and represents the relative deviation of the detector counting rate from the $1/L^2$ rule. Moving the detector to a top, middle and bottom position by means of the lifting gear, it will be possible to observe the shown deviation of few percent within a week.

[2]The SQ-unit equals to amount of fissile material enough to produce nuclear warhead.

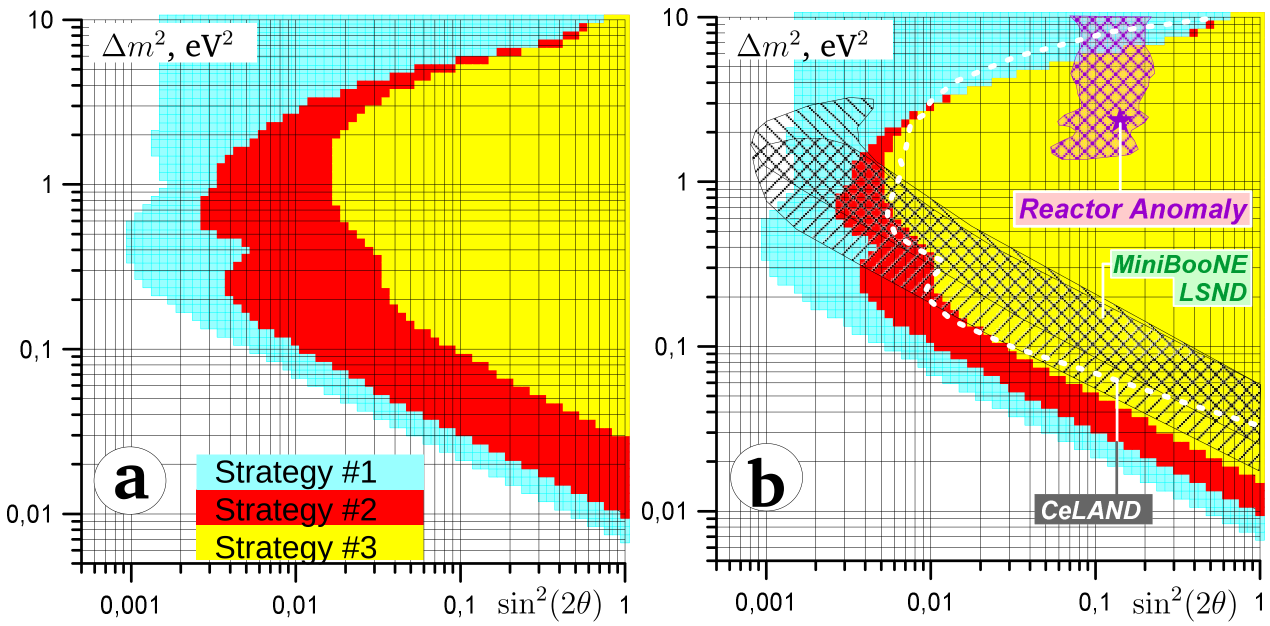

Figure 6.14: Estimation of the DANSS sensitivity at 90%CL to the oscillation parameters in case of one-year measurement. a) Immovable detector in the Middle position. b) The detector operates sequentially in three positions: Top, Middle and Bottom. The two dashed areas correspond to LSND and MiniBooNE results [1], the crossed area to the claim [3], and the dashed curve to the CeLAND proposal [10].

What if the oscillation takes place, but its parameters are different from (6.3)? In order to estimate DANSS sensitivity, numerous MC simulations have been performed and several methods of approach tested. As a result, two measurement policies and three strategies of the data analysis can be considered.

The measurement can be done with an immovable detector or, alternatively, with the detector located sequentially in bottom, middle and top position. In the first case the 1 m detector body is considered as 5 independent sections 20 cm each, so that one could compare five spectra measured with these sections. In the second case the statistics taken in each position is 3 times lower, but the total scanned L-region is 3 times longer (3 meters instead of 1).

According to the first (ever used) strategy of the data analysis, energy spectra measured at each detector position are compared channel-by-channel with the calculated spectra. This strategy requires knowing of the absolute initial neutrino spectrum and flux exactly, as well as the absolute detector efficiency. This method seems to be the most sensitive, but the most susceptible to systematic errors.

Using the second strategy, one compares **relative** spectra shapes instead of their **absolute** values. Here the value of initial neutrino flux and detector efficiency are not used and therefore do not introduce an error.

With the third strategy one observes the evolution of energy spectral intervals with distance, as it was shown in Fig. 6.13. This strategy is the most free of systematic errors because it does not require theoretical calculation of the spectrum shape (which has quite questionable precision) and does not depend on the fuel composition.

Figure 6.14 shows estimated sensitivity (at 90% CL) of the DANSS one-year measurements. It can be seen that the first two strategies using the theoretical spectrum do not differ much for immovable and movable detectors, whereas a detector moving with the third strategy increases sensitivity by a factor of 3. It is also clear that our project is quite competitive with others.

6.1.6 Contribution of JINR Members

JINR plays a leading role in the Project. Up to now most work was performed in the JINR laboratory by the JINR staff: design and creation of the entire mechanical structure (detector strips with WLS fibers, passive and active shielding, lifting system), light extraction system, PMT front-end electronics, data acquisition system, design and creation of the prototype (DANSSino) and test measurements with it. The second participant (ITEP) is responsible for managing with SiPM (front-end electronics and data taking).

6.1.7 Publications, Theses and Conferences

As a result of the project the following

- papers has been published: [8, 9]
- Master theses defended: Zh.V. Nemtsova (VGU, 2011), V.V. Belov (VGU, 2012), M.V. Fomina (VGU, 2012).
- talks [4–7] given at conferences and workshops (LowNu-2009, LowNu-2011, MEDEX-2011, AAP-2013, NANPino-2013, PPP-2014).

6.1.8 Finances

Major sources and amount of finances and major equipment acquired during the project runtime (since 2006) are listed in Tab. 6.1.

Source	Obtained (k$)	Major Equipment acquired
JINR 1100 + RFBR grants + extra-budgetary funds	100	Scintillator strips
	18	Borated polyethylene
	15	Copper M1 plates
	210	VME electronics (crates, etc.)
	100	Front-end electronics
	29	Lifting mechanism PS16
	30/year	Living expenses at KNPP (Udomlya)

Table 6.1: Major sources and amount of finances and major equipment acquired

References

[1] K.N. Abazajian, M.A. Acero, S.K. Agarwalla, et al. “Light Sterile Neutrinos: A White Paper”. In: (2012). arXiv: 1204.5379 [hep-ph].

[2] G. Mention, M. Fechner, Th. Lasserre, et al. “The Reactor Antineutrino Anomaly”. In: *Phys.Rev.* D83 (2011), p. 073006. arXiv: 1101.2755 [hep-ex].

[3] G. Mention. “The reactor antineutrino anomaly”. In: *J.Phys.Conf.Ser.* 408 (2013), p. 012025.

[4] V Egorov and A Starostin. “Solid scintillator detector of the reactor antineutrino DANSS, talk at TAUP 2011”. In: *TAUP*. 2011, pp. 5–9.

[5] V Egorov and A Starostin. “Antineutrino detector development for safeguards in Russia: DANSS, talk at AAP 2011”. In: *AAP* (2011), pp. 15–16.

[6] M Danilov. “Antineutrino Detector for On-Line Monitoring of Nuclear Reactor Parameters and search for short range neutrino oscillations”. In: *Proceedings of the 36th Int. Conf. on High Energy Physics (ICHEP2012). 4-11 July 2012. Melbourne, Australia*. Vol. 1. 2012, p. 511.

[7] M Danilov. “Sensitivity of the DANSS detector to short range neutrino oscillations”. In: *Présentation à la conférence EPS*. 2013. arXiv: 1311.2777 [physics.ins-det].

[8] V. Belov et al. “Registration of reactor neutrinos with the highly segmented plastic scintillator detector DANSSino”. In: *Journal of Instrumentation* 8, P05018 (May 2013), 5018P. arXiv: 1304.3696 [physics.ins-det].

[9] I. Alekseev, V. Belov, V. Brudanin, et al. “DANSSino: a pilot version of the DANSS neutrino detector”. In: *Phys.Part.Nucl.Lett.* 11.4 (2014). arXiv: 1305.3350 [physics.ins-det].

[10] A. Gando, Y. Gando, S. Hayashida, et al. “CeLAND: search for a 4th light neutrino state with a 3 PBq ^{144}Ce-^{144}Pr electron antineutrino generator in KamLAND”. In: (2013). arXiv: 1312.0896 [physics.ins-det].

Chapter 7

Daya Bay Experiment

Editors: D.Naumov, M.Gonchar

Project Title

Daya Bay experiment

Project Leaders

- 2009-2011 — project leader R. Leitner
- 2012-2014 — project leader D. V. Naumov
- 2015-2017 — project leader D. V. Naumov, project leader deputy M. O. Gonchar

Abstract

The main goal of the Daya Bay experiment was to measure the lepton mixing angle θ_{13}. This goal was achieved in 2012 by the Daya Bay Collaboration in a discovery of non-zero value of this angle with a statistical significance exceeding five standard deviations and using only 6 (3 near and 3 far) antineutrino detectors. In subsequent analyses with more data the statistical significance has been increased further. Other targets of the experiment include the following: precise measurement of $\Delta m^2_{\rm ee}$, measurement of the antineutrino flux (normalization and shape), sterile neutrino search, oscillation analysis based on hydrogen capture of recoil neutron from IBD reaction $\bar{\nu}_e + p \to n + e^+$, oscillation analysis using 8 antineutrino detectors, and SuperNovae detection.

keywords: neutrino oscillations, reactor antineutrinos, θ_{13} lepton mixing angle

Project Members From JINR

I. V. Butorov, M. Gonchar, Yu. A. Gornushkin, I. P. Nemchenok, D. V. Naumov, E. A. Naumova, A. G. Olshevskiy, O. Yu. Smirnov.

Project Duration. Approval Date(s)

- 2009-2011 — project approval (project leader R. Leitner)
- 2012-2014 — prolongation (project leader D. V. Naumov)
- 2015-2017 — application for prolongation (project leader D. V. Naumov, project leader deputy M. O. Gonchar)

List of Participating Countries and Institutions

Institute of High Energy Physics, Beijing; East China University of Science and Technology, Shanghai; University of Wisconsin, Madison, Wisconsin, USA; Brookhaven National Laboratory, Upton, New York, USA; National United University, Miao-Li; Joint Institute for Nuclear Research, Dubna, Moscow Region; California Institute of Technology, Pasadena, California, USA; Chinese University of Hong Kong, Hong Kong; Institute of Physics, National Chiao-Tung University, Hsinchu; Nanjing University, Nanjing; Department of Engineering Physics, Tsinghua University, Beijing; Shenzhen Univeristy, Shenzhen; North China Electric Power University, Beijing; Siena College, Loudonville, New York, USA; Department of Physics, Illinois Institute of Technology, Chicago, Illinois, USA; Lawrence Berkeley National Laboratory, Berkeley, California, USA; Department of Physics, University of Illinois at Urbana-Champaign, Urbana, Illinois, USA; Chengdu University of Technology, Chengdu; Shanghai Jiao Tong University, Shanghai; Beijing Normal University, Beijing; College of William and Mary, Williamsburg, Virginia, USA; Department of Physics, Yale University, New Haven, Connecticut, USA; Center for Neutrino Physics, Virginia Tech, Blacksburg, Virginia, USA; Department of Physics, National Taiwan University, Taipei; China Institute of Atomic Energy, Beijing; University of California, Los Angeles, California, USA; Shandong University, Jinan; School of Physics, Nankai University, Tianjin; Department of Physics, University of Cincinnati, Cincinnati, Ohio, USA; Dongguan University of Technology, Dongguan; Department of Physics, The University of Hong Kong, Pokfulam, Hong Kong; Department of Physics, University of Houston, Houston, Texas, USA; Charles University, Faculty of Mathematics and Physics, Prague; University of Science and Technology of China, Hefei; Sun Yat-Sen (Zhongshan) University, Guangzhou; Joseph Henry Laboratories, Princeton University, Princeton, New Jersey, USA; Department of Physics, Applied Physics, and Astronomy, Rensselaer Polytechnic Institute, Troy, New York, USA; China Guangdong Nuclear Power Group, Shenzhen; College of Electronic Science and Engineering, National University of Defense Technology, Changsha; Iowa State University, Ames, Iowa, USA; Xi'an Jiaotong University, Xi'an

7.1 Project Description

7.1.1 Fundamental Scientific Problem Addressed by the Project

The Daya Bay experiment was planned when the least-known neutrino mixing parameter (apart from $\delta_{\rm CP}$) was mixing angle θ_{13}. The best upper limit was $\sin^2 2\theta_{13} < 0.15$ at 90%

C.L. by CHOOZ experiment [1]. Its main goal was to measure $\sin^2 2\theta_{13}$ with sensitivity up to 0.01. The list of goals is much wider:

- Precision $\sin^2 2\theta_{13}$ measurement via rate analysis [2, 3].
- Precision $\sin^2 2\theta_{13}$ and Δm^2_{ee} measurement via rate + shape analysis [4].
- Hydrogen capture based oscillation analysis.
- Sterile neutrino search.
- Reactor antineutrino flux rate measurement.
- Reactor antineutrino flux shape measurement.
- Supernovae detection within SNEWS [5].

Daya Bay started its operation in September, 2011. Physics DAQ with 6 out of 8 detectors running was started in December 2011 and after 50 days of data collection Daya Bay was the first experiment to observe reactor neutrino disappearance [2] with statistical significance higher than $5\,\sigma$. The last two antineutrino detectors were installed during the summer of 2013.

The experiment is currently running and its operation is approved until 2017. Thus the Daya Bay physics program may be expanded in the future.

7.1.2 Specific Project Objectives and Expected Results

Continue data taking and data analysis of the Daya Bay experiment. Within the proposed prolongation we plan to complete the following tasks:

1. Develop own selection of inverse beta decay (IBD) events and of various backgrounds to IBD events which will combine all achievements of other groups in a flexible way and provide a common tool to the Collaboration.
2. Study of background energy spectra. Study of correlations between different sites and antineutrino detectors
3. Perform the data analysis on all of Daya Bay's eight detectors
4. Oscillation analysis of the Daya Bay data, taking into account rate and energy shape information. The goal is the most precise values of $\sin^2 2\theta_{13}$ and Δm^2_{ee}.
5. Oscillation analysis within sterile neutrino hypothesis
6. Oscillation analysis taking into account quantum decoherence
7. Measurement of reactor antineutrino spectra: both absolute value and energy shape
8. Participate in the Daya Bay data taking

One can find a discussion of these tasks in some more details in Section 7.A.

7.1.3 Detector Description

The Daya Bay experiment is located near one of the most powerful nuclear power stations, Daya Bay, near Shenzhen, China. NPP consists of six reactor cores (see Fig. 7.1) located in three sites: Daya Bay (D1, D2), Ling Ao (L1, L2), Ling Ao II (L3, L4). The maximal NPP thermal power is 17.4 GW_{th} (2.9 GW_{th} for each core). The detailed experiment description can be found in [2], [6] and [7].

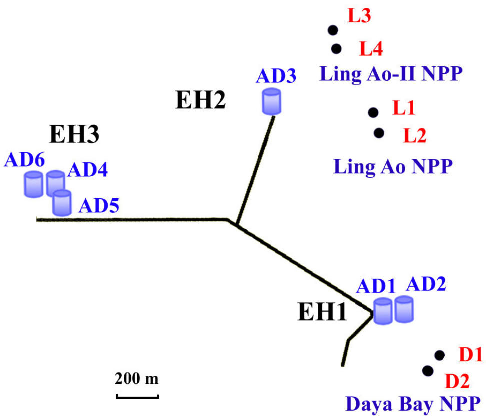

Figure 7.1: Daya Bay experiment layout.

	Overburden	D. B.	L. A.	L. A. II
EH1	280	360	860	1310
EH2	300	1250	480	530
EH3	880	1910	1540	1550

Table 7.1: Approximate overburden (m. w. e.) and distances between detectors and reactor cores (m).

Six (eight planned) identical detectors are installed in three experimental sites: two detectors (EH1) in average 360 m from Daya Bay reactor core, one detector (EH2) in average 500 m from Ling Ao I&II cores and three detectors (EH3) in place with maximum oscillation probability in average 1650 m from all reactor cores. The experimental sites are located underground and connected by a single tunnel. The overburden of the experimental sites as well as the distances between detectors and reactors are listed in Tab. 7.1. The second detector at EH2 and the fourth detector at EH3 are to be installed on summer 2012.

The antineutrino detector (**AD**) utilizes the three-zone scintillator detector structure (see Fig. 7.2).

It consists of three concentric cylindrical volumes. The innermost volume is the target: 3.1 m diameter and height acrylic vessel (**IAV**). It holds 20 t of liquid scintillator, doped by 0.1% of gadolinium. IAV is located inside the outer acrylic vessel (**OAV**) filled with 21 t of undoped liquid scintillator used to catch gammas escaping IAV. The middle volume is called “gamma-catcher”. The OAV is 4 m in diameter and height. It is located in a stainless

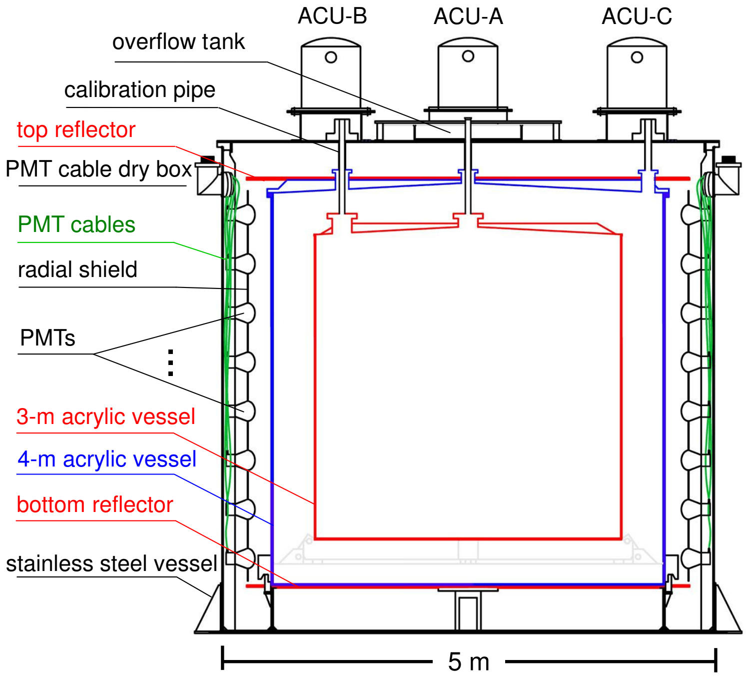

Figure 7.2: The antineutrino detector scheme.

steel vessel (**SSV**) of 5 m diameter and height. The outermost volume is filled with 37 t of mineral oil (**MO**) used as shield against the radiation. The comparison of two near ADs and their performance is presented in [7].

192 8-inch photomultiplier tubes (**PMT**) are installed in 24 columns and 8 rings on the inner surface of SSV to collect the light emitted by scintillation of the LS. The PMTs are recessed inside a black acrylic cylindrical shield located at the equator of PMT bulb used to minimize the light reflection from the walls. Two 4.5 m diameter reflective discs are installed on the top and bottom of the OAV. Their purpose is to increase the light collection and improve the uniformity of energy response. Six 2-inch PMTs are installed on the top and bottom of the AD to monitor LS and GdLS refraction index.

There are three automated calibration units (**ACU**) mounted on top of the SSV. Two units are connected to the IAV: ACU-A can be lowered into the GdLS along the IAV central axis, ACU-B can be lowered near the IAV edge. ACU-C is connected to the OAV and can be lowered into the LS. Each ACU contains a LED light source and two sealed capsules with radioactive isotopes.

Several ADs (two at the DB site, one at the LA site and three at the Far site) are located in the water pool, filled with purified and deoxidized water (1200 t and 1950 t for near and far sites respectively) and used as Cerenkov detectors. Each AD is shielded by $>$2.5 meters of high purity water. The water pool is optically divided into two parts: inner and outer water shield (IWS and OWS), each acting as separate muon detectors. The water shields are covered with PMTs.

RPC[8] modules are mounted to cover the water pool. 2 x 2 m RPC modules are installed in zig-zag mode overlapping each other to increase the spatial resolution. Each RPC module has 4 layers of RPCs.

Each ACU is equipped with several radiation sources which can be deployed separately. LEDs are used to calibrate the PMT timing, single photon response and relative quantum efficiency. Gammas of total energy of 2.5 MeV emitted by ^{60}Co are used to calibrate the energy scale. ^{68}Ge generates pairs of 511 KeV gammas and is used for energy calibration around the threshold. ^{241}Am^{13}C emits neutrons with frequency of 0.5 Hz and is used to analyze the neutron capture time and H/Gd capture ratio.

7.1.4 Basic Methods and Approaches Used in the Project

Observables

Neutrino mixing is described by the PMNS mixing matrix, which consists of 4 parameters: three rotation angles $\theta_{12}, \theta_{23}, \theta_{13}$ and CP-violating phase δ_{CP}.

The θ_{13} mixing angle can be observed in electron neutrino oscillations. The survival probability is given by the following equation:

$$P_{ee} = 1 - \sin^2 2\theta_{13} \sin^2 \Delta_{31} - \cos^4 \theta_{13} \sin^2 2\theta_{12} \sin^2 \Delta_{21} \tag{7.1}$$

$$\Delta_{jk} = 1267 \cdot \frac{\Delta m^2_{jk}}{\text{eV}^2} \frac{L}{\text{km}} \frac{\text{MeV}}{E}, \tag{7.2}$$

where Δm^2_{31} and Δm^2_{21} are the differences of squared neutrino masses.

The usual method of measuring θ_{13} is through observation of the rate of electron antineutrino disappearance in reactor-based experiments. In order to minimize flux related uncertainties several detectors are used. The near detector measures the antineutrino flux, not affected by oscillations, and the far detector measures the oscillated flux.

Electron antineutrinos are detected via the inverse β-decay (**IBD**) reaction:

$$\bar{\nu}_e + p \longrightarrow e^+ + n \tag{7.3}$$

The positron almost immediately releases its energy and annihilates with an electron (prompt signal). The prompt signal visible energy is between 1.022 MeV and 10 MeV. The neutron is thermalized in an average of 28μs and is captured by a Gd nucleus, which then emits several gammas with a total energy of 8 MeV (delayed signal).

Background rates and efficiencies

The following types of backgrounds are taken into account: the accidental coincidence of two random triggers, β-n decaying ^{8}He/^{9}Li isotopes, fast neutrons, ^{13}C$(\alpha, n)^{16}$O interactions and background signals induced by the Am-C radioactive source from ACU.

An accidental event happens when two triggers caused by essential radioactivity and/or neutron interactions are in the detection window. Its rate is determined by counting prompt-like and delayed-like signals separately and calculating the probability of their coincidence in the same time window.

The ACU related background is caused by the Am-C generated neutrons. They can produce gammas via the inelastic scattering in SSV and after the neutron capture on Fe, Cr, Mn, Ni. Both gammas can enter the target region mimicking the prompt and the delayed signal. The ACU background is estimated using the MC simulation.

The α particle emitted from the U/Th decay chain can interact with ^{13}C causing (α, n) reaction, which produces an ^{16}O nucleus, a neutron (delayed signal), and 2.2 MeV gammas (prompt signal). The ^{13}C$(\alpha, n)^{16}$O background rate is determined via MC, after estimating the amount of ^{238}U, ^{232}Th, ^{227}Ac and ^{210}Po in the GdLS based on their cascade decays.

Two other background sources are related to the cosmogenic muons. The long-lived isotopes ^{8}He/^{9}Li can survive the trigger time. They are produced in muon interactions inside the AD. When decaying they emit both a neutron and a β-particle which mimic delayed and prompt signals. The ^{8}He/^{9}Li was determined by fitting the time since the last muon assuming the known decay time of the isotopes.

Fast neutrons are also produced via the muon interaction. They produce the prompt signal by recoiling free protons in the AD, the delayed signal is the fast neutron capture itself. The fast neutron rate is determined by counting the events with prompt energy $>$12 MeV and extrapolating their spectrum to the lower energy region. Summary of detected signal events and expected background is given in Tab. 7.2.

	EH1		EH2	EH3		
	AD1	AD2	AD3	AD4	AD5	AD6
IBD candidates	101290	102519	92912	13964	13894	13731
DAQ live time (days)	191.001		189.645		189.779	
$\epsilon_\mu \cdot \epsilon_m$	0.7957	0.7927	0.8282	0.9577	0.9568	0.9566
Accidentals (/day)	9.54±0.03	9.36±0.03	7.44±0.02	2.96± 0.01	2.92 ± 0.01	2.87 ± 0.01
Fast-neutron (/AD/day)	0.92±0.46		0.62±0.31		0.04±0.02	
^{9}Li/^{8}He (/AD/day)	2.40±0.86		1.20±0.63		0.22±0.06	
Am-C correlated (/AD/day)	0.26±0.12					
^{13}C(α, n)^{16}O (/day)	0.08±0.04	0.07±0.04	0.05±0.03	0.04±0.02	0.04±0.02	0.04±0.02
IBD rate (/day)	653.30±2.31	664.15±2.33	581.97±2.07	73.31 ± 0.66	73.03 ± 0.66	72.20 ± 0.66

Table 7.2: Signal and background summary.

The uncorrelated detection inefficiency is formed by the muon detection inefficiency and the multiplicity selection inefficiency. The muon detection inefficiency is calculated by integrating the vetoed time of each muon with temporal overlaps taken into account. The multiplicity selection inefficiency is determined by calculating the probability of a random trigger to occur in a time window with the IBD event. The estimation of the efficiency values are given in Tab. 7.3.

The additional correction to the number of IBD events are applied due to geometrical effects: the "spill-in" correction takes into account Gd capture of neutrons from the IBD interactions outside the target region, the "spill-out" correction takes into account IBD neutrons leaving the target region. The "spill-in" correction is calculated based on the MC simulation. The "spill-out" correction is included into the Gd capture ratio and studied using the Am-C source and the MC.

	Efficiencies	Correlated	Uncorrelated
Target protons		0.47%	0.03%
Flasher cut	99.98%	0.010%	0.01%
Delayed E cut	90.9%	0.6%	0.12%
Prompt E cut	99.88%	0.10%	0.01%
Multiplicity cut		0.02%	<0.01%
Capture time cut	98.6%	0.12%	0.01%
Gd capture ratio	83.8%	0.8%	<0.1%
Spill-in	105.0%	1.5%	0.02%
Livetime	100.0%	0.002%	<0.01%
Combined	78.8%	1.9%	0.2%

Table 7.3: Summary of the detector efficiencies and uncertainties.

The instrumental background caused by spontaneous light emission by PMTs ("flashers") is effectively rejected by the cuts in which the clustering of detector response is analyzed.

Event selection

The following trigger criteria for the ADs are used: number of hit PMTs>45 and total visible energy>0.4 MeV. Trigger time and charge are saved for each PMT. The energy is reconstructed based on the total number of collected p.e. with the factor of ~163. The factor is determined by fitting 2.506 MeV ^{60}Co peak. The energy resolution is $(7.5/\sqrt{E(\text{MeV})} + 0.9)$% for all ADs.

The water pool events are triggered by the NHIT>12 and marked as muon candidates. Muon candidates with energy deposit inside the AD in a time window $\pm 2\mu$s are marked as AD muons for E>20 MeV and showering muons for E>2.5 GeV.

The IBD events were selected using the following criteria: prompt signal with visible energy between 0.7 and 12 MeV, delayed signal with visible energy between 6 and 12 MeV, time between signals is required to be between 1 and 200 μs. No other signal with energy higher than 0.7 MeV is required in 200 μs before the prompt or after the delayed signal. There should be no WS muons detected in in a time window of 600 μs before the delayed signal, no AD muons in a time window of 1000 μs and no showering muons within one second before the delayed signal.

Correlated		Uncorrelated	
Energy/fission	0.2%	Power	0.5%
IBD/fission	3%	Fission fraction	0.6%
		Spent fuel	0.3%
Combined	3%	Combined	0.8%

Table 7.4: Summary of the reactor uncertainties.

Energy model

According to eq. (7.3) the antineutrino energy is $E_\nu = E_{\text{prompt}} + E_n + 0.78$ MeV, where average neutron energy is ~10 keV and can be neglected. The prompt energy is the positron kinetic energy (scintillation and Cherenkov light) + annihilation energy (scintillation). The detector energy response is not linear due to various scintillator and electronics effects. First of all the deposited energy can be partly lost in the non-scintillating inner acrylic vessel. This effect is taken into account using MC. The non-linear energy scale effects due to scintillator and electronics are determined due to fit to the monoenergetic γ-lines from radioactive sources and continuous $\beta + \gamma$ spectrum extracted from ^{12}B data [4]. Sources were deployed at the center of all ADs regularly (^{68}Ge, ^{60}Co, ^{241}Am-^{13}C) [7] and during a special calibration period in summer 2012 (^{137}Cs, ^{54}Mn, ^{40}K, ^{241}Am-^{9}Be, Pu-^{13}C) with AD1 and AD2 in near-hall EH1. In addition, gamma peaks in all ADs which could be identified with singles and correlated spectra in data (^{40}K, ^{208}Tl, n capture on H, C, and Fe) were included. For source data with multiple gamma-line emissions, f_{scint} is computed for each gamma then summed up, whereas f_{elec} is computed based on the total E_{vis}. The ^{12}B isotopes are produced cosmogenically at the rate of about 900 (60) events/day/AD at the near (far) site. The measured relative nonlinearity of $< 0.3\%$ among 6 ADs [3] is negligible in the context of the energy model.

Figure 7.3 compares the best-fit energy model with the single-gamma, multi-gamma and continuous ^{12}B data used to determine the model parameters. As additional validation, the energy model prediction for the continuous $\beta + \gamma$ spectra from ^{212}Bi, ^{214}Bi and ^{208}Tl decays was compared with the data and found to be consistent.

7.1.5 Contribution of JINR Members

The JINR contribution to the Daya Bay project could be briefly summarized as follows.

- **PPO** production line restoration, production and delivery to Daya Bay (450 000 euros equivalent).
- **Muon veto based on plastic scintillator option**. When planning the Daya Bay experiment plastic scintillator strips were suggested by JINR as a muon veto option for top and in-water tracking systems. This option was abandoned in favor of RPC muon veto option.
- **Liquid scintillator development.** The development of the liquid scintillators (C,H-based, LS, and gadolinium-loaded, Gd-LS), suitable for using in the large-scale Daya Bay experiment was the one of the directions of the JINR team activity.
- **Fast neutron detection method.** The method of tagging fast neutron events based on Flash ADC signals was suggested.
- d**ybOscar package**. We developed a dedicated software package used for the oscillation analyses of the Daya Bay data. Some results of these analyses can be found in the project.
- $3 - \nu$ **oscillation analysis.** Using dybOscar we conduct our own rate + shape oscillation analysis.

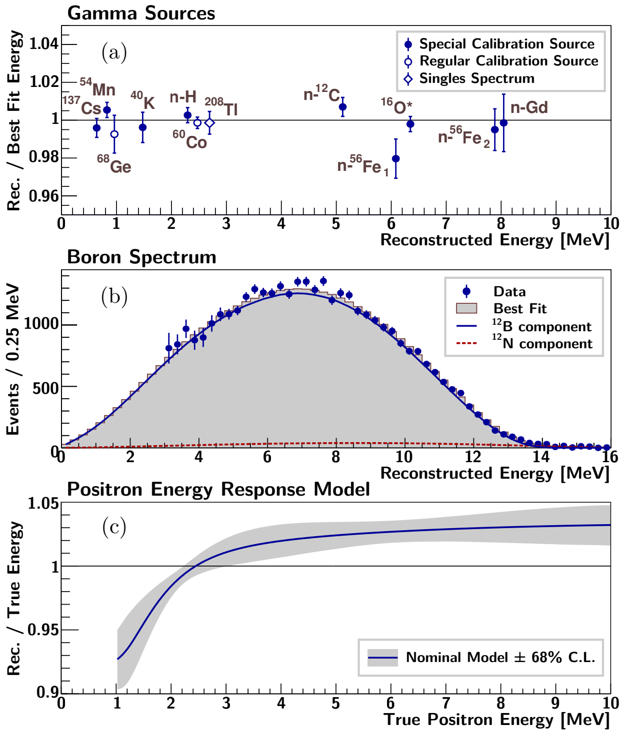

Figure 7.3: (a) Ratio of the reconstructed to best-fit energies of γ lines from calibration sources and singles spectra as described in the text. The error bars represent the total uncertainty on each ratio. The γ from the second-excited state of ^{16}O in the Pu-^{13}C source is denoted $^{16}\mathrm{O}^{*}$. The n-$^{56}\mathrm{Fe}_1$ and n-$^{56}\mathrm{Fe}_2$ labels denote the $\sim$6 MeV and $\sim$7.6 MeV γs, respectively, resulting from the capture of neutrons from the AmC sources placed on top of the AD. (b) Reconstructed energy spectrum (points) compared to the sum (shaded area) of the ^{12}B (solid line) and ^{12}N (dashed line) components of the best-fit energy response model. The error bars represent the statistical uncertainties. (c) AD energy response model for positrons.

- **Search for sterile neutrino.** Using dybOscar we conduct our own search for sterile neutrino. This result is one of our contributions to the Daya Bay Collaboration paper.

More details could be found in Sec. Section 7.B.

7.1.6 Publications, Theses and Conferences

As a result of the project the following:

- papers has been published [2–4, 7, 9–12].
- talks [13–21] given at conferences.

Working within the Daya Bay project the following theses have been completed:

- defended diploma: M.Gonchar (2007), “Plastic scintillator based muon veto system for DayaBay”, thesis advisor D.Naumov; Ilia Butorov (2012), “Vertex reconstruction in the Daya Bay experiment”, thesis advisor M.Gonchar.

- defended master thesis: M.Dolgareva, "Study of quantum decoherence effects in neutrino oscillations in Daya Bay experiment", thesis advisor M.Gonchar.
- expected PhD theses: M.Gonchar (2014), "Measurement of $\sin^2 2\theta_{13}$ and Δm^2_{ee} in Daya Bay experiment", thesis advisor D.Naumov; I. Butorov (2016), "Precision measurement of $\sin^2 2\theta_{13}$ and search for sterile neutrino in Daya Bay experiment", thesis advisor D.Naumov.
- expected doctor thesis: D.Naumov (2014), "Oscillations and interaction of neutrino with matter".

7.1.7 Finances

Major sources and amount of finances and major equipment together with travel expenses acquired during the project runtime are listed in Tab. 7.5 and Tab. 7.6.

Source	Amount requested (k$)	Amount obtained (k$)	Major Equipment acquired	Year
1099		21	Operation Costs	2011
1099		36	Operation Costs	2012
1099 RFBR grant Min.Obr. grant Min.Obr. grant		36 9 0.5 3	Operation Costs Computers and equipment Computers and equipment Salary	2013
1099 RFBR grant	40	 20	Operation Costs Salary	2014
1099 1099 RFBR grant	180 15 60		Operation Costs Computers and equipment Salary	2015–2017

Table 7.5: Major sources and amount of finances and major equipment acquired.

Source	Amount requested (k$)	Amount obtained (k$)	Year
1099		16	2011
1099 RFBR grant Min.Obr. grant		27 2 1	2012
1099 RFBR grant Min.Obr. grant		21 6 2	2013
1099	35		2014
1099	120		2015–2017

Table 7.6: Major sources of finances requested and obtained for travel expenses.

Daya Bay Appendix

7.A Specific Project Objectives and Expected Results

7.A.1 IBD selection and background study

IBD event selection consists of the removal of instrumental background from the spontaneous emission of light by PMTs ("flashers"), which is done by identifying the topology of this type of event, removal of muon background, which is done by placing various requirements on the energy deposit in the water pools and ADs, and selection of the characteristic prompt-delayed IBD signature by requiring:

- prompt energy deposit of 0.7–12 MeV;
- delayed energy deposit of 6–12 MeV;
- capture time in the range 1–200 μs;
- no other signal > 0.7 MeV within $\pm 200 \mu s$ of the IBD candidate.

Figs. 7.4, 7.5 and 7.6 present the energy distributions for prompt and delayed signals for selected IBD candidates, and the time between them.

There are different backgrounds in selected IBD events:

- accidental, when there is association of two random signals with IBD candidate;
- decay of $^{9}\mathrm{Li}/^{8}\mathrm{He}$;
- fast neutron interaction;
- alpha-N interaction;
- Am-C source.

Accidental background, which is the largest source of background, contributing 1.5% of IBD candidates, can be estimated theoretically using the known rate of accidental signal or from data using different methods:

- Off-window method. By definition, the accidental background within the IBD coincidence time window $(1\mu s < t < 200\mu s)$ should be the same as in any other window $(t^{\text{off}} + 1\mu s < t < t^{\text{off}} + 200\mu s)$, where t^{off} is an arbitrary time offset. If t^{off} is large enough to avoid real correlated events (such as for IBD, fast neutron, and ^{9}Li/^{8}He decay), the accidental backgrounds can be estimated by counting the coincidences in the off-window.

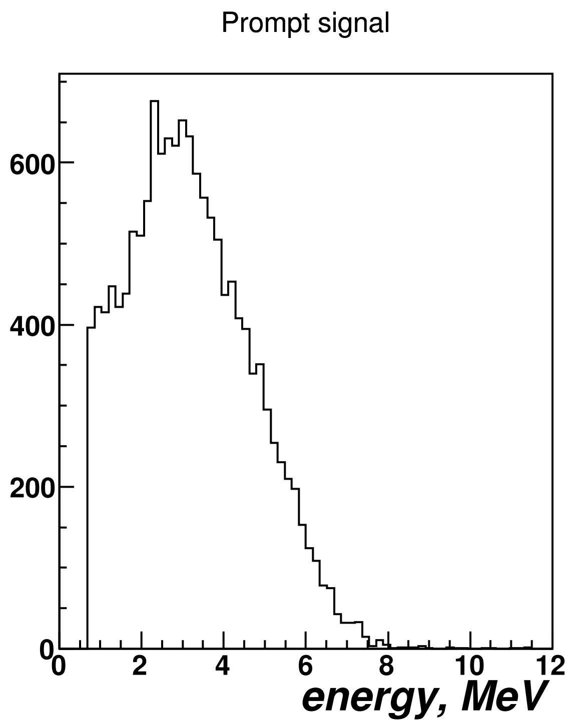

Figure 7.4: Energy of the prompt signals for selected IBD candidates.

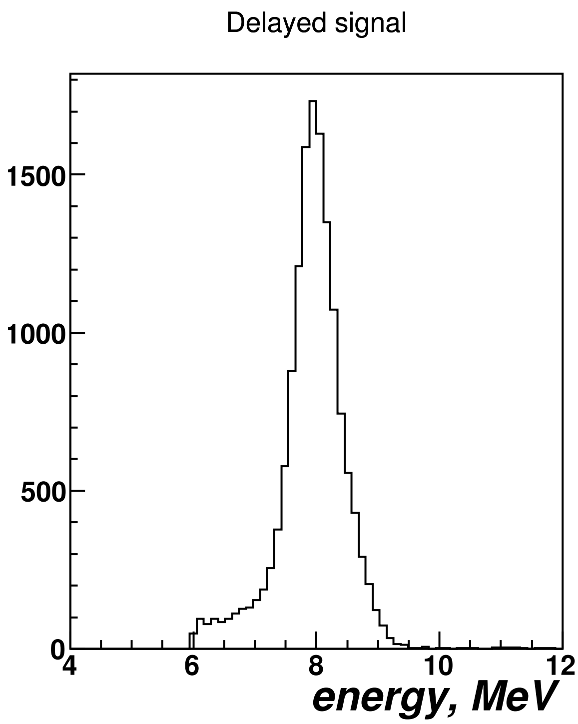

Figure 7.5: Energy of the delayed signals for selected IBD candidates.

- Distance method. Accidental background can be estimated via the distance distribution between prompt and delayed signal vertices. For this estimation it is necessary to have a good procedure for vertex reconstruction.

Other backgrounds are estimated using MC simulation.

Our group is planing to improve the IBD selection cuts and background estimation analysis.

7.A.2 Precision measurements of $\sin^2 2\theta_{13}$ and Δm^2_{ee}.

The uncertainties on values of $\sin^2 2\theta_{13}$ and Δm^2_{ee} are dominated by statistics, hence there is a possibility to improve the accuracy in the future. The projected sensitivities are shown on Fig. 7.7. The systematic error should also be improved with updated knowledge on detector energy response and background contributions. Therefore we are going to continue support of the dybOscar package. We plan to keep the oscillation analysis up-to-date during the entire Daya Bay DAQ process.

The current near term working plan consists of:

- Implement 8 AD analysis based on the latest dataset. Use our own IBD selection and background analysis (see section 7.A.1).

- Update statistical analysis. Check the impact of correlated statistical errors. Study oscillation parameters errors breakup and error budget.

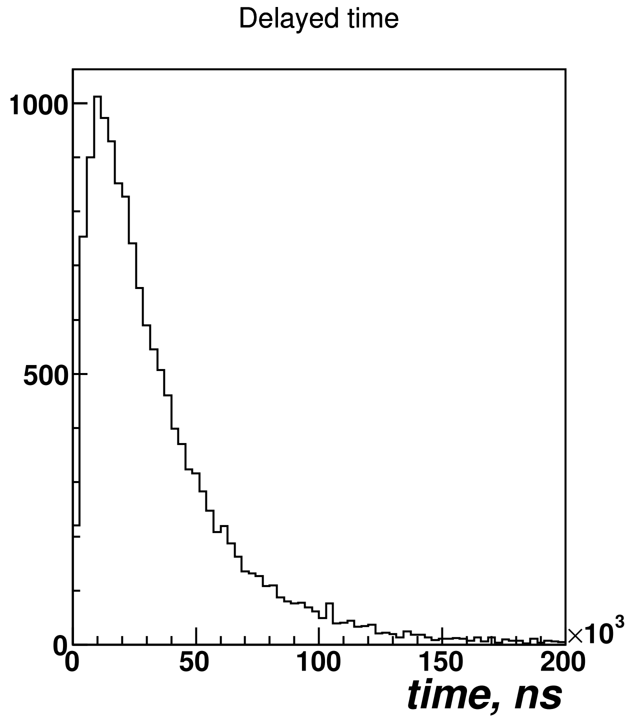

Figure 7.6: Time between prompt and delayed signals for selected IBD candidates.

- Update reactor neutrino flux. Study impact of new reactor flux measurements and predictions ([22, 23]). Update spent nuclear fuel data.

- Keep dybOscar updated to fit needs of $\sin^2 2\theta_{13}$ and Δm^2_{ee} as well as other current and new analyses (sections 7.A.2 to 7.A.2) throughout the life of the project.

Sterile neutrino search

There are several anomalies in neutrino physics which cannot be easily explained in the framework of three neutrinos (see Sec. 2.5.3 for more details). In the scenario with four neutrinos the $\nu_e \to \nu_e$ survival probability can be written as follows:

$$\begin{aligned}1 - P(\bar{\nu}_e \to \bar{\nu}_e) =& 4|U_{e1}|^2|U_{e2}|^2 \sin^2 \frac{\Delta m^2_{21} L}{4E} + 4|U_{e1}|^2|U_{e3}|^2 \sin^2 \frac{\Delta m^2_{31} L}{4E} \\ &+4|U_{e2}|^2|U_{e3}|^2 \sin^2 \frac{\Delta m^2_{32} L}{4E} + 4|U_{e1}|^2|U_{e4}|^2 \sin^2 \frac{\Delta m^2_{41} L}{4E} \\ &+4|U_{e2}|^2|U_{e4}|^2 \sin^2 \frac{\Delta m^2_{42} L}{4E} + 4|U_{e3}|^2|U_{e4}|^2 \sin^2 \frac{\Delta m^2_{43} L}{4E},\end{aligned} \quad (7.4)$$

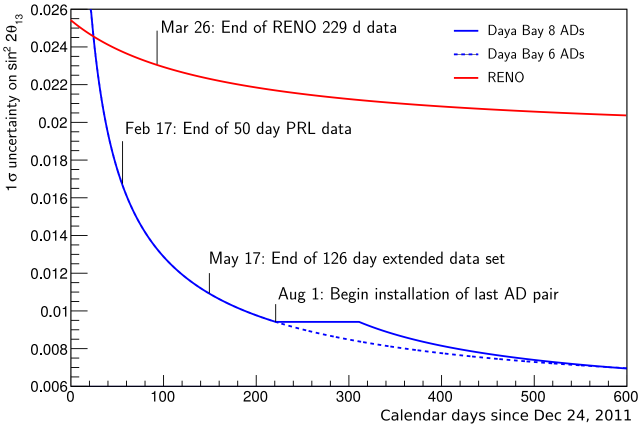

(a) $\sin^2 2\theta_{13}$

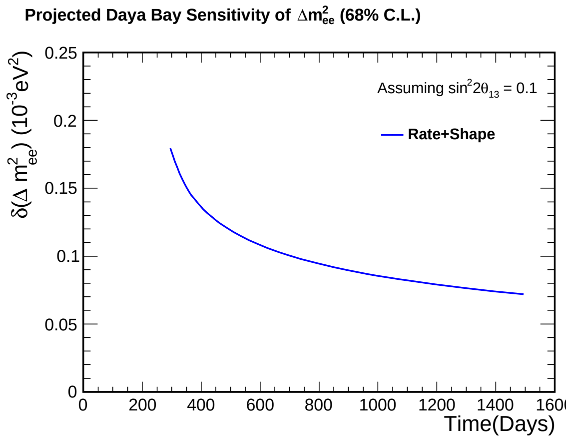

(b) Δm^2_{ee}

Figure 7.7: Daya Bay projected sensitivity.

where

$$
\begin{aligned}
U_{e1} &= \cos\theta_{14}\cos\theta_{13}\cos\theta_{12} \\
U_{e2} &= \cos\theta_{14}\cos\theta_{13}\sin\theta_{12} \\
U_{e3} &= \cos\theta_{14}\sin\theta_{13} \\
U_{e4} &= \sin\theta_{14}.
\end{aligned}
\tag{7.5}
$$

$P(\bar{\nu}_e \to \bar{\nu}_e)$ coincides with the 3-ν formula for $\theta_{14} = 0$. In what follows we adopt the method by Feldman-Cousins [24] to build the confidence contours. The idea of Feldman and Cousins is in the use of a particular ordering principle for construction of *acceptance intervals*. Let us summarize the main steps of their proposal.

- Let $\mathbf{n}$ be a vector of number of events with expected mean value $\boldsymbol{\mu}(\boldsymbol{\theta})$, which depends on a vector of theory parameters $\boldsymbol{\theta}$.
- The probability to observe $\mathbf{n}$ at given $\boldsymbol{\mu}(\boldsymbol{\theta})$ is $P(\mathbf{n}|\boldsymbol{\mu}(\boldsymbol{\theta}))$.
- For every value of $\boldsymbol{\theta}$ construct the acceptance intervals for $\mathbf{n}$ as follows.
  - Generate Gaussian statistics over $\mathbf{n}$, including systematic uncertainties encoded in the covariance matrix
  - For every random $\mathbf{n}$ find $\boldsymbol{\theta}_{\text{best}}$ which maximizes $P(\mathbf{n}|\boldsymbol{\mu}(\boldsymbol{\theta}))$ or minimizes $\chi^2(\mathbf{n},\boldsymbol{\theta})$
  - Calculate $\Delta\chi^2(\mathbf{n},\boldsymbol{\theta},\boldsymbol{\theta}_{\text{best}}) = \chi^2(\mathbf{n},\boldsymbol{\theta}) - \chi^2(\mathbf{n},\boldsymbol{\theta}_{\text{best}})$
  - From the $\Delta\chi^2(\mathbf{n},\boldsymbol{\theta},\boldsymbol{\theta}_{\text{best}})$ distribution find $\Delta\chi^2(\boldsymbol{\theta})_{c,\alpha}$, which corresponds to a probability α to observe the value $\Delta\chi^2(\boldsymbol{\theta})_c$ in a statistical distribution of $\Delta\chi^2(\mathbf{n},\boldsymbol{\theta},\boldsymbol{\theta}_{\text{best}})$.
- The *confidence intervals* are calculated as follows.
  - Find, in data, the best fit point $\boldsymbol{\theta}_{\text{best}}$ and corresponding $\chi^2(\boldsymbol{\theta}_{\text{best}})_{\text{data}}$

- Calculate $\Delta\chi^2(\boldsymbol{\theta}, \boldsymbol{\theta}_{\text{best}})_{\text{data}} = \chi^2(\boldsymbol{\theta})_{\text{data}} - \chi^2(\boldsymbol{\theta}_{\text{best}})_{\text{data}}$
- $\boldsymbol{\theta}$ is accepted in the confidence interval if $\Delta\chi^2(\boldsymbol{\theta}, \boldsymbol{\theta}_{\text{best}})_{\text{data}} < \Delta\chi^2(\boldsymbol{\theta})_{c,\alpha}$

We calculate the Daya Bay sensitivity to sterile neutrinos as follows. We generate a number of samples, randomizing the average prediction by statistical and systematic fluctuations. Each sample is then passed to our Feldman-Cousins procedure to calculate $\Delta\chi^2_{\text{data}} - \Delta\chi^2_{\text{c}}$. Then this function is averaged over the number of samples to obtain the final confidence intervals, which are shown in Fig. 7.8. Currently the Daya Bay sensitivity in the region

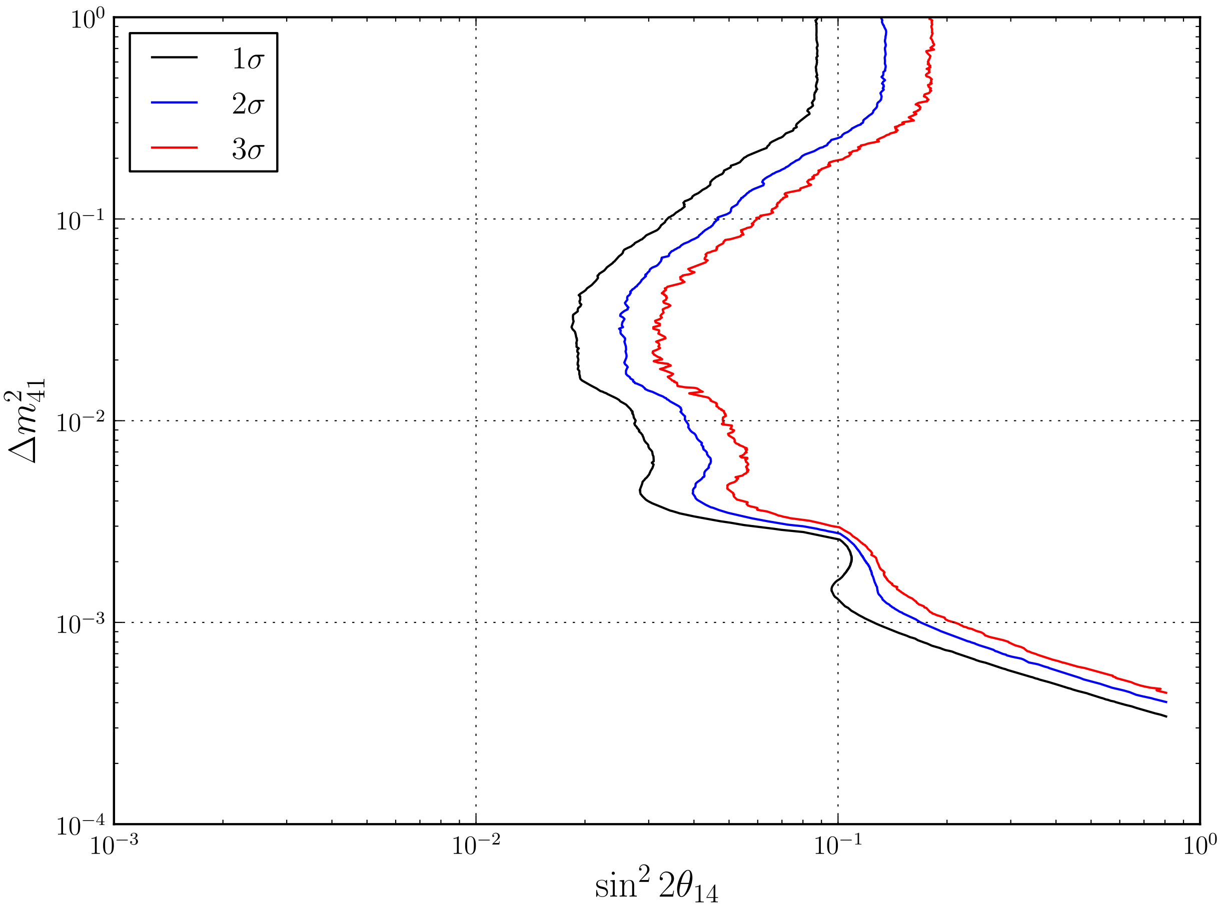

Figure 7.8: Daya Bay sensitivity as a function of Δm^2_{41} and $\sin^2 2\theta_{14}$.

$\Delta m^2_{41} < 0.1$ eV^2 is limited by the accumulated statistics. We plan to complete this analysis with currently accumulated statistics and update the analysis while the statistics increase during the next three years.

Quantum decoherence

As we mentioned in Sec. 2.4 the oscillation formula (2.19) obtained within the plane wave limit should be modified in a more rigorous approach based on a wave-packet descrip-

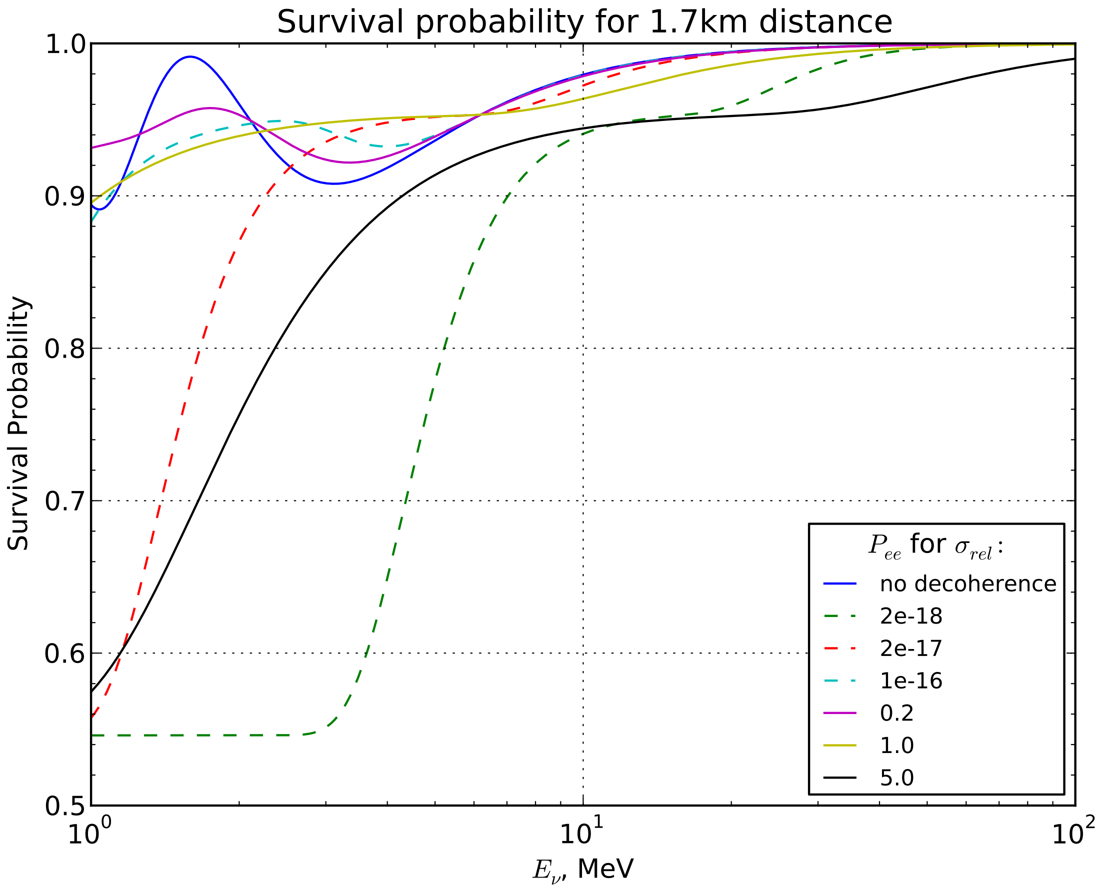

Figure 7.9: Survival probability of $\bar{\nu}_e$ as a function of E at fixed $L = 1.7$ km for some values of σ_E.

tion of neutrino production and detection as shown in formula (2.21). The modification introduces the coherence length, which suppresses the interference (and thus oscillations) at distances exceeding the coherence length. While there exist some theoretical estimates of the coherence length of neutrinos let us note that no experimental limit has been made so far on this subject. The Daya Bay experiment, due to its different baselines, provides us with the data which can effectively place the limits on the coherence length of reactor antineutrinos.

The key parameter for this problem is a relative dimensionless uncertainty of neutrino energy $\sigma_E = \delta E/E$. This parameter is a Lorentz-invariant function of kinematical variables in the production and detection points. For the sake of simplicity we illustrate below its impact on the oscillation pattern considering it as a constant parameter. In Fig. 7.9 we display the survival probability of $\bar{\nu}_e$ as a function of E at fixed $L = 1.7$ km for some values of σ_E. As one can see, values of the σ_E parameter which are either too small or too large drastically change the probability.

Fig. 7.10 illustrates how the energy spectra in near and far Daya Bay detectors vary as a function of σ_E. In Fig. 7.11 we display the

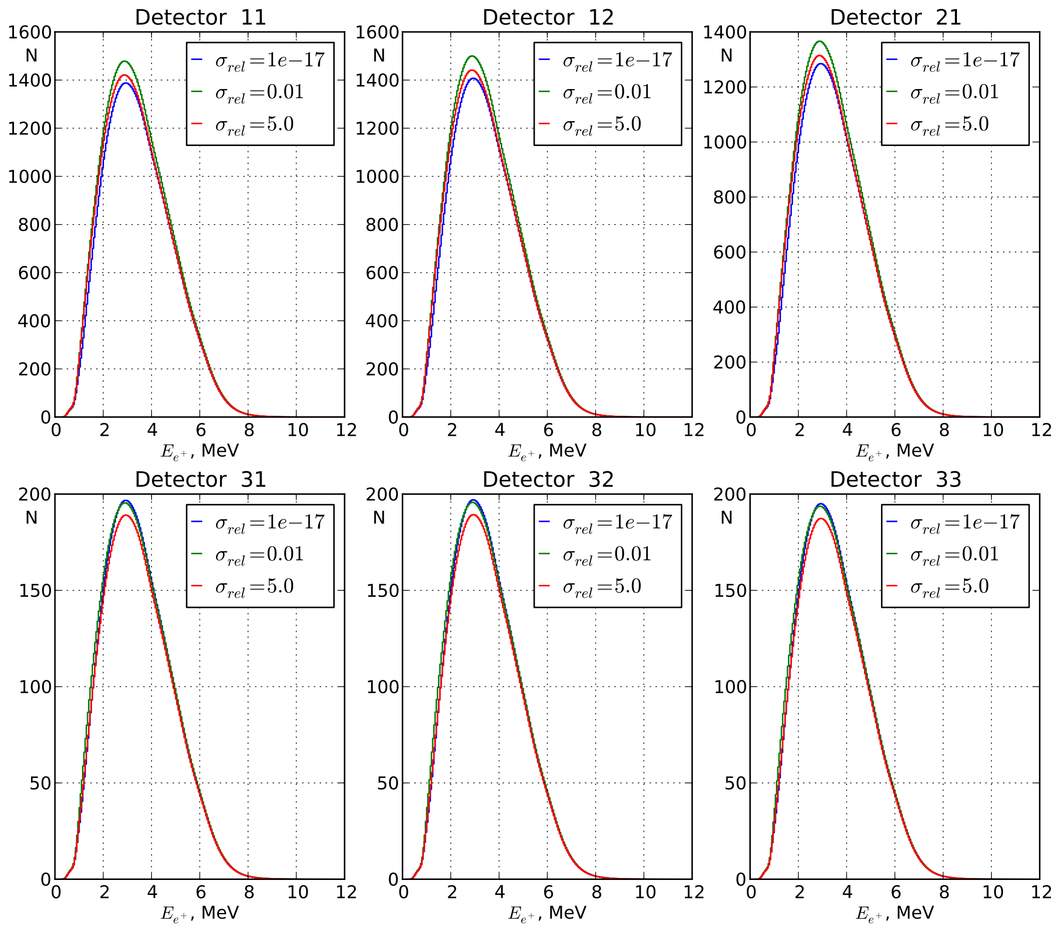

Figure 7.10: Energy spectra in near and far Daya Bay detectors for some values of σ_E.

$$\chi^2(\sigma_E, \sigma_E^{\text{fix}}) = \left(T(\sigma_E^{\text{fix}}) - T(\sigma_E)\right)^{\text{T}} V^{-1} \left(T(\sigma_E^{\text{fix}}) - T(\sigma_E)\right)$$

as a function of σ_E for predictions (T) made with some fixed values of σ_E^{fix}. As one see from these preliminary considerations Daya Bay has a good sensitivity to $\sigma_E \geq 0.1 - 0.2$.

We plan to perform a detailed statistical analysis of this problem taking into account that σ_E is not actually a constant but, rather, a Lorentz-invariant function of kinematical variables.

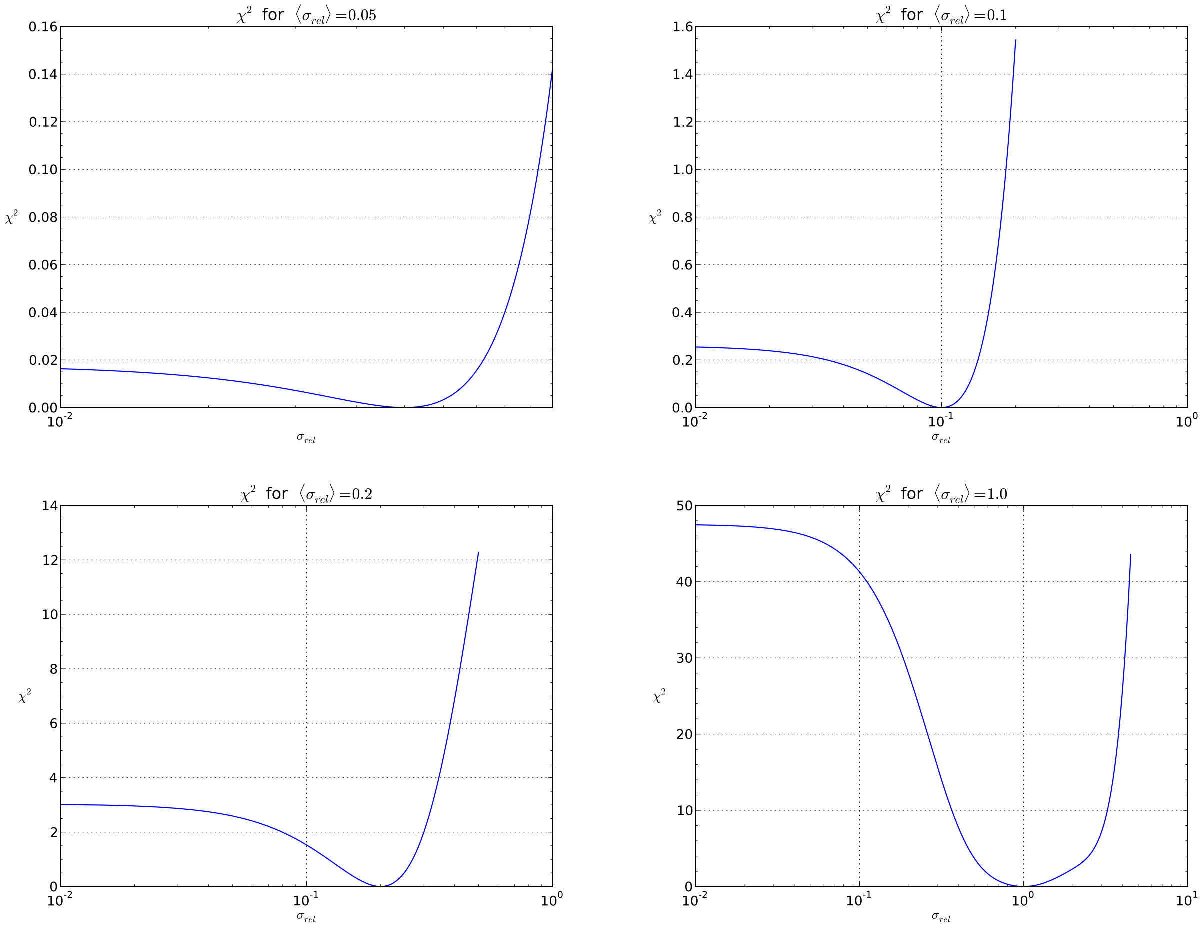

Figure 7.11: χ^2 vs σ_E for predictions made with some fixed values of σ_E^{fix}.

Measurement of reactor antineutrino spectra

The Daya Bay experiment, with the largest statistics of $\bar{\nu}_e$ events ever recorded and the high quality of the data, provides a unique possibility to measure the antineutrino spectra from reactors: both rate and shape information. Our preliminary considerations about this measurement and methods we will use are summarized below.

The number of antineutrinos emitted from a reactor per unit time interval is:

$$\frac{d^2 N_\nu(E_\nu, t)}{dE_\nu dt} = \frac{W_{\text{th}}(t)}{\langle e(t)\rangle} \sum_{i=1}^{N_{\text{iso}}} f_i(t) S_i(E_\nu). \tag{7.6}$$

Here $\frac{d^2 N_\nu(E_\nu,t)}{dE_\nu dt}$ gives the number of antineutrinos per unit time interval and energy interval of the antineutrino. $f_i(t)$ gives the fraction of isotope i in the overall number of nuclei decays, i.e. relative probability to observe a decay of isotope i, $\langle e(t)\rangle = \sum_i e_i f_i(t)$ is the average energy released by all isotopes. Each isotope releases an energy e_i. $W_{\text{th}}(t)$ gives the total energy released by the reactor per unit time interval (power). The ratio

$$N_f = \frac{W_{\text{th}}(t)}{\langle e(t)\rangle}$$

is the number of nuclei fissions per unit time interval. $S_i(E_\nu)$ is the energy spectrum of antineutrinos produced from decays of the given isotope i, i.e. the number density of antineutrino with given energy E_ν. Thus the number of antineutrino per energy interval dE_ν is $S_i(E_\nu)dE_\nu$.

The number of antineutrino interactions with one proton per unit time interval and unit energy interval is given by:

$$\frac{d^2N_{\text{IBD}}(E_\nu,t)}{dE_\nu dt} = \frac{d^2N_\nu(E_\nu,t)}{dE_\nu dt}\frac{\sigma_{\text{IBD}}(E_\nu)}{4\pi L^2}N_p(t)P_{\text{surv}}(E_\nu,L), \tag{7.7}$$

where $\sigma_{\text{IBD}}(E_\nu)$ is the cross-section of $\bar{\nu}+p\rightarrow n+e^+$ at a given antineutrino energy E_ν, N_p gives the number of protons in the detector (generally a function of time), L is the distance between the detector and reactor core. The factor

$$\Phi = \frac{1}{4\pi L^2}\frac{d^2N_\nu(E_\nu,t)}{dE_\nu dt}$$

is the antineutrino flux, i.e. the number of antineutrinos at the distance L from its source (reactor) per unit time interval and unit energy interval. $P_{\text{surv}}(E_\nu,L)$ gives survival probability of antineutrinos on the way from the reactor to the detector.

Once an antineutrino has interacted in the detector its energy is subjected to a number of transformations as follows:

$$E_\nu \rightarrow E_{\text{vis}}^{\text{true}} \rightarrow E_{\text{vis}}^{\text{IAV}} \rightarrow E_{\text{vis}}^{\text{NL}} \rightarrow E_{\text{vis}}^{\text{rec}} \tag{7.8}$$

where

$$E_{\text{vis}}^{\text{true}} = E_e + m_e \equiv E_{\text{vis}}, \tag{7.9}$$

and thus in terms of the visible energy we have

$$\frac{d^3N^d}{dE_{\text{vis}}dE_\nu dt} = \sum_r \frac{d^2N_\nu^{dr}(E_\nu,t)}{dE_\nu dt}\frac{d\sigma}{dE_{\text{vis}}}N_p^d(t)P_{\text{surv}}(E_\nu,L_{dr}) \tag{7.10}$$

The formula (7.6) can be easily generalized for r reactors and d detectors.

$$\frac{d^2N_\nu^{dr}(E_\nu,t)}{dE_\nu dt} = \frac{1}{4\pi L_{dr}^2}\frac{W_{\text{th}}^r(t)}{\langle e_r(t)\rangle}\sum_{i=1}^{N_{\text{iso}}} f_{ir}(t)S_i(E_\nu). \tag{7.11}$$

then

$$\begin{aligned} N_{mn}^d &= \int_{t_m}^{t_{m+1}} dt \int_{E_n}^{E_{n+1}} dE_{\text{vis}} \int_{E_\nu^{min}(E_{\text{vis}})}^{E_\nu^{max}(E_{\text{vis}})} dE_\nu \frac{d^3N^d}{dE_{\text{vis}}dE_\nu dt} \\ &= \sum_{r,i}\int_{t_m}^{t_{m+1}} dt \frac{W_{\text{th}}^r(t)}{\langle e_r(t)\rangle} f_{ir}(t)N_p^d(t)\int_{E_n}^{E_{n+1}} dE_{\text{vis}} \int_{E_\nu^{min}(E_{\text{vis}})}^{E_\nu^{max}(E_{\text{vis}})} dE_\nu \cdot \\ &\cdot \frac{S_i(E_\nu)}{4\pi L_{dr}^2}\frac{d\sigma(E_{\text{vis}},E_\nu)}{dE_{\text{vis}}}P_{\text{surv}}(E_\nu,L_{dr}) \end{aligned} \tag{7.12}$$

The integration over dE_ν is performed between $E_\nu^{min}(E_{\text{vis}})$ and $E_\nu^{max}(E_{\text{vis}})$ where

$$E_\nu^{\text{min}}(E_{\text{vis}}) = \frac{E_e + \widetilde{\Delta}}{1 - \frac{E_e}{m_p}(1 - v_e)}, \quad E_\nu^{\text{max}}(E_{\text{vis}}) = \frac{E_e + \widetilde{\Delta}}{1 - \frac{E_e}{m_p}(1 + v_e)} \tag{7.13}$$

where $\widetilde{\Delta} = \frac{m_n^2 - m_p^2 - m_e^2}{2m_p}$. Since, $m_p \gg E_e$, one can re-write (7.13) as follows

$$E_\nu^{\text{min,max}}(E_{\text{vis}}) \simeq (E_e + \widetilde{\Delta})[1 + \frac{E_e}{m_p}(1 \mp v_e)] = (E_e + \widetilde{\Delta})(1 + \frac{E_e}{m_p}) \mp (E_e + \widetilde{\Delta})\frac{E_e}{m_p}v_e \tag{7.14}$$

Denoting

$$\overline{E}_\nu(E_e) = (E_e + \widetilde{\Delta})(1 + \frac{E_e}{m_p}) \quad \triangle E_\nu/2 = (E_e + \widetilde{\Delta})\frac{E_e}{m_p}v_e$$

and taking into account (7.9), the integration limits in (7.12) can be written as

$$E_\nu^{min,max}(E_{\text{vis}}) = \overline{E}_\nu(E_{\text{vis}}) \mp \triangle E_\nu/2 \tag{7.15}$$

Now approximating the integral over dE_ν by rectangular method one can get

$$N_{mn}^d = \sum_{r,i} \int_{t_m}^{t_{m+1}} dt \frac{W_{\text{th}}^r(t)}{\langle e_r(t) \rangle} f_{ir}(t) N_p^d(t) \int_{E_n}^{E_{n+1}} dE_{\text{vis}} \triangle E_\nu \cdot \tag{7.16}$$
$$\frac{S_i(\overline{E}_\nu(E_{\text{vis}}))}{4\pi L_{dr}^2} \frac{d\sigma(E_{\text{vis}}, \overline{E}_\nu(E_{\text{vis}}))}{dE_{\text{vis}}} P_{\text{surv}}(\overline{E}_\nu(E_{\text{vis}}), L_{dr})$$

Following in the same fashion for the integral over dE_{vis} one can get

$$N_{mn}^d = \sum_{r,i} \int_{t_m}^{t_{m+1}} dt \frac{W_{\text{th}}^r(t)}{\langle e_r(t) \rangle} f_{ir}(t) N_p^d(t) \triangle E_n \triangle E_\nu \frac{S_i(\overline{E}_\nu(\overline{E}_n))}{4\pi L_{dr}^2} \cdot \tag{7.17}$$
$$\cdot \frac{d\sigma(\overline{E}_n, \overline{E}_\nu(\overline{E}_n))}{dE_{\text{vis}}} P_{\text{surv}}(\overline{E}_\nu(\overline{E}_n), L_{dr})$$

where $\triangle E_n \equiv E_{n+1} - E_n$ and $\overline{E}_n = (E_{n+1} + E_n)/2$.

By introducing the notations

$$P_{rim}^d \equiv \int_{t_m}^{t_{m+1}} dt \frac{W_{\text{th}}^r(t)}{\langle e_r(t) \rangle} f_{ir}(t) N_p^d(t) \tag{7.18}$$

$$S_{in} \equiv S_i(\overline{E}_\nu(\overline{E}_n)) \tag{7.19}$$

$$K_{nr}^d \equiv \triangle E_n \triangle E_\nu \frac{1}{4\pi L_{dr}^2} \frac{d\sigma(\overline{E}_n, \overline{E}_\nu(\overline{E}_n))}{dE_{\text{vis}}} P_{\text{surv}}(\overline{E}_\nu(\overline{E}_n), L_{dr}) \tag{7.20}$$

equation (7.17) has a compact form

$$N_{mn}^d = \sum_{r,i} P_{rim}^d S_{in} K_{nr}^d = \sum_i A_{imn}^d S_{in} \tag{7.21}$$

where

$$A^d_{imn} = \sum_r P^d_{rim} K^d_{nr} \tag{7.22}$$

Equation (7.21) can be written in a matrix form if we split the indices into two groups and duplicate n as follows $A^{ndm}_i = A^{ndm}_{in}$, and re-write A as:

$$A^{ndm}_{in} = A^{ndm}_{ik}\delta_{nk}$$

This allows us to introduce two superindices $I = (i, k)$ and $J = (n, d, m)$ and write:

$$N_J = \sum_I A^J_I S_I \tag{7.23}$$

or in matrix notation

$$\mathbf{N} = A\mathbf{S} \tag{7.24}$$

The solution of (7.24) is

$$\mathbf{S} = A^{-1}\mathbf{N} \tag{7.25}$$

The proposed scheme allows us to **separately** measure energy spectra of each isotope. The necessary condition for this method to succeed is the existence and stability of the inverse matrix A. This requires having enough data as a function of time when the reactor fuel burning and filling information are present in the data. Apparently, the suggested scheme requires taking into account the background systematic error study and their propagation. We plan to perform such an analysis within this proposal.

7.B Contribution of JINR Members

7.B.1 Muon veto based on plastic scintillator option

When planning the Daya Bay experiment plastic scintillator strips were suggested by JINR as a muon veto option [6] for top and in-water tracking systems. The parameters of this system are shown in Table 7.7. This option was abandoned in favor of RPC muon veto option.

Almost all the scintillators would be of the same type: 5.25 m$\times$0.2 m$\times$0.01 m extruded polystyrene, co-extruded with a coating of TiO_2-doped PVC. Five 1 mm Kuraray Y-11(200) S-type wavelength-shifting fibers will be glued into 2 mm deep $\times$ 1.6 mm wide grooves in the plastic using optical glue. Six such scintillators are to be placed in a single frame and read out as one 1.2 m-wide unit. Figure 7.12 shows the cross section of one scintillator.

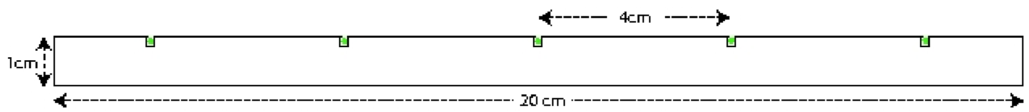

Figure 7.12: Cross-section of a single scintillator strip.

A $1\frac{1}{8}$-inch photomultiplier tube such as a Hamamatsu R6095 or Electron Tubes 9128B is used to read out 30 fibers on each end of the six-scintillator module. The PMTs are run at positive HV, via a system similar to that discussed in [6].

Name	value	unit
number of strips	5304	
length of strip	5.25	m
width of strip	0.2	m
thickness of strip	1	cm
fibers/strip	5	
length of fiber	7.25	m
diameter of fiber	1	mm
strips/module	6	
modules (full/top only)	884/295	
phototubes (full/top only)	1768/530	

Table 7.7: Parameters of scintillator strip detectors

7.B.2 Liquid scintillator development

The development of the liquid scintillators (C,H-based, LS, and gadolinium-loaded, Gd-LS), suitable for using in the large-scale Daya Bay experiment was the one of the directions of the JINR team activity.

The solution of such a complex task included a series of logical steps:

- selection of the liquid solvent;
- selection of gadolinium additive;
- optimization of qualitative and quantitative composition of the scintillators;
- study of the properties of the resulting compositions;
- study of long-term stability of the scintillators;
- development of the production diagram.

JINR responsibility extended to:

- optimization of the qualitative and quantitative composition of the LS;
- study of scintillation and optical properties of the LS;
- study the efficiency of thermal neutrons registration by Gd-LS and LS;
- participation in the development of the production diagram of the LS and Gd-LS;
- production of 1,500 kg of 2,5-diphenyloxazole (PPO), the primary additive for LS and Gd-LS.

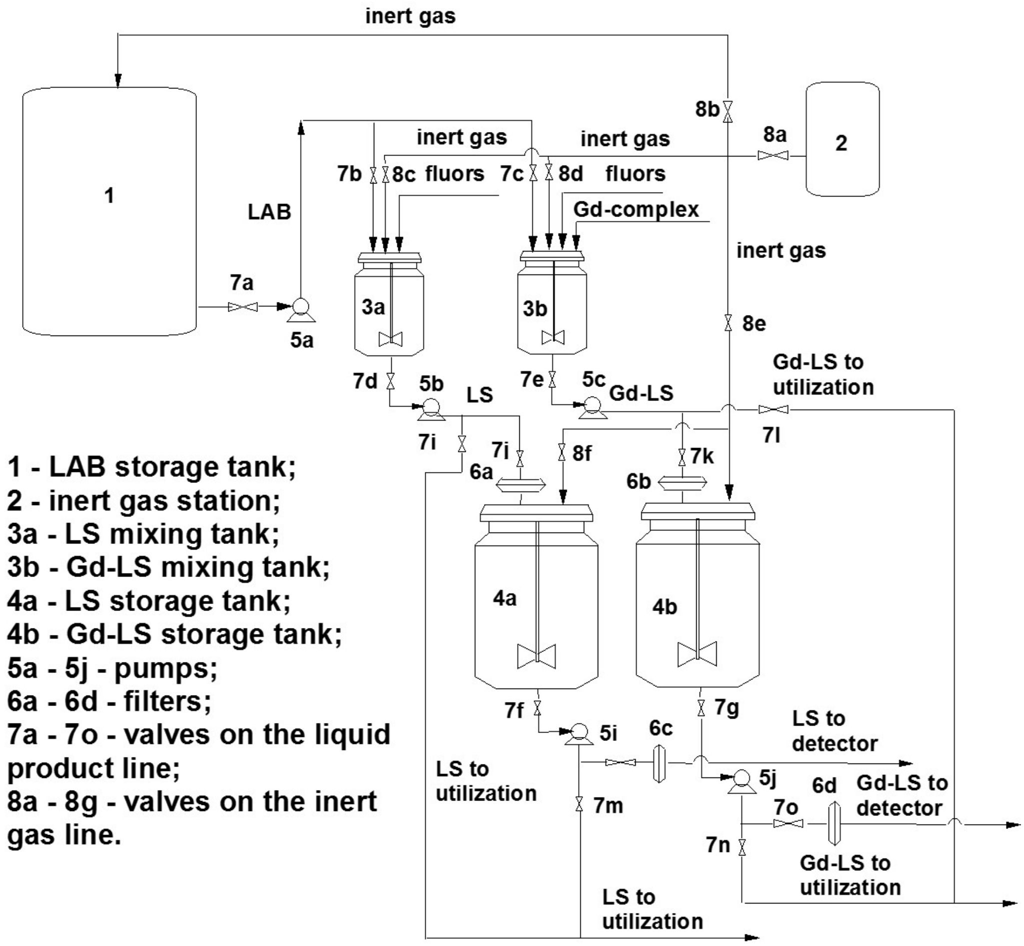

Figure 7.13: The LS and Gd-LS production diagram.

We studied the spectral and optical properties and methods of purification of linear alkylbenzene, a solvent, proposed as the base for LS and Gd-LS. The newly developed scintillation materials exhibit high light output values, transparency and efficiency for thermal neutrons.

The JINR group developed the initial version of the production diagram (Fig. 7.13) of the LS and Gd-LS and justified the selection of the equipment for their production.

7.B.3 Fast neutron detection method

The method of tagging fast neutron events based on Flash ADC signals was suggested in [25].

The 192 photo-multipliers (PMT) installed on the internal wall of a LS tank are used in the reconstruction. The analog signal from each PMT is digitized with a 100 ns integration step to produce the digital signal (ADC). Therefore, each PMT can be characterized by the total charge it detects (q) and the time of the first detected photon (t^0). Thus, an energy release in AD seen by PMTs is characterized by a set of charges (q_k) and front times (t^0_k)

where the index k runs from 1 to 192.

Besides the ADC output the PMTs are grouped together in another readout called Fast (or Flash) ADC (FADC) with 1 ns integration time. 192 PMTs are divided into 6 chains containing 32 PMTs each. Every chain is made of 8 rings and 4 columns of PMTs. The connection scheme, currently implemented in Daya Bay FADC, is shown in the left panel of Fig. 7.14. A possible alternative FADC connection scheme with 6 chains, each composed of 4 rings and 8 columns of PMTs, is shown in the middle panel of the same figure. The original connection of PMTs is shown in the right panel of Fig. 7.14. The output of each FADC chain enumerated by an index (f) is charge (or voltage) as a function of time t: $q_{\rm f}(t)$. The index f runs from 1 to 6.

Fast neutrons mimic the $\bar{\nu}_e$ signal (eq. (7.3)) due to scattering off of free protons which subsequently produce the scintillation light. The idea we have in mind is that the same fast neutron can have a non-negligible multiple scattering off of protons, thus producing multiple prompt flashes with δt too small to be distinguished by ADC but big enough to be identified by FADC, even taking into account the fact that multiple PMTs are connected to a single FADC channel.

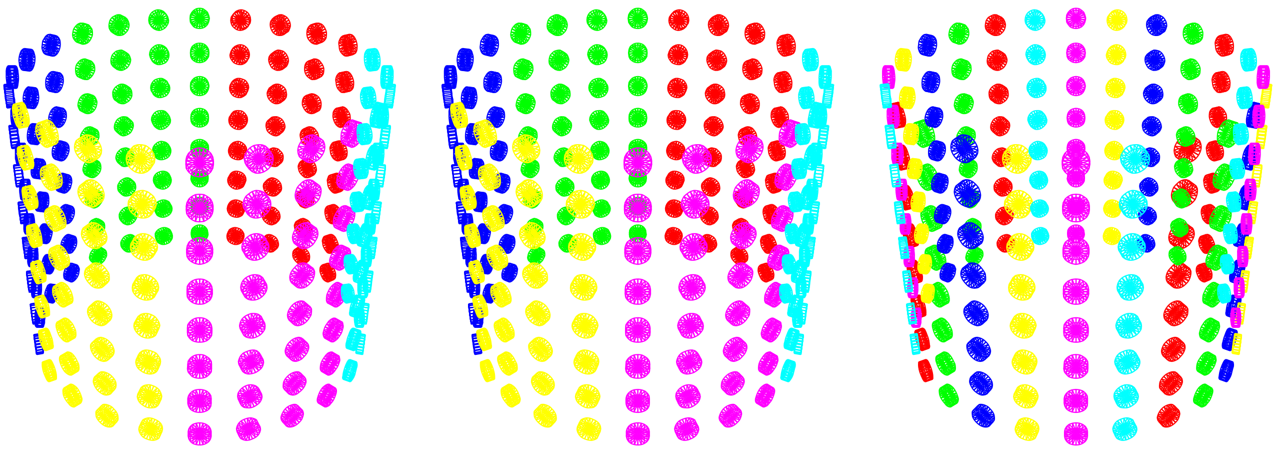

(a) 8 rings 8×4 4 columns (b) 4 rings $\times$ 8 columns (c) 4 rings $\times$ 8 columns

Figure 7.14: PMT connection scheme in FADC chains. Current connection scheme used on far site detectors (a), alternative connection scheme (b), original Daya Bay FADC connection scheme used on near detectors (c).

Therefore, one has at hand two sets of data from ADC and FADC:

- charge seen by a PMT $q_{\rm k}$ and its front time ($t^0_{\rm k}$) from ADC. The index k runs between $(1, 192)$
- charge $q_{\rm f}(t)$ seen by a chain of PMTs grouped in one FADC readout. The index f runs between $(1, 6)$. The time variable is digitized with a 1 ns step.

These data are used to reconstruct the light production "point" and identify multiple flashes of light (which can be used to tag fast neutrons or similar phenomena).

Based on detailed Daya Bay detector MC it was shown that in order to detect fast neutrons by multiple pulse identification we need a resolution on the order of 5 ns. To test our hypothesis we have built a simple detector MC application which can simulate a flash of given intensity and shape inside the detector, calculate expected signal on each ADC/FADC channel and simulated a real signal using random fluctuations. We build the likelihood function $\mathcal{L}_{\text{fadc}}$, which is a joint probability to observe a time & charge distribution of FADC chains for given flashes of light inside detector.

We have limited ourselves to a study of possible identification of a single or double pulse signal structure. We proceed as follows. We simulate two types of events:

- single flash events. These events are simulated as follows. The flash position is simulated uniformly in the AD volume and the total number of photons produced in the flash is scanned.

- double flash events. The simulation is done as follows. The first flash is simulated uniformly in the AD volume. The second flash, with the total number of photons being half of that of the first flash, is simulated with a random vertex position within a sphere corresponding to a random walk of a neutron. The time difference between two flashes varies between 3 ns and 10 ns.

A reconstruction code should attempt to reconstruct the number of flashes, time difference between them and the number of photons produced in each flash. There are four possible outcomes of such a reconstruction. Simulated single flash events can be reconstructed as a single or double flash event. Similarly, simulated double flash events can be reconstructed as a single or double flash event. Here we do not report results of our reconstruction code. Instead we examine the differences in the likelihood functions for these four outcomes. To mimic the results of the reconstruction code we proceed as follows:

- For events **simulated as single flash**

$\underline{1 \to 1}$ and reconstructed as single flash we just assign true simulated values instead of reconstructed values for the number of photons, flash position and starting time:

$$\begin{aligned} N_{\gamma,1}^{\text{tot, rec}} &= N_{\gamma,1}^{\text{tot, true}} \\ \mathbf{R}_1^{\text{rec}} &= \mathbf{R}_1^{\text{true}}. \end{aligned} \tag{7.26}$$

$\underline{1 \to 2}$ and reconstructed as double flash events we proceed as follows. The number of photons in the first flash is reconstructed as $2/3 \cdot N_{\gamma,1}^{\text{tot, true}}$, 3D-position and starting time are assigned to the true position and time respectively. The second flash is reconstructed in the same position with a random time delay between 3 and 10 ns. The number of photons in the second flash is assumed to be $1/3 \cdot N_{\gamma,1}^{\text{tot, true}}$. Thus, in the two reconstructed flashes we preserve the ratio two-to-one for the number of photons in the first and second flashes.

- For events simulated as a double flash we also consider both possibilities for the reconstruction outcomes:

$\underline{2 \to 1}$ reconstructed as a single flash. In this case the reconstructed values are calculated as follows:

$$\begin{aligned} N_{\gamma,1}^{\text{tot, rec}} &= N_{\gamma,1}^{\text{tot, true}} + N_{\gamma,2}^{\text{tot, true}}, \\ \mathbf{R}_1^{\text{rec}} &= \left(N_{\gamma,1}^{\text{tot, true}} + N_{\gamma,2}^{\text{tot, true}}\right)^{-1} \left(N_{\gamma,1}^{\text{tot, true}}\mathbf{R}_1^{\text{true}} + N_{\gamma,2}^{\text{tot, true}}\mathbf{R}_2^{\text{true}}\right) \end{aligned} \tag{7.27}$$

$\underline{2 \to 2}$ reconstructed as double flash. In this case the reconstructed values are calculated as follows:

$$\begin{aligned} N_{\gamma,1}^{\text{tot, rec}} &= N_{\gamma,1}^{\text{tot, true}}, \quad N_{\gamma,2}^{\text{tot, rec}} = N_{\gamma,2}^{\text{tot, true}}, \\ \mathbf{R}_1^{\text{rec}} &= \mathbf{R}_1^{\text{true}}, \quad \mathbf{R}_2^{\text{rec}} = \mathbf{R}_2^{\text{true}}, \\ t_{\text{p},1}^{\text{rec}} &= t_{\text{p},1}^{\text{true}}, \quad t_{\text{p},2}^{\text{rec}} = t_{\text{p},2}^{\text{true}} \end{aligned} \tag{7.28}$$

In order to study FADC's ability to resolve between single and double flash events we build the following variables:

$$\ln\mathrm{P_n} = \ln\frac{\mathcal{L}_{\mathrm{n}\to 2}}{\mathcal{L}_{\mathrm{n}\to 1}}, \tag{7.29}$$

where $\mathcal{L}_{n\to k}$ is the likelihood probability to reconstruct k flashes for an event simulated with n flashes. One can expect that P_1 should be significantly smaller than one (and, accordingly, $\ln\mathrm{P}_1$ should be smaller than zero) because two flashes should not fit well to time and charge distributions seen by FADC chain due to a single flash event. Conversely, P_2 should be larger than one (and, accordingly, $\ln\mathrm{P}_2$ should be larger than zero) because two flashes better fit a double flash event if the parameters are guessed correctly.

The free parameters are: $N_{\gamma,(1,2)}^{\text{tot, true}}, \mathbf{R}_{1,2}^{\text{true}}, t_{\text{p},1,2}^{\text{true}}$. In Figs. 7.15a, 7.15b, we show distributions of the $\ln\mathrm{P_n}$ variable for single flash and double flash events for the total number of photons produced $N_{\gamma}^{\text{tot, true}} = 10^4, 5\cdot 10^4$, respectively, which is roughly equivalent to the Daya Bay detection threshold and the middle of the antineutrino spectra (∼1 MeV and ∼5 MeV). The plots are shown for various time intervals between two flashes. Let us discuss these plots in some detail.

- One might observe that we can resolve between single and double flash events even when close to the threshold energy.
- The separation between single and double flash events suffers from a statistical fluctuation near the threshold. The separation power becomes more apparent when the number of produced photons increases.
- Not only can one disentangle a single flash event from a double flash event, but one can also make a reasonable estimate of the time difference between two flashes.

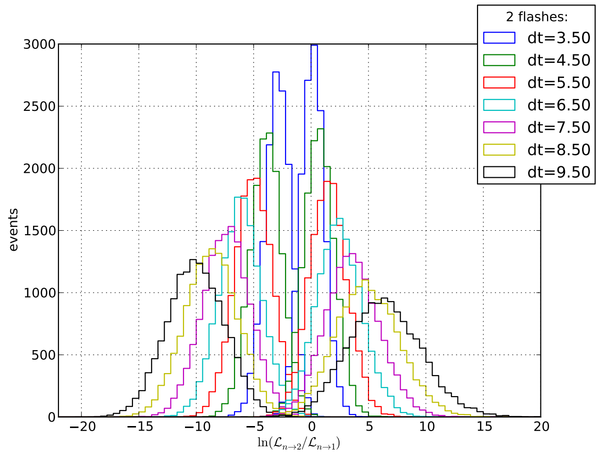

(a) $\ln\mathrm{P_n}$ variable for single flash (dashed) and double flash (solid) events. The total number of photons produced in one (or both) flash(s) is N^{0}.6tot, true$_{\gamma} = 10^4$.

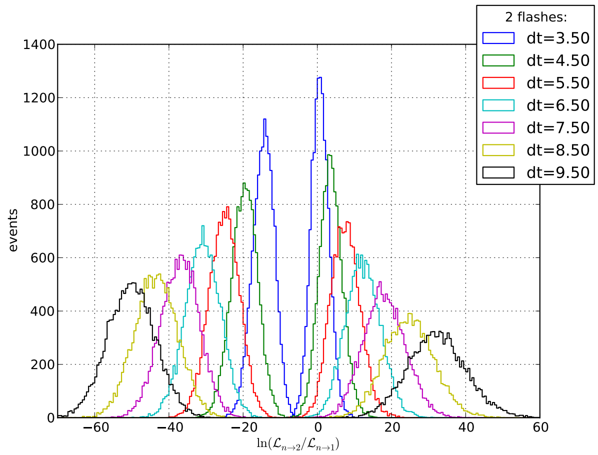

(b) $\ln\mathrm{P_n}$ variable for single flash (dashed) and double flash (solid) events. The total number of photons produced in one (or both) flash(s) is $N_{\gamma}^{\text{tot, true}} = 5 \cdot 10^4$.

7.B.4 dybOscar package

Daya Bay analysis policy requires several groups making independent analyses. Each group may use their own selection cuts, energy reconstruction, background estimation, and analysis techniques. All groups analyze the same set of partly blinded data input with blinded reactor flux, detector target mass, and reactor-detector baselines. The data is unblinded only when all groups cross-check their results and eliminate all inconsistencies. Our group, with our own oscillation analysis package, takes part in the oscillation analysis.

A dedicated software package dybOscar was developed by JINR Daya Bay team[1] for the oscillation analysis of the Daya Bay data.

The package implements all steps of reactor antineutrino spectra prediction for the Daya Bay experiment with possibility to tune and change all possible model parameters. The main programming languages are C++ and python. C++ is used to implement computationally expensive core functionality while python is used as framework and macro language. The package is designed to be modular with ability to substitute different parts of the calculation.

dybOscar is currently used for the following tasks:

1. Oscillation analysis via χ^2 minimization. Based on 6AD data.

2. Sterile neutrino search via Feldman-Cousins approach.

3. Reactor antineutrino spectra measurement.

4. Quantum decoherence study.

[1] with participation of Wei Wang

The package contains several oscillation probabilities: 2ν, 3ν, and $3+1\nu$ cases and oscillation probability with quantum decoherence effects.

The reactor antineutrino flux and spectra are calculated based on information from the Daya Bay power plant: measured daily thermal power W_{th} data and simulated daily relative isotopic fission fractions f_i:

$$\frac{d^2N^{\text{iso}}(E,t)}{dEdt} = \sum_i \left(\frac{W_{\text{th}}(t)}{\sum_j f_j(t) e_j} f_i(t)\, S_i(E)\, c_i^{\text{ne}}(E,t) \right) + S_{\text{SNF}}(E,t), \tag{7.30}$$

where S_i are the neutrino spectra of fissile isotopes. As is usually the case for reactor antineutrino experiments, for ^{235}U, ^{239}Pu and ^{241}Pu isotope spectra S_i we use spectra calculated by Huber et al. [26] based on measurements by Schreckenbach et al. [27–29]. Since these measurements are based only on a short time exposure these spectra lack the contribution of isotopes with life-time longer than exposure time ($\geqslant$12 hours). For the reactor experiments irradiation time is of the order of 1 reactor cycle duration ($\sim$1 year). To take this into account an off-equilibrium correction c_i^{ne} is used from [30]. For ^{238}U spectrum the calculation by Müller et al. [30] is used. Average energy deposited per isotope fission e_i is taken from [31]. S_{SNF} is the contribution from spent nuclear fuel from [32], which doesn't depend on current reactor thermal power.

The IBD cross-section is calculated using the first-order formula from [33]. The number of events in each energy bin for each detector is obtained by integrating the IBD reaction cross section with reactor antineutrino flux and oscillation probability:

$$\frac{dN_{\text{IBD}}(E_e,t)}{dt} = \int_{-1}^{1} d\cos\theta \int_{E_1}^{E_2} dE_e\, \frac{d\sigma_{\text{IBD}}(E_\nu,\cos\theta)}{d\cos\theta} \frac{d^2N_\nu^{\text{iso}}(E_\nu,t)}{dE_\nu dt} \frac{dE_\nu}{dE_e} P_{\text{sur}}(L,E_\nu)$$

with accurate kinematic treatment. The integrals are computed numerically via Gauss-Legendre quadratures with number of reference points depending on the P_{sur} oscillation speed in order to save computation time while keeping the precision.

For the estimation of oscillation parameters we use two approaches: χ^2 estimator and maximum likelihood estimator.

Standard χ^2 with constant covariance matrix and nuisance parameters:

$$\chi^2(\boldsymbol{\theta},\boldsymbol{\eta}) = (\mathbf{D}-\mathbf{T})^T\mathbf{V}^{-1}(\mathbf{D}-\mathbf{T}) + \left[\boldsymbol{\eta}^T\mathbf{V}_{\boldsymbol{\eta}}^{-1}\boldsymbol{\eta}\right] \tag{7.31}$$

where $\boldsymbol{\theta}$ represents unknown oscillation parameters, $\boldsymbol{\eta}$ are known model and detector parameters with uncertainties. D are observed IBD-like events, $\mathbf{T}$ gives theoretical prediction as functions of minimization parameters. $\mathbf{V}$ is a covariance matrix computed for a chosen set of parameter values. $\mathbf{V}$ does not depend on minimization parameters. $\mathbf{V}_{\boldsymbol{\eta}}$ is the usual diagonal error matrix for the known parameters with uncertainties ($\mathbf{V}_{ii}^{\boldsymbol{\eta}} = \sigma_{\eta_i}^2$).

Maximum likelihood estimator χ^2_* with parameter-dependent covariance matrix and nuisance parameters:

$$\chi^2_*(\boldsymbol{\theta},\boldsymbol{\eta}) = (\mathbf{D}-\mathbf{T})^T\mathbf{V}^{-1}(\mathbf{D}-\mathbf{T}) + \left[\boldsymbol{\eta}^T\mathbf{V}_{\boldsymbol{\eta}}^{-1}\boldsymbol{\eta}\right] + \ln\det\mathbf{V} \tag{7.32}$$

This approach is used because it was found that χ^2 with parameter dependent covariance matrix is not a maximum likelihood estimator and may give biased values for the minimization parameters. It especially affects global normalization for which the bias may be up to 5% (overestimation) for current analysis. $\mathbf{V}$ are the functions of minimization parameters.

Minimization of both functions is executed in a sequence for several iterations with the covariance matrix updated based on best fit values of previous iteration. Both approaches are found to give consistent results between each other.

The covariance matrix is calculated in the first-order approximation according to standard formula:

$$V = V_{\text{stat}} + V_{\text{sys}}$$
$$(V_{\text{sys}})_{ij} \approx \sum \frac{\partial T_i}{\partial \boldsymbol{\eta}_k} \frac{\partial T_j}{\partial \boldsymbol{\eta}_m} V^{\eta}_{km},$$

where T_i is the prediction in the i-th bin, η_k gives the k-th nuisance parameter with uncertainty $\sqrt{V_{kk}}$ and possible correlations with other nuisance parameters, described by covariance matrix V^{η}.

In order to build the covariance matrix we take into account more than 400 individual uncertainties:

1. Reactor power, fission fractions, e/fission, SNF flux
2. $\overline{\nu}_e$ isotopes spectra uncertainties, off-equilibrium correction
3. AD normalizations
4. Energy scale, resolution, IAV correction
5. Background rates

7.B.5 $3-\nu$ oscillation analysis

Using dybOscar we conduct our own rate + shape oscillation analysis. The current analysis is based on data from 24 December 2011 to 28 of July 2012 and contains data from 6 antineutrino detectors.

The covariance matrix calculated for this period is shown on Fig. 7.16. We obtain the best fit oscillation parameters:

$$\sin^2 2\theta_{13} = 0.089 \pm 0.008 \tag{7.33}$$
$$\Delta m^2_{31} = (2.62 \pm 0.19) \times 10^{-3}\text{eV}^2 \tag{7.34}$$

The values themselves and confidence contours are compatible with official Daya Bay result highlighted in [4]. The contours are shown on Fig. 7.17.

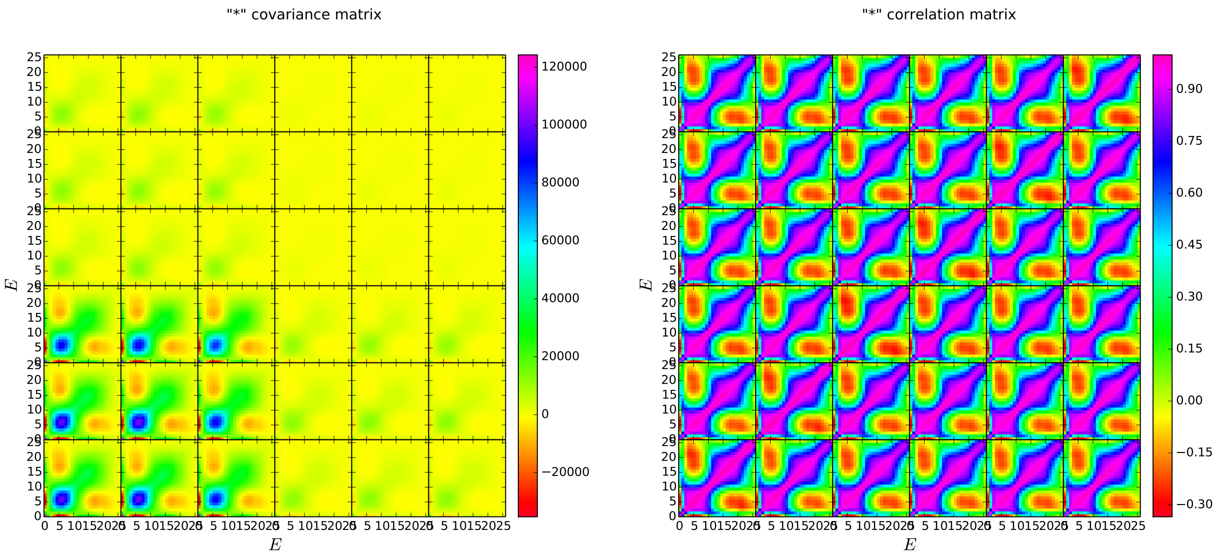

(a) Covariance matrix

(b) Correlation matrix

Figure 7.16: Covariance (a) and correlation (b) matrices used for analysis.

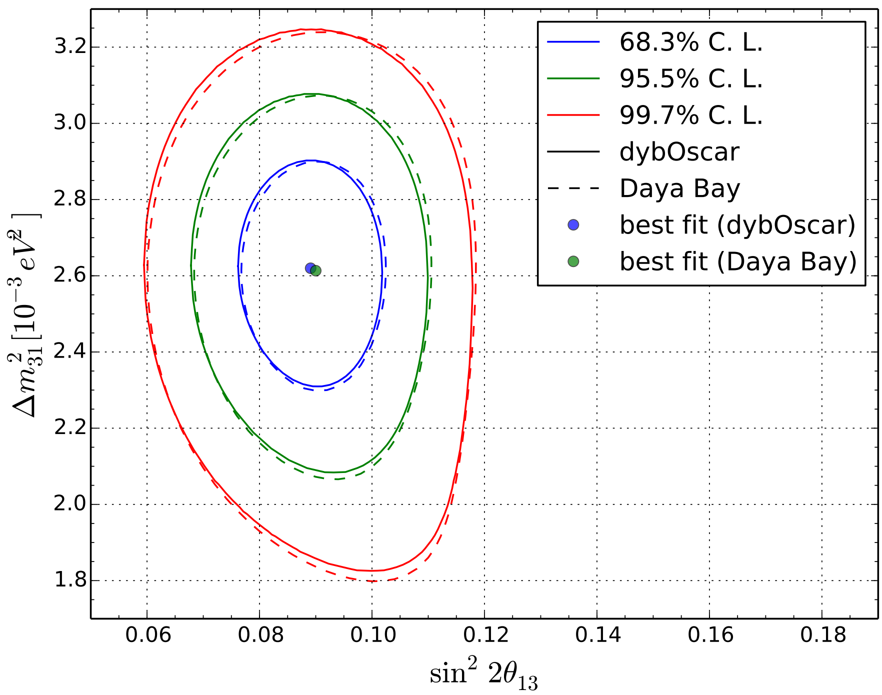

Figure 7.17: Allowed regions for neutrino oscillation parameters.

7.B.6 Search for sterile neutrino

In Fig. 7.18 we display $1, 2, 3\ \sigma$ exclusion contours calculated with Feldman-Cousins method produced by the JINR dybOscar package. The theoretical normalization uncertainty was taken to be 2.7%. The best fit point reads

$$\sin^2 2\theta_{14} = 0.089, \Delta m^2_{41} = 0.213\text{eV}^2$$

This result is one of our contributions to the Daya Bay Collaboration paper [34].

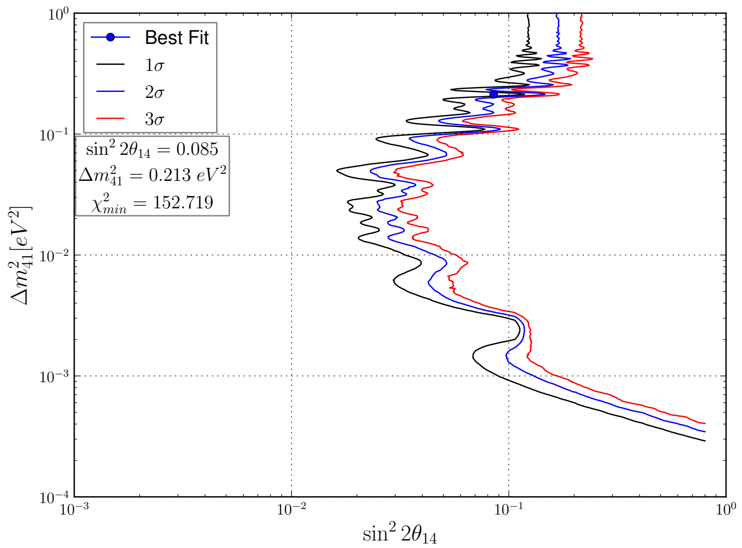

Figure 7.18: $1, 2, 3\ \sigma$ contours calculated with Feldman-Cousins method for the Daya Bay data assuming 2.7% theory normalization uncertainty. The best fit point is also shown.

References

[1] M. Apollonio et al. “Search for neutrino oscillations on a long baseline at the CHOOZ nuclear power station”. In: *Eur.Phys.J.* C27 (2003), pp. 331–374. arXiv: hep-ex/0301017 [hep-ex].

[2] F.P. An et al. “Observation of electron-antineutrino disappearance at Daya Bay”. In: *Phys.Rev.Lett.* 108 (2012), p. 171803. arXiv: 1203.1669 [hep-ex].

[3] F.P. An et al. “Improved Measurement of Electron Antineutrino Disappearance at Daya Bay”. In: *Chin.Phys.* C37 (2013), p. 011001. arXiv: 1210.6327 [hep-ex].

[4] F.P. An et al. “Spectral measurement of electron antineutrino oscillation amplitude and frequency at Daya Bay”. In: *Phys.Rev.Lett.* 112 (2014), p. 061801. arXiv: 1310.6732 [hep-ex].

[5] Pietro Antonioli et al. "SNEWS: The Supernova Early Warning System". In: *New J.Phys.* 6 (2004), p. 114. arXiv: astro-ph/0406214 [astro-ph].

[6] Xinheng Guo et al. "A Precision measurement of the neutrino mixing angle θ_{13} using reactor antineutrinos at Daya-Bay". In: (2007). arXiv: hep-ex/0701029 [hep-ex].

[7] F.P. An et al. "A side-by-side comparison of Daya Bay antineutrino detectors". In: *Nucl.Instrum.Meth.* A685 (2012), pp. 78–97. arXiv: 1202.6181 [physics.ins-det].

[8] Ji-Lei Xu et al. "Design and preliminary test results of Daya Bay RPC modules". In: *Chin.Phys.* C35 (2011), pp. 844–850.

[9] Gonchar M. et al. "A new result of θ_{13} from Daya Bay and a future project Daya Bay II". In: *Proceedings of the DAE Symposium on Nuclear Physics* 57 (2012), pp. 54–58. URL: http://www.sympnp.org/proceedings/57/I9.pdf.

[10] D.V. Naumov. "A short review of most interesting recent results in neutrino physics". In: *Phys. Part. Nucl. Lett.* 9 (2012), pp. 691–695.

[11] D.V. Naumov. "On the Theory of Wave Packets". In: *Phys.Part.Nucl.Lett.* (2013). arXiv: 1209/1717 [quant-ph].

[12] Vadim A. Naumov and Dmitry S. Shkirmanov. "Extended Grimus-Stockinger theorem and inverse square law violation in quantum field theory". In: *Eur.Phys.J.* C73 (2013), p. 2627. arXiv: 1309.1011 [hep-ph].

[13] Naumov D. V. "Precise $\sin^2 2\theta_{13}$ measurement of the Daya Bay experiment". LPP JINR invited seminar — 20.12.2012. 2012.

[14] Naumov D. V. "Measurement of θ_{13} neutrino mixing angle in Daya Bay experiment". LNP JINR seminar — 14.03.2012. 2012.

[15] Naumov D. V. "Neutrino physics: status and perspectives". Russian. INR seminar, Novosibirsk. 03.08.2012. 2012.

[16] Naumov D. V. "Neutrino mixing: status and perspectives". LNP JINR seminar — 08.02.2013. 2013.

[17] Gonchar M. O. "Precise $\sin^2 2\theta_{13}$ measurement by the Daya Bay reactor neutrino experiment". International Symposium on Nuclear Physics (SYMPNP2012) – Delhi, India – 12.2012. 2012.

[18] Gonchar M. O. "Precise $\sin^2 2\theta_{13}$ measurement of the Daya Bay experiment". JINR Scientific Council – JINR, Dubna – 22.02.2013. 2013.

[19] Gonchar M. O. "Precise $\sin^2 2\theta_{13}$ measurement of the Daya Bay experiment". 38th meeting of the PAC for Particle Physics – JINR, Dubna – 29.01.2013. 2013.

[20] Gonchar M. O. "A new result of θ_{13} from Daya Bay and a future project Daya Bay II". The International Workshop on Non-Accelerator New Physics (NANPino2013) – Valday, Russia — 06.2013. 2013.

[21] Naumov D. V. "Current status of neutrino mixing and masses". The International Workshop on Non-Accelerator New Physics (NANPino2013) – Valday, Russia — 06.2013. 2013.

[22] M. Fallot et al. “New antineutrino energy spectra predictions from the summation of beta decay branches of the fission products”. In: *Phys.Rev.Lett.* 109 (2012), p. 202504. arXiv: 1208.3877 [nucl-ex].

[23] N. Haag et al. “Experimental Determination of the Antineutrino Spectrum of the Fission Products of ^{238}U”. In: (2013). arXiv: 1312.5601 [nucl-ex].

[24] Gary J. Feldman and Robert D. Cousins. “A Unified approach to the classical statistical analysis of small signals”. In: *Phys.Rev.* D57 (1998), pp. 3873–3889. arXiv: physics/9711021 [physics.data-an].

[25] I.V. Butorov et al. “Reconstruction with ADC and FADC in Daya Bay”. In: (). DocDB-8439.

[26] Patrick Huber. “On the determination of anti-neutrino spectra from nuclear reactors”. In: *Phys.Rev.* C84 (2011), p. 024617. arXiv: 1106.0687 [hep-ph].

[27] F. Von Feilitzsch, A.A. Hahn, and K. Schreckenbach. “Experimental Beta Spectra From Pu-239 And U-235 Thermal Neutron Fission Products And Their Correlated Anti-Neutrinos Spectra”. In: *Phys.Lett.* B118 (1982), pp. 162–166.

[28] K. Schreckenbach et al. “Determination Of The Anti-Neutrino Spectrum From U-235 Thermal Neutron Fission Products Up To 9.5-MeV”. In: *Phys.Lett.* B160 (1985), pp. 325–330.

[29] A.A. Hahn et al. “Anti-neutrino Spectra From ^{241}Pu and ^{239}Pu Thermal Neutron Fission Products”. In: *Phys.Lett.* B218 (1989), pp. 365–368.

[30] Th.A. Mueller et al. “Improved Predictions of Reactor Antineutrino Spectra”. In: *Phys.Rev.* C83 (2011), p. 054615. arXiv: 1101.2663 [hep-ex].

[31] V. Kopeikin, L. Mikaelyan, and V. Sinev. “Reactor as a source of antineutrinos: Thermal fission energy”. In: *Phys.Atom.Nucl.* 67 (2004), pp. 1892–1899. arXiv: hep-ph/0410100 [hep-ph].

[32] V. Kopeikin, L. Mikaelyan, and V. Sinev. “Antineutrino background from spent fuel storage in sensitive searches for theta(13) at reactors”. In: *Phys.Atom.Nucl.* 69 (2006), pp. 185–188. arXiv: hep-ph/0412044 [hep-ph].

[33] P. Vogel and John F. Beacom. “Angular distribution of neutron inverse beta decay, anti-neutrino(e) + p —> e+ + n”. In: *Phys.Rev.* D60 (1999), p. 053003. arXiv: hep-ph/9903554 [hep-ph].

[34] F.P. An et al. “Search for a Light Sterile Neutrino at Daya Bay”. In: *submitted to Phys.Rev.Lett.* (2014).

Chapter 8

GEMMA Experiment

Editors: V. Brudanin, D. Medvedev, M. Shirchenko

Project Title

Germanium **E**xperiment Searching for **M**agnetic **M**oment of **A**ntineutrino

Project Leaders

- JINR: V.B. Brudanin, V.G. Egorov
- ITEP: A.S. Starostin

Abstract

The goal of the GEMMA project is to measure one of the fundamental parameters of the neutrino, its magnetic moment. The project is realized by studying the antineutrino-electron scattering using HPGe detectors located close to the commercial water-moderated reactor with a thermal power of 3 GW. In the case of observing a nonzero magnetic moment New Physics will be revealed. Moreover, the problem of the neutrino nature could be solved and the scale of the New Physics Λ parameter could be better understood. The experimental results are also of great importance for various astrophysical models and their restrictions. At present experiment GEMMA has the world's best result (see Review of Particle Physics by PDG [1]).

keywords: Reactor antineutrino, Neutrino magnetic moment

Project Members From JINR

V. Belov, V. Brudanin, V. Egorov, D. Medvedev, E. Shevchik, M. Shirchenko, I. Zhitnikov

Project Duration. Approval Date(s)

Data taking with GEMMA-I	2005 – 2009
Project GEMMA-II PAC approval (within JINR Theme #1100)	2009
Start of data taking (planned)	2014

List of Participating Countries and Institutions

JINR — Joint Institute for Nuclear Research, Dubna, Russia; ITEP — Institute of Experimental and Theoretical Physics, Moscow, Russia

8.1 Project Description

8.1.1 Fundamental Scientific Problem Addressed by the Project

In the Standard Model, minimally extended by non-zero neutrino masses (MSM), a very small neutrino magnetic moment (NMM) value, proportional to the neutrino mass, ($\mu_\nu = 10^{-19}(\frac{m_\nu}{1\,\mathrm{eV}})\mu_B$) is predicted, that cannot be observed today experimentally. However, there are a number of theoretical extensions beyond the MSM where Majorana neutrino (transition) magnetic moment could be at a level of $10^{-10\div12}\mu_B$ [2–6]. At the same time it follows from general considerations [7, 8] that the Dirac NMM cannot exceed $10^{-14}\mu_B$.

Therefore an observation of the NMM value higher than $10^{-14}\mu_B$ would be an evidence of New Physics and would indicate undoubtedly [9–11] that neutrino is a Majorana particle (Fig. 8.1). Furthermore, according to [12] a new lepton number violating physics responsible for the generation of NMM arises at the scale Λ which is well below the see-saw scale (10^{16} GeV). For example, if $\mu_\nu = 1.0 \times 10^{-11}\mu_B$ and neutrino mass $m_\nu = 0.3$ eV one finds that $\Lambda \leq 100$ TeV.

It is rather important to make laboratory NMM measurements sensitive enough to reach the $\sim 10^{-11}\mu_B$ region. The Savanna River experiment by Reines's group can be considered as the beginning of such measurements. Over a period of thirty years the sensitivity of reactor experiments has been improved by only a factor of three: from $2 \div 4 \times 10^{-10}\mu_B$ [13, 14] to $6 \div 7 \times 10^{-11}\mu_B$ [15, 16]. Similar limits were obtained for solar neutrinos [17, 18] but due to different neutrino flavor composition these results cannot be directly compared with short-baseline experiments.

The measurements that are carried out with the GEMMA spectrometer [16, 19, 20] at the 3 GWth reactor of the Kalinin Nuclear Power Plant (**KNPP**) give the present world best upper limit on NMM at the level of $2.9 \times 10^{-11}\mu_B$. The aim of the present project is to construct a spectrometer with better experimental parameters to be more sensitive to the possible effect.

A laboratory measurement of the NMM is based on its contribution to the ν-e scattering. For nonzero NMM the ν-e differential cross section is [9] a sum of weak interaction cross section ($d\sigma^W/dT$) and electromagnetic one ($d\sigma^{EM}/dT$):

$$\frac{d\sigma^W}{dT} = \frac{G_\mathrm{F}^2}{2\pi} m[4x^4 + (1+2x^2)^2(1-T/E)^2 - 2x^2(1+x^2)mT/E^2], \tag{8.1}$$

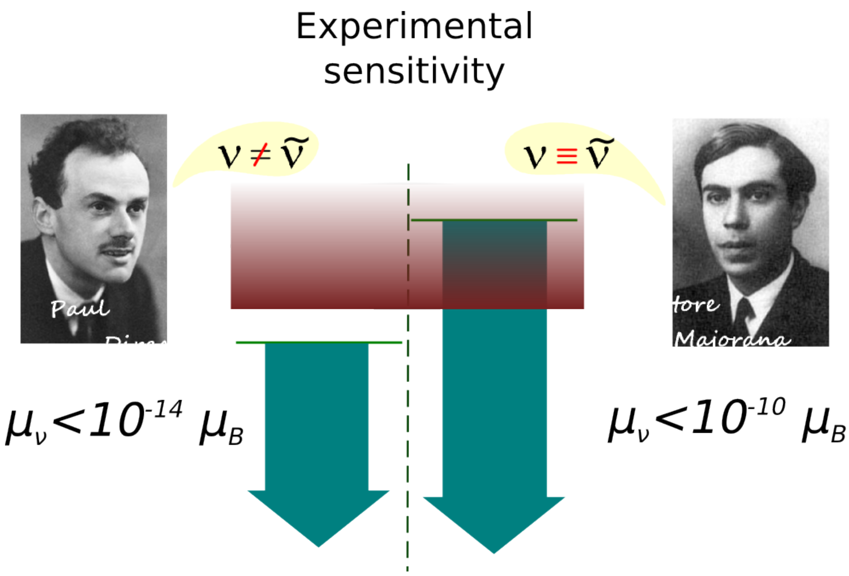

Figure 8.1: Limits for NMM for Dirac (left) and Majorana (right) neutrinos and the present experimental sensitivity.

$$\frac{d\sigma^{EM}}{dT} = \pi r_0^2 (\mu/\mu_B)^2 (1/T - 1/E) \tag{8.2}$$

where E is the incident neutrino energy, T is the electron recoil energy, $x^2 = \sin^2\theta_W = 0.232$ is a Weinberg parameter and r_0 is a classical electron radius ($\pi r_0^2 = 2.495 \times 10^{-25}$ cm^2).

Figure 8.2 shows differential cross sections (8.1) and (8.2) averaged over the typical antineutrino reactor spectrum as a function of the electron recoil energy. One can see that at low recoil energy ($T \ll E_\nu$) the value of $d\sigma^W/dT$ becomes almost constant while $d\sigma^{EM}/dT$ increases as T^{-1}. It becomes evident that the lower the detector energy threshold is the more considerable the increase in the NMM effect with respect to the weak irreducible contribution we can obtain.

8.1.2 Specific Project Objectives and Expected Results

The experimental setup is located under reactor #3 of KNPP where the distance from the center of the core is 10 m. In this way we obtain an enormous antineutrino flux that is equal to 5.4×10^{13}/cm^2/s. The γ-background conditions in the new room are much better (by an order of magnitude), the climate conditions are more stable if compared with GEMMA-I. Furthermore, being equipped with a special lifting mechanism, the spectrometer is movable. It gives us an opportunity to vary, on-line, the antineutrino flux significantly and thus suppress the main systematic errors caused by the possible long-term instability and uncertainties of background knowledge. The mass of the detector is 6 kg (two detectors with a mass of 3 kg each).

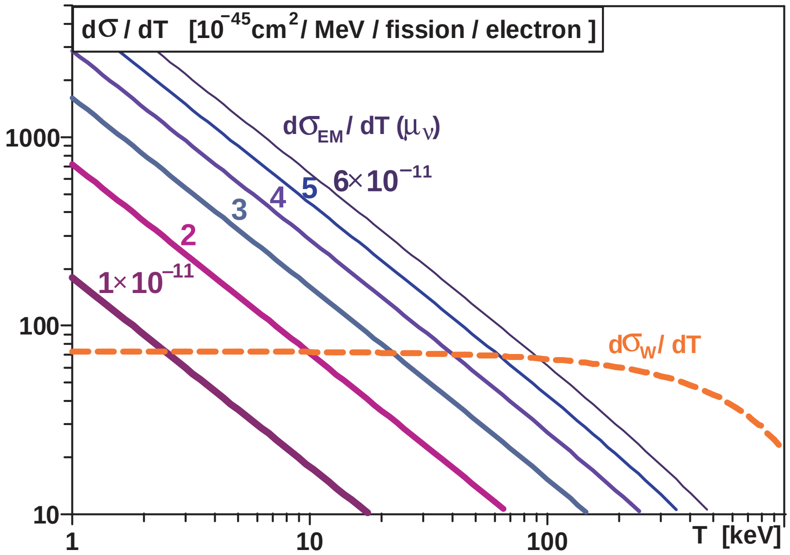

Figure 8.2: Weak and electromagnetic cross-sections calculated for several NMM values.

To avoid the “Xe-problems” the internal part of the detector shielding will be gas tight. A special U-type low-background cryostat (Fig.8.3) is used in order to improve the passive shielding and thus to reduce the external background in the region of interest (**ROI**) down to $0.5 \div 1.0$ keV·kg·day^{-1}.

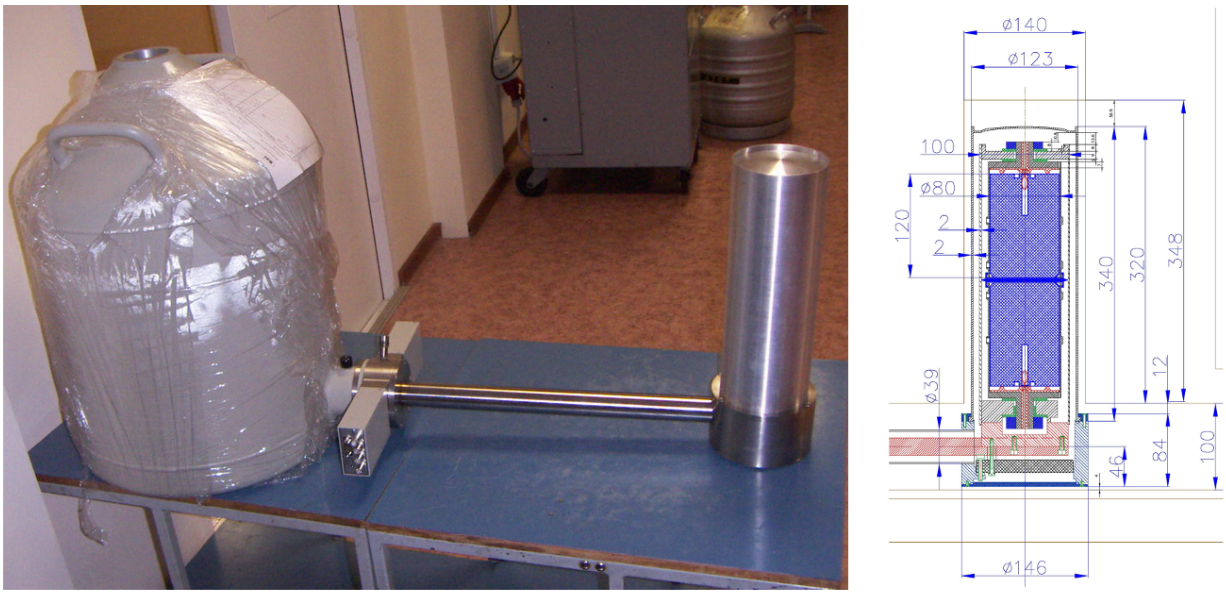

Figure 8.3: The picture of U-type low-background cryostat (left) and the scheme of its “detector” part (right).

Special care is taken to improve antimicrophonic and electric shielding. The effective energy threshold is reduced from 2.8 to 1.5 keV. The neutrino flux monitoring will be available by means of special detector (project DANSS [21]). As a result of all the improvements we will be able to suppress the systematic errors and expect the experimental sensitivity to be at the level of $1 \times 10^{-11}\mu_B$ and thus to reach the region of astrophysical interest.

8.1.3 Basic Methods and Approaches Used in the Project

One of the main project objectives is to suppress the background. It is realized by means of various methods. The detector is surrounded by multilayer passive and active shielding (see next chapter for more details). During the measurement the signals of the HPGe detector, anticompton NaI shielding and outer anticosmic plastic counters as well as dead time information are collected on the event by event basis. The detection efficiency just above the threshold is checked with a pulser. The neutrino flux during the ON reactor period is estimated via the reactor thermal power measured with accuracy of 0.7%. The collected data are processed in several steps. The first step involves different selections aimed to suppress nonphysical and physical backgrounds:

1. **Bad run rejection.** We reject those hour-long runs which correspond to the periods of liquid nitrogen filling and any mechanical or electrical work at the detector site as it could produce noise.

2. **Radioactive noble gas rejection.** It may happen that our experimental setup turns out to be not tight enough against radioactive noble gases. To smooth away this design defect we analyze energy spectra measured during each several hours and check the stability of the γ-background. If any visible excess of 81 keV (^{133}Xe), 250 keV (^{135}Xe) or 1294 keV (^{41}Ar) γ-line occurs the corresponding runs are removed.[1]

3. **Detector noise rejection.** Our Ge detector might happen to become noisy from time to time. In order to reject these noisy periods the low-amplitude count rate is checked second by second and those seconds that contain many events (this parameter is under consideration) are rejected.

4. **Audio-frequency rejection.** We reject those events which are separated by a time interval shorter than 80 ms or equal to $[n \cdot (20.0 \pm 0.1)]$ ms. In this way we suppress the noise caused by mechanical vibrations ("ringing") and the 50 Hz power line frequency.

5. **Fourier rejection.** The real and the artifact signals have different Fourier spectra (see more in detector description and [22]). To exploit this difference we build three plots similar to that shown in Fig.8.4 (E2 vs E1), (E3 vs E2) and (E1 vs E3). These plots were obtained in GEMMA-I experiment. To be able to apply this procedure the detector signal is processed by three parallel independent electronic channels with different shaping time (Fig.8.5).

   The real signal falls into diagonals ($E_1 \simeq E_2 \simeq E_3$) within the energy resolution whereas any nonphysical artifact shows a different pattern. We select only diagonal

[1] In fact these files are used later for the noble gas correction for the rest of the data.

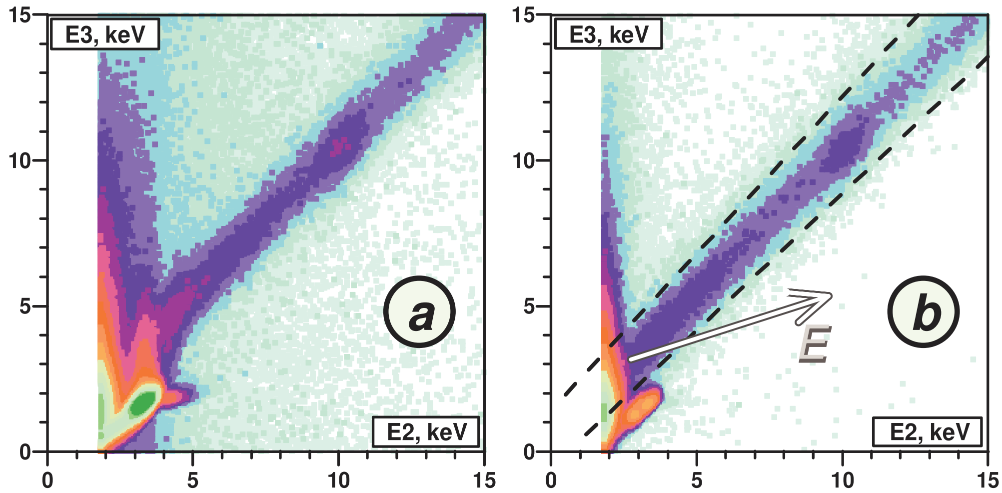

Figure 8.4: Example of the Fourier analysis made with different shaping times: ADC-2 operates with 4 μs pulses and ADC-3 operates with 12 μs pulses. Plot (a) is made before and (b) after the "audio-frequency" rejection; one can see that most of the rejected events are non-diagonal. (The color intensity scale is logarithmic.)

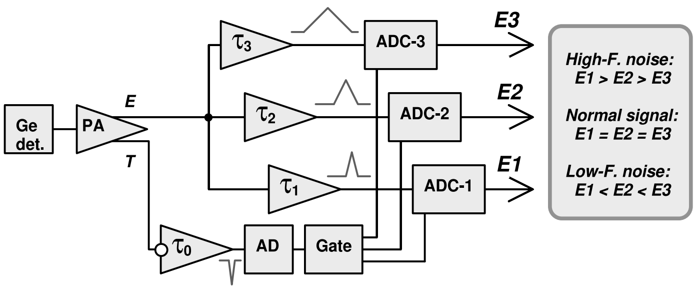

Figure 8.5: Scheme of signal processing for applying the Fourier analysis.

events and thus additionally reject low- and high- frequency noise. To ensure the best cut-off we replace E_1, E_2 and E_3 by their linear combination:

$$E = aE_1 + bE_2 + cE_3 \tag{8.3}$$

where the weights a, b, c are chosen (subjectively) so as to make the vector be antiparallel to the noise gradient (Fig.8.4 b).

After the above rejections we construct energy spectra for the ON and OFF periods and correct[2] them in two steps:

[2]The corrections do not give a significant error to the final result as they affect ON and OFF spectra in the same way.

1. **Noble gas correction.** As our spectrometer is not located in a special laboratory but is instead in the technological room, occasionally there are short operational periods when the concentration of ^{41}Ar, ^{133}Xe and ^{135}Xe in this room becomes higher than usual. Spectra measured under these conditions are used to evaluate the contribution of each radioactive gas to the low energy part of the background. These contributions, normalized to the intensities of the corresponding γ-lines, are then subtracted from those few ON and OFF spectra where small traces of these lines are still present. In this case the value of such correction in the ROI does not exceed 1-2%.

2. **Low energy threshold correction.** The detection efficiency η just above the threshold E_0 is measured with a pulser and is fitted with the function:

$$\eta(E) = \int_{-\infty}^{E} \frac{1}{2\pi\sigma} e^{-\frac{(x-E_0)^2}{2\sigma^2}} dx \tag{8.4}$$

   where σ stands for the detector energy resolution. Experimental spectra are then corrected by function (8.4) which becomes significant in the region of energy threshold.

During long-term measurements it is crucial to establish long-term stability as well. In our case this problem is divided into two main parts: the background constancy and the hardware stability.

The main source of background instability is the presence of noble gases (see "Noble gas correction"). One of the best ways to check the hardware is to control the position of some energy peak, because almost any change in the hardware results in its shift. But in the low background measurements this method could not be applied due to insufficient statistics. That is why we use the following procedure. First we make the binning of overall data. The idea of this binning consists in obtaining enough data in some devoted spectrum lines. The next step is to check if those peaks have some additional broadening because of possible amplification changes during the bin time. If this broadening appears to be large enough (10% or more) we perform the rebinning to find the exact time of the shift and possibly distinguish its origin. Then the data, divided in this way, are transferred to the uniform energy scale (0.1 keV/channel) and only after that are summed up. Thus we automatically reduce the influence of the hardware instability to a negligible level.

As a result we obtain energy spectra S for the ON and OFF periods which must be normalized by the corresponding active times T_{ON} and T_{OFF} and then compared to each other taking into account the additional neutrino dependent term:

$$\frac{S_{\mathrm{ON}}}{T_{\mathrm{ON}}} = \frac{S_{\mathrm{OFF}}}{T_{\mathrm{OFF}}} + m_d \Phi_\nu (W + X \cdot EM). \tag{8.5}$$

The last term includes the fiducial detector mass m_d and the antineutrino flux Φ_ν (known with an accuracy of 1.7% and 3.5%, respectively) multiplied by the sum of two neutrino contributions: the weak one (W), which can be calculated easily using formula (8.1) and is completely negligible in our case, and the electromagnetic one (EM), which is proportional to the squared NMM value:

$$X = \left(\frac{\mu_\nu}{10^{-11}\mu_B}\right)^2. \tag{8.6}$$

Unfortunately the exposition times of ON and OFF periods are not equal. A usual OFF period is much shorter and therefore the final sensitivity is limited by the background uncertainties. However, having significant statistics we can study the background with good precision. It gives us the ability to introduce additional information in our analysis, namely, to state that our background is a smooth curve. To implement this conventional idea we fit the background OFF spectrum in the ROI with a parametrized smooth function (e.g. a sum of Gaussian, exponential and linear functions). We can also use splines for this procedure. All these fits produce slightly different results and their spread is taken into account in the final systematic error.

Then we compare the ON spectrum channel-by-channel with the obtained background curve and extract the X-value (or its upper limit) from Eq. (8.6). This evaluation is more complicated than expected because it is very difficult to count active times T_{ON} and T_{OFF} precisely in a proper way (see [23] for more details). To extract the NMM value we compare the ON spectrum with the obtained curve channel-by-channel (to be more precise, with a narrow corridor with the width given by the fitting uncertainty). Applying this procedure to the total statistics we get the final distribution for X and thus obtain either estimation of nonzero NMM or its upper limit.

8.1.4 Detector Description

The detector (Fig.8.6) is placed inside a cup-shaped NaI crystal with 14 cm thick walls surrounded by 5 cm of electrolytic copper and 15 cm of lead.

Being located just under reactor #3 of KNPP (at a distance of 10 m from the reactor core center) the detector is well shielded against the hadronic component of cosmic rays by the reactor body and technological equipment (overburden 70 m w.e.). The muon component is reduced by a factor of 10 at $\pm 20^\circ$ with respect to vertical line and 3 at $70^\circ \div 80^\circ$. Nevertheless, a part of residual muons are captured in the massive shielding and produce neutrons that scatter elastically in the Ge detector and raise the low energy background. To suppress this effect the spectrometer is covered with additional plastic scintillator plates which produce relatively long μ-veto signals. The effectiveness of the application of passive and active shielding is shown in Fig.8.7. The detector is also movable. It is realized by using a special lifting mechanism that can vary the distance between the detector and the center of the reactor core from 10 to 12 m.

CAMAC and NIM electronic modules are used to control the spectrometer and accumulate information. The spectrometric part of the electronic equipment is comprised of preamplifiers, amplifiers, analogue-to-digital converters, a CAMAC controller, interface, and a computer. Electronic logic modules serve to shape and sum PMT signals and to allow passage of spectrometric signals. The entire information selection and accumulation process is controlled by special programs. Analogue signals from each germanium detector can be written as a separate energy spectrum if they are not accompanied by inhibiting

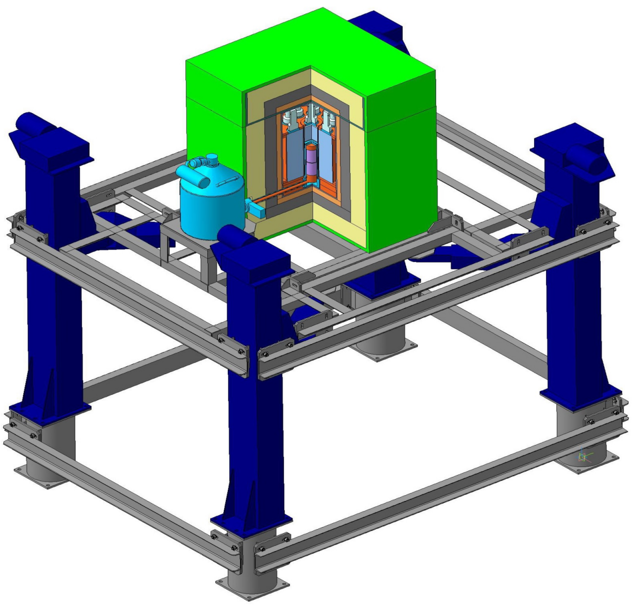

Figure 8.6: Spectrometer GEMMA-II is placed on the lifting mechanism.

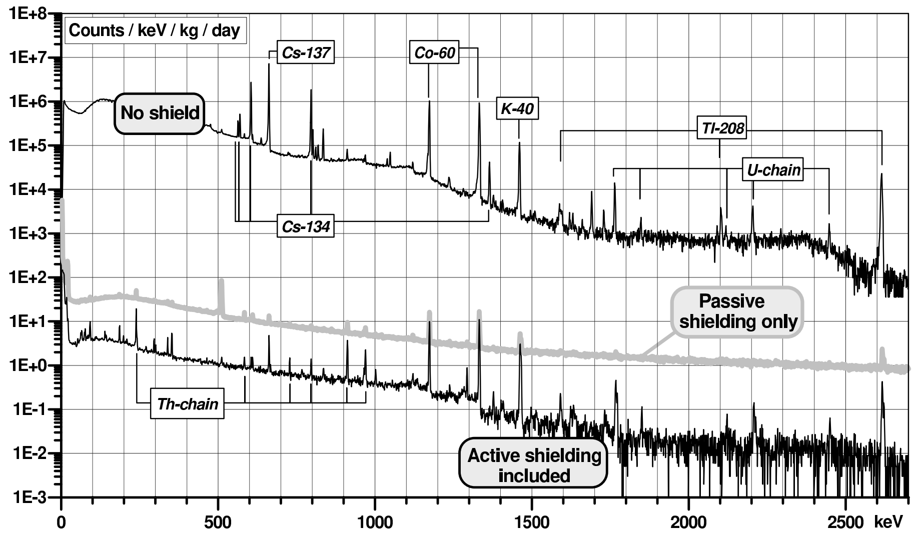

Figure 8.7: The γ-spectra measured at the detector site under different shielding conditions.

signals from the active shielding or other detectors. In addition, signals are selected according to frequency characteristics that allows microphone and electron noise and mains interference to be isolated and eliminated. Microphone noise may be due to boiling and turbulence of liquid nitrogen in the Dewar flask of the detector, vibration of the equipment, and other reasons. Electron noise is caused by mains interference, fluctuation of detector leakage currents, thermal noise of the head field-effect transistor.

In the future (2016–2018) a new type of detector with point contacts will be used. This will allow us to set the ultralow effective threshold on the level of 300 eV. Using several detectors with total mass about 5 kg will give us an opportunity to reach the sensitivity to NMM at the level of $5 \div 10 \times 10^{-12} \mu_B$ and thus go down to the region of astrophysical interest.

8.1.5 Contribution of JINR Members

The contribution of JINR members is predominant.

8.1.6 Publications, Theses and Conferences

As a result of the project the following papers has been published:

1. Beda A. G., Brudanin V. B., Demidova E. V., Vylov Ts., Gavrilov M. G., Egorov V. G., Starostin A. S. and Shirchenko M. V. // Phys. At. Nucl. 2007. V.70. P.1873; hep-ex/0705.4576.

2. Beda A. G. et al. // Phys. At. Nucl. 2004. V.67. P.1948; hep-ex/9706004.

3. Beda A. G. et al. // Advances in High Energy Physics V.2012 (2012), Article ID 350150, 12 pages doi:10.1155/2012/350150.

4. A. Beda et al. GEMMA experiment: three years of the search for the neutrino magnetic moment, Physics of Elementary Particles and Atomic Nuclei Letters, 2010, V.7, №6(162), pp.667-672.

5. A. Beda et al. GEMMA experiment: the results of neutrino magnetic moment search, Physics of Particles and Nuclei Letters, 2013, V.10, №2, pp.139-143.

6. A. Beda et al. Experiment GEMMA: Search for the Neutrino Magnetic Moment, 2010, Proceedings of Science, №297.

7. A. Beda et al. Upper limit on the neutrino magnetic moment from three years of data from the GEMMA spectrometer, 2010, arXiv:1005.2736v1.

8. A. Beda et al. GEMMA experiment: three years of the search for the neutrino magnetic moment, 2009, arXiv:0906.1926v1.

9. A. Beda et al. The new result of the neutrino magnetic moment measurement in the GEMMA experiment, proceedings of the13th Lomonosov Conference on Elementary Particle Physics, 2007.

Conferences:

1. D. Medvedev, The International Workshop on Non-Accelerator New Physics (NANPino-2013), Valday, Russia, 2013 (parallel).

2. D. Medvedev, Sixteenth Lomonosov Conference on Elementary Particle Physics, Moscow State University, Moscow, Russia, 2013 (parallel).
3. D. Medvedev, Wilhelm and Else Heraeus-Seminar Exploring the neutrino sky and fundamental particle physics on the Megaton scale, Bad Honnef, Germany, 2013 (parallel).
4. D. Medvedev, LX International Conference on Nuclear Physics "Nucleus 2010. Methods of Nuclear Physics for Femto- and Nanotechnologies", St.-Petersburg, Russia, 2010, (parallel).
5. D. Medvedev, 58 International Conference on Nuclear Spectroscopy and the Structure of Atomic Nucleus (Nucleus-2008), MSU, Moscow, 2008, (parallel).
6. D. Medvedev, Wilhelm and Else Heraeus-Seminar Exploring the neutrino sky and fundamental particle physics on the Megaton scale (poster), Bad Honnef, Germany, 2013 (parallel).
7. D. Medvedev, European School on High-Energy Physics, JINR-CERN, Bautzen, Germany, 2009, (parallel).
8. V. Egorov, LowNu, Reims, France, 2010 (parallel).
9. V. Egorov, ICHEP-2010, Paris, France, 2010, (parallel).
10. V. Egorov, Seminar at CSNSM IN2P3, Orsay, France, 2011, (parallel).
11. V. Egorov, MEDEX'2011, Prague, Czech Republic, 2011, (parallel).
12. V. Egorov, Symposium on JINR-SA collaboration, South Africa, 2012, (parallel).
13. V. Egorov, ASPERA, Dubna, Russia, 2011, (parallel).
14. V. Egorov,13th Lomonosov Conference on Elementary Particle Physics, MSU, Moscow, Russia, 2007, (parallel).
15. V. Egorov, 4th International Conference on Nonaccelerator New Physics (NANP 03), Dubna, Russia, 2003, (parallel).

8.1.7 Finances

Major sources and amount of finances and major equipment acquired during the project runtime are listed in Tab. 8.1.

Project stage	Funding source	Obtained amount (k$)	Major equipment acquired
Gemma	1100 +	25	Lifting mechanism
I +II	RFBR +	10	Borated polyethylene
	off-budjet	16	Copper
	funds	25	50% of 1.5 kg HPGe detector
		40	50% of 2×3 kg HPGe detectors
		50	Electronics
		20/yr	Travel and living expenses at KNPP (Udomlya)

Table 8.1: Major sources and amount of finances and major equipment acquired

References

[1] J. Beringer et al. "Review of Particle Physics (RPP)". In: *Phys.Rev.* D86 (2012), p. 010001.

[2] L. B. Okun, M. B. Voloshin, and M. I. Vysotsky. "Neutrino electrodynamics and possible consequences for solar neutrinos". In: *Sov. Phys. JETP* 64 (1986), pp. 446–452.

[3] M Fukugita and T Yanagida. "Particle-physics model for the Voloshin-Vysotski-Okun solution to the solar-neutrino problem". In: *Physical Review Letters* (1987). Query date: 2014-04-03. URL: http://adsabs.harvard.edu/abs/1987PhRvL..58.1807F.

[4] S. Pakvasa and J. W. F. Valle. "Neutrino Properties Before and After KamLAND". In: *Proc. Indian Natl. Sci.* Acad. (2004). Proceedings of the Indian National Academy of Sciences on "Neutrinos"., p. 189. arXiv: hep-ph/0301061.

[5] Mikhail Gorchtein et al. "Model independent naturalness bounds on magnetic moments of majorana neutrinos". In: *arXiv preprint hep-ph/0610388* (2006).

[6] Nicole F Bell et al. "Model independent bounds on magnetic moments of Majorana neutrinos". In: *Physics Letters B* 642.4 (2006), pp. 377–383.

[7] Nicole F Bell et al. "How magnetic is the dirac neutrino?" In: *Physical review letters* 95.15 (2005), p. 151802.

[8] Nicole F Bell et al. "Magnetic moments of dirac neutrinos". In: *arXiv preprint hep-ph/0601005* (2006).

[9] Boris Kayser. "Neutrino properties". In: 2008.

[10] Carlo Giunti and Alexander Studenikin. "Neutrino electromagnetic properties". In: *Physics of Atomic Nuclei* 72.12 (2009), pp. 2089–2125.

[11] Alexander Studenikin. "Neutrino magnetic moment: a window to new physics". In: *Nuclear Physics B-Proceedings Supplements* 188 (2009), pp. 220–222.

[12] Nicole F Bell. "How magnetic is the neutrino?" In: *International Journal of Modern Physics A* 22.27 (2007), pp. 4891–4899.

[13] F Reines, HS Gurr, and HW Sobel. "Detection of ν^{-} e-e Scattering". In: *Physical Review Letters* 37.6 (1976), p. 315.

[14] P Vogel and J Engel. "Neutrino electromagnetic form factors". In: *Physical Review D* 39.11 (1989), pp. 3378–3383.

[15] HT Wong et al. "Search of neutrino magnetic moments with a high-purity germanium detector at the Kuo-Sheng nuclear power station". In: *Physical Review D* 75.1 (2007), p. 012001.

[16] AG Beda et al. "First result for the neutrino magnetic moment from measurements with the GEMMA spectrometer". In: *Physics of Atomic Nuclei* 70.11 (2007), pp. 1873–1884.

[17] DW Liu. "Limits on the neutrino magnetic moment using super-kamiokande solar neutrino data". In: *International Journal of Modern Physics A* 20.14 (2005), pp. 3110–3112.

[18] C Arpesella et al. "Direct Measurement of the Be 7 Solar Neutrino Flux with 192 Days of Borexino Data". In: *Physical review letters* 101.9 (2008), p. 091302.

[19] AG Beda et al. "Low-background Ge-NaI spectrometer for measurement of the neutrino magnetic moment". In: *Physics of Atomic Nuclei* 61 (1998), pp. 66–73.

[20] AG Beda et al. "Status of the Experiment on the Measurement of the Neutrino Magnetic Moment with the Spectrometer GEMMA". In: *Physics of Atomic Nuclei* 67.11 (2004), pp. 1948–1952.

[21] I Alekseev et al. "DANSSino: a pilot version of the DANSS neutrino detector". In: *arXiv preprint arXiv:1305.3350* (2013).

[22] E Garcia et al. "Dark matter searches with a germanium detector at the Canfranc tunnel". In: *Nuclear Physics B-Proceedings Supplements* 28.1 (1992), pp. 286–292.

[23] AG Beda et al. "The results of search for the neutrino magnetic moment in GEMMA experiment". In: *Advances in High Energy Physics* 2012 (2012).

Chapter 9

GERDA Experiment

Editors: V.Brudanin, A.Smolnikov, K.Gusev, A.Lubashevskiy

Project Title

GERmanium **D**etector **A**rray to search for neutrinoless double beta decay in ^{76}Ge

Project Leaders

- A.A. Smolnikov
- K.N. Gusev

Abstract

The GERDA experiment at the Laboratori Nazionali del Gran Sasso (**LNGS**) searches for the neutrinoless double beta decay of ^{76}Ge. Bare germanium detectors enriched in the isotope ^{76}Ge are submerged in liquid argon. The cryogenic liquid serves simultaneously as a coolant and a high-purity shield against external radiation. GERDA follows a staged implementation. About 18 kg of enriched semi-coaxial germanium detectors have been deployed in Phase I which started physics data taking in November 2011 and finished in May 2013. An additional 20 kg of novel thick-window BEGe (Broad Energy Germanium) detectors are planned to be deployed in 2014. Phase II will encompass the operation of about 40 kg of enriched germanium detectors. For this phase it is also planned to install light sensors in the liquid argon, in order to detect the scintillation light of the liquid argon to veto background signals. Based on the physics results achieved in Phase I and II, a third phase is conceived in collaboration with the US lead Majorana experiment to explore the full mass range predicted for the inverted mass hierarchy.

keywords: neutrinoless double beta decay, enriched germanium detectors

Project Members From JINR

V. Brudanin, D. Borowicz, V. Egorov, K. Gusev, A. Klimenko, O. Kochetov, A. Lubashevskiy, I. Nemchenok, N. Rumyantseva, E. Shevchik, M. Shirchenko, A. Smolnikov, I. Zhitnikov, D. Zinatulina

Project Duration. Approval Date(s)

- R&D: started in 2006
- 2007-2009 — project approval (GERDA Phase I)
- 2010-2012 — prolongation (GERDA Phase I)
- 2013-2015 — prolongation (GERDA Phase I + Phase II)
- 2016-2018 — application for prolongation (GERDA Phase II + GERDA-MAJORANA)

List of Participating Countries and Institutions

INFN Laboratori Nazionali del Gran Sasso, LNGS, Assergi, Italy; Institute of Physics, Jagiellonian University, Cracow, Poland; Institut für Kern- und Teilchenphysik, Technische Universität Dresden, Dresden, Germany; Joint Institute for Nuclear Research, Dubna, Russia; Institute for Reference Materials and Measurements, Geel, Belgium; Max-Planck-Institut für Kernphysik, Heidelberg, Germany; Dipartimento di Fisica, Università Milano Bicocca, Milano, Italy; INFN Milano Bicocca, Milano, Italy; Dipartimento di Fisica, Università degli Studi di Milano e INFN Milano, Milano, Italy; Institute for Nuclear Research of the Russian Academy of Sciences, Moscow, Russia; Institute for Theoretical and Experimental Physics, Moscow, Russia; National Research Centre “Kurchatov Institute”, Moscow, Russia; Max-Planck-Institut für Physik, München, Germany; Physik Department and Excellence Cluster Universe, Technische Universität München, Germany; Dipartimento di Fisica e Astronomia dell‘Università di Padova, Padova, Italy; INFN Padova, Padova, Italy; Physikalisches Institut, Eberhard Karls Universität Tübingen, Tübingen, Germany; Physik Institut der Universität Zürich, Zürich, Switzerland

9.1 Project Description

9.1.1 Fundamental Scientific Problem Addressed by the Project

Since their discovery neutrinos have been an object of extensive experimental study and the knowledge about their properties has advanced our understanding of weak interactions significantly. Still unanswered, however, is the very fundamental question: whether or not the neutrino is a Majorana particle, like most extensions of the Standard Model assume. The study of double beta decay is the most sensitive approach to answer this question. If the decay occurs without the emission of neutrinos then their Majorana nature is proven. The potential of this method has increased considerably during the last years since a non-zero mass of the neutrinos has been established by the observation of neutrino flavor oscillation.

The observation of neutrinoless double beta decay ($0\nu\beta\beta$) would not only establish the Majorana nature of the neutrino but also provide an estimation of the absolute scale of the neutrino mass.

9.1.2 Specific Project Objectives and Expected Results

The experimental signature of $0\nu\beta\beta$ decay is a peak at the Q-value of the decay. The two most sensitive experiments with the candidate nucleus ^{76}Ge ($Q_{\beta\beta} = 2039.061 \pm 0.007$ keV [1]) were Heidelberg-Moscow (**HDM**) [2] and International GErmanium eXperiment (**IGEX**) [3, 4]. To the end of 2002, when IGEX experiment was completed, they both found no evidence for the $0\nu\beta\beta$ decay of ^{76}Ge and set lower limits on the half-life $T^{0\nu}_{1/2} > 1.9 \cdot 10^{25}$ yr and $> 1.6 \cdot 10^{25}$ yr at 90 % C.L., respectively. The leader of the HDM experiment, and his group had further continued their investigations, and in 2004–2006 has published a claim on an observation of the $0\nu\beta\beta$ decay in Ge [5]. Because of inconsistencies in the latter pointed out recently [6], the present comparison is restricted to the result of Ref. [5]. The claim was very intriguing and, it was very obvious, it had to be verified[1].

Until recently, the claim has not been scrutinized. Currently the most sensitive experiments are KamLAND-Zen [9] and EXO-200 [10] looking for $0\nu\beta\beta$ decay of ^{136}Xe and GERDA employing ^{76}Ge. Nuclear matrix elements (**NME**) calculations are needed to relate the different isotopes. Thus the experiments using ^{136}Xe cannot refute the claim in a model-independent way. GERDA is able to perform a direct test using the same isotope and using largely the same detectors as HDM and IGEX.

The GERDA experiment pursues a staged implementation. The goal of the Phase I (finished in 2013) was to scrutinize the mentioned claim with a total exposure of 20 kg yr. The following phase (GERDA Phase II) aims at exploring half-lives $> 10^{26}$ yr, accumulating 100 kg yr of exposure with a background index $\lesssim 10^{-3}$ counts/(keV kg yr). To reach such background levels, which are more than an order of magnitude below the Phase I value, the collaboration is going to operate ∼30 additional custom-made detectors (∼20 kg of ^{76}Ge) with a new electrode geometry (BEGe detectors), providing superior pulse shape discrimination (**PSD**) performances. In addition, new devices will be installed to identify energy depositions in the liquid argon (**LAr**) surrounding the detector array, through the detection of the induced LAr scintillation light. These events are due to background sources and their detection. In coincidence with a Ge detector signal they can be used as anti-Compton or anti-coincidence veto.

9.1.3 Basic Methods and Approaches Used in the Project

Using enriched ^{76}Ge. Experiments looking for $0\nu\beta\beta$ decay of ^{76}Ge operate germanium diodes normally made from enriched material, i.e. the number of nuclei ^{76}Ge is enlarged from 7.8 % to 86 % or higher. In these types of experiments the source is equivalent to the detector, which yields high detection efficiency.

[1] The main editor remark: Prof. H.V.Klapdor-Kleingrothaus, the leader of the HDM experiment, has reported $T^{0\nu}_{1/2} = (2.23^{+0.44}_{-0.31}) \cdot 10^{25}$ yr. See [7, 8].

Additional advantages of this technique are the superior energy resolution of 0.2 % at $Q_{\beta\beta} = 2039$ keV compared to other searches with different isotopes and the high radiopurity of the crystal growing procedure. Disadvantages are the relatively low $Q_{\beta\beta}$ value since backgrounds typically fall with energy and the relative difficulty to scale to larger mass compared to experiments using liquids and gases.

Ultra low background. The experimental challenge is to have nearly background free conditions in the region of interest (**ROI**) around $Q_{\beta\beta}$. Typically, background levels are quoted in units of counts per keV per kilogram per year, counts/(keV kg yr), since the number of background events roughly scales with the detector mass, energy resolution and running time. Defining Δ as the width of the ROI where a signal is searched for, the expected background is the background index (**BI**) multiplied by Δ in keV and the exposure in kg yr. GERDA has set the goal to keep the expected background below 1 event. For $\Delta = 5$ keV and exposures mentioned above, this implies a BI of 0.01 and 0.001 counts/(keV kg yr), respectively, for the two phases of GERDA. The main feature of the GERDA design is to operate bare Ge detectors made out of ^{enr}Ge in liquid argon. This design concept evolved from a proposal to operate Ge detectors in liquid nitrogen (LN_2) [11]. It allows for a significant reduction in the cladding material around the diodes and the accompanying radiation sources as compared to traditional Ge experiments. Furthermore, the background produced by interactions of cosmic rays is lower than for the traditional concepts of HDM, IGEX or MAJORANA [12] due to the lower Z of the shielding material. Other background sources include neutrons and gammas from the decays in the rock of the underground laboratory, radioactivity in support materials, radioactive elements in the cryogenic liquid (intrinsic, such as ^{39}Ar and ^{42}Ar, as well as externally introduced, such as radon) as well as internal backgrounds in the Ge diodes. These backgrounds were considered in the design and construction phase of GERDA and resulted in specific design choices, selection of materials used and also in how detectors were handled.

Blind analysis. For the first time in the field of $0\nu\beta\beta$ decay search, a blind analysis was performed in order to avoid bias in the event selection criteria. Events with energies within $Q_{\beta\beta} \pm 20$ keV were not processed. After both the energy calibration and the background model were finalized the window was opened except for ± 5 keV around $Q_{\beta\beta}$. After all selections discussed below had been frozen, the data in the $Q_{\beta\beta}$ region were analyzed. The validity of the offline energy reconstruction and of the event selection procedures have been cross-checked with a fully independent analysis. The GERDA collaboration will stay with blinding approach also during Phase II data taking.

Pulse Shape Discrimination. The signature for $0\nu\beta\beta$ decay is a single peak at $Q_{\beta\beta}$. Furthermore, events from $0\nu\beta\beta$ decays have a distinct topology, which allows to distinguish them from γ-induced background. The total energy of $0\nu\beta\beta$ decay is deposited by the two electrons only, which both have a short travel path in a germanium detector. Indeed, more than 90 % of $0\nu\beta\beta$ events are expected to deposit all energy localized within few mm^3 (single-site events, **SSE**). On the other hand, most background events from γ-ray interactions have energy depositions distributed over several detectors and/or at different, well-separated positions within a single detector (multi-site events, **MSE**).

Only events with an energy deposition in a single detector are accepted, resulting in a background reduction by about 15 % around $Q_{\beta\beta}$, with no efficiency loss for $0\nu\beta\beta$ decays. Events in the Ge detectors are rejected if they are in coincidence within 8 μs with a signal from the muon veto. This leads to a further background reduction by about 7 %. Events which are preceded or followed by another event in the same detector within 1 ms are excluded. This allows to reject background events from the ^{214}Bi–^{214}Po cascade (**BiPo**) in the ^{222}Rn decay chain. Less than 1 % of the events at $Q_{\beta\beta}$ are affected by this cut. Due to the low counting rate in GERDA and due to the low muon flux at LNGS, the dead time due to the muon veto and BiPo cuts is negligible. The detector signals are different for SSE and MSE, and also surface events from β or α decays exhibit a characteristic shape. Thus, pulse shape discrimination techniques can improve the sensitivity.

For BEGe detectors, a simple and effective PSD is based on the ratio of the maximum of the current pulse (called A) over the energy E [13, 14]. The A/E cut efficiency is determined from calibration data using events in the double escape peak (DEP) of the 2615 keV γ ray from ^{208}Tl. It is cross-checked with $2\nu\beta\beta$ decays of ^{76}Ge. The acceptance of signal events at $Q_{\beta\beta}$ is $\varepsilon_{PSD} = 0.92 \pm 0.02$, while only 20 % of the background events at this energy survive.

For the semi-coaxial detectors, a PSD method based on an artificial neural network (**ANN**) [14] is used. The signal acceptance $\varepsilon_{PSD} = 0.90^{+0.05}_{-0.09}$ is adjusted with DEP events and the uncertainty is derived from the $2\nu\beta\beta$ spectrum and from events at the Compton edge. About 55 % of the background events around $Q_{\beta\beta}$ are classified as SSE-like and considered for the analysis. Two alternative PSD methods were developed based on a likelihood ratio and on a combination of A/E and the asymmetry of the current pulse; they are used for cross-checks. The three PSD methods use very different training samples and selection criteria but more than 90 % of the events rejected by ANN are also rejected by the two other algorithms. The detailed description of PSD methods used during GERDA Phase I data analysis can be found in Ref. [14].

LArGe test facility for scintillation veto. The double beta decay events normally deposit energy only at one location in a detector (single-site event, SSE) while the large majority of backgrounds will also deposit energy in the liquid argon (**LAr**), which creates scintillation light in LAr and can be detected with photo multiplier tubes (**PMT**). In Phase I of the GERDA experiment liquid argon is used as a passive shield only. To develop additional methods of background reduction the pilot setup Mini-LArGe on the base of LAr scintillator (19 kg of LAr active mass) has been constructed and successfully operated. A long-term stability (about 2 years) with constant light yield of 1300 pe/MeV was achieved. In addition pulse shape discrimination methods were developed which allow to perform gamma / alpha / neutron selection with a strong ($>10^5$) discrimination factor. The power of the LAr scintillation anticoincidence concept for background suppression has been demonstrated. On the basis of experience previously obtained an up-scaled LArGe facility containing 1.4 tons of liquid argon was developed and constructed (see Fig. 9.1).

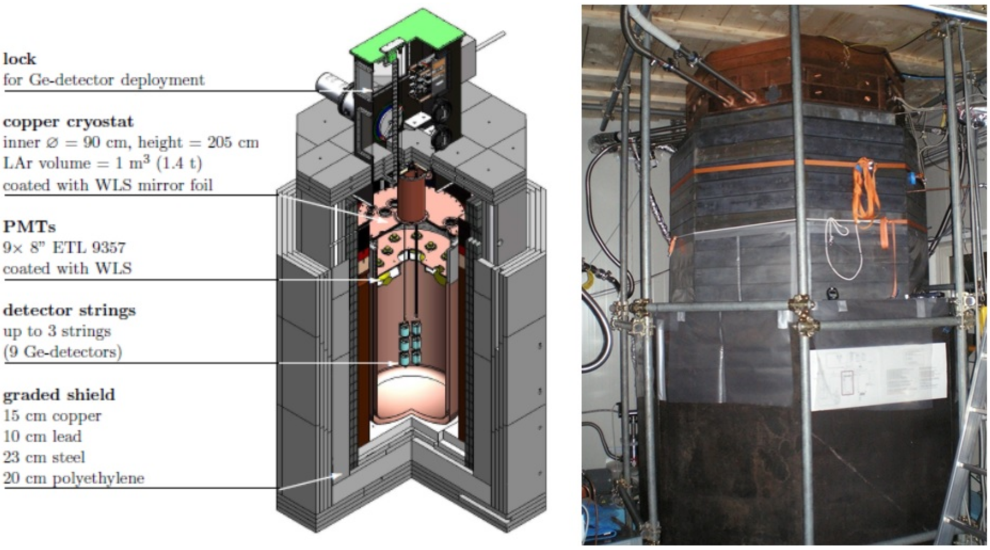

Figure 9.1: Cutaway view of the LArGe setup and photo of the setup. The cryogenic infrastructure, a slow control system, and the DAQ are located adjacent to this setup.

In LArGe, 9 PMTs are used for light detection. The high purity copper cryostat is lined with the wavelength shifting reflector foil. The setup uses a shield consisting of 20 cm polyethylene, 23 cm steel, 10 cm lead and 15 cm copper of increasing radio-purity. Assembly and installation of the LArGe setup in the underground GERDA Detector Laboratory (**GDL**) at LNGS have been finished by the end of 2009. The coaxial and BEGe detectors in different configurations have been deployed in the LArGe cryostat filled with liquid argon and a wide program of measurements with internal and external calibration sources has been carried out.

The efficiency of the LAr scintillation veto was optimized and defined as well as value of background reduction factor due to PSD of signals from the BEGe detector operated inside the LArGe. For instance, it was experimentally established that the internal background from decay of ^{232}Th chain can be suppressed in LArGe by factor > 5000 after applying LAr scintillation veto cut and PSD of signals from the BEGe detector (see Fig. 9.2).

Another task for LArGe emerged after the first GERDA commissioning runs which revealed the need to study the concentration and volume distribution of the cosmogenic isotope ^{42}Ar and its daughter ^{42}K in liquid argon. The simultaneous detection of the scintillation light together with the germanium detector signal is a powerful tool to identify and reject the ^{42}K decay events. Investigations along these lines started at the end of 2010 and continues up to now.

9.1.4 Detector Description

The GERDA experiment is located at the Laboratori Nazionali del Gran Sasso of INFN in Italy. The GERDA experimental setup is shown in Fig. 9.3. At the core of the setup there is

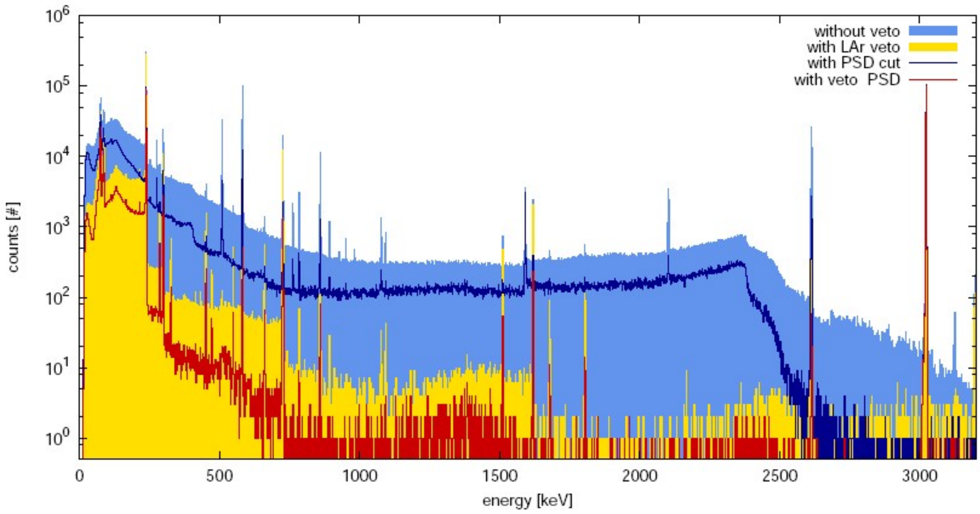

Figure 9.2: The internal ^{228}Th spectrum taken in LArGe.

an array of Ge detectors (Fig. 9.4). They are mounted in low-mass supports and immersed in a 64 m^3 cryostat filled with liquid argon. The LAr serves as cooling medium and shield against external backgrounds. The cryostat is located inside a water tank of 10 m in diameter. Only very small amounts of LAr are lost as it is cooled via a heat exchanger by liquid nitrogen. The 590 m^3 of high purity ($>$0.17 MΩm) water moderate ambient neutrons and γ radiation. It is instrumented with 66 PMTs and operates as a Cherenkov muon veto to further reduce cosmic induced backgrounds to insignificant levels for the GERDA experiment. Muons traversing through the opening of the cryostat without reaching water are detected by plastic scintillator panels on top of the clean room.

In Phase I three semi-coaxial or five BEGe detectors were mounted into each of the four strings which were lowered through a lock separating the clean room from the cryostat. The detector strings with semi-coaxial detectors are housed in 60 μm thin-walled copper containers permeable to LAr (mini-shroud) with a distance of a few mm from the detector outer surfaces (Fig. 9.5). A 30 μm thin copper cylinder (radon shroud) with a diameter of 75 cm encloses the detector array. The custom made preamplifiers are operated in LAr at a distance of about 30 cm from the top of the detector array (Fig. 9.5, Right). The analog signals are digitized by 100 MHz FADCs.

In Phase II we are going to deploy 7 strings of the detectors (30 new BEGe + 7 semi-coaxial from Phase I — in total about 35 kg of $^{\mathrm{enr}}$Ge) mounted in ultra low background holders made from intrinsically pure mono crystalline silicon. Entirely new front-end electronics will provide better energy resolution and PSD capability compare to Phase I. The LAr instrumentation will be implemented in GERDA cryostat in order to detect the scintillation light of the argon as an additional background rejection tool.

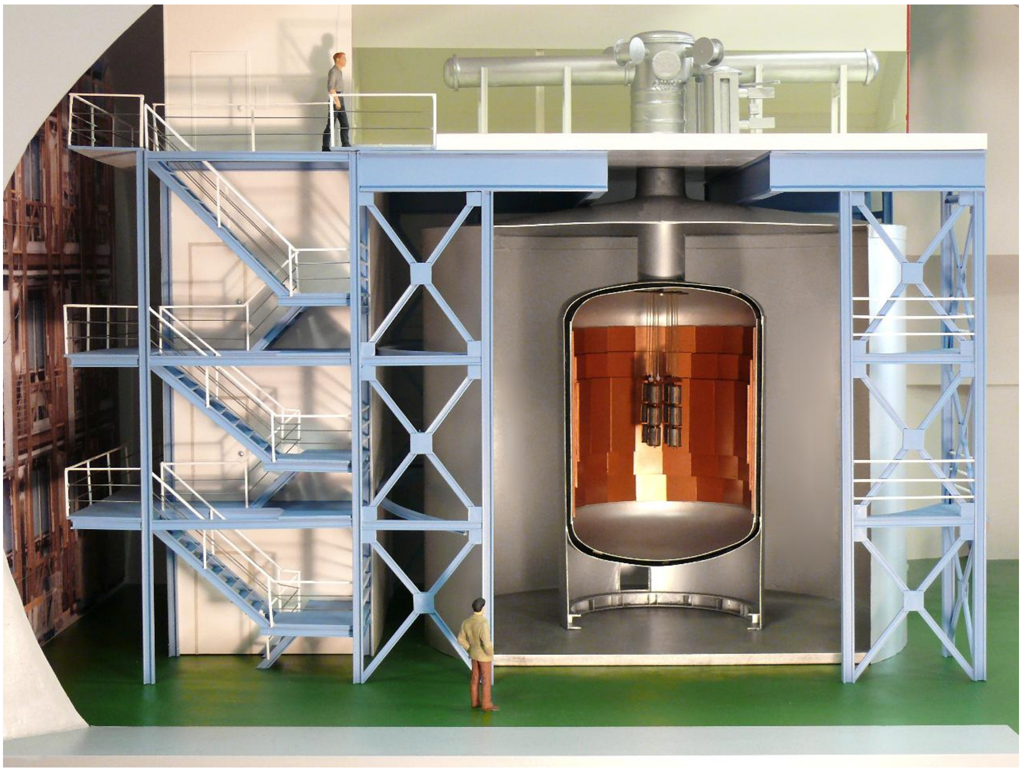

Figure 9.3: Artist's view of the GERDA experiment. The detector array is not to scale.

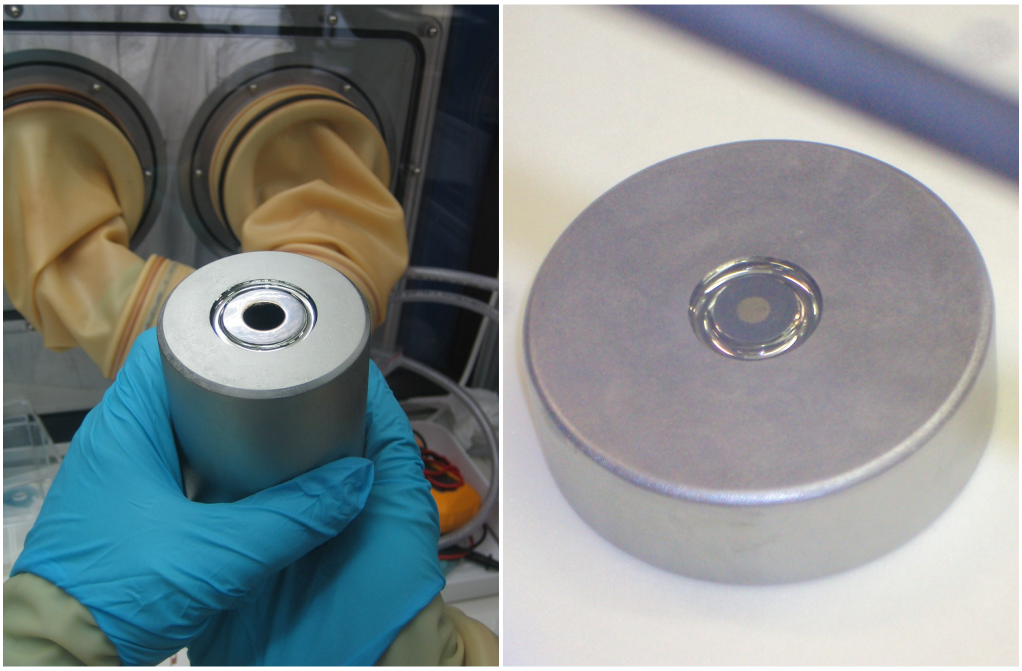

Figure 9.4: A semi-coaxial Phase I (Left) and BEGe Phase II (Right) detectors.

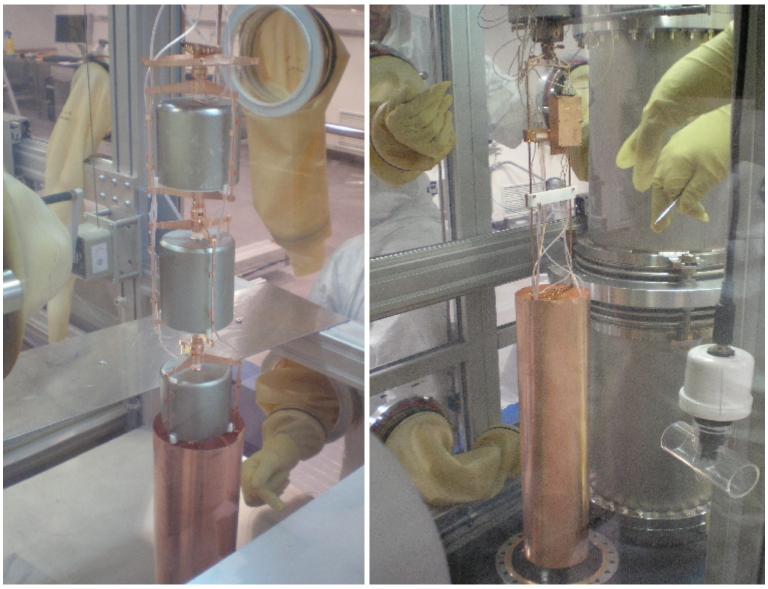

Figure 9.5: Left: a string of three ^{enr}Ge detectors is inserted into the mini-shroud. This work is performed in the glove box of the clean room. Right: closed detector string and 3-channel custom made preamplifier inside a copper box about 30 cm above the string.

9.1.5 Phase I results on $0\nu\beta\beta$ decay of ^{76}Ge

Data acquisition started in November 2011 with eight enriched Ge detectors (ANG 1-5 from HDM and RG 1-3 from IGEX), totaling a weight of 17.67 kg. Five enriched GERDA Phase II detectors of 3.63 kg in total were deployed in July 2012. Results from the data collected until May 2013 (492.3 live days) are reported here. The total exposure considered for the analysis amounts to 21.6 kg yr of Ge detector mass, yielding (215.2 ± 7.6) mol·yr of ^{76}Ge within the active volume. The procedure of the offline analysis of the digitized charge pulses is described in [15].

The energy scale of the individual detectors is determined with ^{228}Th sources once every one or two weeks. The differences between the reconstructed peak positions and the ones from the calibration curves are smaller than 0.3 keV. The energy resolution was stable over the entire data acquisition period. The gain variation between consecutive calibrations is less than 0.05 % [16], which corresponds to $< 30\,\%$ of the expected energy resolution (Full Width Half Maximum, **FWHM**) at $Q_{\beta\beta}$. Between calibrations, the stability is monitored by regularly injecting charge pulses into the input of the amplifiers.

The energy spectrum and its decomposition into individual sources is discussed in [17]. Peaks from ^{40}K, ^{42}K, ^{214}Bi, ^{214}Pb and ^{208}Tl γ rays can be identified as well as α decays from the ^{226}Ra decay chain, and β events from ^{39}Ar. All γ-ray peaks are reconstructed at the correct energy within their statistical uncertainty. The energy resolution (FWHM) of the strongest line (1524.6 keV from ^{42}K) is 4.5 (3.1) keV for the semi-coaxial (BEGe) detectors. These values are about 10 % larger than the resolutions obtained from calibrations. The broadening is due to fluctuations of the energy scale between calibrations. The interpolated FWHM at $Q_{\beta\beta}$ for physics data is detector dependent and varies between 4.2 and 5.7 keV for the semi-coaxial detectors, and between 2.6 and 4.0 keV for the BEGe detectors. The exposure-averaged values are (4.8 ± 0.2) keV and (3.2 ± 0.2) keV, respectively. The corresponding standard deviations σ_E are used for fitting a possible peak at $Q_{\beta\beta}$.

The half-life on $0\nu\beta\beta$ decay is calculated as

$$T_{1/2}^{0\nu} = \frac{\ln 2 \cdot \mathrm{N_A}}{m_{\mathrm{enr}} \cdot N^{0\nu}} \cdot \mathcal{E} \cdot \epsilon \tag{9.1}$$

$$\epsilon = f_{76} \cdot f_{av} \cdot \varepsilon_{fep} \cdot \varepsilon_{psd} \tag{9.2}$$

with N_A being Avogadro's constant, $\mathcal{E}$ the total exposure (detector mass $\times$ live time), and $m_{\mathrm{enr}} = 75.6$ g the molar mass of the enriched material. $N^{0\nu}$ is the observed signal strength or the corresponding upper limit. The efficiency ϵ accounts for the fraction of ^{76}Ge atoms (f_{76}), the active volume fraction (f_{av}), the signal acceptance by PSD (ε_{psd}), and the efficiency for detecting the full energy peak ε_{fep}. The latter is the probability that a $0\nu\beta\beta$ decay taking place in the active volume of a detector releases its entire energy in it, contributing to the full energy peak at $Q_{\beta\beta}$. Energy losses are due to bremsstrahlung photons, fluorescence X-rays, or electrons escaping the detector active volume. Monte Carlo simulations yield $\varepsilon_{fep} = 0.92$ (0.90) for semi-coaxial (BEGe) detectors.

The GERDA background model [17] predicts approximately a flat energy distribution between 1930 and 2190 keV from Compton events of γ-rays of ^{208}Tl and ^{214}Bi decays, degraded α events, and β rays from ^{42}K and ^{214}Bi. The signal region (2039 ± 5) keV and the intervals (2104 ± 5) keV and (2119 ± 5) keV, which contain known γ-ray peaks from ^{208}Tl and ^{214}Bi, respectively, are excluded in the background calculation. The net width of the window used for the evaluation of the constant background is hence 230 keV. The combined energy spectrum around $Q_{\beta\beta}$, with and without the PSD selection, is displayed in Fig. 9.6.

Seven events are observed in the range $Q_{\beta\beta} \pm 5$ keV before the PSD, to be compared to 5.1 ± 0.5 expected background counts. No excess of events beyond the expected background is observed. This statement is strengthened by the pulse shape analysis. Of the six events from the semi-coaxial detectors, three are classified as SSE by ANN, consistent with the expectation. Five of the six events have the same classification by at least one other PSD method. The event in the BEGe data set is rejected by the A/E cut. No events remain within $Q_{\beta\beta} \pm \sigma_E$ after PSD. All results quoted in the following are obtained with PSD.

To derive the signal strength $N^{0\nu}$ and a frequentist coverage interval, a profile likelihood fit of the three data sets is performed. The fitted function consists of a constant term for the background and a Gaussian peak for the signal with mean at $Q_{\beta\beta}$ and standard deviation σ_E. The fit has four free parameters: the backgrounds of the three data sets and $1/T_{1/2}^{0\nu}$, which relates to the peak integral by Eq. (9.1). The likelihood ratio is only evaluated for the physically allowed region $T_{1/2}^{0\nu} > 0$. It was verified that the method has always sufficient coverage. The systematic uncertainties due to the detector parameters, selection efficiency, energy resolution and energy scale are folded in with a Monte Carlo approach which takes correlations into account. The best fit value is $N^{0\nu} = 0$, namely no excess of signal events

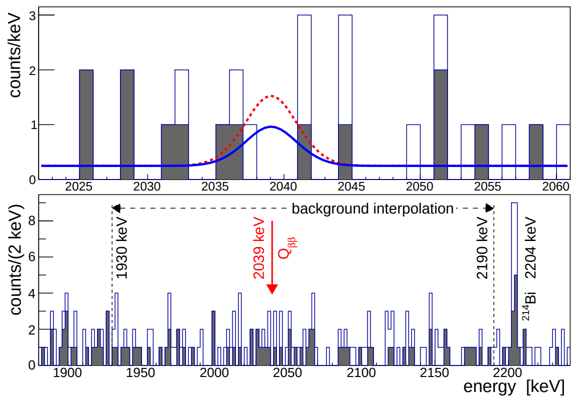

Figure 9.6: The combined energy spectrum from all $^{\mathrm{enr}}$Ge detectors without (with) PSD is shown by the open (filled) histogram. The lower panel shows the region used for the background interpolation. In the upper panel, the spectrum zoomed to $Q_{\beta\beta}$ is superimposed with the expectations (with PSD selection) based on the central value of Ref. [5], $T_{1/2}^{0\nu} = 1.19 \cdot 10^{25}$ yr (red dashed) and with the 90 % upper limit derived in this work, corresponding to $T_{1/2}^{0\nu} = 2.1 \cdot 10^{25}$ yr (blue solid).

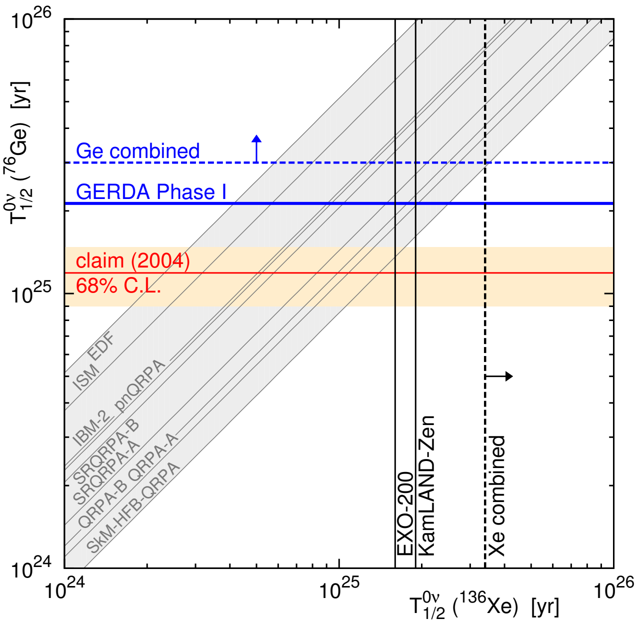

Figure 9.7: Limits (90 % C.L.) on $0\nu\beta\beta$ of ^{76}Ge and ^{136}Xe [9, 10] compared with the signal claim for ^{76}Ge of Ref. [5] (68 % C.L. band). The lines in the shaded gray band are the predictions for the correlation of the half-lives in ^{136}Xe and in ^{76}Ge according to different NME calculations. The selection of calculations and the labels are taken from Ref. [18].

above the background. The limit on the half-life is

$$T^{0\nu}_{1/2} > 2.1 \cdot 10^{25}\ \mathrm{yr} \quad (90\,\%\ \ \mathrm{C.L.}) \tag{9.3}$$

including the systematic uncertainty. The limit on the half-life corresponds to $N^{0\nu} < 3.5$ counts. The systematic uncertainties weaken the limit by about 1.5 %.

The GERDA data show no indication of a peak at $Q_{\beta\beta}$, i.e. the claim for the observation of $0\nu\beta\beta$ decay in ^{76}Ge is not supported. Taking $T^{0\nu}_{1/2}$ from Ref. [5] at its face value, 5.9 ± 1.4 decays are expected in $\Delta E = \pm 2\sigma_E$ and 2.0 ± 0.3 background events after the PSD cuts, as shown in Fig. 9.6. This can be compared with three events detected, none of them within $Q_{\beta\beta} \pm \sigma_E$. The model ($H_1$), which includes the $0\nu\beta\beta$ signal calculated above, gives, in fact, a worse fit to the data than the background-only model (H_0): the Bayes factor, namely the ratio of the probabilities of the two models, is $P(H_1)/P(H_0) = 0.024$. Assuming the model H_1, the probability to obtain $N^{0\nu} = 0$ as the best fit from the profile likelihood analysis is $P(N^{0\nu} = 0|H_1) = 0.01$.

The GERDA result is consistent with the limits by HDM and IGEX. The profile likelihood fit is extended to include the energy spectra from HDM (interval 2000-2080 keV; Fig. 4 of Ref. [2]) and IGEX (interval 2020-2060 keV; Table II of Ref. [3]). Constant backgrounds for each of the data sets and Gaussian peaks for the signal with common $1/T^{0\nu}_{1/2}$ are assumed. Experimental parameters (exposure, energy resolution, efficiency factors) are obtained from the original references or, when not available, extrapolated from the values used in GERDA. The best fit yields $N^{0\nu} = 0$ and the combined limit of

$$T^{0\nu}_{1/2} > 3.0 \cdot 10^{25}\ \mathrm{yr} \quad (90\,\%\ \ \mathrm{C.L.}). \tag{9.4}$$

The Bayes factor is $P(H_1)/P(H_0) = 2 \cdot 10^{-4}$; the claim is hence strongly disfavored. Whereas only ^{76}Ge experiments can test the claimed signal in a model-independent way, NME calculations can be used to compare the present ^{76}Ge result to the recent limits on the ^{136}Xe half-life from KamLAND-Zen [9] and EXO-200 [10].

Figure. 9.7 shows the experimental results, the claimed signal (labeled “claim (2004)”) and the correlations for different predictions, assuming that the exchange of light Majorana neutrinos is the leading mechanism. Within this assumption, the present result can be also combined with the ^{136}Xe experiments to scrutinize Ref. [5]. The most conservative exclusion is obtained by taking the smallest ratio $M_{0\nu}$(^{136}Xe)/$M_{0\nu}$(^{76}Ge)$\simeq 0.4$ [19] of the calculations in Ref. [18]. This leads to an expected signal count of 23.6±5.6 (3.6±0.9) for KamLAND-Zen (EXO-200). The comparison with the corresponding background-only models yields a Bayes factor $P(H_1)/P(H_0)$ of 0.40 for KamLAND-Zen and 0.23 for EXO-200. Including the GERDA result, the Bayes factor becomes 0.0022. Also in this case the claim is strongly excluded. For a larger ratio of NMEs the exclusion becomes even stronger. Note, however, that other theoretical approximations might lead to even smaller ratios and thus weaker exclusions.

The range for the upper limit on the effective electron neutrino mass $m_{\beta\beta}$ is 0.2 – 0.4 eV. This limit is obtained by using the combined ^{76}Ge limit of Eq. (9.4), the recently re-evaluated phase space factors of Ref. [20] and the NME calculations mentioned above.

Intensive preparation for Phase-II of GERDA has been started, 30 new BEGe detectors from ^{76}Ge already produced and tested (about 20 kg ^{76}Ge), in total about 40 kg of detectors will be used.

In Phase-I of the GERDA experiment liquid argon is used as a passive shield only. For the next phases of GERDA additional methods of further reduction of background were developed. In Phase-I of GERDA developed in the LArGe set up methods aimed to reduce background of Ge detectors by using anticoincidence with LAr scintillation signals will be used as well as discrimination by using pulse shape of signals from BEGe detectors.

In addition the methods to reduce background due to cosmogenic ^{42}Ar were developed and tested. Modification of the experimental set ups for Phase-II of GERDA, including the LAr-scintillation veto system assembly inside the GERDA cryostat, will be carried out from the middle of 2014. Physical data-taking in GERDA Phase-II is planned to start from the end of 2014.

Due to the unprecedented low background counting rate and the good energy resolution intrinsic to HPGe detectors, GERDA establishes after only 21.6 kg yr exposure the most stringent $0\nu\beta\beta$ half-life limit for ^{76}Ge. The long-standing claim for a $0\nu\beta\beta$ signal in ^{76}Ge looks strongly disfavored, which calls for a further exploration of the degenerate Majorana neutrino mass scale. This will be pursued by GERDA Phase II aiming for a sensitivity increased by a factor of about 10.

9.1.6 Contribution of JINR Members

JINR Members are playing significant roles in all key parts of GERDA experiment. JINR was responsible for design, production, testing and installation of plastic muon veto system on the top of GERDA cryostat. This veto will be also used for Phase II.

JINR specialists participate heavily in the development of LAr instrumentation. Physicists from our institute are strongly involved in the analysis of GERDA data, especially for Phase II (BEGe) detectors and this contribution will be increased.

JINR members play the central and leading role in the core of GERDA experiment – operations with bare germanium detectors.

9.1.7 Publications, Theses and Conferences

As a result of the project the following

- papers has been published [14, 16, 17, 21–39]
- there are many talks given at conferences and workshops (NANPino-2013, ICATPP-2011, NUCLEUS-2010, NUCLEUS-2009, LAUNCH-2009, TAUP-2009) [40–58].

9.1.8 Finances

Major sources and amount of finances and major equipment acquired (together with travel expenses) during the project runtime are listed in Tab. 9.1.

Funding source	Obtained in 2006-2013 (k$)	Major Equipment acquired and Purpose of expenses
JINR 1100 + RFBR grants + off-budget	75 8 4 2 2 3 5 10	Plastic scintillators for muon veto Electronics for muon veto Mechanical parts of muon veto Alpha-sources Radio-chemical equipment System for coordinate source manipulation Equipment for LARGE test facility Copper, lead, polyethylene for the NIFON gamma-spectrometer
JINR 1100 + RFBR grants + off-budget	30 per year	Travel and living expenses for works at LNGS (Italy), MPIK and TUM (Germany), BNO INR RAS (Baksan, Russia)

Table 9.1: Major sources and amount of finances and major equipment acquired together with travel expenses.

References

[1] Brianna J. Mount, Matthew Redshaw, and Edmund G. Myers. “Double-beta-decay Q values of Se-74 and Ge-76”. In: *Phys.Rev.* C81 (2010), p. 032501.

[2] H.V. Klapdor-Kleingrothaus et al. “Latest results from the Heidelberg-Moscow double beta decay experiment”. In: *Eur.Phys.J.* A12 (2001), pp. 147–154. arXiv: hep-ph/0103062 [hep-ph].

[3] C.E. Aalseth et al. “The IGEX Ge-76 neutrinoless double beta decay experiment: Prospects for next generation experiments”. In: *Phys.Rev.* D65 (2002), p. 092007. arXiv: hep-ex/0202026 [hep-ex].

[4] C.E. Aalseth et al. “The IGEX experiment revisited: A Response to the critique of Klapdor-Kleingrothaus, Dietz and Krivosheina”. In: *Phys.Rev.* D70 (2004), p. 078302. arXiv: nucl-ex/0404036 [nucl-ex].

[5] H.V. Klapdor-Kleingrothaus et al. “Search for neutrinoless double beta decay with enriched Ge-76 in Gran Sasso 1990-2003”. In: *Phys.Lett.* B586 (2004), pp. 198–212. arXiv: hep-ph/0404088 [hep-ph].

[6] Bernhard Schwingenheuer. “Status and prospects of searches for neutrinoless double beta decay”. In: *Annalen Phys.* 525 (2013), pp. 269–280. arXiv: 1210.7432 [hep-ex].

[7] H.V. Klapdor-Kleingrothaus and I.V. Krivosheina. “The evidence for the observation of 0nu beta beta decay: The identification of 0nu beta beta events from the full spectra”. In: *Mod.Phys.Lett.* A21 (2006), pp. 1547–1566.

[8] Hans Volker Klapdor-Kleingrothaus and Irina V. Krivosheina. “Why is the conclusion of the Gerda experiment not justified”. In: *Phys.Part.Nucl.Lett.* 10 (2013), pp. 704–709. arXiv: 1308.2524 [hep-ex].

[9] A. Gando et al. “Limit on Neutrinoless $\beta\beta$ Decay of Xe-136 from the First Phase of KamLAND-Zen and Comparison with the Positive Claim in Ge-76”. In: *Phys.Rev.Lett.* 110.6 (2013), p. 062502. arXiv: 1211.3863 [hep-ex].

[10] M. Auger et al. “Search for Neutrinoless Double-Beta Decay in ^{136}Xe with EXO-200”. In: *Phys.Rev.Lett.* 109 (2012), p. 032505. arXiv: 1205.5608 [hep-ex].

[11] G. Heusser. “Low-radioactivity background techniques”. In: *Ann.Rev.Nucl.Part.Sci.* 45 (1995), pp. 543–590.

[12] J.F. Wilkerson et al. “The MAJORANA demonstrator: A search for neutrinoless double-beta decay of germanium-76”. In: *J.Phys.Conf.Ser.* 375 (2012), p. 042010.

[13] Dusan Budjas et al. “Pulse shape discrimination studies with a Broad-Energy Germanium detector for signal identification and background suppression in the GERDA double beta decay experiment”. In: *JINST* 4 (2009), P10007. arXiv: 0909.4044 [nucl-ex].

[14] M. Agostini et al. “Pulse shape discrimination for GERDA Phase I data”. In: *Eur.Phys.J.* C73 (2013), p. 2583. arXiv: 1307.2610 [physics.ins-det].

[15] M. Agostini, L. Pandola, and P. Zavarise. “Off-line data processing and analysis for the GERDA experiment”. In: *J.Phys.Conf.Ser.* 368 (2012), p. 012047. arXiv: 1111.3582 [physics.data-an].

[16] K.H. Ackermann et al. “The GERDA experiment for the search of $0\nu\beta\beta$ decay in ^{76}Ge”. In: *Eur.Phys.J.* C73 (2013), p. 2330. arXiv: 1212.4067 [physics.ins-det].

[17] M. Agostini et al. “The background in the neutrinoless double beta decay experiment GERDA”. In: *Eur.Phys.J.* C74 (2014), p. 2764. arXiv: 1306.5084 [physics.ins-det].

[18] P.S. Bhupal Dev et al. “Constraining Neutrino Mass from Neutrinoless Double Beta Decay”. In: *Phys.Rev.* D88 (2013), p. 091301. arXiv: 1305.0056 [hep-ph].

[19] Fedor Simkovic et al. “$0\nu\beta\beta$ and $2\nu\beta\beta$ nuclear matrix elements, quasiparticle random-phase approximation, and isospin symmetry restoration”. In: *Phys.Rev.* C87.4 (2013), p. 045501. arXiv: 1302.1509 [nucl-th].

[20] J. Kotila and F. Iachello. “Phase space factors for double-β decay”. In: *Phys.Rev.* C85 (2012), p. 034316. arXiv: 1209.5722 [nucl-th].

[21] M. Agostini et al. “Results on neutrinoless double beta decay of 76Ge from GERDA Phase I”. In: *Phys.Rev.Lett.* 111 (2013), p. 122503. arXiv: 1307.4720 [nucl-ex].

[22] M. Agostini et al. “Measurement of the half-life of the two-neutrino double beta decay of Ge-76 with the Gerda experiment”. In: *J.Phys.* G40 (2013), p. 035110. arXiv: 1212.3210 [nucl-ex].

[23] M. Agostini et al. “LArGe & for active background suppression in GERDA”. In: *J.Phys.Conf.Ser.* 375 (2012), p. 042009.

[24] L. Pandola et al. “Monte Carlo evaluation of the muon-induced background in the GERDA double beta decay experiment”. In: *Nucl.Instrum.Meth.* A570 (2007), pp. 149–158.

[25] Stefan. Schonert et al. “Status of the Germanium Detector Array (GERDA) in the search of neutrinoless beta beta decays of Ge-76 at LNGS”. In: *Phys.Atom.Nucl.* 69 (2006), pp. 2101–2108.

[26] V. Egorov et al. “muCR42beta: Muon capture rates for double-beta decay”. In: *Czech. J. Phys.* 56 (2006), pp. 453–457.

[27] Carla Macolino. “Results on neutrinoless double beta decay from GERDA Phase I”. In: *Mod.Phys.Lett.* A29.1 (2014), p. 1430001. arXiv: 1312.0562 [hep-ex].

[28] M. Agostini et al. “Measurement of the half-life of the two-neutrino double beta decay of Ge-76 with the Gerda experiment”. In: *J.Phys.* G40 (2013), p. 035110. arXiv: 1212.3210 [nucl-ex].

[29] E. Andreotti et al. “HEROICA: an Underground Facility for the Fast Screening of Germanium Detectors”. In: *JINST* 8 (2013), P06012. arXiv: 1302.4277 [physics.ins-det].

[30] C. O’Shaughnessy et al. “High voltage capacitors for low background experiments”. In: *Eur.Phys.J.* C73 (2013), p. 2445.

[31] D. Budjas et al. “Isotopically modified Ge detectors for Gerda: from production to operation”. In: *JINST* 8 (2013), P04018. arXiv: 1303.6768 [physics.ins-det].

[32] Ju.M. Gavriljuk et al. “Working characteristics of the New Low-Background Laboratory (DULB-4900)”. In: *Nucl.Instrum.Meth.* A729 (2013), pp. 576–580.

[33] M. Agostini et al. “LArGe & for active background suppression in GERDA”. In: *J.Phys.Conf.Ser.* 375 (2012), p. 042009.

[34] M. Barnabe-Heider et al. “Operation and performance of a bare broad-energy germanium detector in liquid argon”. In: *JINST* 5 (2010), P10007.

[35] G. Meierhofer. “GERDA: A new neutrinoless double beta experiment using Ge-76”. In: *J.Phys.Conf.Ser.* 312 (2011), p. 072011.

[36] A. Smolnikov. “Development and installation of the GERDA experiment”. In: *J. Phys. Conf. Ser.* 203 (2010), p. 012059.

[37] Anatoly Smolnikov and Peter Grabmayr. “Conversion of experimental half-life to effective electron neutrino mass in 0nubetabeta decay”. In: *Phys.Rev.* C81 (2010), p. 028502.

[38] A. Bettini. “GERDA. Germanium detector array. Search for neutrino-less beta beta decay of Ge-76”. In: *Nucl.Phys.Proc.Suppl.* 168 (2007), pp. 67–69.

[39] A. Gangapshev. “The background of Ge detectors in LArGe after applying pulse shape discrimination and liquid argon scintillation veto”. In: (2011). Proceedings of XV-th International School ”PARTICLES and COSMOLOGY”.

[40] A.V. Lubashevskiy. “42K background mitigation for GERDA Phase II”. In: DPG meeting “Particle physics”, Mainz, Germany. 2014.

[41] A.V. Lubashevskiy. “Status and results of the GERDA experiment”. In: XXXIX th International Workshop on High Energy Physics, Protvino. 2013.

[42] A.A.Smolnikov. In: The International Workshop on Non-Accelerator New Physics (NANPino-2013), ”Valday” resort, Novgorod region, RUSSIA. 2013.

[43] A.V. Lubashevskiy. “The GERDA experiment. Status and results of data taking”. In: 6th International Conference Nuclear Physics in Astrophysics (NPA6), Lisbon, Portugal. 2013.

[44] A.V. Lubashevskiy. In: The International School for AstroParticle Physics (ISAPP), Canfranc, Spain. 2013.

[45] A.V. Lubashevskiy. In: DPG meeting “Hadrons and Nuclei”, Dresden, Germany. 2013.

[46] A.A.Smolnikov. In: VIII International Conference “Nuclear Science and its Application”, Samarkand, Uzbekistan. 2012.

[47] A.A.Smolnikov. In: 24th Rencontres de Blois “Particle Physics and Cosmology”, Blois, France. 2012.

[48] A.V. Lubashevskiy. In: DPG meeting “Hadrons and Nuclei”, Mainz, Germany. 2012.

[49] V.B.Brudanin. In: 62nd International conference “Nuclei 2012”, Voronezh, Russia. 2012.

[50] A.V. Lubashevskiy. In: 62nd International conference “Nuclei 2012”, Voronezh, Russia. 2012.

[51] A.Lubashevsky and A. Smolnikov. In: DPG meeting “Hadrons and Nuclei”, Munster, Germany. 2011.

[52] K.Gusev. In: 13th ICATPP Conference on Astroparticle, Particle, Space Physics and Detectors for Physics Applications, Como, Italy. 2011.

[53] K.Gusev. In: LX International Conference on Nuclear Physics “Nucleus 2010” , St. Peterburg. 2010.

[54] A.A.Smolnikov. In: International Conference on Neutrinos and Dark Matter in Particle, Astroparticle and Nuclear Physics, LAUNCH-09, Heidelberg, Germany. 2009.

[55] A.A.Smolnikov. In: 11th International Conference on Topics in Astroparticle and Undergound Physics TAUP2009, Roma, Italy. 2009.

[56] K.Gusev. In: 59 International Conference “Nucleus 2009”, Cheboksary, Russia. 2009.

[57] A.A.Smolnikov. In: International Workshop on Neutrino Physics, Aarhus, Denmark, Roma, Italy. 2007.

[58] A.A.Smolnikov. In: 14th International Baksan School ”Particles and Cosmology-2007”. 2007.

Chapter 10

JUNO Project

Editors: D.Naumov, M.Gonchar

Project Title

JUNO Experiment

Project Leaders

- 2015–2017 — project leader D.V. Naumov, project leader deputy M.O. Gonchar

Abstract

The Jiangmen Underground Neutrino Observatory (JUNO) is a multipurpose neutrino-oscillation experiment designed to determine neutrino mass hierarchy, precisely measure oscillation parameters, and explore other rich scientific possibilities by detecting reactor antineutrinos from the Yangjiang and Taishan Nuclear Power Plants, observe supernova neutrinos, study the atmospheric, solar neutrinos and geo-neutrinos, and perform exotic searches, with a 20 kiloton liquid scintillator detector of unprecedented 3% energy resolution (at 1 MeV) at 700-meter deep underground.

keywords: neutrino mass hierarchy, precise measurement of neutrino mixing parameters, neutrino detectors of new generation

Project Members From JINR

Anfimov N.V., Biktemerova S.V., Butorov I.V., Chukanov A.V., Dolgareva M.A., Dmitrievsky S.G., Fedoseev D.V., Fomenko K.A., Gonchar M.O., Gornushkin Yu.A., Krasnoperov A.V., Krumshtein Z.V., Morozov N.A., Naumov D.V., Naumova E.A., Nemchenok I.B., Olshevsky A.G., Rybnikov A.V., Sadovskiy A.B., Selyunin A.S., Smirnov O.Yu., Taichenachev D.V.

Project Duration. Approval Date(s)

- 2015–2017 — Project duration
- April 24 2014 — approval by DLNP Scientific Council
- June 2014 — submitted for approval by PAC JINR

List of Participating Countries and Institutions

At this moment the official Collaboration is not formed yet. A preliminary list of countries and institutions is given as follows. Institute of High Energy Physics, Beijing, China; Germany; France; Italy; Switzerland; Russia, Joint Institute for Nuclear Research; Taiwan; USA

10.1 Project Description

10.1.1 Fundamental Scientific Problem Addressed by the Project

Mass hierarchy. The main goal of JUNO is a measurement of neutrino mass hierarchy and precise measurements of neutrino mixing matrix and mass squared splittings. The determination of the neutrino mass hierarchy can be done by precisely measuring the energy spectrum of reactor electron antineutrinos at a distance of 53 km from the reactors. The relative measurement can reach a sensitivity of $\Delta\chi^2 > 16$ in the ideal case of a single reactor and a single detector, and $\Delta\chi^2 > 9$ considering the spread of reactor cores and uncertainties of the detector response [1]. If the absolute value of $\Delta m^2_{\mu\mu}$ measured from accelerator experiments is included with a precision of 1%, the sensitivity to the mass hierarchy can be improved to $\Delta\chi^2 > 25$ and $\Delta\chi^2 > 16$ in the ideal and real case, respectively, as shown in Fig. 10.1.

Precision neutrino mixing measurements. JUNO is going to improve the precision of Δm^2_{21}, Δm^2_{32} and $\sin^2\theta_{12}$ to better than 1%. Considering the precision of $\sin^2\theta_{13}$ can be measured to ~4% by Daya Bay, the unitarity of the neutrino mixing matrix can be probed to a 1% level. The expected precision of mixing parameters by JUNO is listed in Tab. 10.1.

	Current	JUNO
Δm^2_{21}	~3%	~0.6%
Δm^2_{32}	~5%	~0.6%
$\sin^2\theta_{12}$	~6%	~0.7%
$\sin^2\theta_{23}$	~20%	N/A
$\sin^2\theta_{13}$	~4% in a near future	~15%

Table 10.1: Expected precision of mixing parameters by JUNO.

Apart from these ambitious goals the JUNO detector will be able also to solve the following problems.

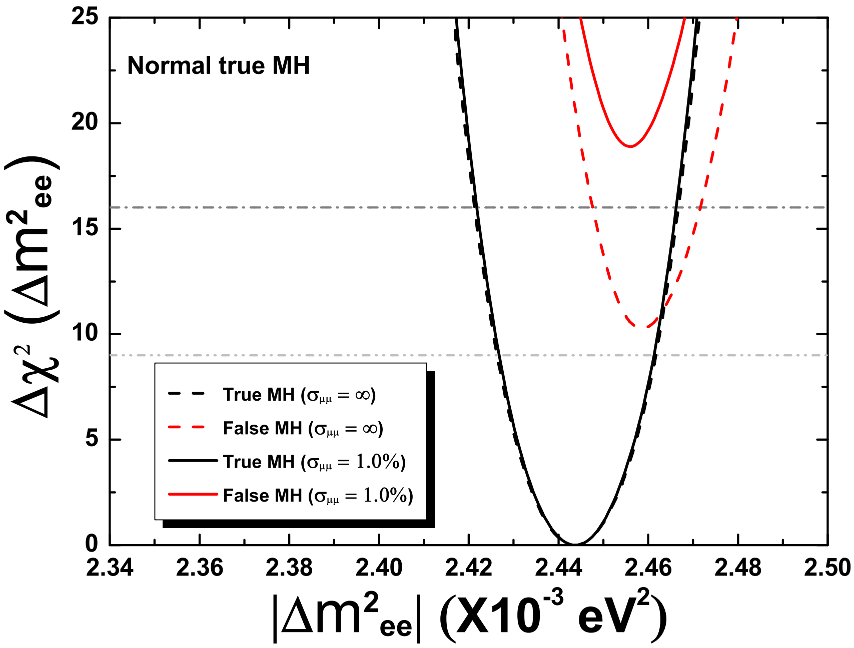

Figure 10.1: The mass hierarchy sensitivity for JUNO. Dash lines represent the relative measurement. Solid lines include the absolute value of $\Delta m^2_{\mu\mu}$ with a precision of 1%.

Supernova neutrinos. So far less than 20 events from SN1987 have been experimentally detected. JUNO would be able to detect about five thousand supernova neutrinos in less than 10 seconds for a SN event as far as 10 kpc away (which corresponds to our Galaxy). These events will be both single and correlated events, which makes their observation a unique feature of JUNO:

- $\bar{\nu}_e + p \to n + e^+$, about 3000 events
- $\bar{\nu}_e + {}^{12}\mathrm{C} \to {}^{12}\mathrm{B}^* + e^+$, about 10-100 events
- $\nu_e + {}^{12}\mathrm{C} \to {}^{12}\mathrm{N}^* + e^-$, about 10-100 events
- $\nu_x + {}^{12}\mathrm{C} \to {}^{12}\mathrm{N}^* + \nu_x$, about 600 events
- $\nu_x + p \to \nu_x + p$, single events
- $\nu_x + e^- \to \nu_x + e^-$, single 3000 events

Geoneutrinos. The statistics of geoneutrinos is expected to be a factor ten larger than that recorded by BOREXINO and KamLAND experiments. However, an observation of these events will be difficult in terms of systematics and will require a careful study.

Diffuse supernova neutrinos. The Diffuse Supernova Neutrino Background is the weak glow of MeV neutrinos and antineutrinos from distant core-collapse supernovae. These neutrinos have not yet been detected. JUNO may be able to observe such events. A careful study of systematics is need though.

Solar neutrinos. Solar neutrinos could be detected by JUNO if the radioactive purity of the detector interior proves to be small enough.

Atmospheric neutrinos. JUNO would be able to record atmospheric neutrinos and therefore JUNO would be able to study CP violation in the lepton sector. It can reach 1-2 σ sensitivity at various ranges of δ. It will make a significant contribution to the overall sensitivity.

Proton decay. JUNO, with a pulse shape readout, will have high efficiency for the $P \to K + \nu$ channel. If no candidate is found and the channel is background free then the upper limit $\tau < 1.6 \times 10^{34}$ years on the proton lifetime can be set, which is very competitive even with respect to LBNE, HyperKamiokande and LENA.

Sterile neutrinos. Sterile neutrinos can be searched for by JUNO as a deficit in the event rate at $\Delta m^2 > 0.1$ eV^2 and as a possible energy spectrum change for the case of $\Delta m^2 \in 10^{-4} \div 10^{-2}$eV^2.

Other possible physics studies with JUNO include

- Indirect dark matter search,
- Non-standard interaction,
- Other probes of new physics.

10.1.2 Specific Project Objectives and Expected Results

The expected results of JUNO experiment will include:

- Measurement of the neutrino mass hierarchy,
- Precise measurement (with accuracy similar to the quark sector) of neutrino mixing matrix and Δm^2 mass squared splittings,
- Possible detection of supernova neutrinos,
- Detection of geoneutrinos,
- Detection diffuse supernova neutrinos,
- Detection of solar neutrinos,
- Detection of atmospheric neutrinos,
- Search for proton decay,
- Search for Sterile neutrinos,
- Indirect dark matter search,

- Studies of non-standard interaction,
- Other probes of new physics.

More details about the physics case of the JUNO experiment can be found in Sec. 10.1.1. However, accomplishing these goals is a long-term project (see below) and apparently none of these goals are possible to attain within the currently proposed 2015-2017 time scale of the JINR project. The current project aims to develop experimental techniques and solve several key goals within the project.

Within this project we expect to:

1. Perform a study of JUNO sensitivity to the mass hierarchy measurement, taking into account systematic uncertainties.
2. Develop the simulation and reconstruction software for the experiment.
3. Perform simulations of various detector design options and estimate possible reconstruction accuracy of the visible energy and interaction position.
4. Perform estimation and modeling of backgrounds.
5. Build an experimental facility at DLNP JINR dedicated to characterization of PMTs to be used by the JUNO experiment,
6. Perform studies of PMT sensitivity to the Earth magnetic field (EMF). Perform studies of different options of PMT protection against the EMF and make a recommendation to the Collaboration for the best option. Perform a feasability study for JINR contribution to the JUNO experiment in design, prototyping, construction and installation of the protection measures against EMF.
7. Perform a feasibility study of the Top Muon Veto detector based on re-using of OPERA Target Tracker detector. This option can be considered as a possible JINR contribution to the JUNO experiment.
8. Perform, in collaboration with the HVSYS company, the development and all required experimental tests of the high voltage system for JUNO PMT. Perform feasibility studies for JINR contribution to the JUNO experiment in design, prototyping, construction and installation of the PMT high voltage system.
9. Develop the software for the global analysis of neutrino oscillation data with the primary goal of combining reactor and accelerator neutrino data to measure the mass hierarchy.

Time schedule.

- end of 2014 — final decision
- 2015 — engineering design, PMT production line manufacturing
- 2016 — Start PMT production, detector production or bidding
- 2017 — Complete civil construction, start detector construction
- 2018 — Start LS production
- 2019 — Complete detector assembly, installation, LS filling
- 2020 — Start data taking.

10.1.3 Basic Methods and Approaches Used in the Project

Physics requirements

Let us define the mean value of cross-section to detect anti-neutrinos, averaged over neutrino spectrum and neglecting oscillations, as

$$\langle\sigma_f\rangle \equiv \int dE S(E)\sigma(E) = 5.8\cdot 10^{-43}\ \text{cm}^{-2}, \tag{10.1}$$

where $S(E)$ is the mean energy spectrum of anti-neutrinos from the reactor. The mean energy released per fission in a reactor is $\langle E_f\rangle = 205$ MeV. The number of fissions per second is given by

$$N_f = 6.24\cdot 10^{21}\text{s}^{-1}\frac{P_{\text{th}}}{\text{GWt}}\frac{\text{MeV}}{\langle E_f\rangle} = 3.04\cdot 10^{19}\text{s}^{-1}\frac{P_{\text{th}}}{\text{GWt}}, \tag{10.2}$$

where P_{th} is the reactor power. A detector with target mass (m_{det}) has number of protons N_p given by

$$N_p = \alpha_p\frac{m_{\text{det}}}{m_{\text{H}}} = 1.26\cdot 10^{34}\alpha_p\frac{m_{\text{det}}}{20\text{ktons}} \tag{10.3}$$

where α_p gives the mass-fraction of hydrogen (free protons). The number of anti-neutrino interactions per time interval t from a reactor displaced from the detector at distance L thus reads:

$$N_{\text{IBD}} = \frac{N_f\langle\sigma_f\rangle N_p t}{4\pi L^2} = 0.53\cdot 10^4\alpha_p\left(\frac{P_{\text{th}}}{\text{GWt}}\right)\left(\frac{m_{\text{det}}}{20\text{ktons}}\right)\left(\frac{t}{\text{year}}\right)\left(\frac{100\text{km}^2}{L^2}\right) \tag{10.4}$$

For $P_{\text{th}} = 37$ GWt and $L = 52$ km, assuming $\alpha_p = 0.12$ one gets

$$N_{\text{IBD}} = 8.74\cdot 10^4\left(\frac{P_{\text{th}}}{37\text{GWt}}\right)\left(\frac{m_{\text{det}}}{20\text{ktons}}\right)\left(\frac{t}{\text{year}}\right)\left(\frac{52\text{km}^2}{L^2}\right) \tag{10.5}$$

The following sources of antineutrinos are taken into account for the JUNO detector: near and far reactors and geo-neutrinos. Since antineutrinos travel from the reactor core to the detector through the Earth we take into account the matter effects according to the general 3$-\nu$ oscillations scheme [2] and using relevant approximations [3].

The expected E_{vis} energy spectrum of the JUNO experiment is shown in Fig. 10.2 where contributions from near and far reactors and geo-neutrinos are also shown. We assume here $\Delta m^2_{\text{ee}} = 2.4\cdot 10^{-3}\text{eV}^2$, normal hierarchy and ideal energy reconstruction.

In the upper left corner of Fig. 10.3 we show the JUNO visible energy spectra calculated assuming $\Delta m^2_{\text{ee}} = 2.44\cdot 10^{-3}\text{eV}^2$ for normal and inverted hierarchy for ideal energy reconstruction. Also the difference of these spectra is shown. As one can see these spectra differ significantly and this is the key to the mass hierarchy. However in reality a finite energy resolution will partially wash out this sensitivity as can be seen from other plots in Fig. 10.3. One could make a reasonable guess from these plots that $\sigma_E = 3\%$ at 1 MeV of visible energy is a necessary requirement to make the mass hierarchy observation possible.

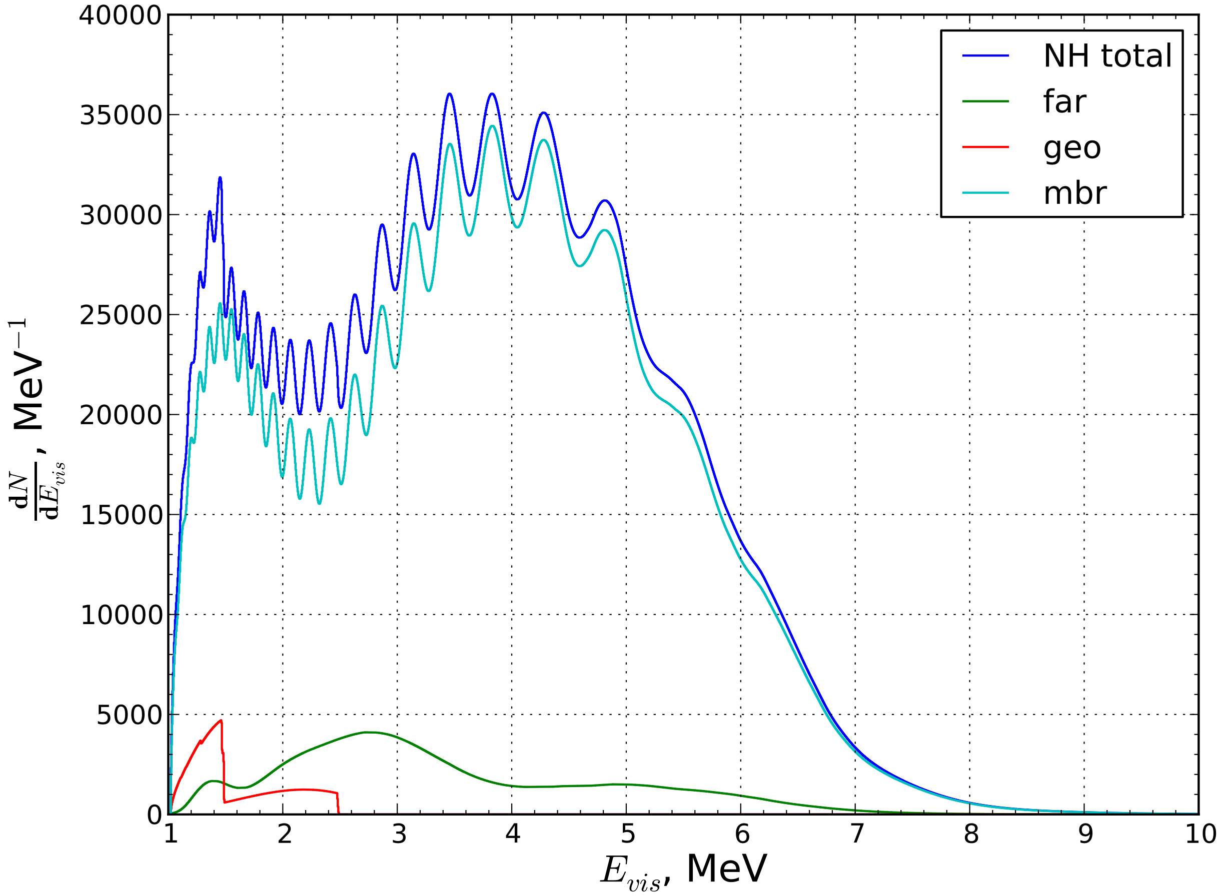

Figure 10.2: The expected E_{vis} energy spectrum of the JUNO experiment assuming $\Delta m^2_{\text{ee}} = 2.4{\cdot}10^{-3}$eV^2, normal hierarchy and ideal energy reconstruction. The contributions from near and far reactors and geo-neutrinos are also shown.

Indeed, an examination of $\delta\chi^2(\sigma_E) = \chi^2(\sigma_E) - \chi^2(\sigma_E = 0)$ shown in left Fig. 10.4 suggests that 3% is needed to achieve the definitive result on the mass hierarchy determination [1].

Therefore, a first requirement is the energy resolution requirement, which can be formulated as

$$\sigma_E = \frac{3\%}{\sqrt{E_{\text{vis}}/\text{MeV}}} = (\frac{2.6\%}{\sqrt{E_{\text{vis}}/\text{MeV}}} + 0.3\%). \tag{10.6}$$

The next requirement is the optimal baseline distance. The optimum can be found as a maximum of $\Delta\chi^2(L) = \chi^2(L) - \chi^2(L = 0)$. The optimal distance found is at $L = 52$ km [1] as can be seen in the right Fig. 10.4.

The chosen location for the detector placement is close to Yangjiang (YJ) and Taishan (TS) reactor complexes, as well as the remote reactors of Daya Bay (DYB) and Huizhou (HZ).

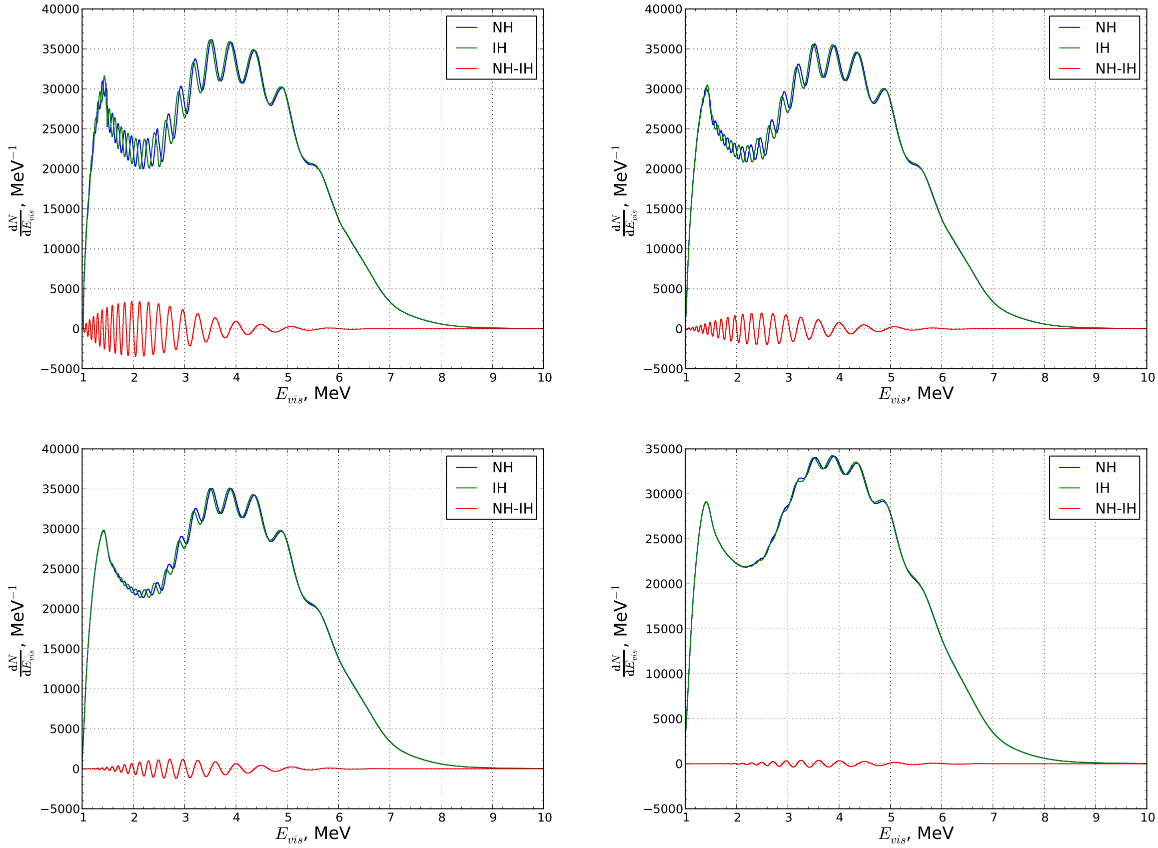

Figure 10.3: JUNO visible energy spectra calculated assuming $\Delta m^2_{\text{ee}} = 2.44 \cdot 10^{-3}\text{eV}^2$ for normal and inverted hierarchy for ideal energy reconstruction (left, up), $\sigma_E = 2\%$ (right, up), $\sigma_E = 3\%$ (left, bottom), $\sigma_E = 5\%$ (right, bottom).

A summary of the power and baseline distribution for the Yangjiang (YJ) and Taishan (TS) reactor complexes, as well as the remote reactors of Daya Bay (DYB) and Huizhou (HZ) is given in Tab. 10.2.

Cores	YJ-C1	YJ-C2	YJ-C3	YJ-C4	YJ-C5	YJ-C6
Power (GW)	2.9	2.9	2.9	2.9	2.9	2.9
Baseline(km)	52.75	52.84	52.42	52.51	52.12	52.21
Cores	TS-C1	TS-C2	TS-C3	TS-C4	DYB	HZ
Power (GW)	4.6	4.6	4.6	4.6	17.4	17.4
Baseline(km)	52.76	52.63	52.32	52.20	215	265

Table 10.2: Summary of the power and baseline distributions for the Yangjiang (YJ) and Taishan (TS) reactor complexes, as well as the remote reactors of Daya Bay (DYB) and Huizhou (HZ).

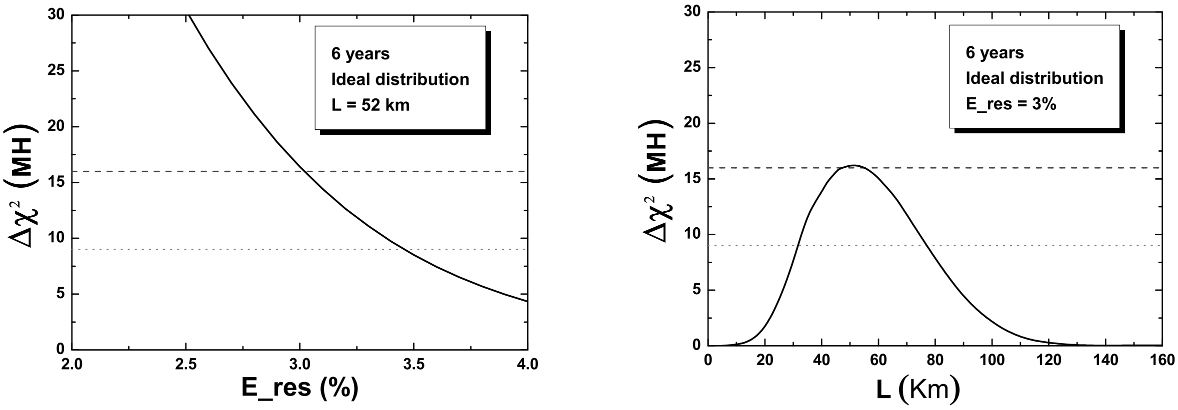

Figure 10.4: Left plot: $\delta\chi^2 = \chi^2(\sigma_E) - \chi^2(\sigma_E = 0)$ vs σ_E. Right plot: $\Delta\chi^2(L) = \chi^2(L) - \chi^2(L = 0)$ vs L. The plots are from [1].

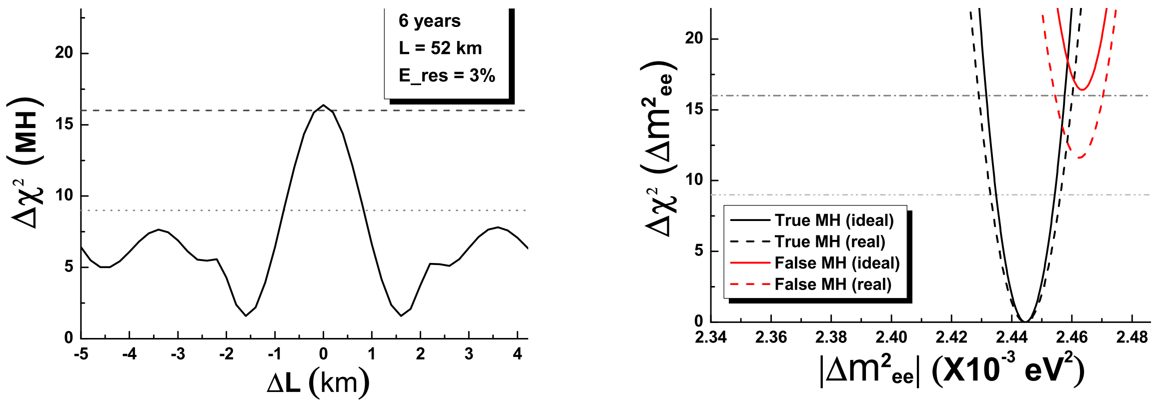

Figure 10.5: The variation (left panel) of the MH sensitivity as a function of the baseline difference of two reactors and the comparison (right panel) of the MH sensitivity for the ideal and actual distributions of the reactor cores.

The baselines to two reactor complexes should be equal. The impact of unequal baselines is shown in the left panel of Fig.10.5, by keeping the baseline of one reactor unchanged and varying that of another. The reduction of sensitivity due to the actual distribution of reactor cores is shown in the right panel of Fig. 10.5, which gives a degradation of $\Delta\chi^2_{\text{MH}} \simeq 5$. In all of the following studies the actual spacial distribution of reactor cores for the JUNO experiment is taken into account [1].

Summary of requirements Let us briefly summarize the main requirements.

- The energy resolution σ_E (see Eq.(10.6)) should not worse than 3% at 1 MeV of the visible energy.

- The optimal baseline is at 52 km.
- The baselines to two reactor complexes should be equal to each other within 200 meters.

How can these requirements be satisfied?

10.1.4 Detector Description

Antineutrino detector. The central detector concept includes two concentric spherical tanks located in a water pool, as shown in Fig. 10.6. The inner acrylic tank is filled with 20 kton linear alkylbenzene (**LAB**) based liquid scintillator (**LS**).

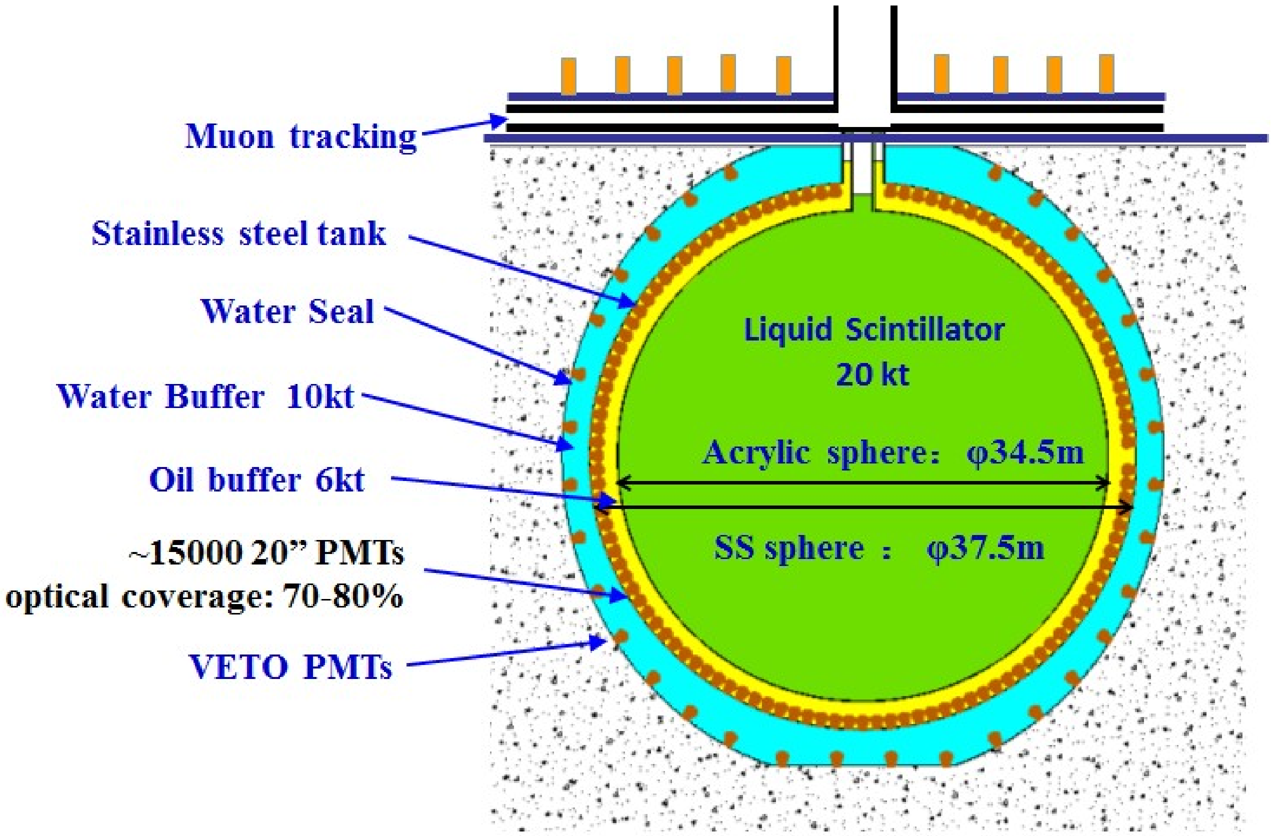

Figure 10.6: A detector concept for JUNO.

The outer stainless steel tank is filled with 6 kton mineral oil as a buffer to protect LS from radioactivity. There are around 15,000 20" photomultiplier tubes (PMTs) installed in the internal surface of the steel tank. Because it is extremely difficult to build both large tanks at the same time, there are other options for the detector design. Option 1 removes the steel tank. The acrylic tank is directly placed into water, which brings a large pressure difference. Mineral oil is replaced by water in this option. PMTs can be installed in a steel frame in water. Option 2 removes the acrylic tank. Instead, small acrylic boxes filled with mineral oil can be made and installed as modules to contain single a PMT or a group of PMTs. There are pipes at the back of each module for mineral oil filling and cabling. The leakage through cables is the major concern. Option 3 uses a balloon to replace the acrylic tank. The balloon is relatively cheap for construction and quick for installation. Experiences from Borexino and KamLAND are very encouraging. There are many technical details of film materials need to be considered, such as the transparency, radon permeability, and the leak check. Option 4 is actually a fall-back plan for option 3. If the balloon fails the liquid scintillator has to be directly filled into the steel tank. In this case the PMTs are immersed in the liquid scintillator, hence the need for special protection. On the other hand, since there is no mineral oil or water buffer, radioactivity from PMTs will increase the trigger rate to more than 1 MHz, which can't be handled by the data acquisition system. An online data reduction algorithm was developed to reduce the trigger rate to less than 1 kHz based on the charge pattern detected by PMTs. However, the energy resolution is affected because of high probability of the overlap between antineutrino signals and radioactivity.

The water pool protects the central detector from natural radioactivity in surrounding rocks. It also serves as a water Cherenkov detector after being equipped with PMTs to tag cosmic muons. There is another muon tracking detector on top of the water pool, used to improve muon detection efficiency and to get better muon tracking.

The reactor electron antineutrino interacts with the proton via the inverse β-decay (IBD) reaction in the liquid scintillator, and releases a positron and a neutron. The positron deposits its energy quickly, providing a prompt signal. The energy of positron carries most of the kinetic energy of the neutrino. The neutron is captured by a proton after an average time of 200 μs, then releases a 2.2 MeV gamma, providing a delayed signal. The coincidence of prompt-delayed signals provides a distinctive antineutrino signature. The estimated IBD reaction rate is 40/day. The dominating background is accidental coincidence coming from two uncorrelated background radiation interactions that randomly satisfy the energy and time correlation for the IBD antineutrino selection. It is designed to be less than 10% of IBD signals and can be precisely measured in data. Other major backgrounds are introduced by cosmic muons, including cosmogenic β-n isotope ^{9}Li/^{8}He and fast neutrons. Both of them are less than 1% after appropriate muon veto.

Energy resolution. 3% energy resolution at 1 MeV corresponds to 1200 photo-electrons per MeV of released energy, which is significantly better performance than the state-of-the-art detectors such as BOREXINO[4] and KamLAND[5]. How we are going to reach this resolution?

- **JUNO spherical geometry and 80% PMT coverage.** The ideal arrangement of 20" PMTs can achieve about 80% coverage. A mixture of 8" PMTs and 20" PMTs was considered, which can reach a similar coverage to the ideal case, while the smaller PMTs can provide better timing for event vertex reconstruction. The option of adding reflection cones into the clearance was studied. With two thin acrylic panels having an air gap, for uniformly distributed events, MC simulation shows $\sim$6% increase in the total number of PEs. Besides, reflecting to local PMTs won't impact the vertex reconstruction.

- **High QE PMTs** are expected to be developed. The quantum efficiency of the photocathode made of super bialkali is expected to reach up to 35%. The traditional dynode can be replaced by the micro channel plate (MCP), which has near 4π acceptance, receiving not only the transmission light but also the refection light with the reflection photocathode at the bottom of PMT, hence largely improving the collection efficiency. A prototype of MCP-PMT has been made and is also undergoing testing in JINR.
- **High transparency of the liquid scintillator.** To reach a high transparency for the liquid scintillator, the production of LAB has been improved and the attenuation length of the raw liquid increased to 20.5 m at 430 nm wavelength. There are various techniques employed for the purification, such as molecular distillation, vacuum distillation and filtration with the Al_2O_3 column. Currently, the attenuation length is increased to 24 m at 430 nm. Other methods, such as lowering the temperature or optimizing the fluor concentration, were studied to improve the light yield. We plan to use a liquid scintillator without Gd nuclei in order to improve the attenuation length. Also, this option has less risk in synthesis and long-term stability and lower irreducible accidental backgrounds from LS, important for a large detector. Without extensive purification one might expect the following radioactive purity of the LS with Gd: 10^{-12} g/g, while the LS without Gd should have about 10^{-16} g/g. The default recipe of LS is LAB + 3g/L PPO + 15mg/L bis-MSB (Daya Bay: safe, very good transparency).

Background. The detector location will have about 700 meters of overburden. This implies a muon minimum energy $E_\mu \simeq 211$ GeV and muon rate $R_\mu \simeq 3.8$ Hz. We assume that the single rates from PMT and LS are expected to be 5 Hz. We further assume good muon reconstruction and similar muon efficiency as in Daya Bay. Under these conditions we estimate the expected background as given in Tab. 10.3.

	B/S, % (Daya Bay)	B/S, % (JUNO)	Techniques
Accidentals	1.4	10	Low PMT radioactivity; LS purification; prompt-delayed distance cut
Fast neutrons	0.1	0.4	High muon detection efficiency (similar to Daya Bay)
$^9Li/^8He$	0.4	0.8	Muon tracking. If a good track is found apply the distance-to-muon track cut ($<$ 5m) and veto 2s. If shower muon, full volume veto 2s

Table 10.3: Estimation of expected background.

10.1.5 Contribution of JINR Members

The JINR group expects to contribute to the project in the following items:

1. Perform a study of JUNO sensitivity to the mass hierarchy measurement, taking into account systematic uncertainties.

2. Develop the simulation and reconstruction software for the experiment.

3. Perform simulations of various detector design options and estimate possible reconstruction accuracy of the visible energy and interaction position.

4. Perform estimation and modeling of backgrounds.

5. Build an experimental facility at DLNP JINR dedicated to characterization of PMTs to be used by the JUNO experiment.

6. Perform studies of PMT sensitivity to the Earth magnetic field (EMF). Perform studies of different options of PMT protection against the EMF and make a recommendation to the Collaboration for the best option. Perform a study a feasibility of JINR contribution to the JUNO experiment in design, prototyping, construction and installing of the protection against EMF.

7. Perform a feasibility study of Top Muon Veto detector based on re-using of OPERA Target Tracker detector. This option can be considered as a possible JINR contribution to the JUNO experiment.

8. Perform, in collaboration with the HVSYS company, the development and all required experimental tests of the high voltage system for JUNO PMT. Perform studies of feasibility of JINR contribution to the JUNO experiment in design, prototyping, construction and installing of the PMT high voltage system.

9. Develop the software for the global analysis of neutrino oscillation data with primary goal of combining reactor and accelerator neutrino data to measure the mass hierarchy.

10.1.6 Publications, Theses and Conferences

Working within our project the following diploma thesis is defended:

1. D.Taichenachev (2014), “Sensitivity studies to mass hierarchy determination with reactor and accelerator neutrinos”, thesis advisor D.Naumov.

10.1.7 Finances

Major sources and amount of finances and major equipment acquired during the project runtime are listed in Tab. 10.4.

Source	Amount requested (k$)	Expences
1099	160	PMT testing laboratory equipment (Tab. 10.5)
1099	32	R&D: PMT HV system, μ-metal
1099	80	Opera TT maintenance
1099	150	Muon veto electronics
1099	15	Computers and equipment
1099	24	Travels

Table 10.4: Major sources and amount of finances and major equipment acquired and or travel expenses.

JUNO Appendix

10.A Specific Project Objectives and Expected Results

10.A.1 JUNO Sensitivity

Our JINR group is performing our own study of JUNO sensitivity to the mass hierarchy determination and precise measurements of neutrino mixing parameters. Below we discuss some preliminary results of this study. Currently, we take into account uncertainties on the following parameters:

- Normalization of reactor neutrino spectrum - $\delta(N_{\text{iso}}) = 3\%$ for each isotope
- Normalization of geoneutrino spectrum $\delta(N_{\text{geo}}) = 20\%$
- Energy resolution $\delta(\sigma_E) = 10\%$
- Mixing angles: $\delta(\sin^2\theta_{12}) = 0.017$; $\delta(\sin^2\theta_{13}) = 0.0025$;
- Solar mass difference $\delta(\Delta m^2_{12}) = 0.24 \cdot 10^{-5}$
- $\delta(\Delta m^2_{ee})$ is taken into account as a pull term for several values of this uncertainty.

A calculated JUNO covariance matrix assuming normal hierarchy with all uncertainties taken into account is shown in Fig. 10.7. We try to address mass hierarchy resolution issues by the following algorithm.

- Calculate averaged prediction for the number of events expected in JUNO $T(E_{\text{vis}})$ as a function of visible energy E_{vis}. Assume some hierarchy and a central value of theory parameters denoted by a vector $\boldsymbol{\eta}_0$.
- Bin it in energy bins $E_{\text{vis},i}$ and make the vector of predictions $\mathbf{T}(\boldsymbol{\eta}_0) = (T_0, \ldots T_n)$.
- Generate fluctuations according to calculated covariance matrix V, taking into account both statistical and systematic uncertainties. Let us denote a fluctuated prediction by a vector $\mathbf{N}$.
- Assuming some mass hierarchy, fit the vector $\mathbf{N}$ by $\boldsymbol{\eta}$ in which only Δm^2_{ee} is a free parameter. Find two sets of parameters $\boldsymbol{\eta}_{\text{N,I}}$.
- Calculate correspondingly

$$\chi^2_{\text{N,I}}(\boldsymbol{\eta}) = (\mathbf{N} - \mathbf{T}_{\text{N,I}}(\boldsymbol{\eta}))^{\mathrm{T}} V^{-1} (\mathbf{N} - \mathbf{T}_{\text{N,I}}(\boldsymbol{\eta})) \,. \tag{10.7}$$

  In (10.7) both $\mathbf{N}$ and V depend on $\boldsymbol{\eta}_0$. We omit this dependence for the sake of compactness.

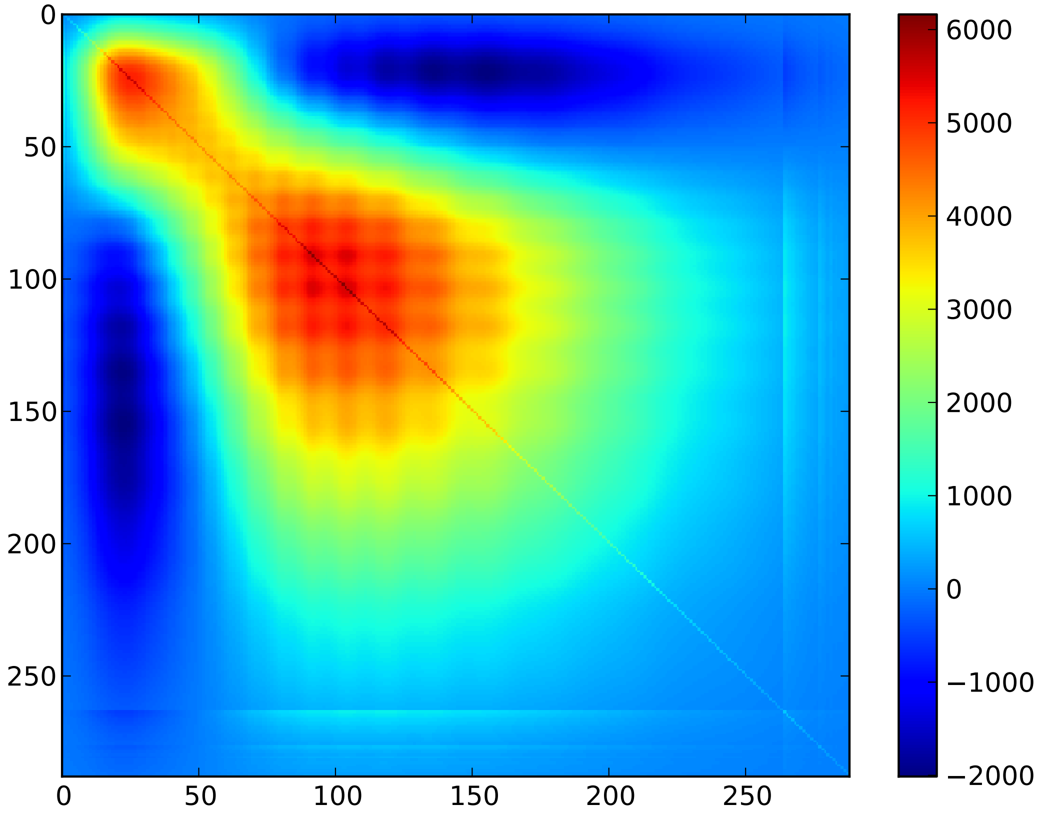

Figure 10.7: Calculated JUNO covariance matrix assuming normal hierarchy with all uncertainties taken into account.

- Calculate
$$\Delta\chi^2 = \chi^2_{\mathrm{N}} - \chi^2_{\mathrm{I}} \tag{10.8}$$
- Make two distributions of $\Delta\chi^2$ in (10.8) for both assumed mass hierarchies $P_{\mathrm{N}}(\Delta\chi^2)$ and $P_{\mathrm{I}}(\Delta\chi^2)$.
- Calculate $\Delta\chi^2_{\mathrm{c}}$ such that:
$$\alpha = \int_{-\infty}^{\Delta\chi^2_{\mathrm{c}}} dx P_{\mathrm{I}}(x) = \int_{\Delta\chi^2_{\mathrm{c}}}^{+\infty} dx P_{\mathrm{N}}(x) \tag{10.9}$$
- We interpret further α as the confidence level for the mass hierarchy determination. Let us note that sometimes $\sqrt{\Delta\chi^2} = \sqrt{\chi^2_{\mathrm{N}} - \chi^2_{\mathrm{I}}}$ is used as a "number of sigmas" estimate [1]. This is a well-motivated approximation for a continuous parameter. However, the mass hierarchy, due to its discrete nature (either normal or inverted, or in

numbers:1 or -1), does not fit into this assumption. This effect was first noticed in [6]. We examine the validity of this assumption in this work.

Mass hierarchy determination

In Fig. 10.8 we show some *preliminary* results of our studies of statistical significance of JUNO mass hierarchy determination as a function of L. Some comments should be made here. We assume a 20kton detector mass in this Figure.

- Interestingly, allowing the detector mass to be adjusted such that the expected number of events is kept the same as for $L = 52$ km, we find an optimal distance at $L \simeq 65$ km.
- Another important remark that should be made is that the sensitivity to the mass hierarchy, in terms of statistical significance, does not follow the $\sqrt{\Delta\chi^2}$ assumption discussed in the previous section, being below that naive prescription.
- The sensitivity drastically depends on the energy resolution σ_E and (not shown here for the sake of compactness) on $\delta(\Delta m^2_{ee})$. The current estimates shown in these figures correspond to $\delta(\Delta m^2_{ee}) = 0.1 \cdot 10^{-3}$eV^2, which is the accuracy given by MINOS. Daya Bay will improve on this accuracy within the next three years (and within our current proposal) to $\delta(\Delta m^2_{ee}) = 0.03 \cdot 10^{-3}$eV^2, which will increase the significance of the mass hierarchy determination. Other additional measurements, either from accelerator, atmospheric or reactor experiments, will help us to improve the situation as well.

Precise measurements of neutrino mixing parameters

Sensitivity to $\sin^2\theta_{12}$ vs Δm^2_{12} of the JUNO experiment, assuming $\sigma_E = 3\%$ and $L = 52$ km, is shown in Fig. 10.9a. The current uncertainty on this parameters is also shown. One can see an order-of-magnitude better expected resolution of these parameters. In Fig. 10.9b we display the same contours but calculated for $L = 70$ km. A similar pair of plots is displayed in Fig. 10.10a, 10.10b.

One might observe that at larger distances both mass hierarchy determination and the precision of neutrino mixing parameters could be measured somewhat better. The price would be about 80% larger detector mass. Also one would need *new* geological surveys, which will increase the overall price and might delay the experiment. We are going to carefully evaluate and discuss, within the Collaboration, all benefits and drawbacks of our proposal.

Study of decoherence effects

As we mentioned in Sec. 2.4, 7.A.2 the quantum decoherence is an effect tightly connected with neutrino oscillations. It has never been observed experimentally. As one can see from our preliminary study displayed in Fig. 10.11 this effect could drastically change

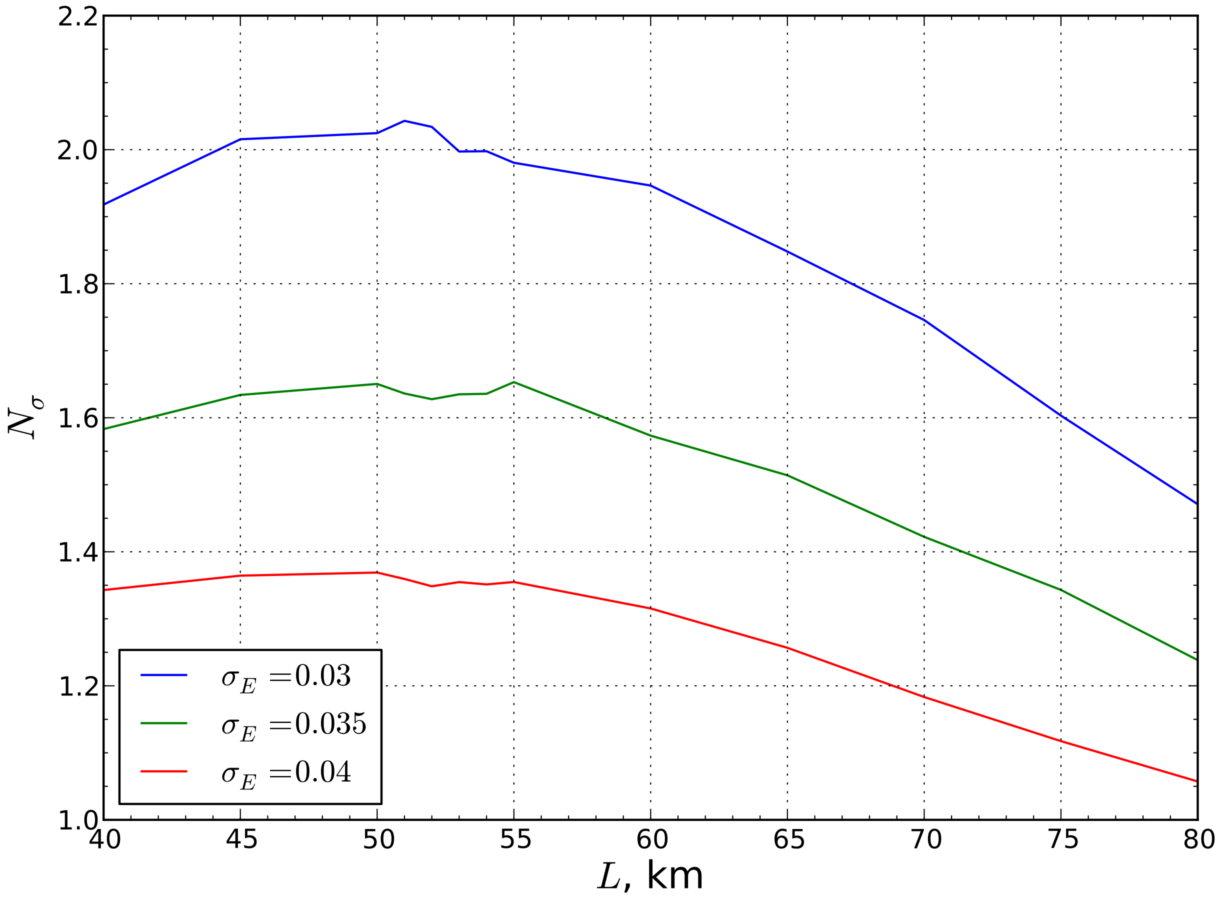

Figure 10.8: Statistical significance of JUNO mass hierarchy determination as a function of L. 20 ktons detector mass is assumed.

the oscillation probability and thus the experimental capability to determine the mass hierarchy. Therefore, as we stressed in this proposal, it is very important to study this effect with Daya Bay and other data as well. At any rate, our studies of JUNO sensitivity will include the quantum decoherence effects.

10.A.2 Simulation and Reconstruction Software

We plan to work on the development of JUNO software. Among other things our work will include development of:

- **Simulation package.** IBD and various background simulation. General tools for simulation.
- **Reconstruction package.** Track and vertex reconstruction. Energy reconstruction.
- **Data analysis tools.**

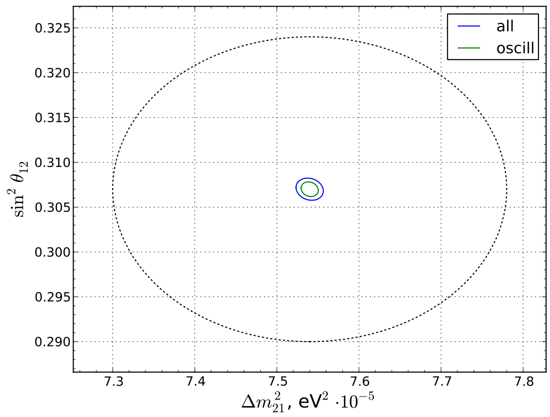

(a) Sensitivity to $\sin^2\theta_{12}$ vs Δm^2_{12} of the JUNO experiment assuming $\sigma_E = 3\%$ and $L = 52$ km. Two contours are shown: "oscill" takes into account uncertainty of oscillation parameters, while "all" takes into account all possible uncertainties included in our analysis. The dashed contour shows the current uncertainty on these parameters.

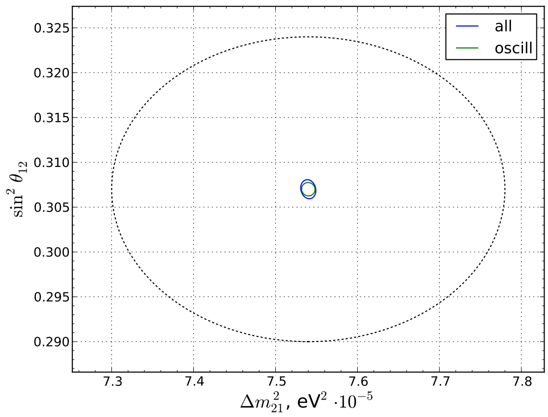

(b) Sensitivity to $\sin^2\theta_{12}$ vs Δm^2_{12} of the JUNO experiment assuming $\sigma_E = 3\%$ and $L = 70$ km and appropriately increasing the detector mass to account for the $1/L^2$ factor. Two contours are shown: "oscill" takes into account uncertainty of oscillation parameters, while "all" takes into account all possible uncertainties included in our analysis. The dashed contour shows the current uncertainty on this parameters.

These tools will help the Collaboration to get solid scientific results. The software will use modern approaches to the management of large projects:

- Geant4 toolkit for particle propagation [7]
- Various simulation kits available like Music for muon tracing, IBD reaction and various backgrounds simulators based on Daya Bay well tested generators
- C++ language for object-oriented programming, python language for simulation, reconstruction and analysis applications managing C++ libraries, ROOT framework for statistical analysis and data book-keeping, as well as other software
- DAQ systems

The planned work should be done in a close collaboration with other colleagues from the JUNO Collaboration.

10.A.3 Detector Design

Currently there are three options for the detector design: acrylic ball with steel truss (see Fig. 10.12a), balloon with steel tank (see Fig. 10.12b) and modules with steel tank (see Fig. 10.13).

Each of these engineering design options will require extensive and careful simulation within the Geant4 toolkit [7]. We will work in this direction to characterize the detector

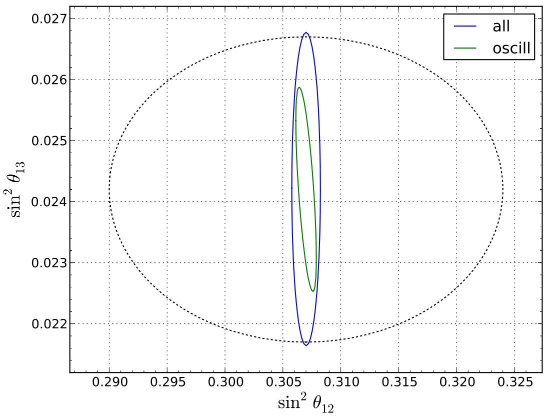

(a) Sensitivity to $\sin^2\theta_{13}$ vs $\sin^2\theta_{12}$ of the JUNO experiment assuming $\sigma_E = 3\%$ and $L = 52$ km. Two contours are shown: "oscill" takes into account uncertainty of oscillation parameters, while "all" takes into account all possible uncertainties included in our analysis. The dashed contour shows the current uncertainty on this parameters.

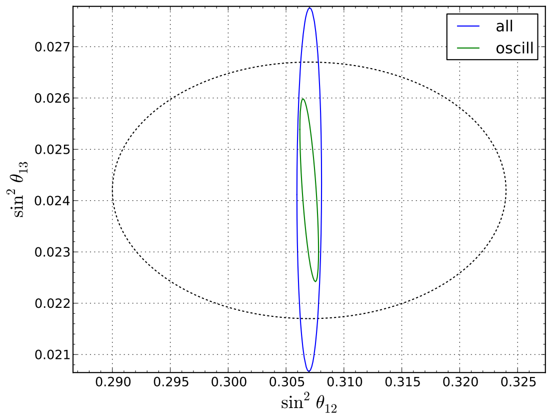

(b) Sensitivity to $\sin^2\theta_{13}$ vs $\sin^2\theta_{12}$ of the JUNO experiment assuming $\sigma_E = 3\%$ and $L = 70$ km and appropriately increasing the detector mass to account for the $1/L^2$ factor. Two contours are shown: "oscill" takes into account uncertainty of oscillation parameters, while "all" takes into account all possible uncertainties included in our analysis. The dashed contour shows the current uncertainty on this parameters.

and study its efficiency in terms of energy and position reconstruction, uniformity and background studies.

10.A.4 Modeling of Backgrounds

We plan to work on accurate modeling and estimation of the most important backgrounds for the JUNO experiment. For example:

- accidental association of two random signals with IBD candidate;
- decay of $^9\mathrm{Li}/^8\mathrm{He}$;
- fast neutron interaction;
- α-N interaction;
- background from future calibration system.

To accomplish these goals we are going to use methods developed by the Daya Bay Collaboration as well as develop our own. In connection with another important task of our project, protection against Earth magnetic field EMF (see Sec. 10.A.7), we plan to examine backgrounds induced by μ-metal used to protect against EMF in one of the options considered. This will require experimental work in a low radioactivity laboratory. We will identify an appropriate laboratory for this purpose.

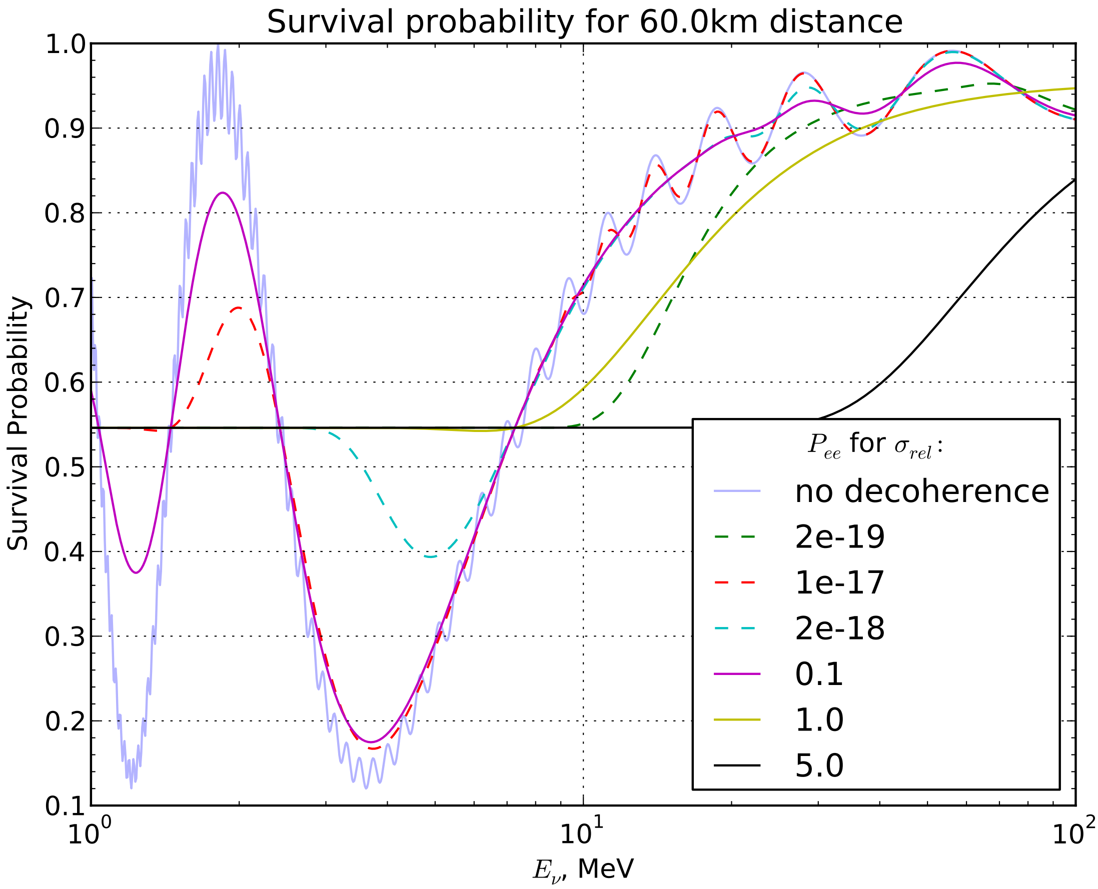

Figure 10.11: Survival probability of $\bar{\nu}_e$ as a function of E at fixed $L = 60$ km for some values of σ_E.

10.A.5 Development of DLNP JINR infrastructure: PMT tests

The main challenge of the JUNO experiment is to measure an $\overline{\nu}_e$ disappearance oscillation pattern at distances of about 50 km from the reactor with a precision which will allow us to see the tiny difference arising from different neutrino mass hierarchies. This is possible only if the oscillation phase L/E is known with high precision, otherwise the hierarchy effects are washed out. The goal of the JUNO experiment is to have energy resolution of $\sim$3% at 1MeV. Taking into account that large liquid scintillator neutrino detectors have reached, so far, resolution of $\gtrsim$6% at 1 MeV, this goal appears very challenging and requires a careful and systematic approach. Main improvements, with respect to detector parameters already achieved in Daya Bay, are expected from:

- Increase of the photon detection coverage up to $\sim$80% by the large number ($\sim$20'000) of 20" PMTs installed in the detector. (To increase this even further an option with additional 8" PMTs installed in the gaps of 20" PMTs is also considered).

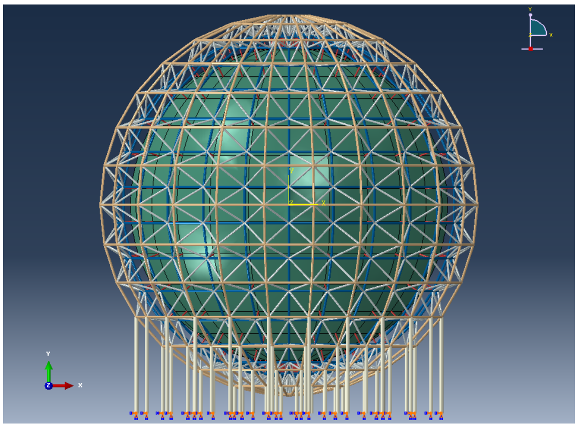

(a) Acrylic ball with steel truss.

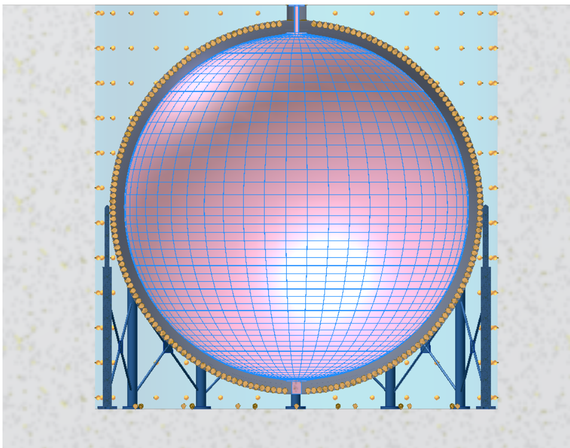

(b) Balloon with steel tank.

- Increase of the Photon Detection Efficiency (PDE) of a large size PMTs by inventing new types of devices with better photocathode coverage, special focusing and micro-channel plate (MCP) amplifier.

- Increase of the light yield and transparency of the liquid scintillator. An optimum between scintillating dopants to the liquid scintillator and the transparency should be found. Moreover, since the presence of Gd for neutron detection dilutes the scintillator transparency and stability, it is proposed to detect neutrons only via nH reaction and exclude Gd dopants.

All of these require careful prototyping and testing, and, taking into account the considerable expertise of the JINR group, we plan to do part of this work at DLNP. In particular, at the present stage of the project the testing and development of PMT specification requirements compatible with expected energy resolution is a main objective.

The planned basic tests of PMTs are:

- Voltage grid optimization for different prototypes supplied to Dubna by the JUNO Collaboration.

- Measurement of PMT integral and zone (at different photocathode points) parameters: photon detection efficiency (PDE), gain, dark noise rate, the single electron response performance (or collected charge spectrum), the transit time spectrum (evaluating the amount of pre-pulse due to the production of photoelectrons directly on the dynodes system and the transit time spread) and the after-pulse probability at the tens of microseconds time scale.

- Study of the Earth magnetic field influence on the performance of this specific type of PMT and requirements of the Earth magnetic field shielding of the experiment.

Some of this work has already started and first results have been obtained. They are described below. The next figures show the 8” prototype PMT delivered by the JUNO Collaboration for tests at JINR, as well as its principal layout. This brand-new prototype already

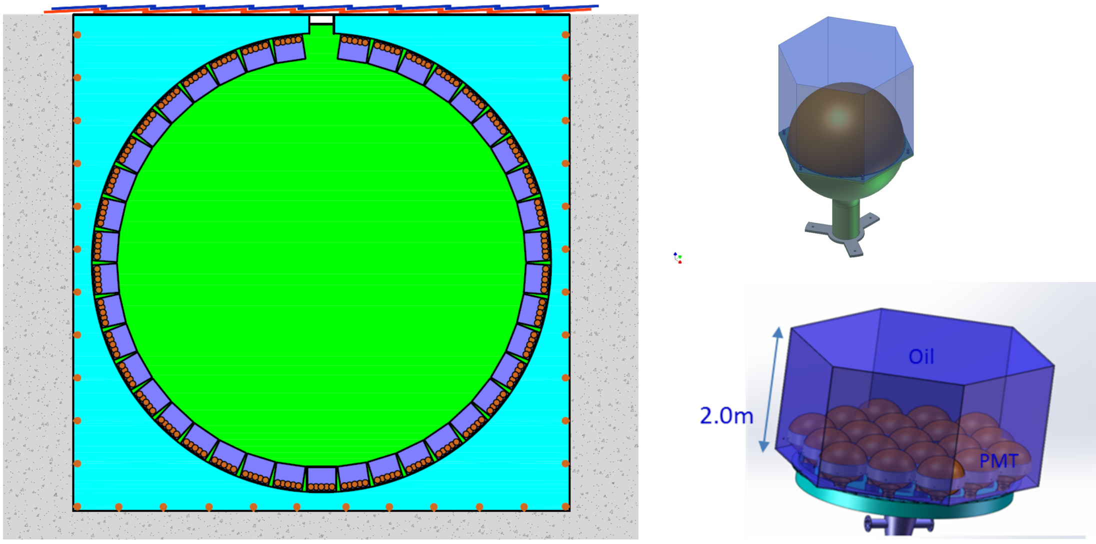

Figure 10.13: Modules with steel tank.

combines some of the required features: increased photocathode coverage, focusing scheme for both up/down hemispheres and two MCP amplifiers. Preliminary tests were performed in order to optimize voltage distribution at focusing and signal electrodes.

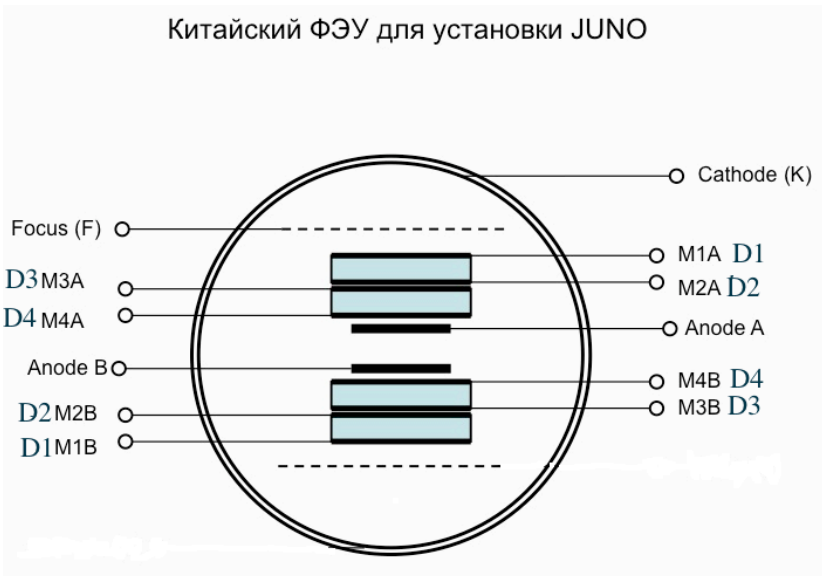

Figure 10.14: The view and principal layout of the 8” PMT prototype.

The PMT signal shape and a single electron spectrum is shown in next Figures. This test allowed us to formulate a specification for the PMT voltage supply, which will be proposed to the JUNO Collaboration.

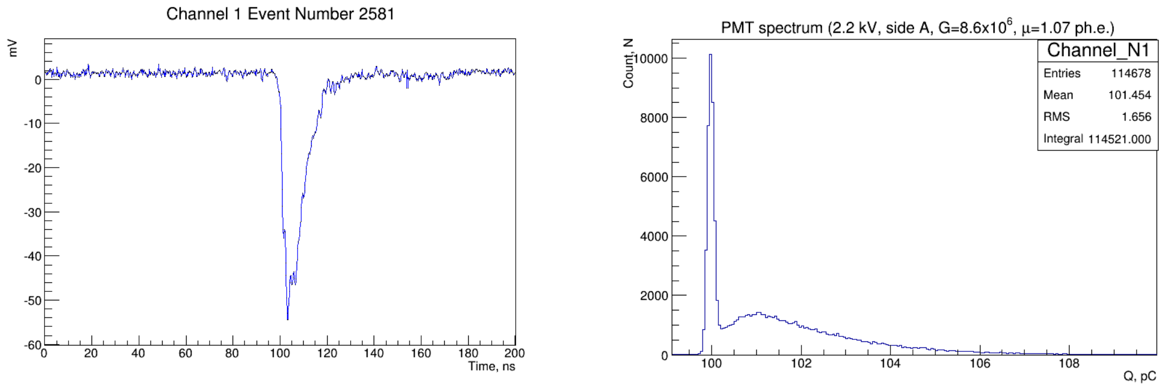

(a) (b)

Figure 10.15: The PMT signal shape (a) and a single electron spectrum (b) measured with 440 nm laser.

To continue this work we are planning to install the PMT test facility at JINR in order to provide a tool for PMT characterization and for studying the PMT sensitivity to magnetic fields. The PMT test facility will consists of two separate rooms: the so called “dark room” and the electronics room. The “dark room” will be supplied with protection against the electromagnetic noise (mesh mounted in the walls) and will be tightly sealed in order to provide a “dark” environment for PMT testing. In general large PMTs are extremely sensitive to the presence of the Earth’s Magnetic Field (EMF): the magnetic field influences the trajectories of photoelectrons between the photocathode and the dynode system degrading the overall performance of the PMT. We are planning to install an EMF compensation system inside the “dark room”. In the simplest case this could be a system of Helmholz coils oriented along the EMF vector, or it could be a system of rectangular coils providing compensation for 3 EMF components. Another room will host the electronics needed for the PMT testing, including HV supplies and data processing systems. We are planning to use picosecond light pulsers in our tests.

Measurements of liquid scintillator light-yield and transparency will be performed at existing facilities at the DLNP radiochemical laboratory.

Two standard methods to compensate for the EMF have been used thus far in the experiments: a PMT screening using a metal with high magnetic permeability (μ - metal) , and magnetic field compensation using a properly designed coil-system. For example, in SuperKamiokande the residual geo-magnetic field is kept at less than 100 mG in every position of the tank by using compensation coils. Another example could be the Borexino detector, where solid μ -metal screens (cone shaped) are used as a passive system to shield PMTs against the EMF. Another interesting method for EMF screening has been recently developed. The screens made of μ -metal wire are used instead of solid screens (as is used in the Dark Side experiment).

The usage of a solid μ-metal shield in a high purity detector has the disadvantage of introducing an additional amount of material that may be a possible source of radioactive contamination, not to mention the cost of the μ -metal needed to protect all of the PMTs. In addition the PMTs remain unprotected against the EMF component along the PMT axis. From this point of view the utilization of wire mesh screens may prove more promising for the JUNO experiment. We are planning to test mesh screens with our test facility.

We plan to purchase standard equipment and construct special equipment for the PMT test laboratory.

№	Item description	Estimated price, USD
1	Rotating table for PMT positioning (Custom made)	15 000
2	Scanning System (Custom made)	15 000
3	Picosecond Laser PiL037X (45 ps, 375 nm) Pulse Generator EIG 1000D and accessories	20 000
4	Power supply for compensating coils	2 000
5	Power supply for PMT (Up to 3.5KV)	3 000
6	Frontend and DAQ system	40 000
7	Oscilloscope	15 000
8	Pulse generator for LED	15 000
9	PMTs for calibration and monitoring	10 000
10	Miscellaneous materials and equipment	25 000
	Total	160 000

Table 10.5: Planned laboratory equipment.

10.A.6 Liquid scintillator

Liquid scintillators are widely used in modern physical experiments. They are indispensable for large-scale detectors in the field of neutrino physics. There are several reasons for this:

- high hydrogen content;
- high transparency;
- the possibility to construct detectors of any shape and configuration;
- fast response;
- possibility of using simple methods of decontamination;
- availability;
- relatively low cost.

Recently extensive experience has been accumulated in the use of LS's in such large-scale detectors as KamLAND, Borexino, Daya Bay, RENO and Double Chooz. However, the prospects of using liquid scintillator in the JUNO detector requires a substantial improvement of its characteristics. For example, the transparency of LS (distance over which the light intensity of self-luminescence is reduced in 'e') should be in the range of 20–25 m.

The development of a liquid scintillator suitable for use in modern, large-scale, next-generation neutrino experiments is the main task of the present project. The scintillator will have the following properties:

- high transparency (20–25 meters);
- high light output (no worse than for the best of the known samples);
- safety in use (high flash point and non-toxicity).

In recent years, linear alkylbenzene (LAB) has attracted special interest as a base compound for the liquid scintillator's preparation. Linear alkylbenzene is the trade name of a mixture of several monoalkyl benzene derivatives. Its main components contain in the side chain from 10 to 13 carbon atoms. About 80%–85% of the LAB components have a 1-phenylalkanes structure (Fig. 10.16a) and 15%–20% — 2-phenylalkanes (Fig. 10.16b) [8].

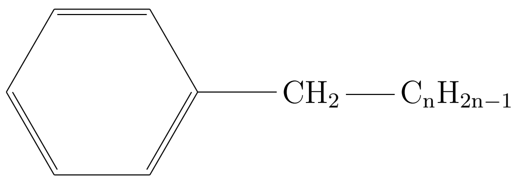

(a) 1-, $n = 8 - 13$

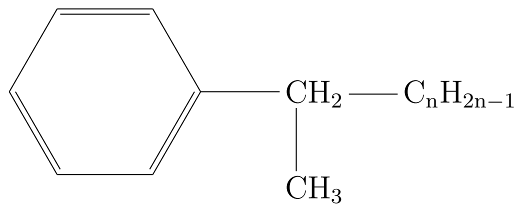

(b) 2-, $n = 7 - 12$

Figure 10.16: 1- and 2- phenylalkanes structure

Linear alkylbenzene is cheap and available, because it is the intermediate product of the manufacture of biodegradable detergents and, therefore, is produced by a number of large petrochemical companies [9, 10]: in Europe — Huels, EniChema and Petresa; in North America — Petresa, Visla and Huntsman; in Japan — Mitsubishi Petrochemicals and Nippon Petroleum; in China — Jinling Petrochemical Corporation Ltd., Nafine Chemical Indstry Group Co., Ltd. and Shidjiazhuang Bingqing Chemical Co., Ltd.; in South Korea — Isu Chemical; in Taiwan — Formosan Union. "Producrion Association Kirishinefteorgsintez", Ltd., is a largest producer of LAB in Russia.

Linear alkylbenzene is already used as the basis of Daya Bay [11–14] and RENO [15, 16] liquid scintillators. Its popularity is due to the following:

- LAB-based LS's have a high light output;
- physical and chemical properties of linear alkylbenzene (high boiling point and flash point, high hydrogen content) fully satisfy the requirements for detectors with a large mass of the working substance used into underground laboratories.

Physical and chemical properties of linear alkylbenzene:

Special gravity [8], g/cm^3	0,858 – 0,862
Boiling point [8], °C	280 – 311
Flash point (Petresa Canada), °C	140
Content of hydrogen atoms (our calculations), cm^{-3}	$6{,}29 \times 1022$

The LNP group accumulated a large ammount of experience in the research and production of linear alkylbenzene based scintillators resulting from work in the Daya Bay collaboration. We are familiar with the properties of LAB and clearly understand how to improve them. For example, it is shown [17] that the samples of linear alkylbenzene contain some nitrogen- and sulfur-containing impurities, which negatively affect the light output and transparency LAB-based LS, despite their low concentration.

Therefore, the first focus of the project will be a specification of the composition of industrial linear alkylbenzene samples and the development of efficient and low cost methods for its purification.

Studying the possibility of using of polyalkylbenzene (a byproduct of industrial production of linear alkyl benzene) as a base of scintillator material will be another direction of investigation. Polyalkylbenzene (PAB) is a mixture of linear alkylbenzene (10%), diphenylalkanes (20%) and dialkylbenzenes (70%). The high content of the dialkylbenzenes in the PAB allows us to expect higher light output for PAB-based scintillators than for LAB-based ones. Polyalkylbenzene is safer than linear alkylbenzene because of its higher flash point (175° C) [18].

10.A.7 PMT protection against Earth magnetic field

Shielding strategies

The new type of PMT is rather sensitive to the Earth magnetic field (EMF). The limiting value of the EMF is about 0.06 G. It means that the possible maximal value of EMF 0.6 G should be shielded with a factor of 10. Four possible strategies for EMF shielding are proposed:

- Compensation of EMF by a set of current coils on the pool walls.
- Shielding of EMF by the μ-metal sheets on the pool walls.
- Complete detector shielding by μ-metal mesh screen.
- Both coil and μ-metal shielding.

Simulation code

The screening effects were simulated by using the 2D POISSON code [19] and 3D TOSCA [20].

The 2D code was used for the preliminary simulations for estimation of the principal effect. Final effects were simulated using 3D TOSCA. In some simulations, when the number of mesh elements was too high for the TOSCA assumption, only the POISSON code was used.

Preliminary conclusions

1. The cheapest strategy for EMF compensation is the utilization of compensation coils.
2. Some effects may lead to uncompensated values of EMF at more than 0.06 G:
   - Uncompensated values of the transverse component of the magnetic field from the compensation coils.
   - Time variation of EMF.
   - Spatial variation of the magnetic field inside the pool due to design iron elements in the pool walls, design and technical equipment of the building and pool.
3. The system of compensation coils should be added to the μ-metal shielding of each detector.

10.A.8 Top Muon Veto Detector

An important source of background in the JUNO experiment is the cosmogenic background, which is able to produce ^{9}Li/^{8}He isotopes that decay in the β-n mode and produce a signal very similar to the IBD signal in the detector.

The JUNO detector design (see Fig. 10.6) includes the Top Muon Veto detector, which, along with the water Cerenkov detector, has to suppress the cosmogenic background down to the 1% level.

Several options are still under consideration for the Top Muon Veto detector: RPCs as in the Daya Bay experiment, liquid scintillator cells, and plastic scintillator strips. The latter option is particularly attractive, as the plastic scintillator strips have proven to be effective, robust and reliable detectors by a large neutrino experiments, like MINOS and OPERA.

The OPERA experiment stopped data taking at the CNGS neutrino beam in 2012. It is processing the data now. The decommissioning of the setup starts in 2015. The whole apparatus will be dismounted. One of the main electronic detectors of the OPERA experiment, the Target Tracker, is still in a very good shape. Due to the high quality of the plastic scintillator, the performance of this detector (in particular, the amplitude of the response to the muon crossing the scintillator strips of the TT and its efficiency to the muon registration) degrades very slowly (less than 1.5% per year) which makes it suitable for use in another experiment after the decommissioning.

In total, the surface of the 496 modules of the TT provides 2783 m^2 of X-Y coverage with 99% efficiency at 0.3 p.e. threshold. The JUNO Collaboration expressed its interest to exploit the TT as the Top Muon Veto detector to effectively suppress the major background from the cosmic muons. An efficient tracking detector like the TT can register the trajectory of the muon, and, therefore, indicate the region within the Antineutrino Detector where

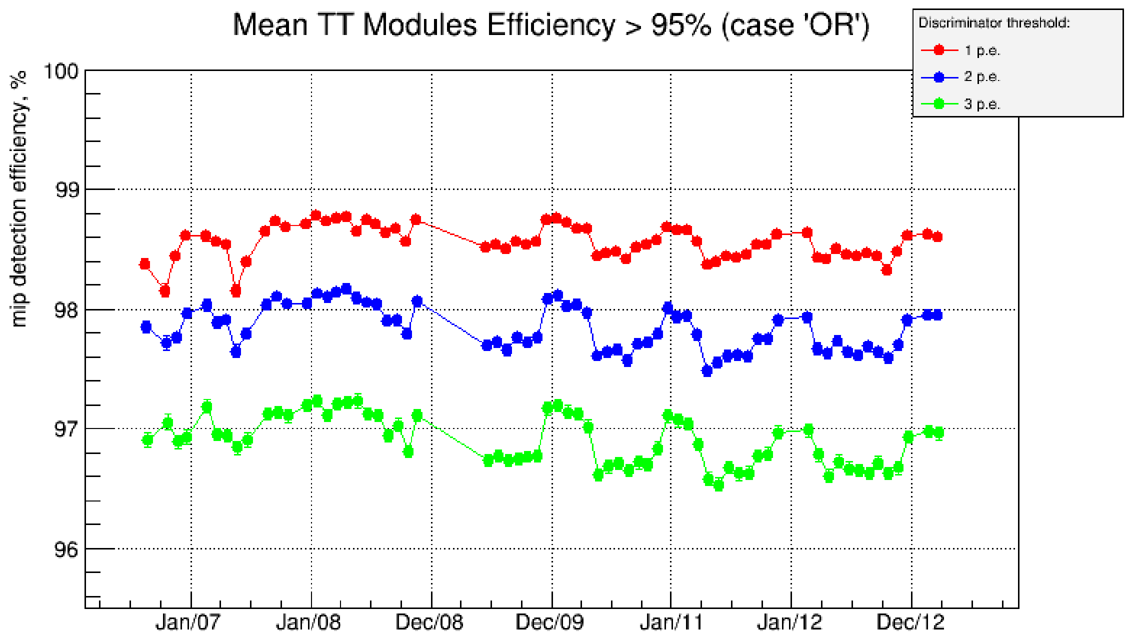

Figure 10.17: The change in the TT efficiency during the OPERA operation as measured by the JINR group with cosmic muons. The short time variation is related to the state of the magnetic field, either on or off, depending on the neutrino beam operation.

the ^{9}Li/^{8}He isotopes may be produced along the muon path. This region is to be vetoed during a certain time time window, rather than excluding the entire detector (is estimated to be ~8% of the AD volume) thus increasing the detector efficiency.

To be adapted to the JUNO experiment, the TT modules must be equipped with new electronics (Front-End Boards and DAQ system). The groups which participated in the TT construction for OPERA (Frascatti, Dubna and Strasbourg), have expressed their interest in development of the Top Veto system for JUNO, based on the existing components of the TT (the modules and the PMTs) and new electronics.

The design of the VETO detector is under study now, in particular how the performance of the new detector will depend on the new electronics, and to what degree its design and characteristics will match the JUNO requirements for background suppression.

The JINR group was the active member of the Target Tracker team in the OPERA experiment. The group was involved in all stages of the project, starting with the PS production along with the AMCRYS company from Ukraine, through the modules assembly, their calibration, the apparatus assembly in the experimental hall in Gran Sasso Underground Laboratory and, finally, the full responsibility for the data processing. JINR also made an in-kind contribution in the TT construction equivalent to ~250 kEuros, so in case of the recuperation of the TT and its application in the JUNO experiment, the efficiency of those investments will be greater.

Although a big part of the Top Muon Veto detector can be considered as existing, significant work has to be done for the realization of the project. In addition to the DAQ upgrade, the support platform has to be created at the JUNO site, and the TT modules have to be transported there.

Given the contribution of JINR to the OPERA TT creation and running the JINR participation in the realization of the JUNO Top Muon veto project based on the OPERA TT detectors is very natural and advantageous. In particular, even the JINR financial contribution of about 80 k$ to the OPERA decommissioning, which is required for 2015–2016, becomes a contribution to the preparation of the JUNO Top Muon veto construction. In addition to that we plan to use our expertise for prototyping of the veto detector and working with it at JINR to measure and optimize the parameters, test new electronics and DAQ, develop new calibration software and finally choose the veto construction configuration. We estimate the amount of resources required for materials and equipment of this test bench at JINR to be about 150 k$.

10.A.9 High Voltage System for JUNO PMTs

The detector is fully covered by 20 thousand PMTs reading out scintillation light produced by ionizing particles. The technical challenge is a new type of PMT with high efficiency, which floats in a liquid scintillator. The PMT has large dimensions (50 cm in diameter), is supplied by a High Voltage, and operates with thresholds at single photoelectron level. All of these technical parameters produce complicating issues for the High Voltage System (HVS). One such issue is the complicated task of supplying a PMT with HV via cables in a liquid environment. The HVS must be stable with voltage variations at level of a few Volts and ripple less than a millivolt.

The best candidate is a High Voltage System based on Cockroft-Walton diode-capacitive multipliers – CW-HVS. The CW-HVS is intended for powering of large arrays of PMTs with up to ten thousand channels in large-scale physical experiments. The basic conceptual ideas of the system:

- Generation of high voltage directly in the place of its consumption;
- Small intrinsic power dissipation, less than 0.05 W/channel;
- No need for expensive high-voltage cables and connectors;
- High stability of output voltages – not more than 0.05%;
- PMT protection against current overload;
- Remote control of all channels.

The application of Cockroft-Walton diode-capacitive voltage multipliers for PMT power supply makes it possible to generate the entire voltage grid necessary for operation, from relatively low base voltage that is directed to a high-voltage cell along the flat cable. In comparison with traditional power supply systems for PMTs which use various voltage dividers, the multiplier system has a number of obvious advantages:

- The high-voltage cable and the HV connector to each PMT are substituted with a cheap, flat cable to which many PMTs are connected simultaneously. It allows one to decrease distinctly the cost of the cable equipment, the amount of cabling and the mass of the whole facility.
- High energy efficiency of the voltage multiplier dramatically lowers the heat losses in the PMT power supply circuit. As a rule, in the absence of PMT light loads the energy consumed by such a cell does not exceed 50 mW. At the PMT maximum light load it does not exceed 200 mW. For comparison, at the same light loads the dividing system will consume 3-6 W constantly. In fact, all of this energy dissipates as heat inside the facility.
- Deep servo feedback inside the HV cell stabilizes the voltage at each PMT and provides its perfect loading characteristics.
- Considerably lower cost of the high-voltage supply of the PMT channel is stipulated not only by the absence of expensive high-voltage cables and connectors, but also by the lower cost of the HV source itself, as its power is much lower than in the traditional system. The reduction in the cost of a multiplier type high-voltage system, in comparison to the traditional one, is 3-4 times.

At present there are 8” PMT prototypes based on MCP produced by Chinese collaborators. In the framework of the project we are planning to investigate these PMTs and develop dedicated CW-HVS system. The parameters for CW-HVS prototype are listed in tables 10.6. Etimated price ≃10 000 USD.

Table 10.6: The main characteristics of the Design of a prototype for a high-voltage power supply integrated readout system 8” PMT experiment JUNO.

Maximal number of serviced channels	127
Power	USB port of the computer
Basic system bus voltage, V	LV - 5V, BV - 24
System interface	RS-485
Communication lines with computer	USB-2.0
Working temperature range, ˚C	(-10) - (+40)
Humidity,%	0-80
Dimensions, mm x mm x mm	70x50x22
Weight, kg	0.15

a) USB system bus adapter.

The scheme of PMT connection, grounded	cathode
Regulation range of the anode voltage, V	1500-2500[1]
Operating voltage, V	+2300[1]
Step of regulation of the anode voltage, V	$0,25$

b) High voltage cell for 8” PMT (continued).

The systematic error of the output voltage, %	3%
Stability of a PMT voltage, %	0.05%
Output voltage temperature coefficient, ppm/°C	100
Voltage distribution on the dynode system PMT from the cathode to the anode:	
Focusing electrode, V	+300
D1, V	+400
D2, V	+1200
D3, V	+1300
D4, V	+2100
Anode, V	+2300
Maximum average anode current limit, mkA	100
Interference from the driver to PMT anode loaded at 50 Ohm, peak to peak, not more than, mkV	20
Cell voltage, V	+5, +24
Power dissipation by one cell, not more than, VA	0.1
Control channel protocol	RS-485

b) High voltage cell for 8” PMT.

10.A.10 Global analysis of neutrino oscillation data

The mass hierarchy measurement will be a difficult and challenging international effort. The practically achievable sensitivity of any single experiment in the world is rather limited. Therefore, we believe that a joint global analysis of all presently available and future data would yield the most solid evidence for the mass hierarchy pattern. Since our group has great experience in both theory and experiment, especially in neutrino oscillation analyses and large-scale software construction, we decided to make our own “Dubna fitter” to meet this requirement. The work will join various people from BLTP and DLNP JINR including significant portion of young people and students.

We began the development of this software, and the first two experiments which we have considered are JUNO and NOVA. We plan to complete this analysis to see what the combined sensitivity of these experiments would be. Eventually, we will include other experiments like T2K, LBNE, LBNO, RENO-50 and others.

The software under development is highly flexible, using modern approaches in programming and data handling.

References

[1] Yu-Feng Li et al. “Unambiguous Determination of the Neutrino Mass Hierarchy Using Reactor Neutrinos”. In: *Phys.Rev.* D88.1 (2013), p. 013008. arXiv: 1303.6733 [hep-ex].

[1] will be optimized and determined after additional studies

[2] Mattias Blennow and Alexei Yu. Smirnov. "Neutrino propagation in matter". In: *Adv.High Energy Phys.* 2013 (2013), p. 972485. arXiv: 1306.2903 [hep-ph].

[3] F. Capozzi, E. Lisi, and A. Marrone. "Neutrino mass hierarchy and electron neutrino oscillation parameters with one hundred thousand reactor events". In: *Phys.Rev.* D89 (2014), p. 013001. arXiv: 1309.1638 [hep-ph].

[4] G. Alimonti et al. "Science and technology of BOREXINO: A Real time detector for low-energy solar neutrinos". In: *Astropart.Phys.* 16 (2002), pp. 205–234. arXiv: hep-ex/0012030 [hep-ex].

[5] K. Eguchi et al. "First results from KamLAND: Evidence for reactor anti-neutrino disappearance". In: *Phys.Rev.Lett.* 90 (2003), p. 021802. arXiv: hep-ex/0212021 [hep-ex].

[6] X. Qian et al. "Statistical Evaluation of Experimental Determinations of Neutrino Mass Hierarchy". In: *Phys.Rev.* D86 (2012), p. 113011. arXiv: 1210.3651 [hep-ph].

[7] S. Agostinelli et al. "GEANT4: A Simulation toolkit". In: *Nucl.Instrum.Meth.* A506 (2003), pp. 250–303.

[8] *ТУ 2414-028-05766480-2006*.

[9] Е.Н. Ивашкина et al. "Совершенствование процесса дегидрирования высших парафинов на основе нестационарной кинетической модели". In: *Известия Томского Политехнического Университета* 310 (2 2007).

[10] К.Р. Ланге and Л.П. Зайченко. *Поверхностно-активные вещества: Синтез, свойства, анализ, применение*. Профессия, 2004. isbn: 9785939130684. url: http://books.google.ru/books?id=pncSPwAACAAJ.

[11] F.P. An et al. "A side-by-side comparison of Daya Bay antineutrino detectors". In: *Nucl.Instrum.Meth.* A685 (2012), pp. 78–97. arXiv: 1202.6181 [physics.ins-det].

[12] F.P. An et al. "Observation of electron-antineutrino disappearance at Daya Bay". In: *Phys.Rev.Lett.* 108 (2012), p. 171803. arXiv: 1203.1669 [hep-ex].

[13] F.P. An et al. "Improved Measurement of Electron Antineutrino Disappearance at Daya Bay". In: *Chin.Phys.* C37 (2013), p. 011001. arXiv: 1210.6327 [hep-ex].

[14] F.P. An et al. "Spectral measurement of electron antineutrino oscillation amplitude and frequency at Daya Bay". In: *Phys.Rev.Lett.* 112 (2014), p. 061801. arXiv: 1310.6732 [hep-ex].

[15] J.K. Ahn et al. "Observation of Reactor Electron Antineutrino Disappearance in the RENO Experiment". In: *Phys.Rev.Lett.* 108 (2012), p. 191802. arXiv: 1204.0626 [hep-ex].

[16] H.S. Kim. "Finding an event vertex using a weighting method in RENO". In: *New Physics: Sae Mulli* 62.6 (2012), pp. 631–635.

[17] P Huang et al. "Study of attenuation length of linear alkyl benzene as LS solvent". In: *Journal of Instrumentation* 5.08 (2010), P08007. url: http://stacks.iop.org/1748-0221/5/i=08/a=P08007.

[18] *ТУ 2414-025-05766480-2006*.

[19] L.M. Billen J.H. Young. “POISSON SUPERFISH”. In: (1996).

[20] A.G.A.M. Armstrong, C.P. Riley, and J. Simkin. “Tosca User Guide: three-dimensional static electromagnetic/electrostatic analysis package: version 3.1 may 1982”. In: (1982).

Chapter 11

NOVA Experiment

Editors: A. Olshevskiy, O. Samoylov

Project Title

NOVA experiment

Project Leaders

- 2014–2016 — project leader A.G. Olshevskiy, project leader deputy O.B. Samoylov

Abstract

The "**N**uMI **O**ff-Axis ν_e **A**ppearance" (**NOvA**) is a new generation accelerator long baseline neutrino experiment which is studying oscillations of muon-type to electron-type neutrinos. Its ultimate goal is to precisely measure the parameters of the neutrino mixing matrix, the neutrino mass hierarchy and CP violation effects in the lepton sector. The NOvA apparatus consists of a Near Detector on the Fermilab site where the muon neutrinos are produced, and a Far Detector 810 km distant, both of similar construction and both situated 14 mrad off-axes to the neutrino beam. The complete 14 kton Far Detector and 220 ton Near Detector filled with liquid scintillator will already reach full data-taking capability in 2014. The following 6 years of data taking are optimized for running with both neutrino and anti-neutrino beams.

keywords: neutrino oscillations, accelerator neutrinos, muon neutrino, electron neutrino, neutrino mass hierarchy, lepton CP-violation

Project Members From JINR

N.V. Anphimov, S.M. Bilenky, A.E. Bolshakova, S.G. Dmitrievskiy, A.G. Dolbilov, A.A. Dolmatov, Yu.A. Gornushkin, V.V. Korenkov, C.T. Kullenberg, K.S. Kuzmin, V.A. Matveev, D.V. Naumov, V.A. Naumov, A.G. Olshevskiy, O.N. Petrova, A.B. Sadovsky, O.B. Samoylov, I.M. Shandrov, A.P. Sotnikov

Project Duration. Approval Date(s)

- 2014–2016 — project approval

List of Participating Countries and Institutions

Argonne National Laboratory, USA; University of Athens, Greec; Banaras Hindu University, India; California Institute of Technology, USA; Cochin University of Science and Technology, India; Institute of Physics of the Academy of Sciences of the Czech Republic; Charles University in Prague, Faculty of Mathematics and Physics, Institute of Particle and Nuclear Physics, Czech Republic; University of Cincinnati, USA; Czech Technical University, Czech Republic; University of Delhi, India; Joint Institute For Nuclear Research, Dubna, Russia; Fermi National Accelerator Laboratory, USA; Universidade Federal de Goias, Brazil; Indian Institute of Technology, Guwahati, India; Harvard University, USA; Indian Institute of Technology, Hyderabad, India; University of Hyderabad, India; Indiana University, USA; Iowa State University, USA; University of Jammu, India; Lebedev Physical Institute, Russia; Michigan State University, USA; University of Minnesota, Crookston, USA; University of Minnesota, Duluth, USA; University of Minnesota, Minneapolis, USA; The Institute for Nuclear Research, Moscow, Russia; Panjab University, India; University of South Carolina, Columbia, USA; South Dakota School of Mines and Technology, USA; Southern Methodist University, USA; Stanford University, USA; University of Sussex, UK; University of Tennessee, Knoxville, USA; University of Texas, Austin, USA; Tufts University, USA; University of Virginia, Charlottesville, USA; Wichita State University, USA; Winona State University, USA; The College of William and Mary, USA

11.1 Project Description

11.1.1 Fundamental Scientific Problems Addressed by the Project

NOvA is designed to address three fundamental questions in neutrino physics:

- What is the ordering of the neutrino masses?
- What is the the value of CP-violating phase in the lepton sector? This phase together with CP-violating phase in the quark sector is responsible for matter-antimatter symmetry in the Universe.
- Precise measurement of the oscillation parameters governing oscillations of muon neutrinos to electron neutrinos.

11.1.2 Specific Project Objectives and Expected Results

The main goals of NOvA are precise measurements of parameters governing $\nu_\mu \to \nu_e$ and $\nu_\mu \to \nu_\mu$ oscillations. With a six-year run, altering neutrino and anti-neutrino beams, NOvA can unambiguously resolve the neutrino mass hierarchy at $> 95\%$ C.L. for over a third of possible values of $\delta_{\rm CP}$. For other values of the CP-violation phase, NOvA will provide $\delta_{\rm CP}$-dependent hierarchy determination plus improved measurements of θ_{13}, θ_{23}, $|\Delta m^2_{13,23}|$, and $\delta_{\rm CP}$ itself, which is also very important for global analysis of the neutrino oscillation data.

11.1.3 Basic Methods and Approaches Used in the Project

The NOvA apparatus consists of a Near Detector on the Fermilab site, where the muon neutrinos are produced by the NuMI facility, and a Far Detector placed 810 km away. Both detectors are of similar construction based on a large volume liquid scintillator tracking calorimeter technique, and both are situated 14 mrad off-axes to the neutrino beam, optimizing the signal-to-background ratio.

NOvA will run with a 700 KW NuMI proton beam for three years in neutrino mode and three years in antineutrino mode. The sensitivities are largely based on analysis techniques that were used by the MINOS experiment. It is expected to be able to achieve somewhat better sensitivities as additional techniques are incorporated made possible by NOvA's finer segmentation and greater active fraction of the detector.

Matter effect are expected to play a crucial role in the NOvA sensitivity to the mass hierarchy and $\delta_{\rm CP}$ measurement.

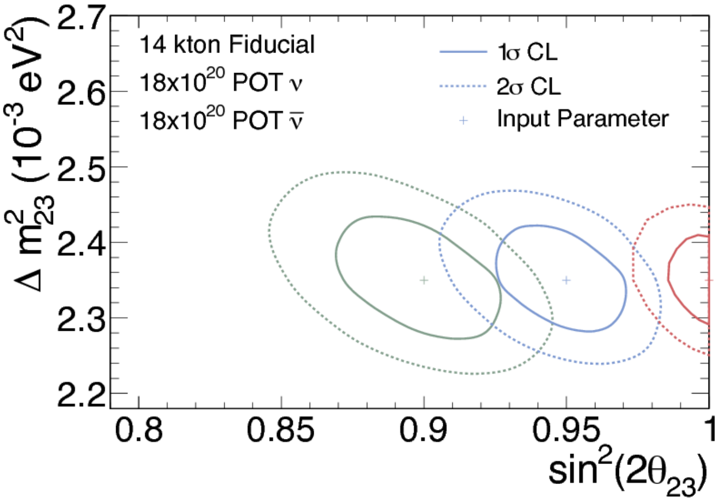

Figure 11.1: One and two standard deviation NOvA sensitivity contours for a joint measurement of Δm^2_{23} and $\sin^2(2\theta_{23})$ for three possible values of these parameters indicated by the crosses. The single parameter measurement of $\sin^2(2\theta_{23})$ will be somewhat more sensitive than the extreme limits of the displayed contours.

ν_μ Disappearance

The disappearance rate of ν_μ charged current events measures $\sin^2(2\theta_{23})$. The latest MINOS measurement of this parameter yields $\sin^2(2\theta_{23}) = 0.97^{+0.03}_{-0.08}$ [1]. NOvA should be able to make a measurement that is about a factor of two to three more accurate. Fig. 11.1 shows the NOvA sensitivity for three possible values of $\sin^2(2\theta_{23})$. We will also gain more information about θ_{23} from $\nu_\mu \to \nu_e$ oscillations.

ν_e Appearance

The formula for $\nu_\mu \to \nu_e$ oscillations taking into account matter effect involve more oscillation parameters than that of ν_μ disappearance. The corresponding oscillation probability is largely proportional to product of $\sin^2(2\theta_{13})$ and $\sin^2(\theta_{23})$, and considerably depends on the mass ordering (through the matter effect) and by CP-violation. A convenient way to see the dependences is through bi-probability plots. These plots show the region of possible NOvA measurements of $\nu_\mu \to \nu_e$ and $\bar{\nu}_\mu \to \bar{\nu}_e$ oscillation probabilities, given a set of oscillation parameters. These parameters include $\sin^2(2\theta_{13})$, which is fixed to 0.095, a value consistent with the recent reactor measurements [2, 3], and $\sin^2(\theta_{23})$. Fig. 11.2 show bi-probability plots for $\sin^2(\theta_{23}) = 1.00$ and 0.97, respectively. The CP-violating phase δ_{CP} traces out the ovals and the multiplicity of ovals represents the two possible mass orderings and, for the right Fig. 11.2, the ambiguity of whether θ_{23} is larger or smaller than $\pi/4$.

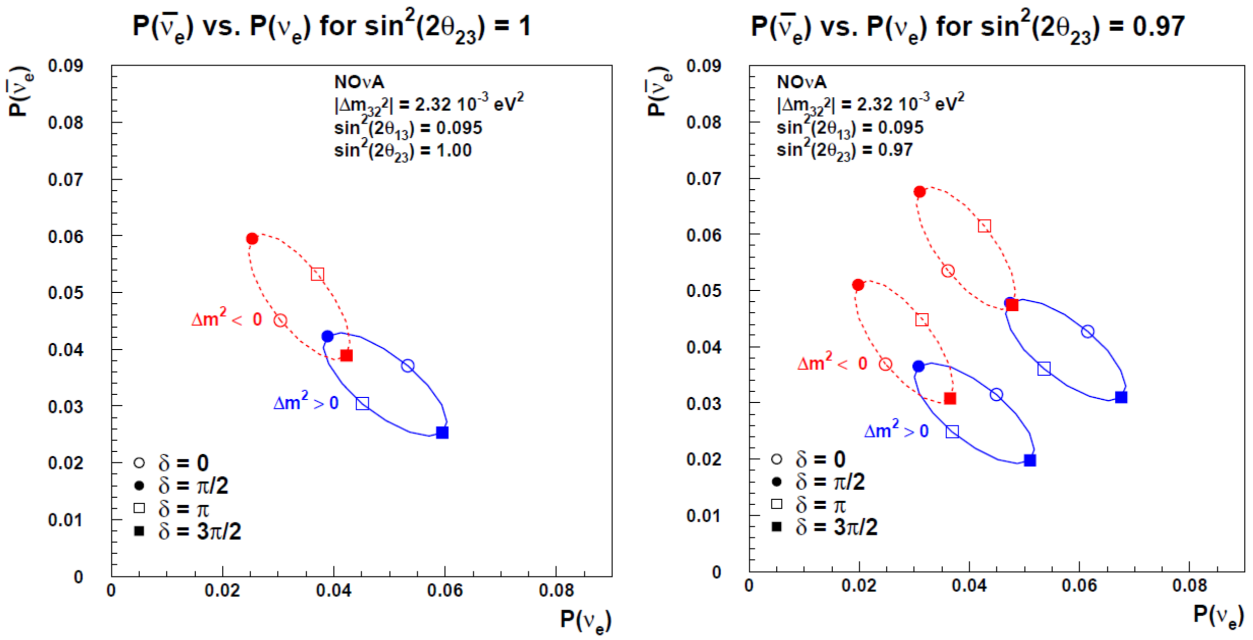

Figure 11.2: Bi-probibility plot for $\sin^2(\theta_{23}) = 1.00$ (left) and 0.97 (right). See text for explanation.

A useful way to visualize what NOvA will be capable of is to superimpose one and two standard deviation contours on the bi-probability plots. For example, Fig. 11.3 shows these contours for a favorable set of parameters, normal mass ordering and $\delta_{\mathrm{CP}} = 3\pi/2$. The mass ordering is resolved to more than two standard deviations, the θ_{23} ambiguity is resolved at two standard deviations, and CP-violation is established to almost two standard deviations. This occurred because the matter effect and the CP-violating effect went in the same direction, so there was no ambiguity.

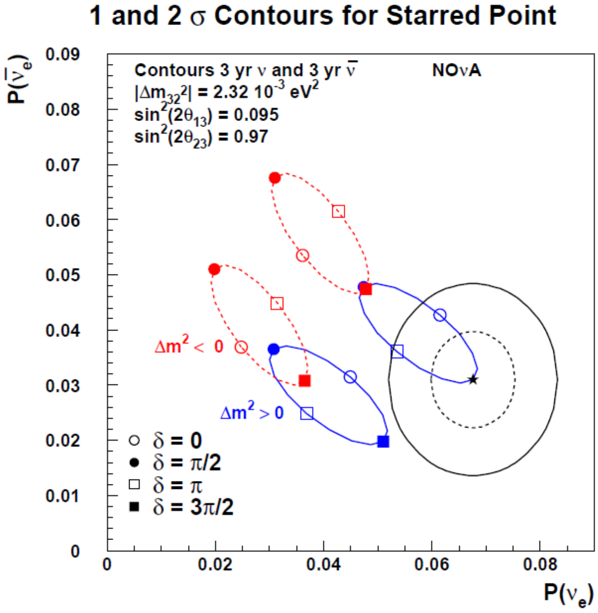

Figure 11.3: Bi-probability plot for $\sin^2(2\theta_{23}) = 0.97$ with NOvA expected 1 and 2 standard deviation contours superimposed on the starred point.

Combined Analysis Potential

An unfavorable set of parameters for NOvA sensitivity would be one in which the matter effect and the CP-violating effect go in opposite directions so that there is an ambiguity as to which direction each went. In that case the θ_{23} ambiguity is resolved, but the mass ordering is not, and, therefore, there is little information on the CP-violating phase.

If Nature holds such a situation, then the only way to resolve the mass ordering in the short-term is to compare NOvA measurements of $\nu_\mu \to \nu_e$ oscillations with those from an experiment with a different baseline. The only experiment that meets such requirement is a 295 km baseline experiment T2K running now in Japan [4, 5].

The algorithm for resolving the mass ordering is quite simple. If NOvA measures a higher probability of $\nu_\mu \to \nu_e$ oscillations than T2K does, then the mass ordering is normal. If it is the opposite, it is inverted. This is because NOvA and T2K will see the identical CP-violation, but T2K will see a much smaller matter effect due to its shorter baseline. The only caveat in this algorithm is that the comparison must be done at the same point in the oscillation phase, and the two experiments run at different average phases. Fig. 11.4 shows the bi-probability plots in which the NOvA measurements have been extrapolated to the same oscillation phase as the T2K measurements. A comparison of the two plots shows that the algorithm works for all values of $\delta_{\rm CP}$.

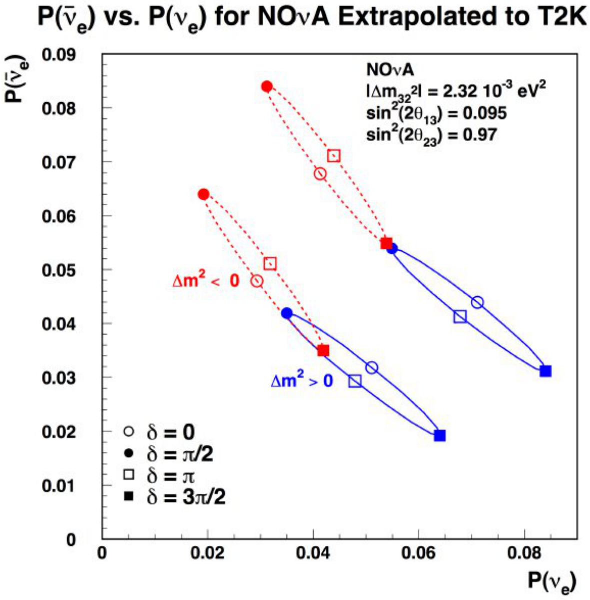

Figure 11.4: Bi-probability plot for $\sin^2(2\theta_{23}) = 0.97$ for NOvA extrapolated to the average oscillation phase of T2K.

One should also take into account that the significance of NOvA and T2K measurements will increase considerably if some of the neutrino parameters are known from future experiments of a different type. As we know, the present neutrinoless double beta decay experiments are close to being sensitive to the region of neutrino masses in the case of inverted hierarchy. Moreover, the planned long baseline reactor experiments will also tackle the hierarchy problem through another effect of interference of atmospheric and solar neutrino mass differences. So, the precise measurements performed by NOvA will be of utmost interest for the global analysis of neutrino oscillation data and paving the way for optimization of the experiments at even larger baselines (for example, LBNE).

11.1.4 Detector Description

The NOvA far detector is located off the Ash River Trail in northern Minnesota, 810 km from the NuMI target. The Ash River Trail is the most northern road in the United States near the NuMI beam line. The NOvA near detector is located on the Fermilab site about 1 km from the NuMI target (see Fig. 11.5). Neutrino oscillations are studied by comparing events in the near detector, where the neutrino oscillations are negligible, with those in the far detector. Using this comparison greatly reduces the systematic error, since uncertainties in the flux, cross-sections, and hadronic interactions largely cancel in the comparison.

Figure 11.5: A plan view of the MINOS access tunnel from the vertical MINOS shaft to the MINOS hall. The location of a Near Detector NOvA cavern is shown.

Generally speaking, the NOvA detectors can be described as totally active tracking liquid scintillator calorimeters. The basic cell of the far detector is a column or row of liquid scintillator with approximate transverse dimensions 4 cm by 15.6 m and longitudinal dimension 6 cm encased in a highly reflective polyvinyl chloride (**PVC**) container. A module of 32 cells is constructed from two 16-cell PVC extrusions glued together and fitted with appropriate end pieces. Twelve modules make up a plane, and the planes alternate in having their long dimension horizontal and vertical. The far detector will consist of a minimum of 928 planes, corresponding to a mass of 14 kt.

The NOvA near detector is identical to the far detector except that it is smaller, 3 modules high by 3 modules wide, with 192 planes. Behind the near detector proper is a muon ranger, which is a sandwich of ten 10-cm iron plates, each followed by two planes of liquid scintillator detectors. NOvA has also constructed a near detector prototype called the NDOS (Near Detector On the Surface) which has been running since November 2010 on the surface at Fermilab, off axis to both the NuMI and Booster neutrino beams. Fig. 11.6 contains a drawing of the NOvA detectors.

The detector cell is a PVC-tube filled with mineral oil containing scintillator. In each tube there is a wavelength shifting (**WLS**) fiber looped down the length of the cells with both ends of the fiber being read out by a single pixel of an avalanche photo diode (**APD**). Each APD is connected to one FEB which contains one ASIC, ADC and FPGA for the digital

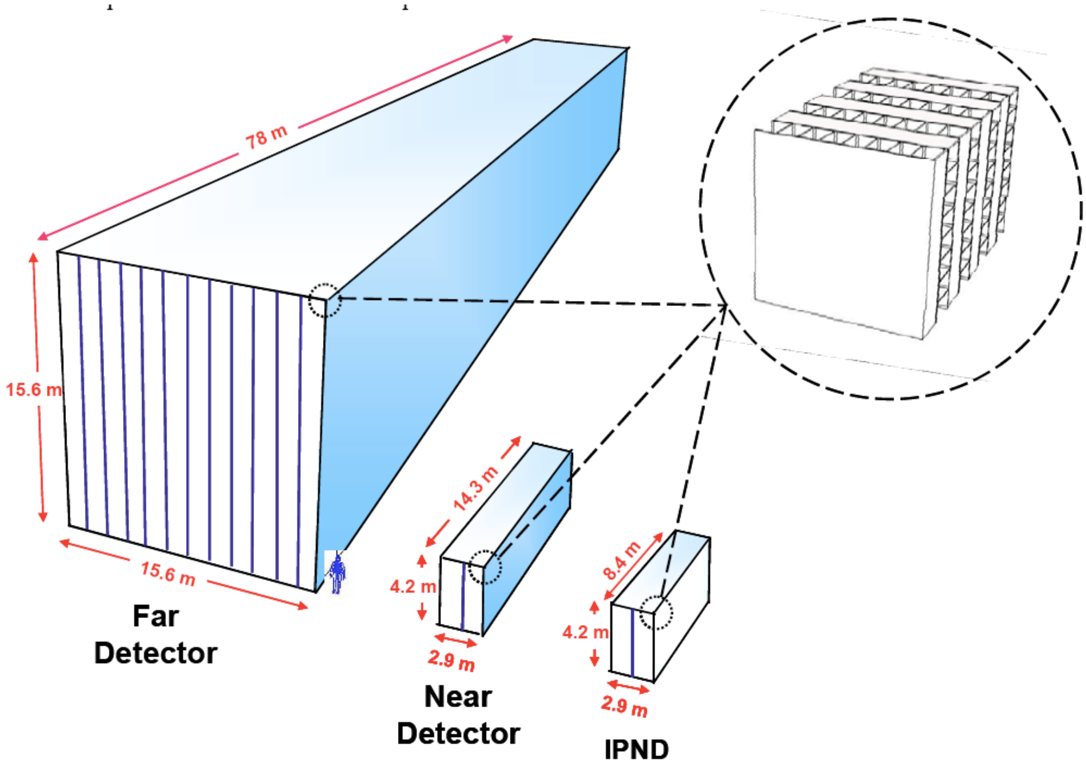

Figure 11.6: Drawings of the NOvA far and near detectors. The human figure at the base of the far detector is to indicate the scale.

signal processing. The signal from the APD is amplified and shaped by a custom ASIC to produce a waveform shown in figure 11.7 which has a 380 ns rise time and 7 us fall time. The waveforms from the detector cells are multiplexed as 8 to 1 and sampled by 16 MHz ADC (2 MHz sampling frequency per channel). A dual correlated sampling (**DCS**) algorithm is used to establish a rising edge triggered threshold under which the sampling points are zero suppressed. This algorithm allows one to get time resolution FWHM of about 800 ns. To reach better time resolution (about 100 ns) a multipoint algorithm is being developed.

Additional details of the NOvA detectors' designs can be found in the Technical Design Report [6] and recent NOvA paper [7].

11.1.5 Contribution of JINR Members

Joining the NOvA experiment at this stage the Dubna group can make an important contribution to the detector commissioning, calibration, development of data quality control tools, running and physics analysis of the data. Significant expertise was gained by JINR members in previous neutrino and particle physics experiments for these tasks: the work on novel photo-detectors for calorimeters, construction of OPERA Target Tracker detector, development of algorithms and tools for alignment and data quality monitoring, physics analysis of neutrino interaction data in OPERA and NOMAD, measurement of hadron pro-

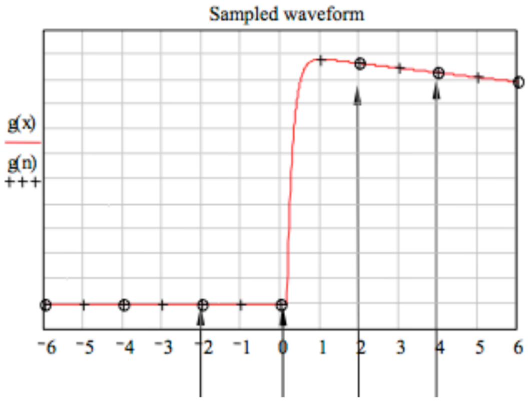

Figure 11.7: The signal from APD is shaped by FEB ASIC and sampled with a 2 MHz digitization clock.

duction cross sections, theoretical description of neutrino interaction and oscillation data, and many others.

The JINR group is primary involved in the following activities:

- Electronics tests, both APD and FEB: IV-curves, parameters studying, cross-talk investigation, optimization for next generation of photodetectors.
- Data processing, developments of the DAQ formats and multipoint algorithm.
- Reconstruction and event topology identification.
- Theoretical studies for cross-sections and neutrino propagation through the matter.

11.1.6 Publications, Theses and Conferences

As a result of the project the following talks has been given on the workshops: NOvA Meeting [8], "JINR neutrino program" [9], Prospects of Particle Physics: Neutrino Physics and Astrophysics [10].

11.1.7 Finances

Major sources and amount of finances and major equipment and travel expences acquired during the project runtime are listed in Tab. 11.1.

Source	Amount requested (k$)	Expences
1099	60	Laboratory equipment
1099	90	JINR VCR
1099	150	Maintenance and Operating
1099	150	Travels
Grant	60	Travels

Table 11.1: Major sources and amount of finances and major equipment acquired and travel expences.

References

[1] P. Adamson et al. "Measurement of Neutrino and Antineutrino Oscillations Using Beam and Atmospheric Data in MINOS". In: *Phys.Rev.Lett.* 110.25 (2013), p. 251801. arXiv: 1304.6335 [hep-ex].

[2] F.P. An et al. "Observation of electron-antineutrino disappearance at Daya Bay". In: *Phys.Rev.Lett.* 108 (2012), p. 171803. arXiv: 1203.1669 [hep-ex].

[3] F.P. An et al. "Improved Measurement of Electron Antineutrino Disappearance at Daya Bay". In: *Chin.Phys.* C37 (2013), p. 011001. arXiv: 1210.6327 [hep-ex].

[4] K. Abe et al. "Evidence of Electron Neutrino Appearance in a Muon Neutrino Beam". In: *Phys.Rev.* D88 (2013), p. 032002. arXiv: 1304.0841 [hep-ex].

[5] K. Abe et al. "Observation of Electron Neutrino Appearance in a Muon Neutrino Beam". In: *Phys.Rev.Lett.* 112 (2014), p. 061802. arXiv: 1311.4750 [hep-ex].

[6] G. Feldman et al. *NOvA Technical Design Report*. http://www-nova.fnal.gov/nova_cd2_review/tdr_oct_23/tdr.htm. [Online; accessed 07-October-2007]. 2007.

[7] R.B. Patterson. "The NOvA Experiment: Status and Outlook". In: *Nucl.Phys.Proc.Suppl.* 235-236 (2013), pp. 151–157. arXiv: 1209.0716 [hep-ex].

[8] Samoylov, O. "JINR Application to Join NOvA". NOvA meeting. Oct. 2013.

[9] Olshevskiy, A. "NOvA Experiment". Workshop JINR neutrino program. Dec. 2013.

[10] Samoylov, O. "NOvA Experiment". Workshop on Prospects of Particle Physics: Neutrino Physics and Astrophysics. Jan. 2014.

Chapter 12

OPERA Experiment

Editors: Yu. Gornushkin

Project Title

OPERA experiment: the search of the $\nu_\mu \rightarrow \nu_\tau$ oscillations at the CNGS neutrino beam

Project Leaders

- Yu.A. Gornushkin

Abstract

OPERA [1] is a long-baseline neutrino experiment designed to observe, for the first time, the $\nu_\mu \rightarrow \nu_\tau$ oscillation in direct appearance mode through the detection of the production of the corresponding τ lepton in the CNGS ν_μ beam [2] over a baseline of 730 km.

OPERA has an hybrid detector consisting of two instrumented targets, each followed by a muon spectrometer. Each target is a succession of walls of "ECC bricks" interleaved with planes of scintillator strips. The ECC bricks are made of 56 1-mm thick lead plates, providing the mass, interleaved with emulsion films with a micrometric resolution. The total number of ECC bricks is about 150000 for a total target mass of ~ 1.2 kton.

The OPERA detector is located in the Gran Sasso underground laboratory (LNGS) in Italy. The CNGS beam has run for five years, from 2008 till the end of 2012, delivering a total of 17.97×10^{19} protons on target yielding 19505 neutrino interactions recorded in the OPERA targets. So far the OPERA Collaboration reported the observation of four ν_τ candidates. The total expected background as the sum of all the ν_τ decay channels is 0.22 ± 0.025 events. This implies that OPERA can already exclude the absence of the $\nu_\mu \rightarrow \nu_\tau$ oscillation signal at 4.2 σ. The analysis of the data is still in progress.

Thanks to a good electron identification capability of OPERA and to the small contamination of ν_e in the CNGS neutrino beam, the experiment has also performed a search for the $\nu_\mu \rightarrow \nu_e$ transitions. In data collected during the 2008-2009 beam runs, OPERA observed 19 ν_e candidate events with an expectation of 19.4 ± 2.8 (syst) events from the ν_e beam

contamination, 1.4 event from standard 3-flavour oscillation and 0.4 events miss-classified as ν_e interactions. This result has been used to set a limit on the mixing with additional, not yet observed, hypothetical non-standard neutrino mass eigenstate [3].

In addition to the neutrino oscillation physics, the OPERA detector is used to study cosmic rays in the TeV region. In particular, thanks to the magnetic spectrometer, OPERA measured the cosmic muon charge ratio $R_\mu \equiv N_{\mu+}/N_{\mu-}$ for single and for multiple muon events [4].

keywords: neutrino oscillations, electronic detectors, nuclear photoemulsions

Project Members From JINR

I.A. Bodnarchuk, A.V. Chukanov, S.G. Dmitrievsky, Yu.A. Gornushkin, Z.V. Krumshtein, A.G. Olshevskiy, A.B. Sadovsky, A.S. Sheshukov, A.A. Nozdrin, A.A. Sotnikov, Yu.P. Petukhov, G.A. Ososkov, S.G. Zemskova.

Project Duration. Approval Date(s)

The first proposal was in 2004 aiming the Target Tracker detector construction.
Extensions:

- 2007: data taking begins, JINR developes software and starts data analysis;
- 2009: JINR gets responsibility for the electronic detectors analysis, scanning station under development in Dubna;
- 2010: data analysis of electronic detectors and emulsion analysis at JINR;
- 2013: active participation in the final data analysis.

List of Participating Countries and Institutions

Joint Institute for Nuclear Research, Russia; Brussels, ULB, Belgium; Zagreb, RBI, Croatia; Annecy-le-Vieux LAPP, Strasbourg IPHC, France; Hambourg, Hambourg University, Germany; Nagoya, Nagoya University; Toho, Toho University, Japan; Bari, University Bari, INFN, Italy; Naples, INFN, Italy; Padua, University Padova, Italy; Rome, INFN, Italy; Frascati, LNF, Italy; Salerno, University Salerno, Italy; Gran Sasso, LNGS, Italy; Bologna, INFN, Italy; Bern, University Bern, Switzerland; LPI, ITEP, MSU SINP, INR RAS, Moscow, Russia

12.1 Project Description

12.1.1 Fundamental Scientific Problem Addressed by the Project

The OPERA neutrino experiment is designed to perform the first observation of neutrino oscillations in direct appearance mode in the $\nu_\mu \rightarrow \nu_\tau$ channel, via the detection of the τ-leptons created in charged currents (**CC**) ν_τ interactions. A discovery of the $\nu_\mu \rightarrow \nu_\tau$ transitions via their direct observation would unambiguously confirm the hypothesis of the responsibility of this oscillation channel for the results of the accelerator neutrino disappearance experiments, as well as the deficit of the atmospheric neutrinos. It is the important, and still missing, tile in the 3-components neutrino oscillation theory.

12.1.2 Specific Project Objectives and Expected Results

The project was proposed at CERN in 1998 [1]. JINR joined the experiment in 2003 and took active part in the detector construction. The hybrid setup installation was completed in 2007, and from 2008 until 2013 the detector was taking data at the CNGS neutrino beam. The goal of the project is a direct detection of tau neutrinos in the ν_μ beam at a distance of 730 km as a result of oscillations. Given the number of the protons on target (**p.o.t.**) provided by CERN (can be transformed to the number of neutrinos produced), the total mass of the detector, the cross-sections, and all the detection efficiencies, the total number of the tau neutrinos to be observed is expected at the level of $5-6$, but with a very low background of about 0.2 events, thanks to unique resolution of the nuclear photoemulsion. The final goal is the first direct discovery of $\nu_\mu \rightarrow \nu_\tau$ oscillations in appearance mode and with a confidence level of 5 σ. Also, a complementary oscillation mode $\nu_\mu \rightarrow \nu_e$ is studied, thanks to a high detection efficiency of the ν_e in the nuclear emulsions. Cosmic particles physics is a subject of the investigation with the OPERA detector as well.

12.1.3 Basic Methods and Approaches Used in the Project

The hybrid detector, located in the underground Gran Sasso Laboratory (**LNGS**), consists of an emulsion/lead target with an average mass of about 1.2 kt, complemented by electronic detectors. It is exposed to the CERN Neutrinos to Gran Sasso beam (**CNGS**), with a baseline of 730 km and a mean energy of 17 GeV.

To achieve the OPERA experiment goals, the direct detection of tau neutrinos appearing in the beam as a result of oscillations, one needs a massive detector (to be able to detect neutrinos) with a very good spatial resolution (to be able to detect short lived tau leptons). These requirements seem to be in contradiction, unless we use a hybrid detector and the so called Emulsion Cloud Chambers technique. The last one assumes the detector target built of the large amount of modules (**"bricks"**) each of which consists of the thin layers of lead interlaced with the nuclear photoemulsion films. When neutrino interacts with a nucleus in the lead layer, the reaction products leave their tracks in the emulsion, so the vertex can be precisely reconstructed. In case of τ neutrinos, the τ lepton, produced in the

CC interaction, has a track length of a few hundred microns on average (at the CNGS beam energy) and can be recognized in the emulsion films.

The analysis starts with the identification of the event vertex brick by processing the data from the electronic detectors. Here, as in any other electronic detector, standard tracking techniques, hadron and electromagnetic shower reconstruction, as well as other methods used in the experimental high energy physics, are applied. After the identified brick is extracted, its emulsion layers are thoroughly searched by the automatic scanning microscopes, which recognize and store in the computer memory information on the Argentum grains which appear along the charged particle track when it transverse the nuclear photoemulsion layer. The individual grains are combined in so called microtracks (the fragments of the track available within one emulsion layer). Then the microtracks are combined in a whole track by matching each other, thanks to the submicronic spatial resolution. With all the tracks and the event vertex reconstructed, the kinematic event analysis is performed, as the momentum estimation and particle identification is also available with the emulsions [5]. The main technique in the tau neutrino search in OPERA is based on the possibility to recognize the short-lived tau lepton in the emulsion when it is produced in the CC interaction of the tau neutrino with the detector target thanks to its impressive spatial resolution. At the energies of the CNGS beam, the tau lepton has, on average, a track length of a few hundreds of microns, hence a very peculiar "kink" topology is well recognizable in the ECC brick (Fig. 12.1).

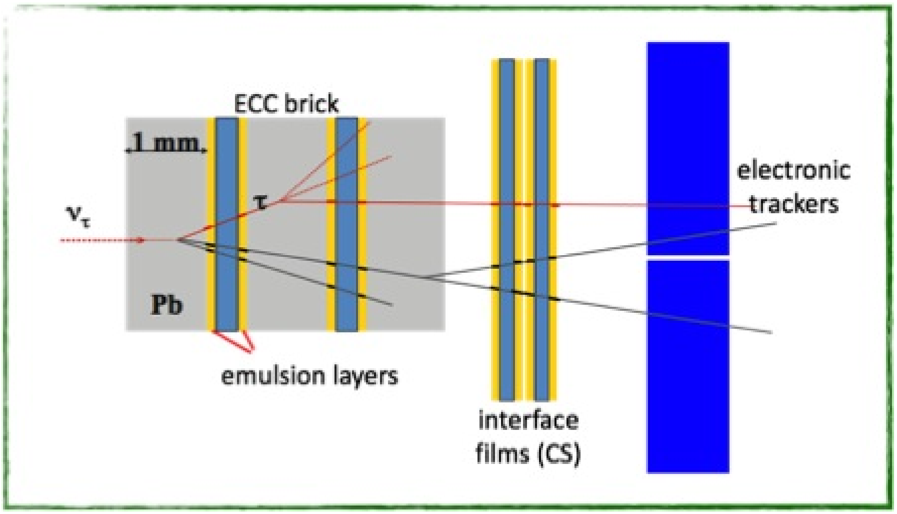

Figure 12.1: ECC ν_τ detection principle

The performance of the automatic scanning microscopes working in the European labs, including JINR, is now at the level of 20-40 cm^2 per hour. In Japan, the newest microscope can take the information about all the tracks with an average speed of up to 3000 cm^2 per hour and is going to be increased further. The automatic microscopes act as readers for the information stored in the emulsions, and transmit the 3D tracking information to the computer memory for data analysis. This is, in fact, not much different from the analysis methods in more conventional electronic tracking detectors.

12.1.4 Detector Description

The OPERA detector [6] is designed to tackle a challenging task: achieving micrometric tracking accuracy over a very large detector volume spanning about $(6.5 \times 6.5 \times 8)$ m^3. The scale of the required granularity is set by the flight length of τ leptons, which, for the CNGS beam, has a roughly exponential distribution with a mean of about 600 μm. This challenge was addressed by using nuclear emulsion based trackers. Another important constraint is related to the practical impossibility to analyze the full emulsion surface $\mathcal{O}(0.1$ km$^2)$, even with the state-of-the art automatic scanning technology. This, together with other constraints, resulted in a highly modular target made of units based on the Emulsion Cloud Chamber (**ECC**) technique, hereafter called bricks, interspersed with pairs of planes of horizontal and vertical scintillator strips (called Target Tracker or **TT** [7]) that allow locating with a resolution about some cm the unit in which the neutrino interaction occurred.

A brick is composed of 57 emulsion films interleaved with 56.1 mm thick, lead plates for a mass of 8.3 kg. Its thickness along the beam direction corresponds to about 10 radiation lengths and its transverse size is 128×102 mm^2. A film consists of two 44 μm layers deposited on each side of a 205 μm plastic base. When a τ neutrino interacts with the target in the ECC brick through charged current weak interaction, a tau lepton is produced and decays shortly after a few hundreds microns. This produces a very special, so called "kink" decay topology, which is well recognizable in the nuclear photoemulsions (Fig. 12.1).

Another key ingredient for the experiment are the Changeable Sheet (**CS**) doublets [8], attached to the downstream face of each brick. This pair of films allows a relatively fast feedback on the prediction of the electronic detectors (**ED**) and provides a prediction of the event position in the brick at the $\mathcal{O}(10)$ μm level, thus greatly helping the vertex location. Finally a magnetic spectrometer system instrumented with Resistive Plate Chamber (**RPC**) detectors and high-precision Drift Tubes (**DT**), is used for the task of identifying muons and measuring their charge and momentum. A good muon identification capability is essential to reduce the background to τ decays from charmed particles produced in charged current ν_μ interactions.

The detector (Fig. 12.2) is divided into two identical units called Super Modules (SM), each consisting of a target and a spectrometer section. The average number of bricks has been about 140000 for a target mass of about 1.2 kt. OPERA was exposed to the CNGS ν_μ beam [2] at a long-baseline, 730 km away from the source. The neutrino beam, produced by 400 GeV-protons accelerated in the SPS machine of CERN, has an average energy of about 17 GeV, optimized for the observation of tau neutrino CC interactions in the OPERA detector. In terms of interactions, the contamination of muon antineutrino is 2.1 %, the electon neutrino and antineutrino both give contaminations below 1 %, while the intrinsic τ neutrino component (from D$_s$s decays in the CNGS target and beam-dump) is of $\mathcal{O}(10^{-6})$, hence negligible.

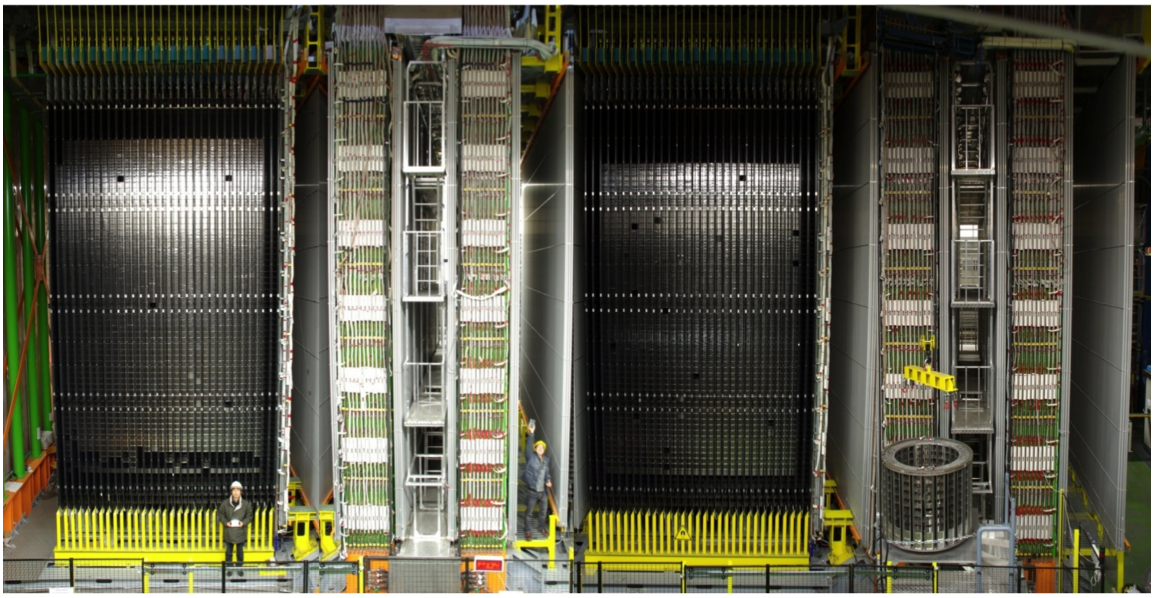

Figure 12.2: OPERA detector

The CNGS beam has run for five years, from 2008 till the end of 2012, delivering a total of 17.97×10^{19} protons on target yielding 19505 neutrino interactions recorded in the OPERA targets.

The events triggered by the neutrino beam, in coincidence with the two 10.5 μs long CNGS spills 50 ms distant (”on-time” events), are those used for neutrino oscillation studies. Every time a charged particle belonging to ”on-time” events produces a signal in the TT, a brick finding algorithm selects the bricks with the highest probability to contain the neutrino interaction. The efficiency of this procedure is 83% in a sub-sample where up to 4 bricks per event are processed. The selected brick is removed from the target by special precise robot, called Brick Manipulating System (**BMS**) and the corresponding CS doublet is detached from it and developed in a dedicated underground facility. The two emulsion films are scanned in one of the dedicated scanning stations of the Collaboration. The measurement of emulsion films is performed through fast automated microscopes with a scanning speed greater than 20 cm^2/h. The tracking efficiency was evaluated to be about 90%, the position resolution being at the sub-micron level. The angular resolution is of the order of one milliradian. The residuals between electronic detectors’ predictions and CS tracks are $\sim$1 cm. If any track originating from the interaction is detected in the CS, the brick is brought to the surface laboratory and exposed to high-energy cosmic rays for alignment purposes and then unpacked. Its emulsion films are developed and sent to the scanning laboratories of the Collaboration for event location studies. All CS tracks are searched for in the most downstream film of the brick. The CS to brick connection is achieved with a position accuracy smaller than 100 μm and a slope accuracy of the order of 10 mrad. Tracks that have been successfully located in a CS doublet are followed upstream through the corresponding brick (scan-back) until they stop. This is interpreted as a signature of either a primary or a secondary vertex. A general scanning (no angular pre-selection) is then performed in a 2 cm^3 volume around the stopping points in order to reconstruct the vertex topology with micrometric precision. In order to detect decay topologies, every located vertex is carefully investigated by means of a dedicated procedure.

Once an interesting secondary vertex topology is found, it is analyzed through kinematical criteria which depend on the decay channel under investigation and are based on particle angles and momenta measured in the emulsion films.

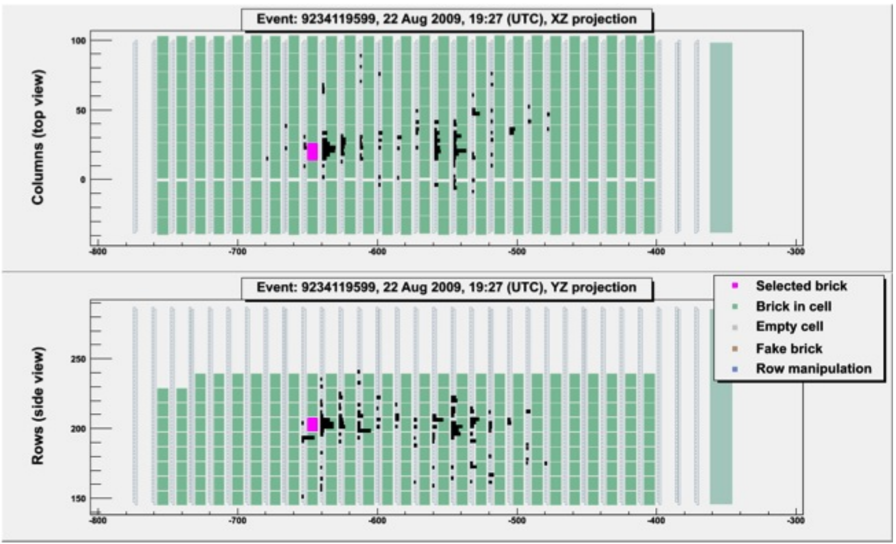

Figure 12.3: The first ν_τ event candidate as it is registered by the OPERA electronic detectors

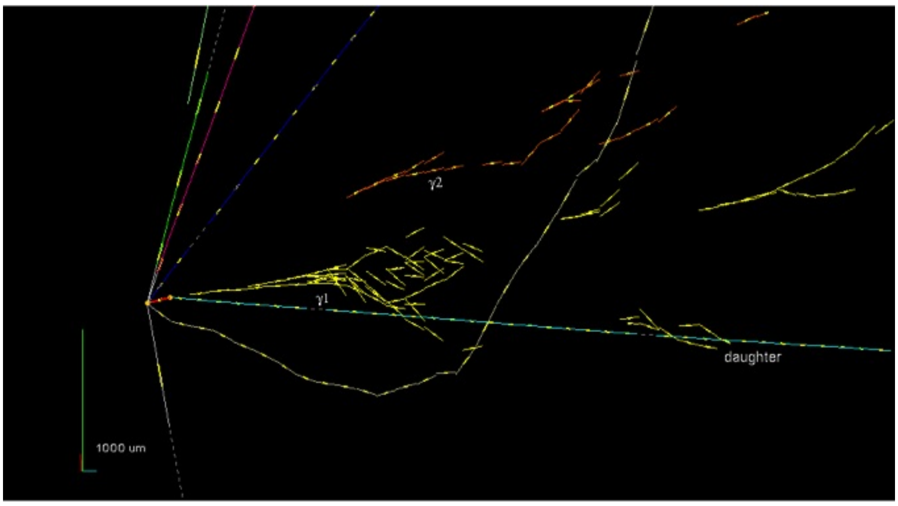

Figure 12.4: The first τ neutrino event candidate as it is seen in the OPERA emulsions

Results

So far the OPERA Collaboration reported the observation of the four tau neutrino candidates: the first in the 2009 run data with a hadronic one-prong decay topology [9] (see Fig. 12.3 and Fig. 12.4), the second in the 2011 run data with an hadronic three-prong decay topology [10], the third one in the 2012 run data with a muonic decay topology [11] and in 2014, the Collaboration annonced the registration of the fourth candidate — in the one prongtau decay mode [12].

The total expected background as a sum of all the τ decay channels is 0.22 ± 0.025 events. This implies that OPERA can already exclude the absence of the $\nu_\mu \rightarrow \nu_\tau$ oscillation signal at 4.2 σ. Thanks to the good electron identification capability of OPERA and to the small contamination of ν_e in the CNGS neutrino beam, the experiment has also performed a search for the $\nu_\mu \rightarrow \nu_e$ [3]. In data collected during the2008-2009 beam runs, OPERA observed 19 ν_e candidate events with an expectation of 19.4 ± 2.8 (syst) events from the ν_e beam contamination, 1.4 event from standard 3-flavour oscillation and 0.4 events miss-classified as ν_e interactions. This result has been used to set a limit on the mixing with additional, not yet observed, hypothetical non-standard neutrino mass eigenstate (Fig. 12.5). In addition to the neutrino oscillation physics, the OPERA detector is used to study cosmic rays in the TeV region. In particular, thanks to the magnetic spectrometer, OPERA measured the cosmic muon charge ratio $R_\mu \equiv N_{\mu+}/N_{\mu-}$ for single and for multiple muon events [4].

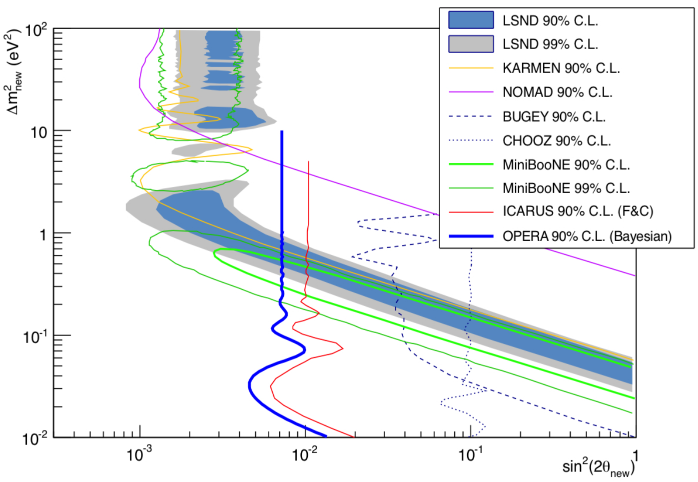

Figure 12.5: The new limits on the LSND-MiniBooNe non-standard oscillation parameters set by the OPERA experiment

12.1.5 Contribution of JINR Members

The JINR group has participated in the OPERA experiment since its very early stages in 2002. Making use of its experience in the production of high quality plastic scintillator and the detectors that use them, the JINR group, along with the AMCRYS-H institute in Kharkov (Ukraine), organized the production of the scintillator strips, the elements of the Target

Tracker which is the main tracking detector of the OPERA experiment. The strips were produced according to the coextrusion technology (scintillator core and the light reflecting coat are extruded simultaneously providing ready-to-go counters) under the control and supervision of JINR. The Target Tracker module's production from the strips was performed at IRES (Strasbourg, France). An international team from France and JINR worked for 3 years assembling 500 modules with a total surface of 5500 m^2. Physicists, engineers, and technicians from JINR took an active role in this work. In parallel to the module's assembly work, the full calibration of the modules was performed by JINR physicists. After production, the modules were transported to the underground laboratory in Gran Sasso (Italy) where they were assembled in walls of 7 by 7 m^2 and installed in the OPERA detector. Again, JINR physicists actively participated in the assembly and performed almost all of the alignment and survey work. After the commissioning of the detector in 2007, and the commencement of the data collection, the JINR group developed a software package for the Target Tracker data analysis to determine which of the target bricks have the highest probability to contain the neutrino interaction vertex. Starting in 2009, this software was used by the OPERA Collaboration as a main software tool for the electronic detector data analysis. As a part of the software package, an event display with rich functionality was developed and widely used by the collaboration for the visual data inspection. Starting in 2010, the JINR group was fully responsible for the electronic detectors data analysis and the vertex bricks determination, a very important part of the analysis chain.

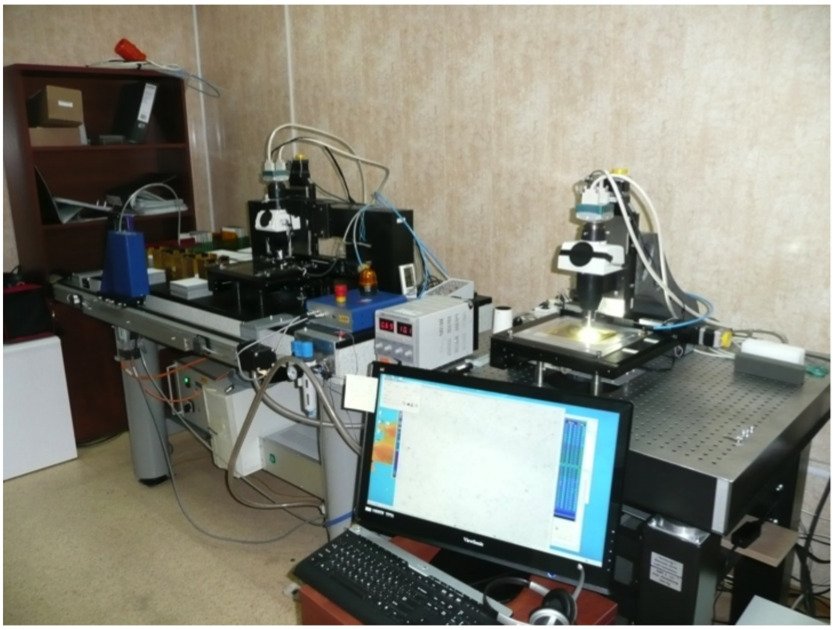

Figure 12.6: Emulsion scanning stations in Dubna

JINR also takes part in the emulsion data analysis. There are two automatic emulsion scanning stations that were created in Dubna, which allow us to perform the emulsion analysis at JINR. As with other institution, JINR searches through the emulsion bricks and looks for the oscillation event candidates (Fig. 12.6).

The JINR group also takes part in the Monte Carlo simulation. One of the major backgrounds for the tau decay is hadronic reinteractions in the bricks, since they can mimic the tau lepton decay topologies. JINR developed a software for the simulation of this processes and estimation of the background contribution.

The JINR contribution in the OPERA experiment is greatly appreciated by the Collaboration. On more than 12 occasions JINR group members have reported the results of the experiment at major international conferences (see below).

12.1.6 Publications, Theses and Conferences

As a result of the project the following

- papers has been published [1–11]
- Master thesis A.Sheshukov, T.Ruadze defended.
- talks given at conferences:

Lomonosov 2013	Moscow, Russia	Dmitrievsky Sergey
Colloquium Prague V13	Prague, Czech Republic	Gornushkin Yury
NeuTel 2013	Venice, Italy	Dmitrievsky Sergey
HEPFT 2013	Protvino, Russia	Sheshukov Andrey)
TAUP 2011	Munich, Germany	Chukanov Artem
TAU 2010	Manchester, UK	Gornushkin Yuri
Epiphany 2010	Cracow, Poland	Dmitrievsky Sergey
Neutrino 2010	Aphenes, Greece	Gornushkin Yury
NUINT 2009	Barcelona, Spain	Naumov Dmitry
Crimea 2008	Yalta, Ukraine	Chukanov Artem
ICHEP 2006	Moscow, Russia	Gornushkin Yuri

12.1.7 Finances

Major sources and amount of finances and major equipment acquired and travel expences during the project runtime are listed in Tab. 12.1.

Source	Requested (k$)	Obtained (k$)	Expences
1099	450	450	Contribution in the Target Tracker detector, Laboratory of automatic nuclear emulsion scanning (climatized clean room with two automatic microscopes, equipped with robot and infrastructure)
1099	200	200	Travels

Table 12.1: Major sources and amount of finances and major equipment acquired

References

[1] M.Guler et al. "An appearance experiment to search for $\nu_\mu \rightarrow \nu_\tau$ oscillations in the CNGS beam: experimental proposal". In: (2000).

[2] Ed. K. Elsener. "The CERN Neutrino beam to Gran Sasso (Conceptual Technical Design)". In: ().

[3] N.Agafonova et al. "Search for $\nu_\mu \rightarrow \nu_e$ oscillations with the OPERA experiment in the CNGS beam". In: *JHEP* 1307 (2013), p. 004. arXiv: 1303.3973.

[4] N.Agafonova et al. "Measurement of TeV atmospheric muon charge ratio with the full OPERA data". In: (2014). arXiv: 1403.0244.

[5] N. Agafonova et al. "Momentum measurement by the Multiple Coulomb Scattering method in the OPERA lead emulsion target". In: *New J.Phys.* 14 (2012), p. 013026. arXiv: 1106.6211 [physics.ins-det].

[6] R. Acquafredda et al. "The OPERA experiment in the CERN to Gran Sasso neutrino beam". In: *JINST* 4 (2009), P04018.

[7] T. Adam et al. "The OPERA experiment target tracker". In: *Nucl.Instrum.Meth.* A577 (2007), pp. 523–539. arXiv: physics/0701153 [physics].

[8] A. Anokhina et al. "Emulsion sheet doublets as interface trackers for the OPERA experiment". In: *JINST* 3 (2008), P07005. arXiv: 0804.1985 [physics.ins-det].

[9] N.Agafonova et al. "Observation of a first ν_τ candidate in the OPERA experiment in the CNGS beam". In: *Phys.Lett* B691 (2010), p. 138.

[10] N.Agafonova et al. "New results on ν_τ appearance with the OPERA experiment in the CNGS beam". In: *JHEP* 1311 (2012), p. 36.

[11] N.Agafonova et al. "Evidence for $\nu_\mu \rightarrow \nu_\tau$ appearance in the CNGS neutrino beam with the OPERA experiment". In: *Phys.Rev.D* 89.5 (2014), p. 051102. arXiv: 1401.2079.

[12] INFN press release. "The fourth transformation of neutrinos". In: *www.infn.it.* (2014).

Chapter 13

SuperNEMO Experiment

Editors: V.Brudanin, O.Kochetov

Project Title

Search for neutrinoless double beta decay with NEMO-3 and the next generation double beta decay experiment SuperNEMO

Project Leaders

- France: F. Piquemal
- JINR: O.I. Kochetov

Abstract

The NEMO-3 experiment, located in the Modane Underground Laboratory (**LSM**), is searching for neutrinoless double beta decay. The experiment has been taking data since 2003 with a range of isotopes: ^{48}Ca, ^{82}Se, ^{96}Zr, ^{100}Mo, ^{116}Cd, ^{130}Te and ^{150}Nd. The main isotopes are $\sim$7 kg of ^{100}Mo and $\sim$1 kg of ^{82}Se. Since no evidence for neutrinoless double beta decay has been found, a 90% CL lower limit on the half-life of this process is derived. From this we determine an upper limit on the effective Majorana neutrino mass.

The data are also interpreted in term of alternative models, such as weak right-handed currents or Majoron emission. NEMO-3 has also performed precision measurements of the standard model double beta decay process for several isotopes. Measurements of this process are important for reducing the uncertainties on nuclear matrix elements. A precise measurement on the half-life for the double beta decay of ^{130}Te and a comparison with the conflicting results from geochemical experiments has also been performed.

SuperNEMO is a next-generation double beta decay experiment based on the successful tracking plus calorimetry technology of the NEMO-3 experiment. Due to its unique tracking and particle identification capabilities of the SuperNEMO experiment, not only might it be able to discover neutrinoless double beta decay, but it may also be able to determine the underlying physics mechanism. Due to the separation of source and detector, SuperNEMO

can study a range of isotopes such as ^{48}Ca, ^{82}Se and ^{150}Nd. The total isotope mass will be in a range of 100-200 kg. With this isotope mass a sensitivity to a half-life greater than 10^{26} years can be reached. This could give access to Majorana neutrino masses of about 50 meV, depending on the value of the nuclear matrix elements.

Construction of a prototype module (DEMONSTRATOR) has started and will be ready in 2015. The main challenges for the international R&D project are source foils production, radiopurity, calorimeter energy resolution and tracker construction. Two modules of the BiPo detector used to measure source foils radiopurity have been installed in the Canfranc Underground Laboratory, Spain.

keywords: Double beta decay, Majorana neutrinos.

Project Members From JINR

V. Brudanin, V. Babin, V. Egorov, D. Filosofov, D. Karaivanov, A. Klimenko, O. Kochetov, V. Kovalenko, I. Nemchenok, A. Rahimov, Yu. Shitov, A. Shurenkova, A. Smolnikov, V. Timkin, V. Tretyak, Yu. Yushkevich

Project Duration. Approval Date(s)

NEMO-3 data taking	2003 – 2011
NEMO-3 data processing	up to now
R&D of the Trial SuperNEMO section (DEMONSTRATOR)	2006 – 2011
Project PAC approval (within JINR Theme #1100)	2013
Producing of the Detector elements in JINR	2011 – 2014
The DEMONSTRATOR Mounting at LSM, France	2014
Start of data taking with DEMONSTRATOR (planned)	2015

List of Participating Countries and Institutions

PHC, Université de Strasbourg, CNRS/IN2P3, F-67037 Strasbourg, France; INL, Idaho National Laboratory, 83415 Idaho Falls, USA; INR, Institute of Nuclear Research, MSP 03680 Kyiv, Ukraine; ITEP, Institute of Theoretical and Experimental Physics, 117259 Moscow, Russia; CNRS/IN2P3, Centre dÉtudes Nucléaires de Bordeaux Gradignan, UMR5797, F-33175 Gradignan, France; Université Bordeaux, CENBG, UMR 5797, F-33175 Gradignan, France; JINR, Joint Institute for Nuclear Research, 141980 Dubna, Russia; University College London, WC1E 6BT London, United Kingdom; University of Manchester, M13 9PL Manchester, United Kingdom; USMBA, Universite Sidi Mohamed Ben Abdellah, 30000 Fes, Morocco; University of Texas at Austin, 78712-0264 Austin, Texas, USA; IEAP, Czech Technical University in Prague, CZ-12800 Prague, Czech Republic; LPC, ENSICAEN, Université de Caen, CNRS/IN2P3, F-14032 Caen, France; IFIC, CSIC - Universitat de Valencia, Valencia, Spain; Universitat Autònoma Barcelona, Barcelona, Spain; Saga University, Saga 840-8502, Japan; LSCE, CNRS, F-91190 Gif-sur-Yvette, France; FMFI, Commenius University, SK-842 48 Bratislava, Slovakia; Jyväskylä University, 40351 Jyväskylä, Finland; MHC, Mount Holyoke College, 01075 South Hadley, Massachusetts, USA; Charles University in

Prague, Faculty of Mathematics and Physics, CZ-12116 Prague, Czech Republic.

13.1 Project Description

13.1.1 Fundamental Scientific Problem Addressed by the Project

Experimental search for the neutrinoless double beta decay ($0\nu\beta\beta$) is the most practical way to establish the charge-conjugation property of the neutrino. This process (Fig. 13.1) supposes the violation of the total lepton number conservation law by two units and is possible only if the neutrino is a Majorana particle ($\nu \equiv \bar{\nu}$) with nonzero effective mass. The probability of $0\nu\beta\beta$-decay is given by

$$W = G_{0\nu} \cdot |\mathcal{M}_{0\nu}|^2 \cdot \langle m_\nu \rangle^2 \tag{13.1}$$

with $G_{0\nu} \sim Q^5_{\beta\beta}$ as a phase space factor and $\mathcal{M}_{0\nu}$ as the nuclear matrix element (**NME**). As a result, an observation of $0\nu\beta\beta$-decay would allow one to determine the absolute neutrino mass scale.

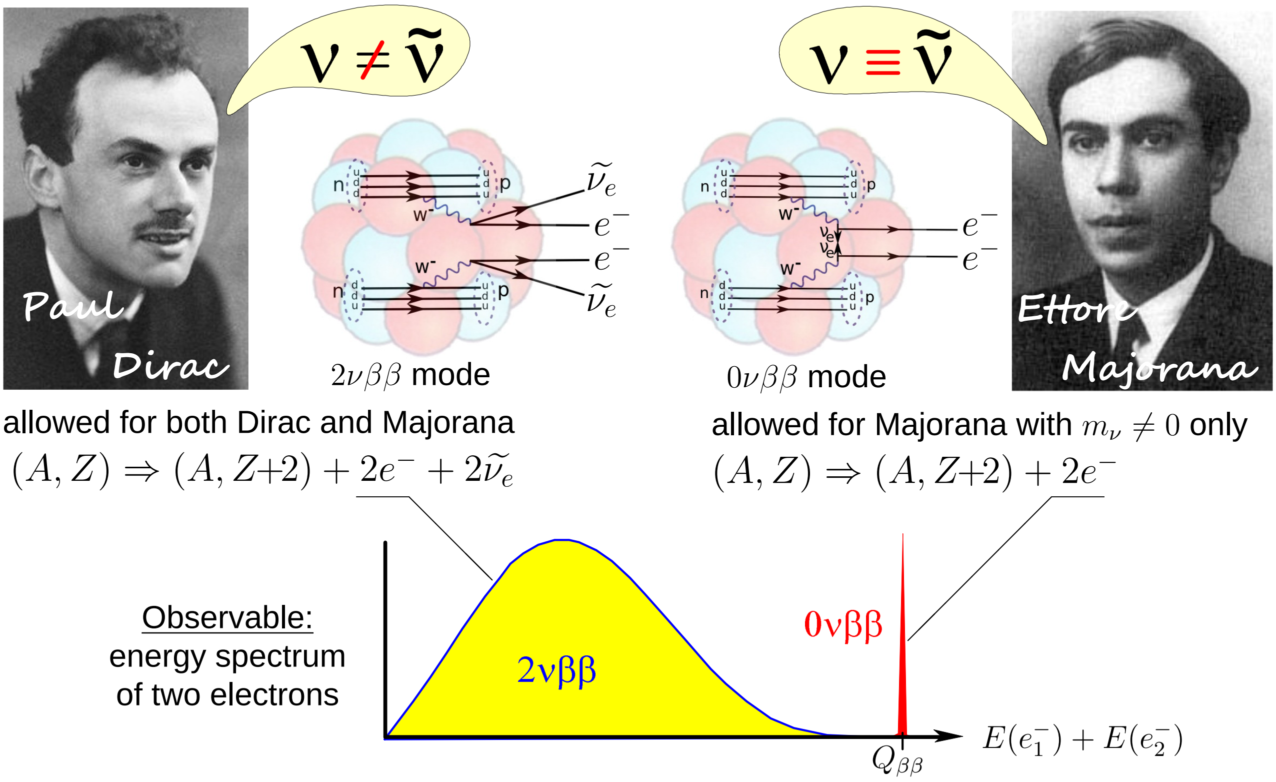

Figure 13.1: Dirac or Majorana neutrino nature and two modes of $\beta\beta$-decay.

Contrary to the neutrinoless version, two-neutrino double beta decay ($2\nu\beta\beta$) is an allowed but very rare second-order weak interaction process. The measurement of its rate is important because it constitutes the main background in the search for the $0\nu\beta\beta$-decay signal, and provides with valuable input for the $\mathcal{M}_{0\nu}$ theoretical calculations (see, e.g. [1–4] and refs therein).

13.1.2 Specific Objectives of the NEMO Project

Initially, the idea for NEMO was to create a low-background spectrometer which could be installed in the Modane Underground Laboratory (LSM, Modane, France) and detect $\beta\beta$-decay with combined tracking and calorimetric techniques. A thin $\beta\beta$-sample produced of an appropriate enriched isotope was proposed to be surrounded with a large ($\sim$1 m) tracking volume filled with He gas at atmospheric pressure and an outer scintillator calorimeter. Thin wires operating in Geiger mode would allow for reconstruction of trajectories for both β-particles in a weak magnetic field. Such a combination of tracking, calorimetric and time-of-flight information would provide very precise $\beta\beta$-event signature, thus suppressing the background. Knowing the vertex of each event, one could use a source foil composed of several parts and thus investigate $\beta\beta$-decay of several isotopes simultaneously.

13.1.3 Retrospective NEMO Review

A prototype NEMO-1 shown in Fig. 13.2 was built in 1988 and demonstrated [5] operability of the tracking method.

The second step was made in 1992. Spectrometer NEMO-2 [6] contained $\sim$1m^2 foil of isotopic enriched material (^{100}Mo, ^{116}Cd, etc.) surrounded with 1 m^3 tracking volume filled with He gas and transpierced with number of thin wires. The energy of both β-particles was measured with two scintillator walls (8×8 PMTs each). Informal JINR participation in the NEMO project began at this stage with the production of 128 plastic scintillator blocks for the NEMO-2 detector.

The goal of the third step, NEMO-3 experiment [7], was a search for the $0\nu\beta\beta$-decay and an investigation of the $2\nu\beta\beta$-decay of several isotopes. Compared to NEMO-2, the detector was supplemented with vertical magnetic field and could accept 20 times higher mass of a sample. Due to a precise signature NEMO-3 was capable of identifying e^-, e^+, γ-rays, α-particles, and allowed for discrimination of signal events from background. The full kinematic pattern of an event available with the NEMO-3 track-calorimetric approach is very useful for the study of the underlying $\beta\beta$ decay mechanism.

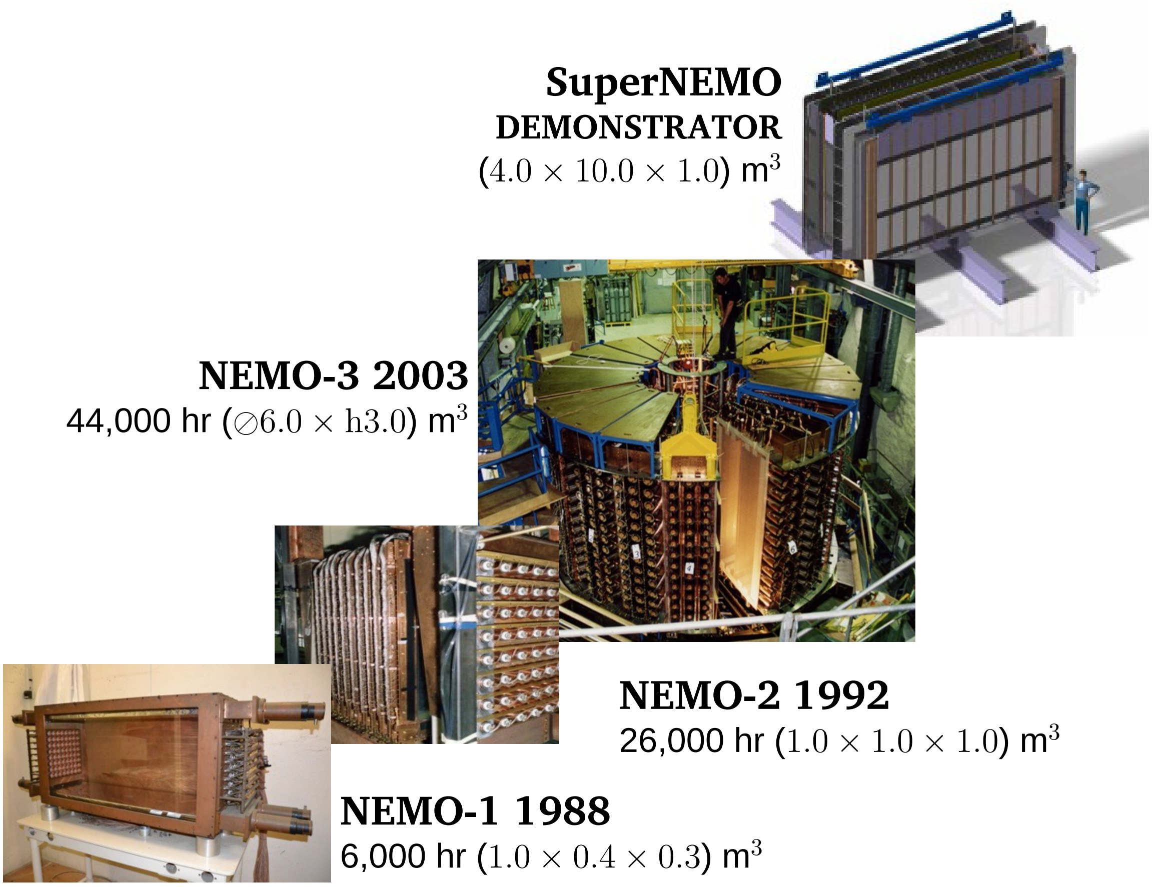

Figure 13.2: From NEMO-1 to SuperNEMO.

The possibility of probing new physics scenarios of light Majorana neutrino exchange and right-handed currents is planned for the next generation neutrinoless $\beta\beta$ spectrometer SuperNEMO [8] which could deal with 100 kg of isotopic enriched samples. Its ability to study different isotopes and track the outgoing electrons provides a means to discriminate different underlying mechanisms for the neutrinoless $\beta\beta$ decay by measuring the half-life and the electron angular and energy distributions.

13.1.4 Description of the NEMO-3 detector and its results

The NEMO-3 detector (Figs. 13.3 and 13.4) had a cylindrical shape and was composed of twenty equal sectors. It contained almost 9 kg of 7 different $\beta\beta$ isotopes in the form of thin ($\sim$ 50 mg/cm^2) source foils located vertically in the middle of tracking volume surrounded by a calorimeter.

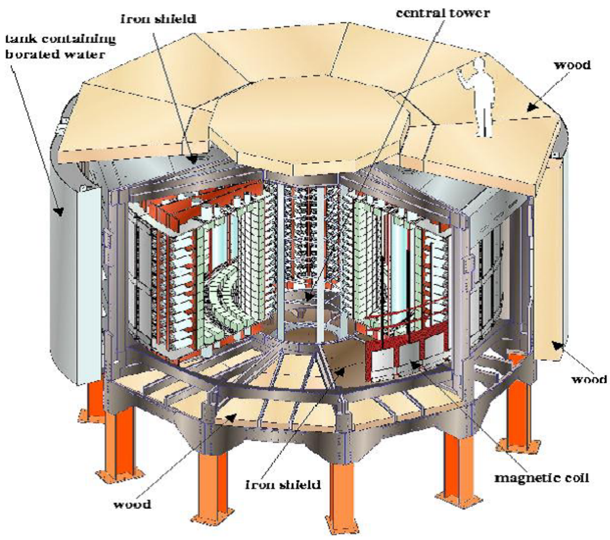

Figure 13.3: Schematic view of the NEMO-3 detector.

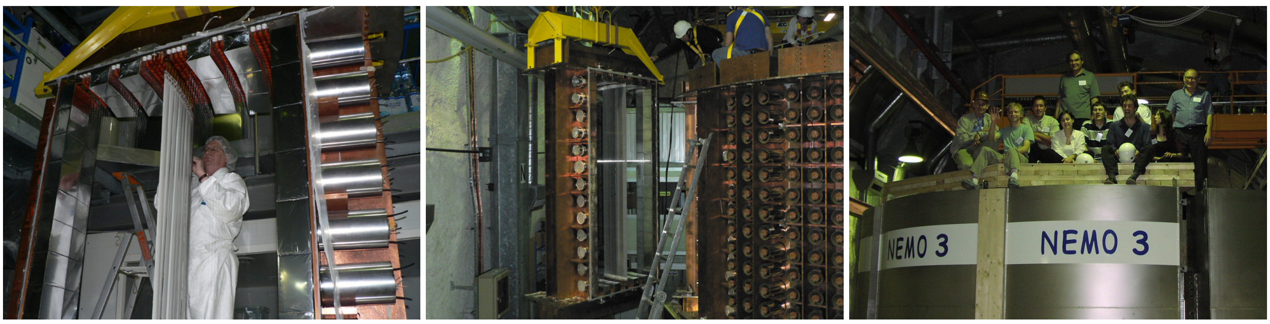

Figure 13.4: Mounting of the ^{100}Mo foil (left), one of 20 sectors (middle) and shielding (right).

The tracking chamber was made of 6180 open octagonal drift cells operating in Geiger mode. The position resolution for tracking was 0.6 mm in the horizontal plane and 0.8

cm in the vertical direction. The calorimeter comprised 1940 plastic scintillator blocks coupled to low radioactivity photomultipliers. Time and energy resolution (FWHM) for 1 MeV electrons was 250 ps and 15%, respectively. A weak magnetic field of $\sim$25 Gauss was used for e^+/e^- discrimination by the track curvature. The detector was shielded by 18 cm of low activity iron against external γ-rays and by 30 cm of borated water against neutrons. A more detailed description of the detector and its characteristics can be found in [9].

Events are selected requiring two reconstructed electron tracks originating from a common vertex in the source foil. The cut on the minimal energy of 200 keV deposited by each electron in the calorimeter is used.

The background can be classified in three groups: internal (from radioactive contamination of the source), external (from incoming γ-rays), and from the tracking volume, principally due to the radon. All three were measured with the NEMO-3 data [10].

The detector was operating in the Modane Undeground Laboratory located in the Frejus tunnel at a 4800 m w.e. depth. The data collection started in February 2003 and completed in January 2011. The first part of the data taken before October 2004 (Phase-I) is characterized by relatively high radon activity of ~ 1 Bq inside the 28 m^3 volume of tracking chamber. Then the radon level was reduced by a factor of $\sim$6 after installation of a radon trapping facility (the Phase-II).

The $2\nu\beta\beta$-decay half-lives have been measured in NEMO-3 for seven available $\beta\beta$ isotopes. The results of the measurements are summarized in Table 13.1. For all isotopes the energy sum spectrum, the single-electron energy spectrum, and angular distribution were measured.

Isotope	Mass (g)	$Q_{\beta\beta}$ (keV)	S/BG	$T_{1/2}$ (10^{19} years)			ref.
^{100}Mo	6914.0	3034	76	0.711	$\pm$ 0.002(stat)	$\pm$ 0.054(syst)	[11]
^{82}Se	832.0	2998	3	9.6	$\pm$ 0.3(stat)	$\pm$ 1.0(syst)	[11]
^{116}Cd	405.0	2813	10.3	2.88	$\pm$ 0.04(stat)	$\pm$ 0.16(syst)	[12]
^{150}Nd	37.0	3371	2.8	0.911	$^{+0.025}_{-0.022}$(stat)	$\pm$ 0.063(syst)	[13]
^{96}Zr	9.4	3350	1.0	2.35	$\pm$ 0.14(stat)	$\pm$ 0.16(syst)	[14]
^{48}Ca	7.0	4263	6.8	4.4	$^{+0.5}_{-0.4}$(stat)	$\pm$ 0.4(syst)	[12]
^{130}Te	454.0	2527	0.5	70	$\pm$ 9(stat)	$\pm$ 11(syst)	[15]

Table 13.1: NEMO-3 results of $2\nu\beta\beta$ half-life measurements

As the main $\beta\beta$-source in NEMO-3 experiment was ^{100}Mo, the most detailed analysis was done just for this isotope. Energy and angular distributions of $\beta\beta$ events for ^{100}Mo obtained in 1468 effective days of Phase-II are shown in Fig. 13.5.

These distributions can be used to test different NME calculation models. Thus according to [16] the intermediate ^{100}Tc nucleus should contribute to the $\beta\beta$-decay of ^{100}Mo mainly by the 1^+ ground state, which corresponds to a Single State Dominance (**SSD**) model [17] contrary to the commonly used High State Dominance (**HSD**) model. Figure 13.6 demon-

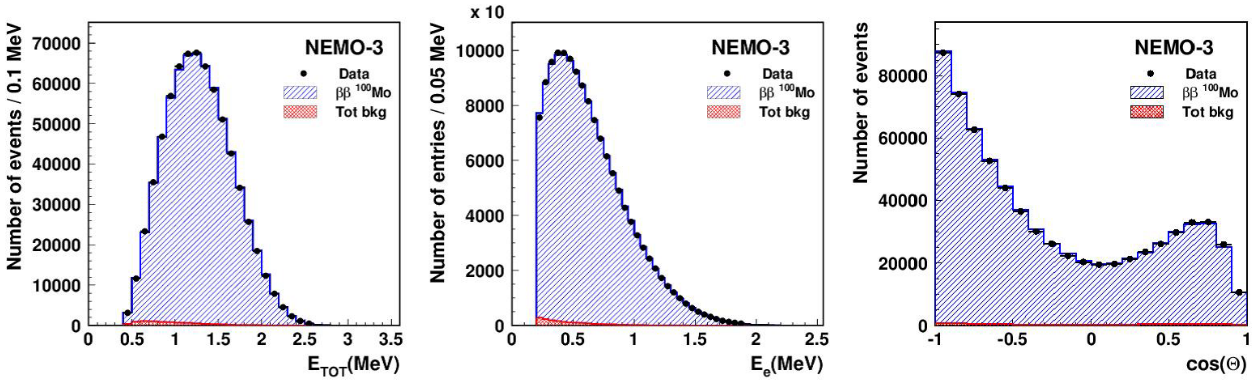

Figure 13.5: Total energy, individual electron energy and angular distribution of two-electron events from ^{100}Mo (4 years data of Phase-II).

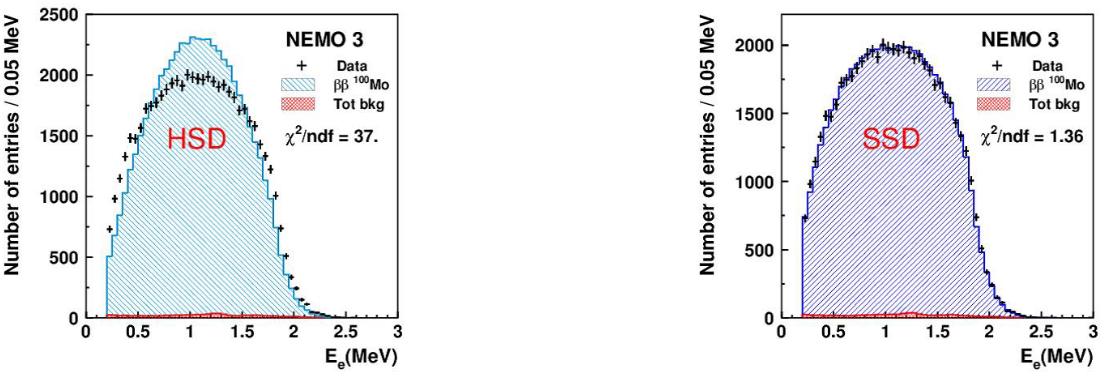

Figure 13.6: Single electron energy distribution for two-electron events with the energy sum above 2 MeV from ^{100}Mo compared to HSD (left) and to SSD (right).

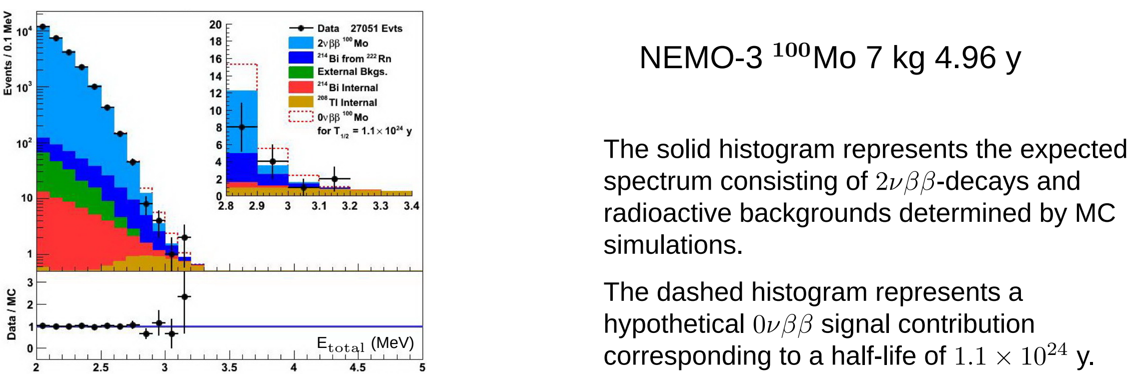

Figure 13.7: Distribution of the $\beta\beta$ energy sum, E_{total} and the ratio between the observed and the expected distributions from MC simulations.

strates that our data are apparently incompatible with HSD while in a good agreement with SSD.

The data taken from February 2003 to October 2010 has been used for the search of the $0\nu\beta\beta$-decay. It corresponds to 4.96 effective years of data collection. The total mass of 6914 g of ^{100}Mo in form of metallic and composite foils was studied. Figure 13.7 shows the spectrum of the $\beta\beta$ energy sum for $E_{\rm total} > 2$ MeV, exhibiting good agreement between the data and MC. The tail of the $E_{\rm total}$ distribution above 2.8 MeV in linear scale is shown in inset of Fig. 13.7. In the energy window $E_{\rm total} = [2.8 - 3.2]$ MeV around the $Q_{\beta\beta}$-value of ^{100}Mo there are 15 events observed compared to 18.0 ± 0.6 expected events. As no event excess is observed in the data above the background expectation, a 90%CL limit on the $0\nu\beta\beta$-decay of ^{100}Mo probability and corresponding upper limit on the effective Majorana neutrino mass is set:

$$\mathrm{T}_{1/2}(0\nu\beta\beta) \geq 1.1 \times 10^{24}\ \mathrm{y}\ , \qquad \langle m_\nu \rangle < (0.3 - 0.9)\ \mathrm{eV}\ , \tag{13.2}$$

where the range is determined by existing uncertainties in the nuclear matrix element and phase space calculations.

13.1.5 SuperNEMO: detector of the next generation

The next step in the search for $0\nu\beta\beta$-decay requires a sample of much higher mass ($\geq$100 kg) and therefore could be done only with a new detector of the next generation. The expected improvement in performance of SuperNEMO compared to its predecessor NEMO-3 is shown in Table 13.2 which compares the parameters of the two experiments.

Parameter	NEMO-3	SuperNEMO
Isotope and its mass	^{100}Mo, 7 kg	^{150}Nd or ^{82}Se, 100 - 200 kg
Efficiency	8%	$\sim$30%
Energy resolution (FWHM)	8% @ 3 MeV	4% @ 3 MeV
Internal ^{208}Tl contamination in $\beta\beta$ foil	$<$ 20 μBq/kg	$<$ 2 μBq/kg
Internal ^{214}Bi contamination in $\beta\beta$ foil	$<$ 300 μBq/kg	$<$ 10 μBq/kg (if ^{82}Se)
Internal Radon contamination in tracker	$\sim$ 5 - 6 mBq/m^3	$<$ 0.1 mBq/m^3
$T_{1/2}(0\nu\beta\beta)$ sensitivity	$> 1 \times 10^{24}$ y	$> 2 \times 10^{26}$ y
$\langle m_\nu \rangle$ sensitivity	$\leq$ (310 - 790) meV	$\leq$ (30 - 100) meV

Table 13.2: From NEMO-3 to SuperNEMO

The proposed SuperNEMO will be built upon the NEMO-3 choice of combined tracking + calorimetry technology. It gives the ability to measure individual electron tracks, vertices, energies and time of flight, and to reconstruct fully the kinematics and topology of an event. Its capabilities include the identification of γ-rays and α-particles, as well as distinguishing electrons from positrons with a magnetic field, form the basis of background rejection. An important feature of NEMO-3 which is kept in SuperNEMO is the fact that the $\beta\beta$-decay source is separate from the detector, allowing several different isotopes to be studied.

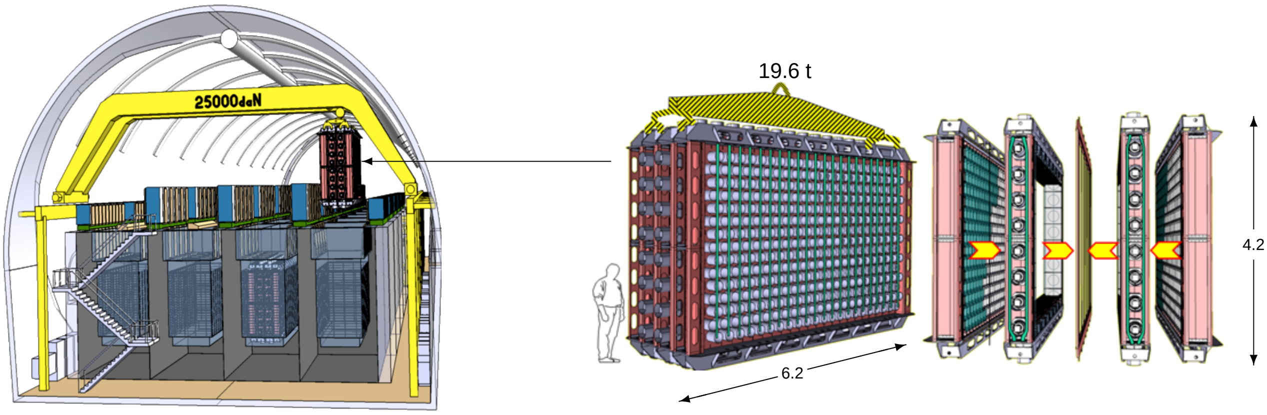

Figure 13.8: SuperNEMO modules in the extended LSM (left). One of 20 modules (right).

The SuperNEMO detector (Fig. 13.8) consists of 20 independent modules. Each module is approximately equivalent to the former NEMO-3 and will contain about 5-7 kg of a thin (~ 40 mg/cm^2) sample foil surrounded by a gas tracking chamber followed by calorimeter walls. The tracking volume contains more than 2000 wire drift chambers operated in Geiger mode, which are arranged in nine layers parallel to the foil. The calorimeter is divided into $\sim$1000 blocks which cover most of the detector outer area and are read out by low background photomultiplier tubes.

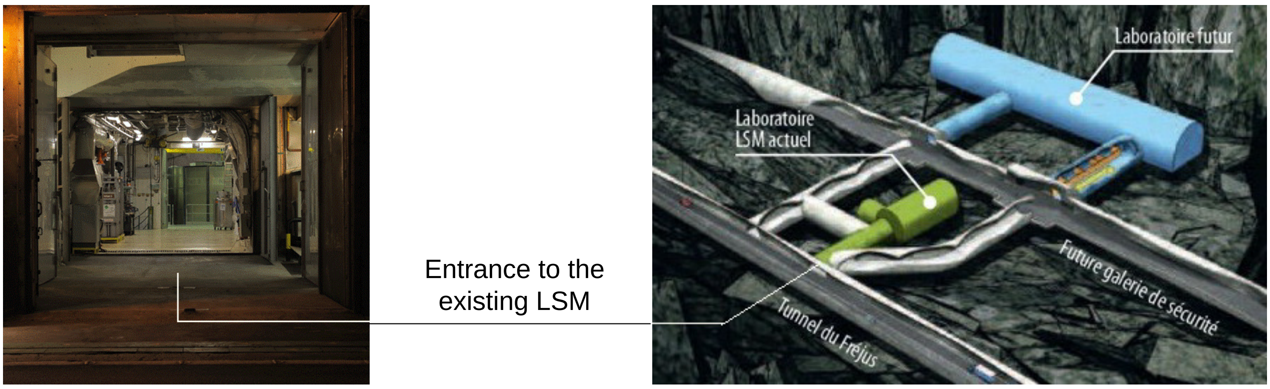

Figure 13.9: Modane Underground Laboratory (LSM) and its extension.

The existing underground laboratory (LSM, Fig. 13.9) is too small to satisfy the requirements, and is now being extended significantly. Excavation work will take few years and it is a good time for R&D, which is in progress, in order to ensure the improvements shown in Tab. 13.2.

Choice of source isotope for SuperNEMO

The choice of isotope for SuperNEMO is aimed at maximizing the $0\nu\beta\beta$ signal over the background of $2\nu\beta\beta$-decay and other nuclear decays mimicking the process. Therefore the isotope must have a long $2\nu\beta\beta$ half-life, and high endpoint energy and phase space factor $G_{0\nu}$ ($T_{1/2}(0\nu\beta\beta) \sim G_{0\nu}^{-1}$).

The enrichment possibility on a large scale is also a factor in selecting the isotope. The main candidate isotopes for SuperNEMO have emerged to be ^{82}Se, ^{150}Nd and ^{48}Ca. The first sample of 4 kg of ^{82}Se has already been enriched and is currently undergoing purification. The SuperNEMO collaboration is investigating the technical possibility of enriching large amounts of ^{150}Nd via the method of atomic vapor laser isotope separation. However, the collaboration has not ruled out other possible sources.

BiPo detector for ultra high radiopurity materials screening

SuperNEMO will search for a very rare process, therefore it must maintain ultra-low background levels. The source foils must be radiopure, and their contamination with naturally radioactive elements must be precisely measured. The most important source contaminants are ^{208}Tl and ^{214}Bi, whose decay energies are close to the neutrinoless signal region. SuperNEMO requires source foil contamination to be less than 2 μBq/kg for ^{208}Tl and less than 10 μBq/kg for ^{214}Bi.

BiPo is an auxiliary low background detector [18], specially designed for the measurement of ultra low radioactivity level in ^{208}Tl (^{232}Th chain) and ^{214}Bi (^{238}U chain) of SuperNEMO double beta source foils and more generally of thin materials (few tens of mg/cm^2). The idea of the measurement is shown in Fig. 13.10.

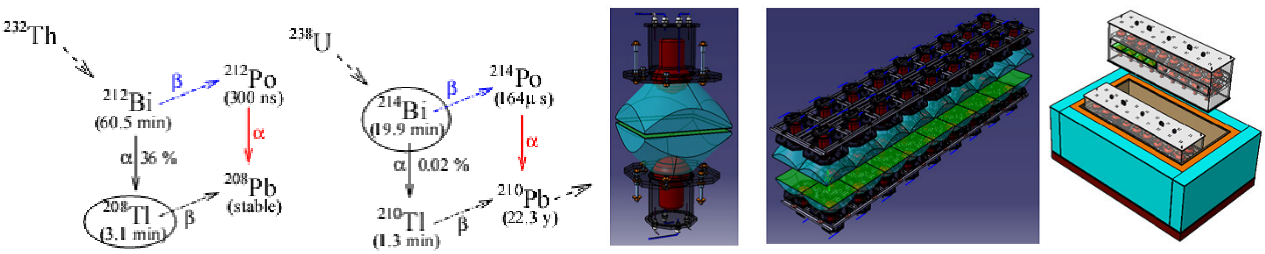

Figure 13.10: Idea of the BiPo ($\beta - \alpha$ delayed coincidences in $\sim 4\pi$ geometry).

Several versions of the detector were designed within the SuperNEMO collaboration, and finally the measurements of the first SuperNEMO samples have been started with BiPo-1,-2,-3 modules in Modane (France) and Canfranc (Spain). Ultra low activity in ^{208}Tl, of the order of 200 mBq/kg, has been observed with BiPo-3 for a special irradiated mylar, a candidate for the matrix for the SuperNEMO double beta source foils. It shows the high sensitivity of the BiPo-3 detector. Samples of thin PVA (**PolyVinyl Alcohol**) pads (100 μm thickness) are currently under measurement in the BiPo-3 detector (Fig. 13.11) since September 2013. PVA will be used to be mixed with ultra pure enriched Selenium powder to develop the SuperNEMO $\beta\beta$ sources foils. The goal is to validate the PVA radiopurity at a level of 20 mBq/kg in ^{208}Tl.

Figure 13.11: BiPo-3 detector in Canfranc (installing samples and outer shielding).

SuperNEMO calorimeter R&D

SuperNEMO aims to improve the calorimeter energy resolution to 7% FWHM @ 1 MeV (4 % @ the $Q_{\beta\beta}$ energy). To reach this goal, several ongoing studies are investigating the choice of calorimeter parameters such as scintillator material (organic plastic or liquid), and the shape, size and coating of calorimeter blocks. These are combined with dedicated development of PMTs with low radioactivity and high quantum efficiency (Fig. 13.12).

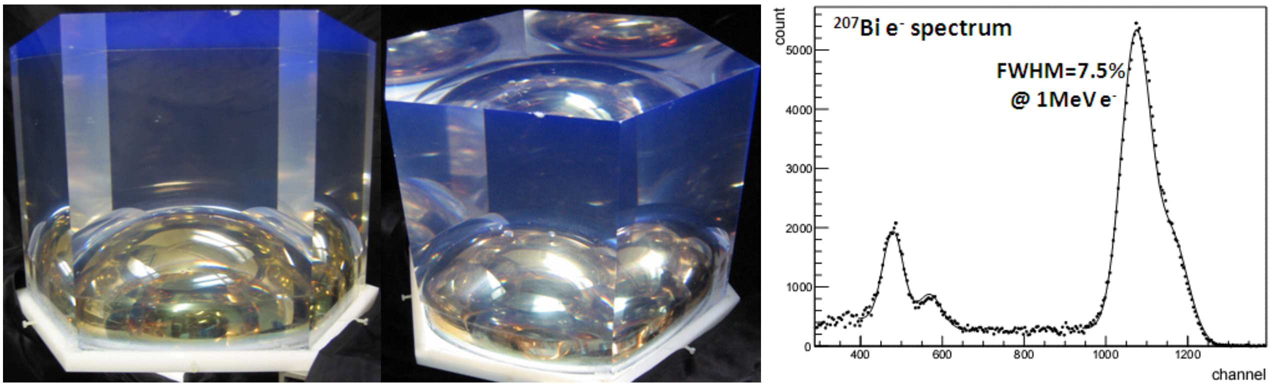

Figure 13.12: Square and hexagonal scintillator shape for SuperNEMO and their typical energy resolution measured with ^{207}Bi electron source.

SuperNEMO tracker R&D

The SuperNEMO tracker consists of octagonal wire drift cells operated in Geiger mode. Each cell is around 4 m long and has a central anode wire surrounded by 8–12 ground wires, with cathode pickup rings at both ends. Signals can be read out from the anode and/or cathodes to determine the position at which the ionizing particle crossed the cell.

The tracking detector design study looks at optimizing its parameters to obtain high efficiency and resolution in measuring the trajectories of $\beta\beta$-decay electrons, as well as of α-particles for the purpose of background rejection. The tracking chamber geometry is being investigated by means of detector simulations and comparison of the different possible layouts. In addition, several small prototypes have been built to study the drift chamber cell design and size, wire length, diameter and material, and gas mixture.

A SuperNEMO module will contain several thousand drift cells with 8–12 wires each. The large total number of wires requires an automated wiring procedure, thus a dedicated wiring robot is developed for the mass production of drift cells.

SuperNEMO conclusion

An extensive R&D program is underway to design the next-generation neutrinoless double beta decay experiment SuperNEMO. It will extrapolate the successful technique of calorimetry plus tracking of NEMO-3 to 100 kg of source isotope, aiming to reach a neutrino mass sensitivity of $\sim$ 50 meV in 2020. Due to its modular approach, SuperNEMO can start operation in stages.

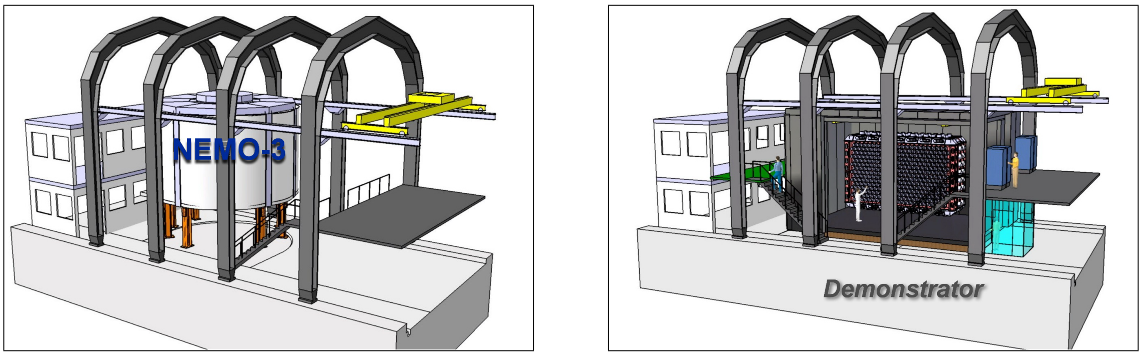

Figure 13.13: SuperNEMO Demonstrator will replace NEMO-3 in the existing LSM.

The first trial module of the future SuperNEMO detector (so-called Demonstrator) is being built now. In fact, it is as big as the previous NEMO-3 and will replace it in the existing LSM (Fig. 13.13) at the end of 2014 while all twenty modules will be running by 2017-2020 (Fig. 13.14).

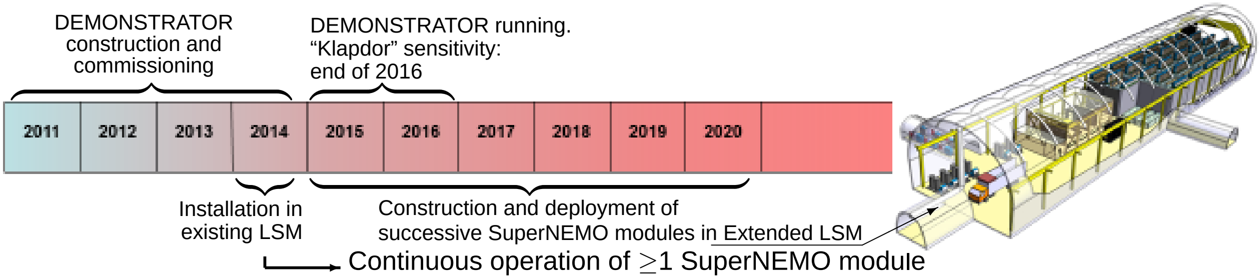

Figure 13.14: SuperNEMO schedule.

Neutrinoless double beta decay is powerful way of addressing the most fundamental particle physics questions including lepton number violation and the absolute scale of neutrino mass. Tracking based detectors offer a unique approach to the detection of the $\beta\beta$ process in which the topology of the decay is fully reconstructed.

Apart from producing a clear "smoking gun" signature of the process these detectors offer a superior background rejection capability. As such, they are complementary to pore calorimeter experiments such as GERDA, GUORE, SNO+. Moreover, as demonstrated by NEMO-3 and SuperNEMO, once the process is detected the measurement of the individual energies of the electrons emitted in the decay and the angular distribution between them may allow the underlying physics mechanism of $0\nu\beta\beta$-decay.

13.1.6 Contribution of JINR Members

- MC simulation of the SuperNEMO detector design, performance evaluation.
- Development of tracking software, $\beta\beta$-event selection criteria, background estimations.
- Development of databases, data acquisition, slow control, and data analysis software.
- Participation in the development and creation of the calorimeter and veto systems based on plastic scintillators.
- Development of calibration and monitoring system on the basis of radioactive sources produced in JINR.
- Conduction of low background measurements screening radioactive purity of enriched $\beta\beta$-decay sources and structural materials for the SuperNEMO Demonstrator with a big HPGe-detector (600 cm^3) delivered by JINR.
- Participation in the development and creation of the ultra low-background BiPo-3 spectrometer aimed to measure radiopurity of $\beta\beta$-decay source foils.
- Creation of the electromagnetic source of mono-energetic electrons for quality control of plastic scintillators used in the calorimeter and the veto system.

13.1.7 Publications, Theses and Conferences

As a result of the project the following

- papers has been published on NEMO-3 [9–15, 19–22],
- papers has been published on SuperNEMO [8, 18, 23],
- Theses defended: V.E.Kovalenko (PhD), "Study of the double beta decay of Mo-100 in the NEMO-3 experiment" (2006) and V.B.Brudanin (DPhil), "Experimental research of double beta-decay" (2001).
- talks given by JINR members at conferences: MEDEX09, MEDEX11, MEDEX13 (Prague, CZ), XX Rencontres de Blois, XXIV Rencontres de Blois (Blois, FR), EPS HEP 2009 (Krakow, PL);
  by other SuperNEMO collaboration members: IoP-2014, NOW-2010, TIPP-2011, TAUP-2011,-2013, Blois-2013, etc.

13.1.8 Finances

Major sources and amount of finances and major equipment acquired during the project runtime are listed in Tab. 13.3.

Project stage	Funding source	Obtained amount (k$)	Major equipment acquired Major equipment acquired
NEMO-2,3	JINR	1000	Scintillators, mechanics, etc.
(1991-2010)	1100	300	Travel expenses (LSM, Modane)
SuperNEMO	+	150	Trial scintillators for Demonstrator
(2005-2013)	extra-	20	Calibration r/a sources
	-budgetary	30	R&D of purification proc. for ^{82}Se
	funds	30/yr	Travel expenses (LSM, Modane)

Table 13.3: Major sources and amount of finances and major equipment acquired

References

[1] J. Suhonen and O. Civitarese. “Weak-interaction and nuclear-structure aspects of nuclear double beta decay”. In: *Phys.Rept.* 300 (1998), pp. 123–214.

[2] J. Suhonen and O. Civitarese. “Review of the properties of the $0\nu\beta\beta$ nuclear matrix elements”. In: *J.Phys.* G39 (2012), p. 124005.

[3] A. Faessler, V. Rodin, and F. Simkovic. “Nuclear matrix elements for neutrinoless double-beta decay and double-electron capture”. In: *J.Phys.* G39 (2012), p. 124006. arXiv: 1206.0464 [nucl-th].

[4] F. Simkovic et al. “$0\nu\beta\beta$ and $2\nu\beta\beta$ nuclear matrix elements, quasiparticle random-phase approximation, and isospin symmetry restoration”. In: *Phys.Rev.* C87.4 (2013), p. 045501. arXiv: 1302.1509 [nucl-th].

[5] D. Dassie et al. “Double beta decay prototype detector with multiwire drift tubes in the Geiger mode”. In: *Nucl.Instrum.Meth.* A309 (1991), pp. 465–475.

[6] R. Arnold et al. “Performance of a prototype tracking detector for double beta decay measurements”. In: *Nucl.Instrum.Meth.* A354 (1995), pp. 338–351.

[7] D. Dassie et al. “NEMO-3: A Detector to investigate the neutrino mass in the 0.1-eV range”. In: (1994).

[8] R. Arnold et al. “Probing New Physics Models of Neutrinoless Double Beta Decay with SuperNEMO”. In: *Eur.Phys.J.* C70 (2010), pp. 927–943. arXiv: 1005.1241 [hep-ex].

[9] R. Arnold, C. Augier, A.M. Bakalyarov, et al. "Technical design and performance of the NEMO 3 detector". In: *Nucl.Instrum.Meth.* A536 (2005), pp. 79–122. arXiv: physics/0402115 [physics].

[10] J. Argyriades et al. "Measurement of the background in the NEMO 3 double beta decay experiment". In: *Nucl.Instrum.Meth.* A606 (2009), pp. 449–465. arXiv: 0903.2277 [nucl-ex].

[11] R. Arnold et al. "First results of the search of neutrinoless double beta decay with the NEMO 3 detector". In: *Phys.Rev.Lett.* 95 (2005), p. 182302. arXiv: hep-ex/0507083 [hep-ex].

[12] V.I. Tretyak. "The NEMO-3 results after completion of data taking". In: *AIP Conf.Proc.* 1417 (Dec. 2011), pp. 125–128. url: %7Bhttp://www.osti.gov/scitech/servlets/purl/22003963%7D.

[13] J. Argyriades et al. "Measurement of the Double Beta Decay Half-life of Nd-150 and Search for Neutrinoless Decay Modes with the NEMO-3 Detector". In: *Phys.Rev.* C80 (2009), p. 032501. arXiv: 0810.0248 [hep-ex].

[14] J. Argyriades et al. "Measurement of the two neutrino double beta decay half-life of Zr-96 with the NEMO-3 detector". In: *Nucl.Phys.* A847 (2010), pp. 168–179. arXiv: 0906.2694 [nucl-ex].

[15] R. Arnold et al. "Measurement of the Double Beta Decay Half-life of ^{130}Te with the NEMO-3 Detector". In: *Phys.Rev.Lett.* 107 (2011), p. 062504. arXiv: 1104.3716 [nucl-ex].

[16] J Abad et al. "An estimation of the rates of (two-neutrino) double beta decay and related processes". In: *Journal de Physique Colloques* 45.C3 (1984), p. 9.

[17] F. Simkovic, P. Domin, and S.V. Semenov. "The Single state dominance hypothesis and the two neutrino double beta decay of Mo-100". In: *J.Phys.* G27 (2001), pp. 2233–2240. arXiv: nucl-th/0006084 [nucl-th].

[18] J. Argyriades et al. "Results of the BiPo-1 prototype for radiopurity measurements for the SuperNEMO double beta decay source foils". In: *Nucl.Instrum.Meth.* A622 (2010), pp. 120–128. arXiv: 1005.0343 [physics.ins-det].

[19] R. Arnold et al. "Measurement of double beta decay of Mo-100 to excited states in the NEMO 3 experiment". In: *Nucl.Phys.* A781 (2007), pp. 209–226. arXiv: hep-ex/0609058 [hep-ex].

[20] R. Arnold et al. "Limits on different Majoron decay modes of Mo-100 and Se-82 for neutrinoless double beta decays in the NEMO-3 experiment". In: *Nucl.Phys.* A765 (2006), pp. 483–494. arXiv: hep-ex/0601021 [hep-ex].

[21] R. Arnold et al. "Search for Neutrinoless Double-Beta Decay of ^{100}Mo with the NEMO-3 Detector". In: (2013). arXiv: 1311.5695 [hep-ex].

[22] R. Arnold et al. "Investigation of double beta decay of ^{100}Mo to excited states of ^{100}Ru". In: *Nucl.Phys.* A925 (2014), p. 25. arXiv: 1402.7196 [nucl-ex].

[23] J. Argyriades, R. Arnold, C. Augier, et al. "Spectral modeling of scintillator for the NEMO-3 and SuperNEMO detectors". In: *Nucl.Instrum.Meth.* A625 (2011), pp. 20–28. arXiv: 1004.3779 [physics.ins-det].

Chapter 14

EDELWEISS Experiment

Editors: E. Yakushev

Project Title

EDELWEISS, **E**xpérience pour **DE**tecter **L**es **W**imps **E**n **S**ite **S**outerrain.

JINR project title: EDELWEISS. A Search for Cold Dark Matter with Cryogenic Detectors at LSM Underground Laboratory.

Project Leaders

- EDELWEISS spokesman: J. Gaskon (IPNL, Lyon, France)
- JINR: E.A. Yakushev

Abstract

The EDELWEISS program searches for direct evidence of Dark Matter WIMPs from the Milky Way galaxy through their scattering of Ge nuclei within cryogenic Ge crystals. The EDELWEISS detectors are cryogenic (work temperature is about 20 mK) Ge bolometers with simultaneous measurement of phonon and ionization signals. The comparison of the two signals provides a highly efficient event-by-event discrimination between nuclear recoils (induced by WIMP and also by neutron scattering) and electrons. The minimal target of the experiment is to achieve sensitivity to an important class of SUSY models ("Focus Point") predicting the cross-section between a nucleon and a WIMP of the order of 10^{-44} cm^2, corresponding approximately to one collision per day per 500 kg of matter. EDELWEISS collaboration demonstrated that the main background limiting the sensitivity of the Ge based (and other) experiments arises from the inability to reject events occurring close to the surface of the detector, for which a deficient charge collection can mimic the ionization yield of nuclear recoils. Despite successes in reducing the surface contamination in EDELWEISS (mostly due to ^{210}Pb daughters), sensitivity levels were still limited to $5 \cdot 10^{-43}$ cm^2.

Therefore detectors for EDELWEISS were developed with an innovative interleaved electrode design (ID detectors), able to discriminate against events occurring within 1 mm from the detector surface. The FID800 detector's technology developed in the experiment in 2012–2013 (Fully InterDigitized 800 grams detectors) shows unprecedented and world-leading improvement of surface background suppression. New 800 g FID detectors added progressively to the experiment to enhance the sensitivity to WIMPs. The aim is to reach, by 2016, the sensitivity on the $4 \cdot 10^{-45}$ cm^2 level in successful competition with other world-leading dark matter search experiments.

keywords: Dark matter, direct WIMP search, Cryogenic Ge detectors, Background radiation, Underground physics

Project Members From JINR

V. Brudanin, A. Lubashevskiy, D. Filosofov, S. Rozov, E. Shevchik, L. Perevoshchikov, Yu. Gurov, E. Yakushev

Project Duration. Approval Date(s)

The first stage of the EDELWEISS program (without JINR participation)	2000-2003
Approval of JINR participation in the EDELWEISS project.	November 13-14, 2006
Prolongation of the project for 2009–2013 has been approved	June 22-23, 2009
Prolongation of the project for 2013–1015	January 2012
EDELWEISS-I, $\sigma_{\mathrm{SI}} = 2 \cdot 10^{-42}$ cm^2	2002
EDELWEISS-II, Ge bolometers of traditional design, $\sigma_{\mathrm{SI}} = 5 \cdot 10^{-43}$ cm^2	2008
EDELWEISS-II innovated HPGe detectors with interleaved electrodes, $\sigma_{\mathrm{SI}} = 4.4 \cdot 10^{-44}$ cm^2	2009-2012
EDELWEISS-III commissioning	2012-2013
EDELWEISS-III, 3000 kg d, $\sigma_{\mathrm{SI}} = 5 \cdot 10^{-45}$ cm^2	2014
EDELWEISS-III, 12000 kg d, $\sigma_{\mathrm{SI}} < 1 \cdot 10^{-45}$ cm^2	2017

List of Participating Countries and Institutions

CEA, Centre d'Etudes Saclay, IRFU, 91191 Gif-Sur-Yvette Cedex, France; CEA, Centre d'Etudes Saclay, IRAMIS, 91191 Gif-Sur-Yvette Cedex, France; CNRS-Néel, 25 Avenue des Martyrs,38042 Grenoble cedex 9, France; CSNSM, Université Paris-Sud, IN2P3-CNRS, bat 108, 91405 Orsay, France; IPNL, Université de Lyon, Université Lyon 1, CNRS/IN2P3, 4 rue E. Fermi 69622 Villeurbanne cedex, France; Karlsruhe Institute of Technology, Institut für Prozessdatenverarbeitung und Elektronik, 76021 Karlsruhe, Germany; Karlsruhe Institute of Technology, Institut für Experimentelle Kernphysik, 76128 Karlsruhe, Germany; Karlsruhe Institute of Technology, Institut für Kernphysik, 76021 Karlsruhe, Germany; Laboratoire Souterrain de Modane, CEA-CNRS, 1125 route de Bardonnèche, 73500 Modane,

France; Laboratory of Nuclear Problems, JINR, Joliot-Curie 6, 41980 Dubna, Moscow region, Russia; University of Oxford, Department of Physics, Keble Road, Oxford OX1 3RH, UK; Department of Physics and Astronomy, University of Sheffield, Hounsfield Road, Sheffield S3 7RH, UK

Figure 14.1: EDELWEISS collaboration (April, 2014).

14.1 Project Description

14.1.1 Fundamental Scientific Problem Addressed by the Project

Experimental data on the cosmic microwave background, combined with other astronomical and astrophysical data, have significantly improved the precision of the fundamental parameters in the cosmological model [1]. As the precision of cosmological and astronomical observations improves, there are stronger indications that the mass of galaxies and clusters consists mostly of dark matter [2–4], an unknown form of matter that neither emits nor absorbs electromagnetic radiation. At the same time, it is very intriguing that the most favored solution to the problem of hierarchy in particle physics, Supersymmetry (**SUSY**), predicts very naturally that the Universe is filled with weakly interacting massive particles (**WIMPs**). In a large range of parameters of SUSY models, the predicted WIMP density matches what is required from cosmological observations. The prospect of discovering SUSY particles at the LHC is thus very exciting. However, a key element to confirm that WIMPs are indeed present in our Galactic halo would be to observe the nuclear recoils arising from the rare collisions of these particles with atoms in the laboratory. This is the fundamental scientific problem addressed by the EDELWEISS project. Thus conducting EDELWEISS experiment with participation from JINR naturally extends our experimental programs in CERN. At the same time, to actively participate in the dark matter search experiment, JINR will apply accumulated experience in low background studies mainly connected with neutrino physics. This will prove useful as the main constraints for dark matter search experiments are the extremely low event rates, below 1 event per day per

100 kg of matter, and tiny WIMP-deposited energy, below of 100 keV. Therefore a successful experiment must overcome these experimental challenges, which are similar to those of neutrino related experiments. Direct dark matter search experiments must have sufficient target mass coupled with long and stable data acquisition. Detectors must have a good energy resolution and low threshold. And, especially, reduction of background is critically important. The EDELWEISS experiment address all these experimental challenges using several innovative techniques, as described in subsequent sections.

14.1.2 Specific Project Objectives and Expected Results

The direct observation of the interaction of WIMPs in a terrestrial detector would be of tremendous importance to particle physics and cosmology. WIMPs are expected to interact with ordinary matter. A process that can be used for WIMP detection is its elastic scattering off nuclei. Inelastic scattering could also be used in principle, as could scattering of electrons, but the rate of these processes are expected to be (much) smaller. Dozens of experiments worldwide, too numerous to be listed in this white book, are using, or plan to use, elastic scattering to search for neutralino dark matter, or WIMP dark matter in general. The small expected detection rate, and the necessity of suppressing any ionizing radiation passing through the detector, are reasons to shelter these experiments from cosmic rays, e.g. by placing them in mines or underground laboratories. Generally, with the notable exception, only the energy deposited in the detector during the elastic scattering can be measured. This energy is of the order of a few keV for typical WIMP masses and speeds in the galactic halo. The kinetic energy of the recoiling nucleus is converted partly into scintillation light or ionization energy (giving an electric current) and partly into thermal energy (heating up the detector). In cryogenic detectors (the EDELWEISS and similar), a simultaneous measurement of both ionization and thermal energy allows the discrimination of nuclear recoils from electrons produced in radioactive decays or otherwise. This discrimination, however, cannot distinguish whether the nuclear recoil was caused by a WIMP or an ambient neutron. The detector needs to be cooled to a temperature significantly below that of liquid helium so that its low heat capacity converts a small deposited energy into a large temperature increase.

In the early 1980s, a number of groups began researching cryogenic detectors, operating in the milliKelvin temperature range, for applications in neutrino physics and dark matter searches. After over two decades of development, the technique has matured and there are numerous science results that have been obtained with cryogenic detectors. These results cover a wide range of topics: contributions to x-ray astronomy, the spectrometry of heavy biomolecules, the detection of extremely rare events (e.g., neutrino-less double beta decay), and several dark matter results. The main reason for beginning an intense technology development program more than twenty years ago was the clearly identified need for lower energy threshold and better energy resolution in massive detectors for rare event searches. Cryogenic detectors were, and are, considered to be a most promising technique, requiring only milli-eV for producing a countable information carrier, compared with $\sim$3 eV for semiconductor detectors and in the region of $\sim$100 eV for scintillators. For large Ge absorbers of a few hundred grams, energy resolutions of the order ∼100 eV with thresholds around 1 keV and below have been demonstrated. Although good energy resolution may not appear to be a top priority for measuring the largely featureless energy spectra of WIMP induced nuclear recoil, it is rather important for identifying backgrounds. As there will always be some form of background, especially when measurement periods have to be at the scale of many months or years, its identification is of paramount importance for a dark matter experiment, which aims to discover WIMP interactions.

A further important issue is scalability. Cryogenic detectors can be scaled to large masses relatively easily. Individual modules have already been developed and optimized; scaling up merely requires the production of more modules and a larger cold space in a dilution refrigerator.

The EDELWEISS experiment is dedicated to the search for non-baryonic cold dark matter in the form of WIMPs. The direct detection principle consists of the measurement of the energy released by nuclear recoils produced in an ordinary matter target (Ge) by elastic collisions of WIMPs from the Milky Way galaxy. The EDELWEISS detectors are cryogenic (work temperature is ∼20 mK) Ge bolometers with simultaneous measurement of phonon and ionization signals as shown in Fig. 14.2. The comparison of the two signals provides a highly efficient event-by-event discrimination between nuclear recoils (induced by WIMP and also by neutron scattering) and electrons.

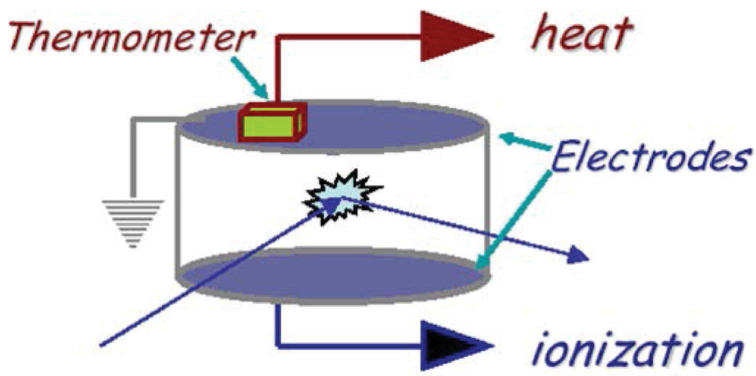

Figure 14.2: Scheme of EDELWEISS detection principle of a heat and ionization detector.

In first stages of EDELWEISS it has been found that main limitation of ”classical” detectors arises from incomplete charge collection for near surface events. To reach required sensitivities for the cross-section of interest for SUSY Models (10^{-44} cm^2) it was necessary to improve the rejection capabilities of the detectors in parallel with the active mass. For this purpose, EDELWEISS developed new detectors with an innovative interleaved electrodes design with active rejection of near surface events: the so called ID detectors.

During all stages of the EDELWEISS experiment, the collaboration continued worked in 2 main directions: accumulation of statistic with already build bolometers and testing and calibration of newly developed detectors which allowed further active rejection of different backgrounds. Until recently the main results from the EDELWEISS experiment were collected with 10 ID detectors (each with mass about 400 g). In the fourteen-month running period, data from the detectors were collected for 85% of the time, the rest being equally shared between regular maintenance operations (detector regenerations and cryogenic fluid refills) and unscheduled stops. The data set consists of the digitized pulse shapes of all channels of the detectors. An event is recorded each time the heat signal on any detector in the tower crosses an online trigger level. The data were analyzed offline by two independent analysis chains. An average FWHM baseline resolution is 1.2 keV for the heat signals and 0.9 keV for the fiducial ionization signals. The initial WIMP search data set comprises a total of 325 days for the ten detectors plus 92 days for two ID detectors in the early commissioning run. For the WIMP search, coincident events between two bolometers, or with a trigger in the muon veto within an appropriate time window are rejected. The final exposure of 427 kg d is calculated from the selected live-time and the effective fiducial mass of 160 g. WIMP candidates are then selected in the 1.64σ nuclear recoil band. This results in an effective exposure of 384 kg d.

Observed distributions: Fig. 14.3 shows the scatter-plot of ionization yield as a function of recoil energy for the WIMP search data over all detectors. The red band represents the

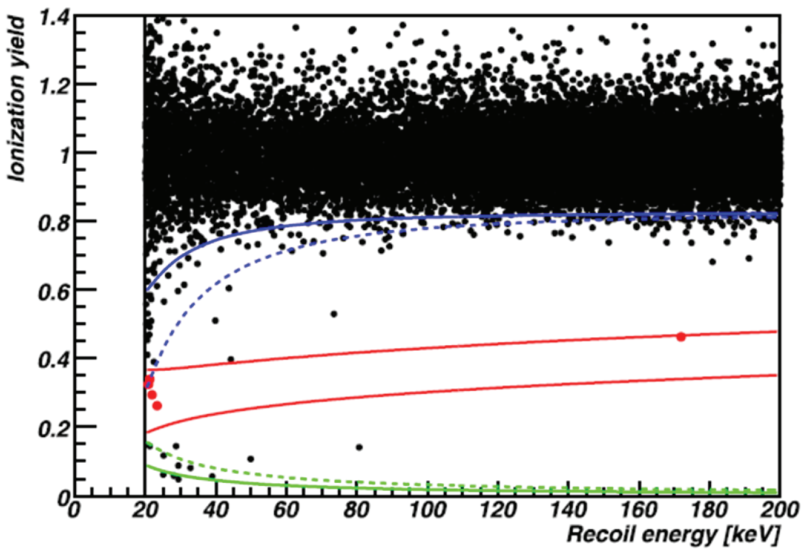

Figure 14.3: Ionization yield vs recoil energy of fiducial events recorded by EDELWEISS-II in an exposure of 427 kg d. The WIMP search region is defined by recoil energies between 20 and 200 keV, and an ionization yield inside the 90% acceptance band (full red lines, corresponding to an effective exposure of 384 kg d). WIMP candidates are highlighted in red. The average (resp. worst) one-sided 99.99% rejection limits for electron recoils are represented with a continuous (resp. dashed) blue line. The average (resp. worst) ionization thresholds are represented with a continuous (resp.dashed) green line.

average nuclear recoil for the ten detectors. In the recoil energy range from 20 to 200 keV, a total of $1.8 \cdot 10^4$ fiducial events are identified. The rate in the energy range from 20 to 50 keV is 0.14 events/keV/kg/day.

The observed signal has been compared with the background estimates: The potential sources of background in the WIMP search region were estimated using both calibration data, simulations, and the measured backgrounds outside the nuclear recoil band. Three potential sources are considered: γ-rays, surface events and neutron scattering.

The two main sources of γ-rays are the continuous background between 20 and 200 keV ($1.8 \cdot 10^4$ in the WIMP search data) and the cosmogenic activation doublet at $\sim$10 keV ($1 \cdot 10^4$ events). Gaussian fluctuations of the ionization and heat measurement cannot account for the presence of events inside the nuclear recoil band above 20 keV. In particular, assuming that the four observed events below 24 keV are due to a 10.4 keV γ-ray requires fluctuations by 7–12 σ on the fiducial ionization signals, depending on the event. Non-Gaussian fluctuations may be more important, for example those associated with events involving an interaction near the surface of the guard region where the charge is not well collected. But such fluctuations are difficult to predict with precision in a model-independent way. However, an empirical estimation can be obtained using the results of the ^{133}Ba γ-calibration, where a background of $3 \cdot 10^{-5}$ NR candidates per fiducial photon was observed. As the spectrum between 20 and 200 keV is very similar in ^{133}Ba calibration and WIMP search runs, it can be expected that the same process would proportionally yield a background of less than 0.9 events in the NR band at 90% CL.

The predicted number of unrejected surface events is estimated by multiplying the number of observed low-ionization yield events before the rejection of surface events ($\sim$5000) by the upper limit on the measured rejection rate ($6 \cdot 10^{-5}$ at 90% CL). This results in 0.3 events. A deficient suppression of events due to surface β-contaminants is thus an unlikely explanation for the events observed in the nuclear recoil band.

As another source of surface events, alpha radioactivity is estimated to generate a negligible leakage from calibration measurements with alpha sources.

The muon veto efficiency was measured using two different methods, one from internal coincidences within the veto, and the other using bolometer-veto coincidences. The measured efficiency to veto a muon entering the cryostat is compatible with 100%, being larger than 92.8% at 90% CL. The observation of 260 coincidences between the bolometers and the muon veto before any fiducial, energy or ionization yield cuts corresponds to an average rate of muon-induced events of 0.17 ± 0.01 events per kg d. Of these, 0.008 ± 0.004 events per kg d appear as single events in the NR band above 20 keV. Scaling this number to the exposure of the WIMP search data and considering the lower limit on the muon veto efficiency measurement, this corresponds to an expected background of less than 0.4 events at 90% CL in the WIMP search.

The contribution of neutrons from radioactive decays in the rock and concrete surrounding the experiment and the lead shield has been improved with more reliable GEANT4 simulations. The simulation of the effect of the polyethylene shield on an external neutron flux was tested by comparison with data recorded with a strong neutron source (10^5 s^{-1}) positioned at different locations around the experiment outside the shields. Following this work, the upper limit on the number of nuclear recoil events due to the flux of neutrons going through the polyethylene shield is 0.11. The contribution from neutron sources inside the polyethylene shield has been calculated following measurements of the U/Th contents of relevant materials, and the study of additional sources. The summed upper limit of the contributions from the contamination of the lead and polyethylene shields and their steel supports, as well as the copper cryostat itself, is 0.21 events.

A potentially more important neutron source has been identified as the connectors and cables located inside the cryostat, which could induce up to 1.1 nuclear recoil events. Summing all the 90% CL upper limits from the different sources, we arrive at an estimated background of less than 3.0 events in 384 kg d. The Poisson probability to fluctuate from 3 to 5 events or more is 18%. Interpreted as a central value, the background estimate indicates no evidence for WIMP events. However, in terms of understanding the nature of the observed background, the observation of 5 events indicates that the well quantified part of our background model, corresponding to at most 3 events, fails to explain the data. Given the small number of observed events, the data distributions in energy and ionization yield do not help confirm or infirm the validity of part or all of the background model. The statistics of the additional sample of events where more than one detector triggered in coincidence is not sufficient to yield useful information on the nature of the background.

Elastic cross-section: The 90% CL upper limits on the WIMP-nucleon spin-independent (SI) cross-section derived from the present data are shown as a function of the WIMP mass in Fig. 14.4. A cross-section of $4.4 \cdot 10^{-44}$ cm^2 is excluded at 90% CL for a WIMP mass of

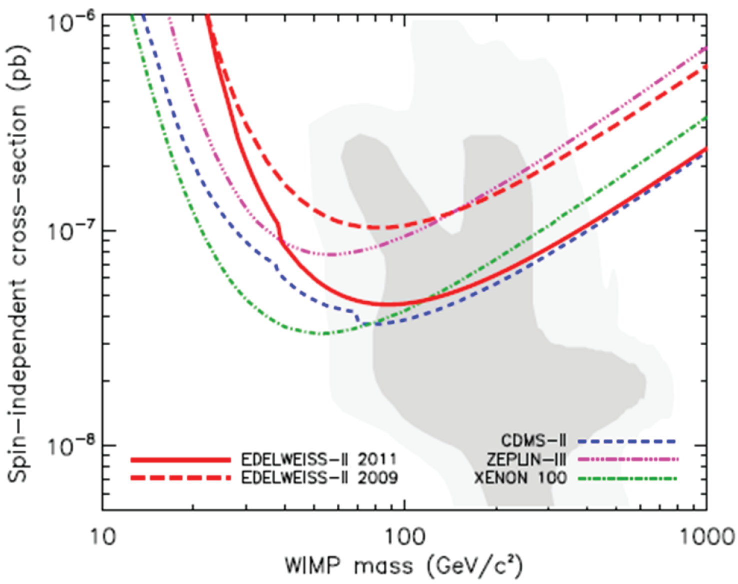

Figure 14.4: Limits on the cross-section for spin-independent scattering of WIMPs on the nucleon as a function of WIMP mass, derived from the present work, together with the limits (on the moment of the publication of the results) from CDMS [5], ZEPLIN [6] and XENON100 [7]. The shaded area correspond to the 68% and 95% probability regions of the cMSSM scan from Ref. [8].

85 GeV/c^2. At higher WIMP masses the sensitivity becomes comparable to that of the our main competitor — the CDMS experiment.

Inelastic cross-section: The inelastic dark matter scenario has been proposed to reconcile the dark matter modulation signal claimed by DAMA/LIBRA and the null results in other direct detection experiments. Fig. 14.5 shows the limit obtained for a mass splitting $\delta = 120$ keV. Our limit excludes the DAMA region above ~90 GeV/c^2, improving by ~10 GeV/c^2 the CDMS limit of Ref. [9]. For WIMP masses larger than ~200 GeV/c^2, EDELWEISS excludes cross-section values that are half of those excluded by CDMS. This is due, in large part, to the absence of WIMP candidates in the energy range between 23.2 keV and 172 keV, whereas CDMS observes three events in that same range.

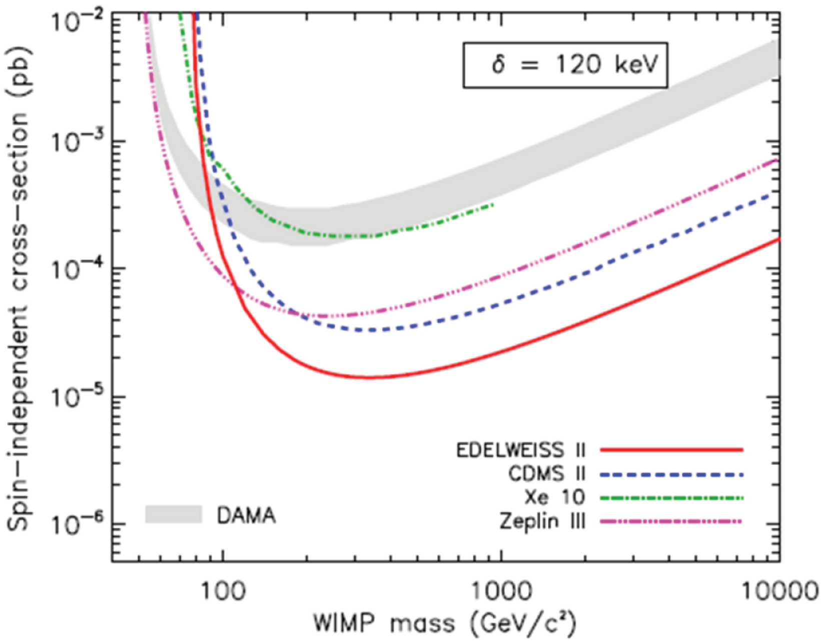

Figure 14.5: Inelastic WIMP-nucleon cross-section limits at 90% CL as a function of WIMP mass, for a mass splitting value $\delta = 120$ keV. Also shown are the limits from XENON10 [10], ZEPLIN-III [11] and CDMS [9] (from a dedicated analysis). The 95% allowed DAMA contour, as estimated in [9] from [12], is shown in light gray.

Combined limit with CDMS: The use of the same target material allowed the CDMS and EDELWEISS collaborations to combine their direct dark matter search results. A straightforward method of combination was chosen for its simplicity before data were exchanged between the experiments. The total data set represents 614 kg d equivalent exposure. The upper limit on the WIMP-nucleon spin-independent cross-section is derived: a cross section of $3.3 \cdot 10^{-44}$ cm^2 is excluded at 90% C.L. for a WIMP mass of 90 GeV/c^2 where this analysis is most sensitive (Fig. 14.6). At higher WIMP masses the combination improves the individual limits, by a factor 1.6 above 700 GeV/c^2.

Low mass WIMP search: In 2012 EDELWEISS has extended its WIMP search from the traditional region (~100 GeV/c^2) to the so-called low mass WIMP region (~10 GeV/c^2). The result obtained by EDELWEISS is depicted in Fig. 14.7. For WIMPs of mass 10 GeV/c^2,

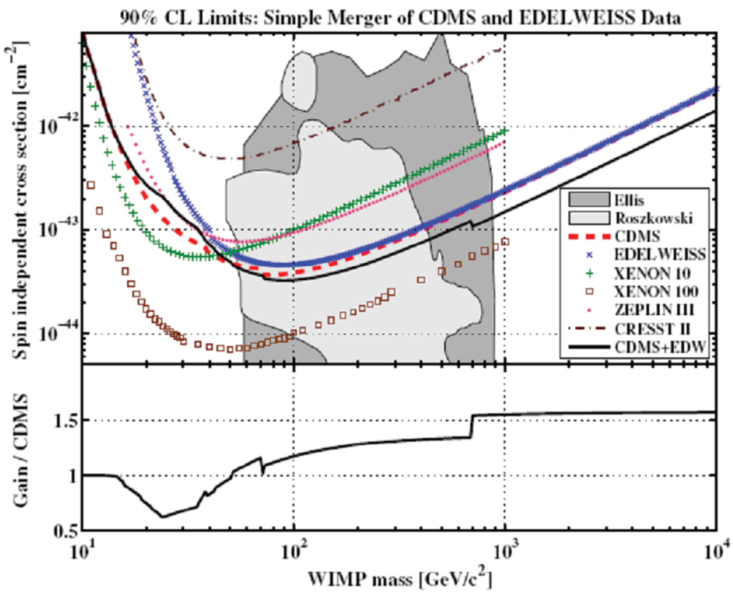

Figure 14.6: Top: 90% C.L. optimum interval upper limits on spin-independent WIMP couplings to nucleons as a function of WIMP mass, from the individual CDMS (red dashes) and EDELWEISS (EDW, blue crosses) experiments, and from their simple merger (continuous black line). Also represented are latest limits from the XENON100 (brown boxes), XENON10 [10] (green crosses), CRESST-II(brown dot-dashed line) and ZEPLIN-III [6] (pink dots) experiments, and supersymmetric parameter-space predictions [8, 13] (filled gray regions). Bottom: gain obtained from the combination with respect to individual limits of CDMS and EDELWEISS. Below masses of 50 GeV/c^2, the combined limit is weaker than the best individual one; at higher masses, the gain is up to a factor 1.57.

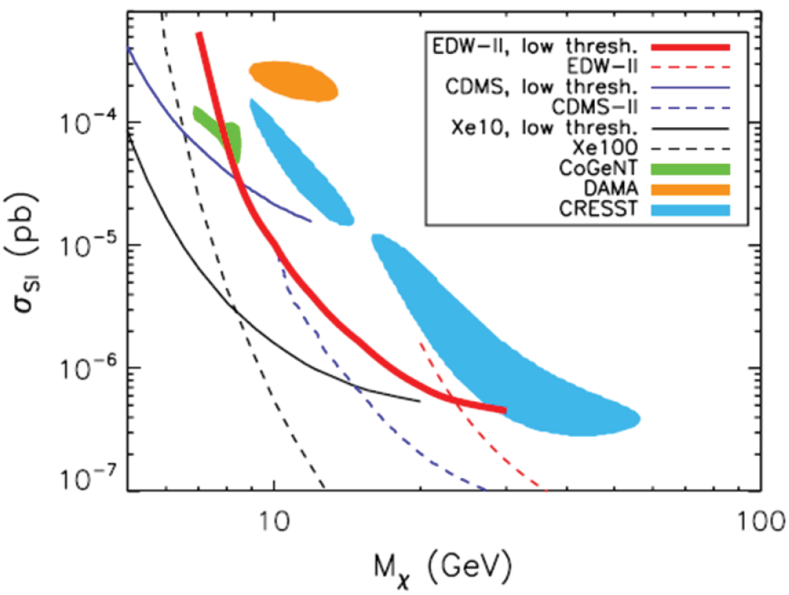

Figure 14.7: 90% C.L. Poisson limit on $\sigma_{\rm SI}$ as a function of WIMP mass derived from the analysis of the four EDELWEISS bolometers (bold red line).

the observation of one event in the WIMP search region results in a 90% C.L. limit of $1.0 \cdot 10^{-41}$ cm^2 on the spin-independent WIMP-nucleon scattering cross-section, which constrains the parameter space associated with the findings reported by the CoGeNT, DAMA and CRESST experiments.

Search for Axions: Due to the extremely low background level achieved in the experiment a highly sensitive search for axion signals was performed in 2003. The result is demonstrated in Fig. 14.8.

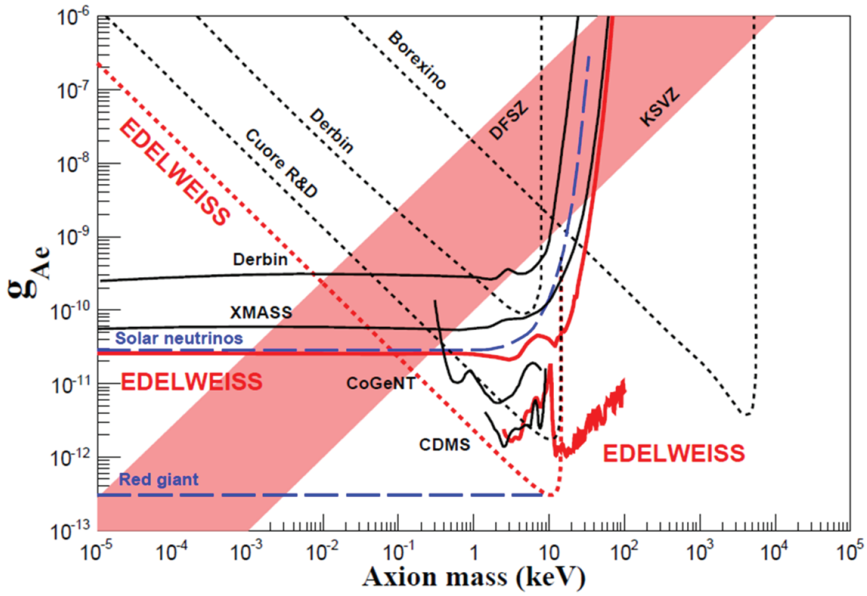

Figure 14.8: Summary of the constraints obtained by EDELWEISS on the g_{Ae} axion coupling as a function of m_A. The EDELWEISS limits are in red. See more details in [14].

Towards $\sigma_{SI} = 10^{-45}$ cm^2 sensitivity: To go beyond the achieved performance, EDELWEISS required a number of improvements in the setup and detector performance. At the new stage of the experiment (phase EDELWEISS-III), the aim of the project is, at a minimum, an order of magnitude improvement of the sensitivity. For this, increasing of the statistics tenfold to over 3000 kg days requires essential suppression of the expected background index. From our data it's clear that for the success of EDELWEISS-III, the neutron background associated with residual radioactivity of electronics, connectors and the cables located on the cryostat inside of the shield must be decreased by an order of magnitude at a minimum. Another potential source of unwelcome background has been detected in intensive γ-calibrations and appear to be connected with bulk events in the intermediate electric field region defined by main and guard electrodes. To address this problem, and further reduce surface background, a new generation of detectors with interleaved electrodes also covering the lateral surfaces of the crystal have been developed: the fully interdigitized (FID800) bolometers (Figs. 14.9).

With twice the mass (800 g) and better volume-to-surface ratio, FID800 detectors exhibit a fiducial mass of $\sim$600 g, much increased from the $\sim$160 g of ID400 detectors. Further

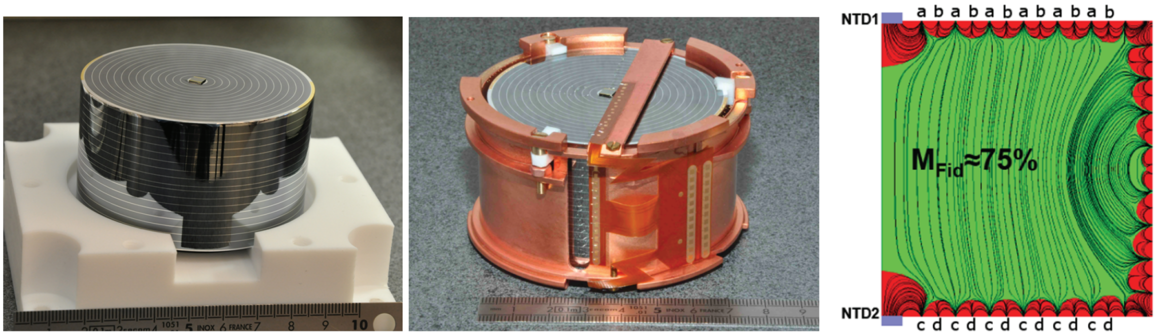

Figure 14.9: Photos of FID800 detector without (left) and with holder (center). Right: Calculations performed for the new FID800 detector show the improved fiducial volume of 75%, which is defined by the electrical field lines.

benefit comes from using two, rather than one, NTD sensors for phonon measurements and new surface treatments to improve further on the rejection efficiency of near surface events. A set of four FID800 detectors have been successfully tested at LSM in 2011 and, for example, 411663 gammas were detected as fiducial events during a ^{133}Ba calibration while all near surface events were rejected resulting in an empty nuclear recoil band Fig. 14.10.

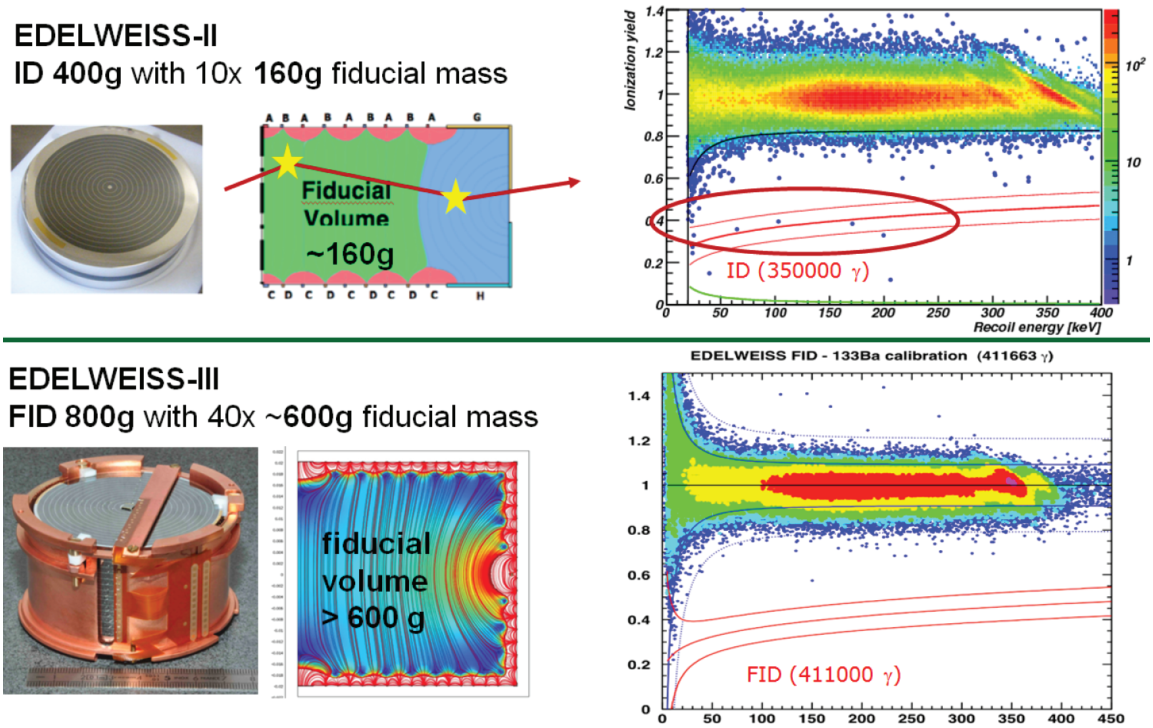

Figure 14.10: Comparison of ID400 and new FID800 EDELWEISS detectors.

In the upgraded EDELWEISS setup 36 FID800 detectors with cumulative fiducial mass 22 kg were installed in February 2014 (Fig. 14.11). The upgrade implies improved cryogenics, new cabling, installation of additional polyethelyne shielding between the lead layer and the cryostat, supplementary muon veto modules, use of the new integrated DAQ and electronics, e.g. implementation of fast ionization channel with 40 MS/s. The next goal of the project consists of an exposure of 3000 kg day to reach a WIMP-nucleon scattering cross-section sensitivity of better than $5 \cdot 10^{-45}$ cm^2. The further development continues towards improvement of read-outs and detectors and will also profit from more cryogenic test stands becoming available in laboratories. The detector R&D on longer term aims to reach a few 100 eV thresholds on both ionization and heat channels while on shorter term use a heat-only detector with the threshold of 2 keV to probe low-mass WIMPs. The ongoing research, together with the detailed studies of the background conditions in LSM, in particular, muon-induced neutrons, establishes a good base for next generation dark matter experiments, EURECA, a 1-ton cryogenic detector array.

Figure 14.11: Left: 36 FID800 detectors installed in EDELWEISS cryostat. Right: The EDELWEISS FID800 detectors.

Milestones during current stage of the EDELWEISS project are :

- 2012 : Building and testing of 24 HPGe crystals, delivery of the crystals to CSNSM (accomplished).
- Spring 2012 – Autumn 2013 : Delivery (production) of FID800 detectors (accomplished).
- 2012–2013: Delivery of the upgrades (cryogenics, wiring, electronics, internal shield) (accomplished).

- 2013–2014: Installation of detectors (accomplished).
- 2013–2014: Installation of wiring & new electronics boxes (partly accomplished).
- 2013: Installation of internal shield (partly accomplished).
- 2012-2013: Upgrade of cryogenics (partly accomplished).
- 2013 : Tests FID800 detectors at the underground site (accomplished).
- May 2014 : Start data taking.
- End of 2014 : More than 3000 kg day statistics will be delivered with FID800.
  – 22 kg fiducial mass (all detectors installed)
  – If no events $< 5 \cdot 10^{-45}$ cm^2
- 2015-2017 : Accumulation of data with all detectors (up to 12000 kg day ($< 10^{-45}$ cm^2), potential of WIMP discovery, search for the seasonal variations, preparation to EURECA experiment.

Figure 14.12 shows results that the EDELWEISS experiment is expected to achieve with the present setup.

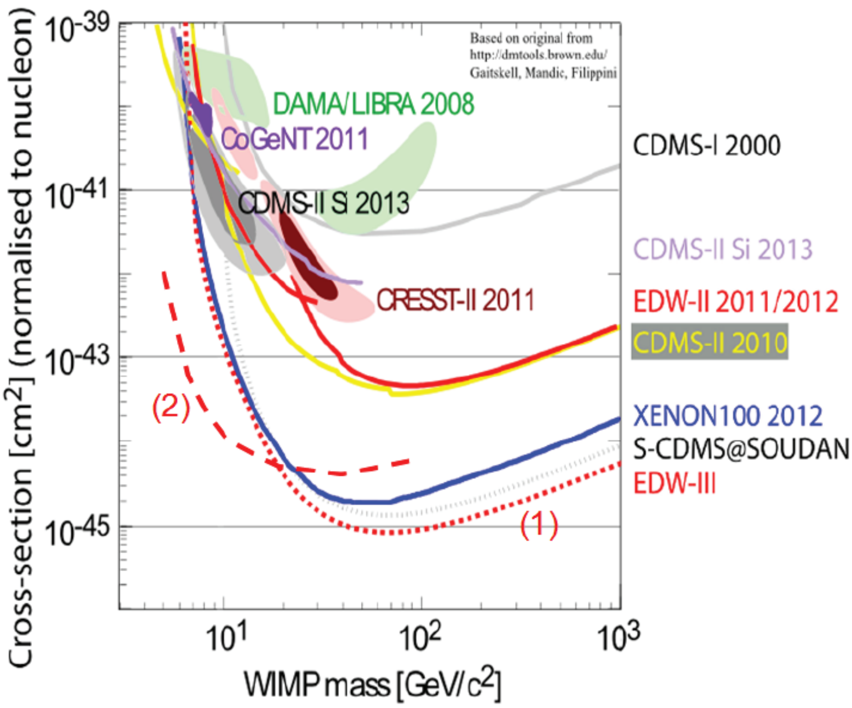

Figure 14.12: Expected results of EDELWEISS after accumulation of 12000 kg day of data. (1) corresponds to ”Standard” WIMP: $E_{\mathrm{R}} > 15$ keV, no events; (2) corresponds to Low-mass WIMP: 1200 kg day with 4 FID800 working in a special mode with HEMT allowing 300 eV FWHM and $E_{\mathrm{R}} > 3$ keV.

14.1.3 Detector Description and Basic Methods Used in the Project

The heart of the EDELWEISS experiment is ^{3}He-^{4}He dilution cryostat with HPGe detectors-bollometeres. The EDELWEISS experimental setup (Fig. 14.13) is located in the Laboratoire Souterrain de Modane (LSM) in the Frejus tunnel connecting France and Italy, under 1800 m of rock overburden (~4700 m.w.e.). In the laboratory, the resulting muon flux is 4 $\mu/\mathrm{m}^2/\mathrm{day}$ (10^6 times less than at see level), and the fast neutron flux has order $\sim 10^{-6}$ cm^2/s. The EDELWEISS shielding concept includes the surrounding of detectors by 20 cm of Pb (include internal layer from archaeological roman lead), 50 cm of polyethylene and active μ-veto (100 m^2 of plastic scintillator panels). When the shields are closed the cryostat environment is supplied with 9 l/min flux of radon-free air. The dilution cryostat setup with all shielding is located in an air-tight and pressurized clean room of class 1000. To reduce microphone noise due vibrations the cryostat is located on a pneumatic suspension. The radioactivity levels of all construction materials were tested prior to their use.

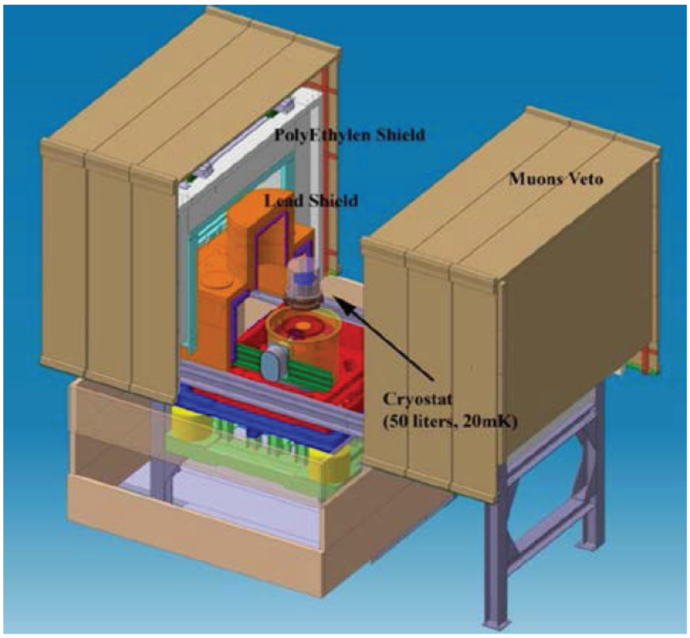

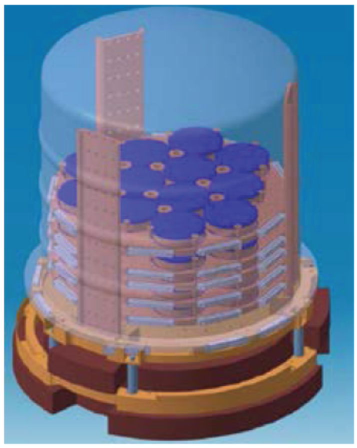

Figure 14.13: Scheme of EDELWEISS setup. Left picture shows whole setup, including detectors in dilution cryostat and shields; right picture is a zoom of detector tower.

In the first years of the EDELWEISS experiment it was found that main limitation of ”classical” detectors arises from incomplete charge collection for near surface events. To reach sensitivities to the cross-section of interest for SUSY Models (10^{-44} cm^2) it was necessary to improve the rejection capabilities of the detectors in parallel with the active mass. For this purpose, the EDELWEISS collaboration developed new detectors with an innovative interleaved electrode design with active rejection of near surface events: the so called ID detectors.

The principle of the ID detector is the following: the concentric electrodes are alternatively polarized with potential as, e.g., given in Fig. 14.14 (left part). In the bulk of the detector, the field lines are vertical and all the charges are collected on the A and C electrodes. On the top and bottom surfaces, the field lines are roughly parallel to the surface and the charge is collected on either A and B, or C and D. Thus, the rejection of events with a signal on either the A or C electrode (or C and D) effectively removes all interaction occurring at depths of less than 1 mm below the detector surface.

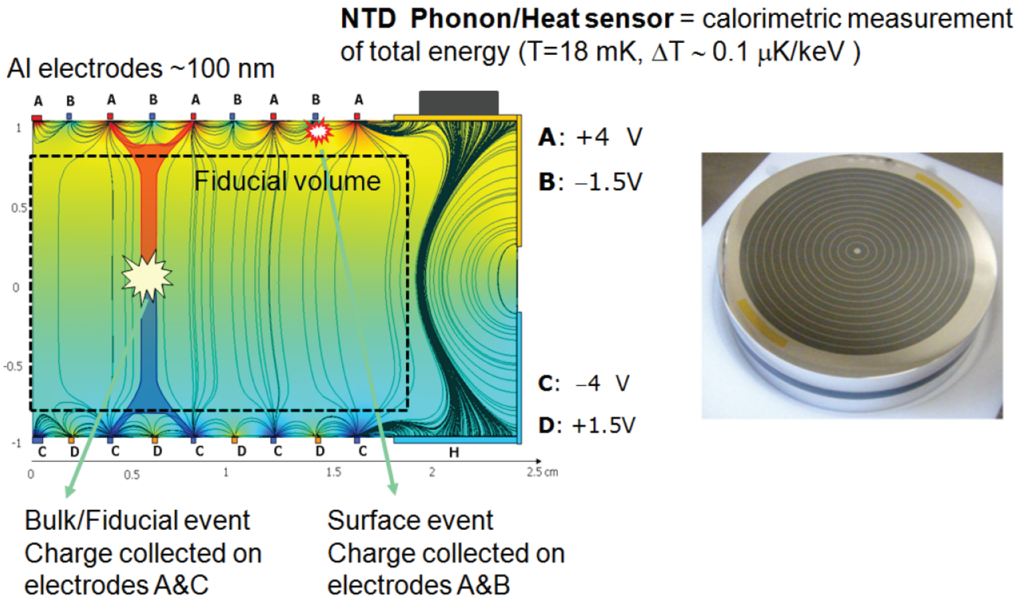

Figure 14.14: 400 grams detector with interleaved electrode scheme (right) and it cross section (left). Fiducial volume defined by applying potentials of $+4$, -1.5, , -4, $+1.5$ V on the A, B, C and D electrodes, respectively.

Detector calibration is performed in the follow way:

Fiducial volume: The fraction of the detector volume associated with the fiducial selection is measured by using the rate of events in the photopeaks at 9.0 and 10.4 keV due to the decay of the cosmogenically induced isotopes ^{65}Zn and ^{68}Ge, expected to be homogeneously distributed in the crystal. The exposure-weighted average fiducial mass is 160±5 g. Nuclear recoil selection: Neutron calibrations were performed at the beginning and end of the fourteen month-long run. The ionization yield distribution of all fiducial events recorded during these calibrations is shown on Fig. 14.15. Gamma-ray rejection: The rejection factor for electron recoils in the NR band was measured with extensive and regular γ-ray calibrations using ^{133}Ba sources. The scatter plot of the measured ionization yield as a function of recoil energy for all calibration data is shown on Fig. 14.16. For the second phase of EDELWEISS this results in a measured rejection factor of $(3 \pm 1) \cdot 10^{-5}$.

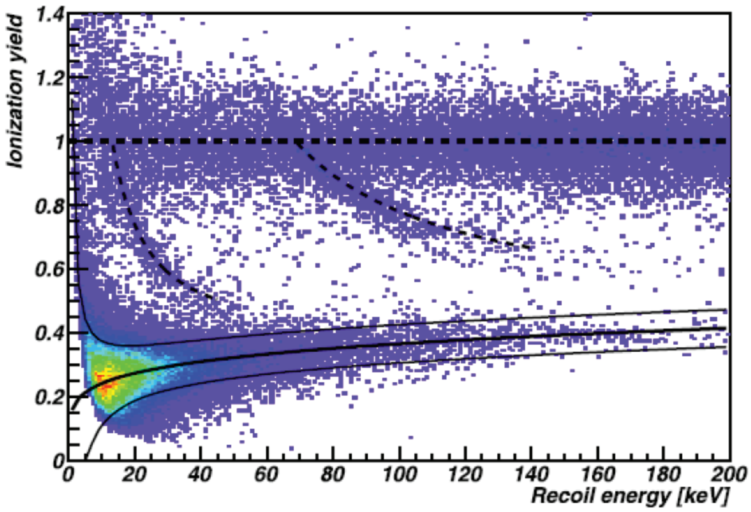

Figure 14.15: Distribution of the ionization yield versus recoil energy for fiducial events recorded during neutron calibrations for 10 Ge-ID detectors. The full lines represent the parametrization of Ref. [15] for nuclear recoils and the 90% CL nuclear recoil band. In addition to pure electron and nuclear recoils, inelastic nuclear recoils are visible with associated electromagnetic energies of 13.26 and 68.75 keV, due to the deexcitation of short-lived states of ^{73}Ge created by neutron diffusion (dashed lines).

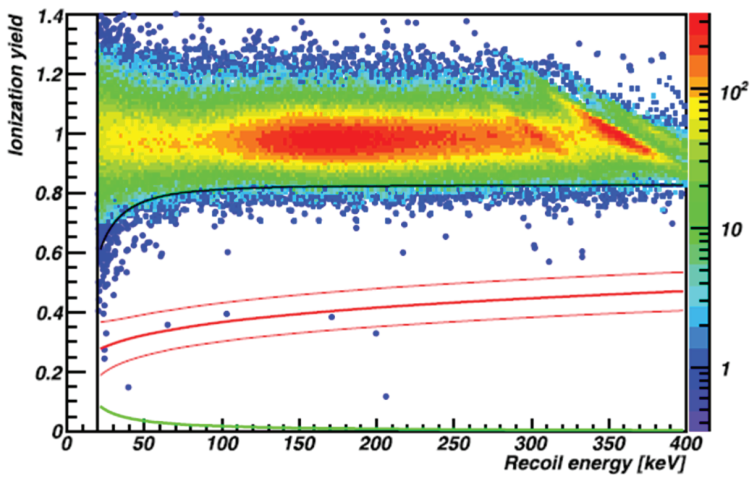

Figure 14.16: Distribution of the ionization yield versus recoil energy for fiducial events recorded by Ge-ID detectors during all γ-ray calibrations regularly performed with ^{133}Ba sources. The same period selection and quality cuts are applied as in the WIMP search. The top line represents the 99.99% lower limit of the electron recoil band for typical noise conditions. The bottom (green) line is the typical ionization threshold, while the 90% CL nuclear recoil region is represented as a red band.

14.1.4 Contribution of JINR Members

The Dubna team of the EDELWEISS experiment is formed on the basis of Department of Nuclear Spectroscopy, DLNP. This department has huge, almost 50-years, experience in high-precision nuclear spectroscopy using semiconductor and scintillator detectors in general and 20 years of experience in the study of rare processes in underground environments (like $\beta\beta$-studies in particular).

The Dubna team participates and makes a commitment to follow parts of the EDELWEISS project:

1. Assembly and commissioning of each new stage of the experiment;
2. Data taking (including daily routine procedures, as well as regular and special calibration runs);
3. Low background study and development of methods of neutron and radon detection;
4. Development new detectors;
5. Detector simulations, data acquisition and data analysis.

Assembly and commissioning, data taking: From the start of the EDELWEISS experiment the Dubna team participated in its commitment to detector assembly, from commissioning of the EDELWEISS environment (clean room operation and procedures, developing procedures of operation with radioactive sources on the site, etc) to participation in cryostat assembly and detector installation and wiring.

Our responsibility also includes the on-site certification of sources before use in EDELWEISS. We participate in commissioning and debugging of electronics and data taking. The data taking process includes the need for detector regeneration every day. This requires participation in shift duties, shared between experts on data taking among few EDELWEISS institutions. This work is partly done from Dubna by network.

Low background study and development of methods of neutron and radon detection: For unbiased interpretation of results of dark matter experiments it is critically important to have a wide knowledge and understanding of all background sources. Not only the size of the background, but also how it changes change with time are important. The main activities of the Dubna team are connected with experimental and MC studies of backgrounds. Experimental studies include:

a) Participation in material selection process (measurements on designated materials performed at LSM HPGe low background spectrometer and alpha spectrometer build by the JINR team);

b) Continuous monitoring of fast neutrons and the building of high sensitive, low background detection systems at JINR is performed in parallel with WIMP data taking;

c) Measurement of fast neutrons produced by muons in coincidence with EDELWEISS muon veto system;

d) Measurement of thermal neutrons and the building of low background neutron detection system at JINR;

e) Monitoring of radon level at close proximity to the EDELWEISS cryostat, and at the storage and at exit of the anti-radon factory with two high sensitivity (1 mBq/m^3) and low background radon detection system built in JINR.

Main results of the above studies are:

1. We measured fast and thermal neutron levels and the changes over time at the LSM underground laboratory. Continuous measurements of neutron flux are already continued for about 8 years. Long measurements with the neutron detector allowed us to estimate of stability of the neutron flux to be $< 4\%$ (90% CL).
2. We measured the neutron flux inside of EDELWEISS shields. Thermal neutron flux detected inside of the shields has been found to be $7.3 \pm 1.8 \cdot 10^{-9}$ neutron/cm^2/sec. This is the first independent measurement of neutron flux in close proximity to dark matter search detectors. The obtained results are in agreement with later results from the WIMP search.
3. Using our neutron detector and Ge detector data we directly demonstrated the effectiveness of the EDELWEISS neutron shield with a strong neutron source placed in different positions outside of the shield.
4. We achieved a level of ^{222}Rn at the EDELWEISS cryostat proximity below 50 mBq/m^3. With continuous control of the radon level at the time of WIMP data taking, the gamma background at EDELWEISS has been reduced by several factors. Performed by our group, the arrangement of anti-radon protection for EDELWEISS experiment is shown in Fig. 14.17.

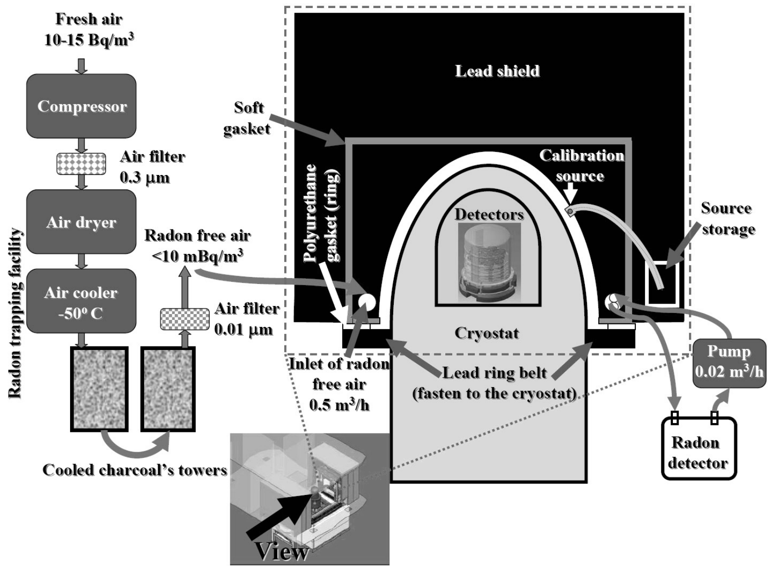

Figure 14.17: Scheme of radon environment of EDELWEISS cryostat. Only the upper part of the shield is shown. All anti-radon equipment and the detector were produced with JINR participation.

5. We use the radon detector to control tightness of the shield. We found experimentally that even a small gap introduce a significant and easily measurable radon contamination of air. the importance of such control can not be underestimated for such experiments as EDELWEISS, searching extremely rare WIMP-nucleon scattering events.

6. By MC and by direct calibrations with β-sources we demonstrated that low energy events have a source in trace surface contamination by radon progenies.
7. Using MC parameters, made by us, for fiducial volume cuts for ID detectors were estimated.

Detectors built by the JINR group for the EDELWEISS experiment are shown on the Fig. 14.18. In 2011 the EDELWEISS collaboration decided to extend its research area to low mass WIMPs using low threshold point contact HPGe detectors developed by JINR.

Figure 14.18: Detectors built by JINR to study background at the EDELWEISS environment. Top: The left picture is of the detector of fast neutrons; middle one is detector of thermal neutrons (on the wall); on the right is the radon detection system installed at the EDELWEISS clean room and measuring air around of the cryostat; Bottom: The left picture is another highly sensitive radon detector developed by JINR; Right: Photo of the vacuum chamber of the alpha spectrometer containing electronic module (preamplifier, shaping amplifier, power supply, vacuum control module).

As a first step one $\sim$240 g detector has been delivered to the EDELWEISS site. The detector has been installed in an available cryostat Fig. 14.19 and tested during 2012 inside of the available EDELWEISS-I low background shield.

Four-point contact detectors with total mass 1800 g will be delivered to the EDELWEISS site by the JINR group in 2014. The detectors are implemented in the low background cryostat with low-noise FET and preamplifier. After the low mass WIMP search (thus obtaining

Figure 14.19: Left: Work with HPGe point contact detector at EDELWEISS site (S. Rozov). Right: The point contact detector wrapped in roman lead.

proper background measurement) this setup will be used for search of coherent neutrino scattering at the Kalininskaya nuclear power plant.

14.1.5 Publications, Theses and Conferences

As a result of the project the following

- papers has been published: [14, 16–30],
- Master theses defended: A. Frolova (Irkutsk State University, 2010), D. Trynkova (Irkutsk State University, 2011),
- PhD thesis defended: A. Lubashevskiy (2010), ”Results of WIMP search at EDELWEISS experiment”,
- talks given at conferences and workshops:

  Plenary talks

  1. E. Yakushev, ”Search for Dark Matter with Ultra-sensitive Ge Detectors at the Underground Laboratory of Modane”, The International Workshop on Prospects of Particle Physics: ”Neutrino Physics and Astrophysics”, January 26 - Ferbuary 2, 2014, Valday, Russia.
  2. E. Yakushev, ”Dark matter - JINR at EDELWEISS and EURECA ”, German-JINR projects in Astroparticle Physics: status and perspectives, ОИЯИ, Дубна, Россия, 2013.
  3. E. Yakushev, ”Development of Low Energy Threshold HPGe Detectors at JINR”, The International Workshop on Non-Accelerator New Physics, 2013 E. Yakushev,

"Search for dark matter with ultra-sensitive bolometric Ge detectors at the Underground Laboratory of Modane (EDELWEISS)", International Workshop «40 years IN2P3-JINR collaboration anniversary», 2013.

4. E. Yakushev, "Development of Low Energy Threshold HPGe Detectors at JINR ", International Workshop "Low Threshold Detectors and Their Application in Neutrino Physics", 2012.
5. Е. Якушев для коллаборации EDELWEISS, "Прямой поиск небарионной темной материи с HPGe болометрами в эксперименте EDELWEISS, Рабочее совещание по возможности применения сцинтилляционных кристаллов LiF в экспериментах по поиску частиц темной материи", ИЯИ РАН, Москва, Москва, Россия, 2012.
6. E. Yakushev, "Neutron Background Measurements", First ULISSE@FREJUS Workshop, 2012 E. Yakushev, "Neutron background measurements at the Modane Underground Laboratory" 12nd Topical Workshop in Low Radioactivity Techniques, CNRS and Laboratoire Souterrain de Modane, 2006.
7. E. Yakushev, "New Measurements of Neutron Flux at LSM", Международное совещания «Настоящее и будущее экспериментов по двойному бета распаду в Европе», 2006.
8. A.V.Lubashevskiy, "Investigation of the background caused by ^{222}Rn daughters products" Conference: Searching for Dark Matter, Les Houches, Франция 2009.

Section talks:

1. S. Rozov, "Создание источника нейтронов с прецизионно определенной активностью для целей низкофоновых измерений", XVIII конференция молодых учёных и специалистов ОМУС-2014, ОИЯИ, Дубна, Россия.
2. S. Rozov, "Измерение потока нейтронов внутри горной породы в подземной лаборатории LSM", XVIII конференция молодых учёных и специалистов ОМУС-2014, ОИЯИ, Дубна, Россия.
3. S. Rozov, "Возможность регистрации сверх низких нейтронных потоков с использованием задержанных гамма переходов в Ge-73.", XVI конференция молодых учёных и специалистов ОМУС-2012, ОИЯИ, Дубна, Россия.
4. S. Rozov, "Development of low energy threshold HPGe detectors in JINR", LXII International Conference on Nuclear Physics "Nucleus-2012", Voronezh State University, Voronezh, Russia, 2012.
5. E. Yakushev, "Radon in LSM underground laboratory", LXII International Conference on Nuclear Physics "Nucleus-2012", Voronezh State University, Voronezh, Russia, 2012.
6. S. Rozov, "Neutron flux in EDELWEISS-II experiment", LX International Conference on Nuclear Physics, "Nucleus-2012", Voronezh State University, Voronezh, Russia, 2012.

7. S. Rozov, ”Фон нейтронов в эксперименте по прямому поиску темной материи EDELWEISS-II” S. Rozov, ”Измерение потока тепловых нейтронов в подземной лаборатории LSM”, Международное совещание по ядерной спектроскопии и структуре атомного ядра, Чебоксары, Россия 2009.

8. A.V.Lubashevskiy, ”Precision measurements of ^{210}Bi beta spectrum with EDELWEISS” International Conference on Nuclear Physics, 2010.

9. A.V.Lubashevskiy, ”Идентификация и устранение фоновых событий в эксперименте по поиску небарионной темной материи EDELWEISS”, Международное совещание по ядерной спектроскопии и структуре атомного ядра, Чебоксары, Россия 2009.

14.1.6 Finances

Major sources and amount of finances and major equipment together with major travel expenses acquired during the project runtime are listed in Tab. 14.1.

Source	Amount obtained (k$)	Major Equipment acquired
1100 and RFBR	64	Detection systems for measurements of low flux of fast neutrons (one for LSM, one for R&D in Dubna
1100 and RFBR	40	Detection systems for measurements of low flux of thermal neutrons (one for LSM, one for R&D in Dubna
1100 and RFBR	55	Radon detectors (2 for LSM, 2 for JINR)
1100 and RFBR	20	Low background alpha detection system, alpha detectors (1 for EDELWEISS at LSM, 1 for R&D in Dubna)
1100 and RFBR	50	Electronic components (spectroscopy amplifiers, HV supplies, crates, acquisition systems, etc for R&D works in Dubna
1100 and RFBR	35	Vacuum components and equipments for R&D works in Dubna
1100 and RFBR	17	Clean room equipments for R&D works in Dubna
1100 and RFBR	12	Calibration sources
1100 and RFBR	15	Computers and computer equipments
1100	21 per year	Travel expenses

Table 14.1: Major sources and amount of finances and major equipment acquired.

References

[1] H.V. Peiris et al. “First year Wilkinson Microwave Anisotropy Probe (WMAP) observations: Implications for inflation”. In: *Astrophys.J.Suppl.* 148 (2003), p. 213. arXiv: astro-ph/0302225 [astro-ph].

[2] Robert Caldwell and Marc Kamionkowski. “Dark matter and dark energy”. In: *Nature* 458 (2009), pp. 587–589.

[3] Gianfranco Bertone et al. “Particle Dark Matter: Observations, Models and Searches”. In: (2010). Ed. by Gianfranco Bertone.

[4] Claude Amsler et al. “Review of Particle Physics”. In: *Phys.Lett.* B667 (2008), pp. 1–1340.

[5] Z. Ahmed et al. “Search for Weakly Interacting Massive Particles with the First Five-Tower Data from the Cryogenic Dark Matter Search at the Soudan Underground Laboratory”. In: *Phys.Rev.Lett.* 102 (2009), p. 011301. arXiv: 0802.3530 [astro-ph].

[6] V.N. Lebedenko et al. “Limits on the spin-dependent WIMP-nucleon cross-sections from the first science run of the ZEPLIN-III experiment”. In: *Phys.Rev.Lett.* 103 (2009), p. 151302. arXiv: 0901.4348 [hep-ex].

[7] E. Aprile et al. “First Dark Matter Results from the XENON100 Experiment”. In: *Phys.Rev.Lett.* 105 (2010), p. 131302. arXiv: 1005.0380 [astro-ph.CO].

[8] Leszek Roszkowski, Roberto Ruiz de Austri, and Roberto Trotta. “Implications for the Constrained MSSM from a new prediction for $b \to s\gamma$”. In: *JHEP* 0707 (2007), p. 075. arXiv: 0705.2012 [hep-ph].

[9] Z. Ahmed et al. “Search for inelastic dark matter with the CDMS II experiment”. In: *Phys.Rev.* D83 (2011), p. 112002. arXiv: 1012.5078 [astro-ph.CO].

[10] J. Angle et al. “Constraints on inelastic dark matter from XENON10”. In: *Phys.Rev.* D80 (2009), p. 115005. arXiv: 0910.3698 [astro-ph.CO].

[11] D. Yu. Akimov et al. “Limits on inelastic dark matter from ZEPLIN-III”. In: *Phys.Lett.* B692 (2010), pp. 180–183. arXiv: 1003.5626 [hep-ex].

[12] R. Bernabei et al. “New results from DAMA/LIBRA”. In: *Eur.Phys.J.* C67 (2010), pp. 39–49. arXiv: 1002.1028 [astro-ph.GA].

[13] John R. Ellis et al. “Update on the direct detection of supersymmetric dark matter”. In: *Phys.Rev.* D71 (2005), p. 095007. arXiv: hep-ph/0502001 [hep-ph].

[14] E. Armengaud et al. “Axion searches with the EDELWEISS-II experiment”. In: *JCAP* 1311 (2013), p. 067. arXiv: 1307.1488 [astro-ph.CO].

[15] O. Martineau et al. “Calibration of the EDELWEISS cryogenic heat-and-ionisation germanium detectors for dark matter search”. In: *Nucl.Instrum.Meth.* A530 (2004), pp. 426–439. arXiv: astro-ph/0310657 [astro-ph].

[16] E. Armengaud et al. “Background studies for the EDELWEISS dark matter experiment”. In: *Astropart.Phys.* 47 (2013), pp. 1–9. arXiv: 1305.3628 [physics.ins-det].

[17] B. Schmidt et al. "Muon-induced background in the EDELWEISS dark matter search". In: *Astropart.Phys.* 44 (2013), pp. 28–39. arXiv: 1302.7112 [astro-ph.CO].

[18] G.A. Cox et al. "A multi-tiered data structure and process management system based on ROOT and CouchDB". In: *Nucl.Instrum.Meth.* A684 (2012), pp. 63–72.

[19] E. Armengaud et al. "A search for low-mass WIMPs with EDELWEISS-II heat-and-ionization detectors". In: *Phys.Rev.* D86 (2012), p. 051701. arXiv: 1207.1815 [astro-ph.CO].

[20] A.S. Frolova et al. "Neutron Background from the (alpha, n) Reaction on C-13 in the EDELWEISS-II experiment on direct search for weakly interacting particles of nonbaryonic cold dark matter". In: *Phys.Part.Nucl.Lett.* 8 (2011), pp. 786–788.

[21] H. Kraus et al. "EURECA". In: *PoS* IDM2010 (2011), p. 109.

[22] Z. Ahmed et al. "Combined Limits on WIMPs from the CDMS and EDELWEISS Experiments". In: *Phys.Rev.* D84 (2011), p. 011102. arXiv: 1105.3377 [astro-ph.CO].

[23] E. Armengaud et al. "Final results of the EDELWEISS-II WIMP search using a 4-kg array of cryogenic germanium detectors with interleaved electrodes". In: *Phys.Lett.* B702 (2011), pp. 329–335. arXiv: 1103.4070 [astro-ph.CO].

[24] V. Yu. Kozlov et al. "A detection system to measure muon-induced neutrons for direct Dark Matter searches". In: *Astropart.Phys.* 34 (2010), pp. 97–105. arXiv: 1006.3098 [astro-ph.IM].

[25] H. Kraus et al. "EURECA: The future of cryogenic dark matter detection in Europe". In: *PoS* IDM2008 (2008), p. 013.

[26] E.A. Yakushev et al. "Search for cold dark matter non-baryonic particles in the EDELWEISS-II experiment". In: *Russ.Phys.J.* 53 (2010), pp. 611–615.

[27] S. Rozov et al. "Monitoring of the thermal neutron flux in the LSM underground laboratory". In: (2010). arXiv: 1001.4383 [astro-ph.IM].

[28] E. Armengaud et al. "First results of the EDELWEISS-II WIMP search using Ge cryogenic detectors with interleaved electrodes". In: *Phys.Lett.* B687 (2010), pp. 294–298. arXiv: 0912.0805 [astro-ph.CO].

[29] A. Broniatowski et al. "A new high-background-rejection dark matter Ge cryogenic detector". In: *Phys.Lett.* B681 (2009), pp. 305–309. arXiv: 0905.0753 [astro-ph.IM].

[30] S. Fiorucci et al. "Identification of backgrounds in the EDELWEISS-I dark matter search experiment". In: *Astropart.Phys.* 28 (2007), pp. 143–153. arXiv: astro-ph/0610821 [astro-ph].